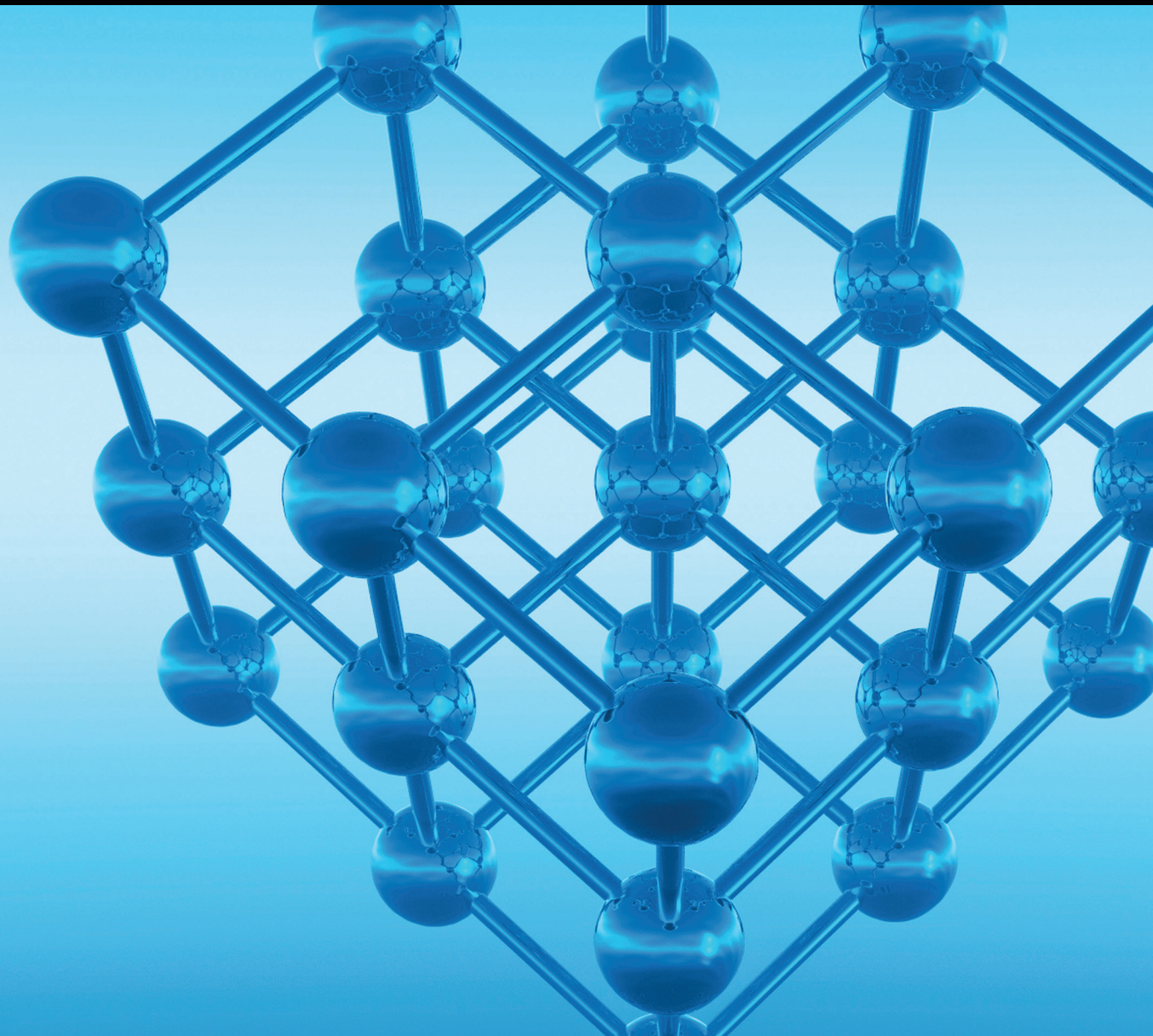


# Self-Assembled and Artificial Surfaces/Interfaces: From Soft Matter to Metamaterials

Lead Guest Editor: Duyang Zang

Guest Editors: Yuri Tarasevich, Liyuan Zhang, Sujata Tarafdar, and Changlin Ding



---



## **Self-Assembled and Artificial Surfaces/Interfaces: From Soft Matter to Metamaterials**

Advances in Condensed Matter Physics

---

## **Self-Assembled and Artificial Surfaces/Interfaces: From Soft Matter to Metamaterials**

Lead Guest Editor: Duyang Zang

Guest Editors: Yuri Tarasevich, Liyuan Zhang, Sujata Tarafdar,  
and Changlin Ding



Copyright © 2018 Hindawi. All rights reserved.

This is a special issue published in "Advances in Condensed Matter Physics." All articles are open access articles distributed under the Creative Commons Attribution License, which permits unrestricted use, distribution, and reproduction in any medium, provided the original work is properly cited.

## **Editorial Board**

Bohdan Andraka, USA

Ward Beyermann, USA

Golam M. Bhuiyan, Bangladesh

Luis L. Bonilla, Spain

Ashok Chatterjee, India

Ram N. P. Choudhary, India

Oleg Derzhko, Ukraine

Gayanan Fernando, USA

Jörg Fink, Germany

Yuri Galperin, Norway

Prasenjit Guptasarma, USA

Da-Ren Hang, Taiwan

Jan A. Jung, Canada

Joseph S. Poon, USA

Leonid Pryadko, USA

Charles Rosenblatt, USA

Mohindar S. Seehra, USA

Sergei Sergeenkov, Brazil

Sergio E. Ulloa, USA

Markus R. Wagner, Germany

Gary Wysin, USA

Kiyokazu Yasuda, Japan

Fajun Zhang, Germany

Jiandi Zhang, USA

# Contents

## **Self-Assembled and Artificial Surfaces/Interfaces: From Soft Matter to Metamaterials**

Duyang Zang , Yuri Tarasevich , Liyuan Zhang, Sujata Tarafdar , and Changlin Ding  
Editorial (2 pages), Article ID 9701423, Volume 2018 (2018)

## **Enhanced Coffee-Ring Effect via Substrate Roughness in Evaporation of Colloidal Droplets**

Yongjian Zhang , Xubo Chen, Fenggang Liu, Lei Li, Jun Dai, and Teng Liu  
Research Article (9 pages), Article ID 9795654, Volume 2018 (2018)

## **The Effect of Geometrical Parameters on Resonance Characteristics of Acoustic Metamaterials with Negative Effective Modulus**

Xiao-Le Yan, Li-Mei Hao , Mei-Ling Men, and Zhi Chen   
Research Article (8 pages), Article ID 4847036, Volume 2018 (2018)

## **Droplet Drying Patterns on Solid Substrates: From Hydrophilic to Superhydrophobic Contact to Levitating Drops**

Sujata Tarafdar , Yuri Yu. Tarasevich , Moutushi Dutta Choudhury, Tapati Dutta, and Duyang Zang  
Review Article (24 pages), Article ID 5214924, Volume 2018 (2018)

## **Formation of Hierarchical Porous Structure via Breath Figure Method**

Yongjian Zhang and Zhiguang Li   
Research Article (6 pages), Article ID 1265479, Volume 2018 (2018)

## **Effect of Direct Current on Solid-Liquid Interfacial Tension and Wetting Behavior of Ga-In-Sn Alloy Melt on Cu Substrate**

Limin Zhang , Ning Li, Hui Xing, Rong Zhang , and Kaikai Song  
Research Article (7 pages), Article ID 6328976, Volume 2018 (2018)

## **Anomalous Reflection of Acoustic Waves in Air with Metasurfaces at Low Frequency**

Huajun Chen   
Research Article (7 pages), Article ID 5452071, Volume 2018 (2018)

## **Photocatalytic Surface Modification of PI Film for Electroless Copper Plating**

Wenxia Zhao , Zenglin Wang, Liang Qiao, Shiwei Liu, Hongjian Zhao, and Yani Yan  
Research Article (8 pages), Article ID 1619581, Volume 2018 (2018)

## **Tadpole-Shaped POSS-Based Copolymers and the Aggregation Behavior at Air/Water Interface**

Lin Zhu, Fang Chen , Xiaoyan Ma, Xiu Qiang, Zhiguang Li, Chen Dong, and Duyang Zang  
Research Article (10 pages), Article ID 3787843, Volume 2018 (2018)

## Editorial

# Self-Assembled and Artificial Surfaces/Interfaces: From Soft Matter to Metamaterials

Duyang Zang<sup>1</sup>,<sup>ID</sup> Yuri Tarasevich<sup>2</sup>,<sup>ID</sup> Liyuan Zhang,<sup>3</sup>  
Sujata Tarafdar<sup>4</sup>,<sup>ID</sup> and Changlin Ding<sup>1</sup>

<sup>1</sup>Department of Applied Physics, Northwestern Polytechnical University, Xi'an, China

<sup>2</sup>Laboratory of Mathematical Modeling, Astrakhan State University, Astrakhan, Russia

<sup>3</sup>Department of Chemical Engineering, Monash University, Melbourne, VIC, Australia

<sup>4</sup>Condensed Matter Physics Research Center (CMPRC), Physics Department, Jadavpur University, Kolkata, India

Correspondence should be addressed to Duyang Zang; [dyzang@nwpu.edu.cn](mailto:dyzang@nwpu.edu.cn)

Received 26 April 2018; Accepted 26 April 2018; Published 29 May 2018

Copyright © 2018 Duyang Zang et al. This is an open access article distributed under the Creative Commons Attribution License, which permits unrestricted use, distribution, and reproduction in any medium, provided the original work is properly cited.

Surfaces or interfaces play an essential role in achieving the performance of materials, including both the mechanical and the physical/chemical properties. The interfaces dominate the behavior of many types of materials ranging from traditional condensed matter to soft condensed matter, such as nanoparticles, thin solid films, colloids, and electrorheological fluids. The surfaces/interfaces can be obtained via various approaches, say from self-assembly to completely artificial design. The appropriate design of artificial surface structure can be utilized to manipulate the electromagnetic waves or sound waves. Despite the fact that the topic has a long history of research, it still remains a challenge to get a full understanding of the formation mechanisms and the functionalities of these interfaces, because of the coupling between surfaces/interfaces with external fields and the complexity of multiscale interactions. In this special issue, we have invited several papers that address these concerns.

Evaporation induced self-assembly and pattern formation is one of the simplest but important approaches to fabricate ordered structures. In the first paper of the topical issue, S. Tarafdar et al. have reviewed the various patterns obtained from droplet drying ranging from simple solutions to complex biological liquids. The review includes both experimental observations and theoretical and simulation results and highlights the effect of contact angle on the formation of these patterns. In the second paper, Y. Zhang et al. have reported that the increase in substrate roughness can

lead to enhanced coffee-ring effect. By contrast to the self-assembly caused by direct evaporation, the so-called breath figure method has a droplet nucleation process which serves as a template for the formation of porous structures. At an appropriate condition, hierarchical porous structures can be obtained, as reported in the third paper by Z. Li et al.

The self-assembly on surfaces/interfaces is of great importance to fabricate two-dimensional functional materials, where the spreading of building block solution on the interfaces plays a central role. In the fourth paper, M. Li et al. have presented a study on diffusion behavior of an ink droplet on silk woven fabrics and found that the woven structure can lead to anisotropic diffusion dynamics of ink. In the fifth paper, F. Chen et al. have found that the aggregation behaviors of copolymers at the air-water interface are dependent on the block ratios. The different aggregation processes lead to varied interfacial rheological properties and Langmuir-Blodgett (LB) film morphologies.

Artificial surfaces/interfaces provide an alternative approach to achieve unique functionalities, e.g., metamaterials. With proper arrangement of these surfaces/interfaces, acoustic waves or electromagnetic waves can be manipulated as required. In the sixth paper, X.-L. Yan et al. have obtained a precisely controllable unit structure with negative effective modulus by shifting the sizes of the unit cell. In the seventh paper, using a sessile drop method, L. Zhang et al. have investigated the effect of direct current (DC) on the wetting

behavior of Cu substrate by Ga–25In–13Sn liquid alloy at room temperature. In the eighth paper, H. Chen has proposed and numerically investigated an acoustic metasurface made of a composite structure of cavity and membrane, which can steer the reflected waves at will. In the ninth paper, W. Zhao et al. have investigated surface modification of polyimide (PI) film through TiO<sub>2</sub> photocatalytic treatment, which shows that the photocatalytic treatment is an environmentally friendly and effective method for the surface modification of PI films.

We hope this collection of articles will be useful to the condensed matter/material science community and inspire further research in new directions.

*Duyang Zang  
Yuri Tarasevich  
Liyuan Zhang  
Sujata Tarafdar  
Changlin Ding*

## Research Article

# Enhanced Coffee-Ring Effect via Substrate Roughness in Evaporation of Colloidal Droplets

**Yongjian Zhang** , **Xubo Chen**, **Fenggang Liu**, **Lei Li**, **Jun Dai**, and **Teng Liu**

*Shaanxi Key Laboratory of Surface Engineering and Remanufacturing, Xi'an University, Xi'an 710065, China*

Correspondence should be addressed to Yongjian Zhang; zhangyongjian@mail.nwp.edu.cn

Received 17 January 2018; Accepted 1 April 2018; Published 7 May 2018

Academic Editor: Yuri Tarasevich

Copyright © 2018 Yongjian Zhang et al. This is an open access article distributed under the Creative Commons Attribution License, which permits unrestricted use, distribution, and reproduction in any medium, provided the original work is properly cited.

The analysis of dried drop patterns has various applications in research fields like archeology, medical practice, printing, and so on. In this paper, we studied the evaporation and pattern formation of polytetrafluoroethylene (PTFE) colloid droplets on smooth substrate and rough substrates with different roughness. We found that the evaporation of droplets shows remarkable coffee-ring effect on smooth substrate and that the cross-section of the ring is wedge-shaped with its thickness decreasing from the edge to the center. However, with increasing roughness, the effect strengthened, with the section of the coffee-ring changing from wedge- to hill-shaped. The contact angle decreased with increasing roughness, leading to an increase in evaporation rate. Moreover, wicking led to additional evaporation, which also enhanced capillary flow, moving more particles to the edge. In addition, the rough structure of the substrate inhibited the back-flow of the capillary flow, preventing the particles' move to the center. The formation of radial wrinkles on the edge also led to particle retention, preventing them from moving to the center. All these factors contribute to the decreased width and increased height of the coffee-ring pattern after evaporation on rough surfaces. It is an effective method to regulate the deposition pattern of evaporating droplet by changing the substrate roughness.

## 1. Introduction

Droplet evaporation is one of the most common physical phenomena occurring both in nature and in many industrial processes [1, 2]. Droplets containing relatively little volatile substance always form complex patterns after evaporation [3, 4]. Many studies have been conducted to understand the formation mechanism of the coffee-ring effect, as well as the formation of cracks in the patterns and ways to regulate this process. In 1997, Deegan et al. [5], who first revealed the mechanism of coffee-ring pattern formation via colloidal droplet evaporation, noted the important role of capillary flow on mass transport caused by uneven evaporation. Thereafter, many research groups studied the regulation of coffee-ring effect in different ways [6–9], including changing the shape of the suspended particles, adjusting the PH value of the dispersion, and using electrowetting method of controlling the movement of the contact line. In a recent study, the coffee-ring effect was effectively suppressed to achieve a uniform deposition of particles by introducing the

linear polymer polyethylene oxide (PEO) into SiO<sub>2</sub> colloidal droplets [10].

Another common phenomenon accompanied by droplet evaporation is the appearance of cracks. Sometimes the cracks, especially nanocracks, can serve as a template, for example, the preparation of nanowires [11]. But in most cases, such as the film making, large-area coating, cracks need to be suppressed. Chiu et al. [12] noted that cracks emerge when the deposition pattern thickness exceeds a critical value. Under these conditions, the release of elastic energy can be greater than the dissipated energy of crack formation. A variety of crack pattern morphologies can be formed during droplet evaporation, including spiral [13], wavy like [14], ring-shaped [15], and radial [16]. Boulogne et al. [17] studied the factors affecting crack morphology, such as particle properties, dispersant type, and drying conditions. Recently, we found that, after evaporation, polytetrafluoroethylene (PTFE) colloidal droplets can form radial cracks, owing to the formation of a similarly shaped stress field within droplets during evaporation process, which has been confirmed via formed radial

wrinkles during evaporation (confirmed by the formation of radial wrinkles) [16]. Moreover, evaporation of biological drops, such as blood, often leads to interesting crack patterns which contain valuable information for diagnosis [18].

Despite progress being made in regulating the coffee-ring effect and crack formation during droplet evaporation, the methods used often change the nature of the droplet itself, for example, by introducing polymers, inorganic particles, or changing the particle shape, which is unfavorable for producing a high-purity vapor-deposited film. Thus, it is necessary to adopt alternative approaches to regulate droplet evaporation. It has been reported that the substrates play an important role in pattern formation of drying drops [19]. We tried to change the substrate properties but not the droplet composition. This can be achieved by changing only the roughness of the substrate. Currently, there are very few studies of droplet evaporation on substrates with different roughness [20]. Accordingly, the mechanism by which roughness affects crack formation is unclear. To better understand these processes, in the present study we investigate evaporation and the patterns of colloidal droplets on a smooth glass slide substrate and glass substrates with different roughness. We reveal the influence of roughness to droplet evaporation, crack nucleation, and growth mechanism, thus providing a framework for the preparation of multifunctional films using evaporating method.

## 2. Methods and Materials

**2.1. Materials.** The colloidal suspension was made by dispersing polytetrafluoroethylene (PTFE) nanoparticles into water with a weight fraction of 60% by sonication for 30 minutes. The average radius of the particles is  $\sim 50$  nm, with a dynamic viscosity is  $6 \text{ mm}^2/\text{s}$  and a density of  $1.5 \text{ g/cm}^3$ . The water used in the experiments was purified with an Ultrapure Water System (EPED, China) with a resistivity of  $18.25 \text{ M}\Omega\cdot\text{cm}$ . The substrates used in the experiment include smooth glass slide and the glass slide polished by sand paper with different mesh size. In the polishing process, the sand paper was slid three times over the substrates under the same compressive stress. All substrates were cleaned in ultrasonic cleaners filled with alcohol and acetone successively.

**2.2. Morphology and Roughness Characterization.** The roughness of the substrates and the deposition pattern were measured using a laser scanning confocal microscope (ZEISS, LSM 800). To obtain more information of the morphology and structure of the evaporated deposition, the deposited patterns were studied using a scanning electron microscope (SEM, ZEISS-SUPRA-55). The section of the deposition pattern was also analyzed using laser scanning confocal microscope, confirming the thickness change in the radius direction of the pattern. Static contact angles were determined using the sessile drop method on a contact angle measurement apparatus (Powereach, JC2000D, China).

**2.3. Evaporation Experiments.** Droplets of the colloidal solution ( $\sim 0.2 \mu\text{L}$ ) were deposited with a microsyringe (total volume:  $1 \mu\text{L}$ ) on the substrate, which was cleaned thoroughly by alcohol and distilled water and dried in a drying oven. The evaporation process and the final deposited pattern were observed using optical microscopy (Olympus, BX51). For the evaporation process, images were recorded by means of a video recorder at 25 frames/s. All the experiments were carried out at room temperature  $\sim 22 \pm 2^\circ\text{C}$  and at relative humidity of  $\sim 45 \pm 5\%$ .

## 3. Results and Discussion

**3.1. Roughness and Contact Angle of the Substrate.** To study the influence of substrate roughness on the evaporation of the PTFE droplet, we characterized the surface morphology and roughness of the substrate. The results of laser scanning confocal microscopy are shown in Figures 1(a)–1(d) and the corresponding static contact angles on the different substrates are shown in Figures 1(e)–1(h). All the droplets for the experiment were dropped naturally. The static contact angle of the suspension on the smooth substrate was  $37^\circ$ . With increasing roughness, the contact angle decrease, as shown in Figures 1(e)–1(h) ( $35^\circ$ ,  $30^\circ$ ,  $27^\circ$ , and  $25^\circ$ , respectively).

A numerical relationship exists between the roughness and contact angle. In the Wenzel model,  $\cos \theta^* = r \cos \theta$ , where  $\theta^*$  is the apparent contact angle of the sessile drop on the substrate,  $r$  is the roughness of the smooth substrate, and  $\theta$  is the intrinsic contact angle (i.e., the contact angle for the ideal smooth substrate). The value of  $r$  will increase when the roughness increases and the value of  $\theta$  is constant. Thus, theoretically,  $\theta^*$  will decrease when  $r$  increases (i.e., the rougher the substrate, the smaller the contact angle). Our experimental results are in agreement with this relationship.

**3.2. Evaporation Patterns on Different Substrates.** Figure 2 shows the evaporation patterns of PTFE droplets deposited on smooth and rough substrates. The cross-sections of the smooth and rough substrates are shown in Figures 2(c) and 2(f), respectively. On the smooth substrate, the pattern is thicker near the edge and gradually becomes thin toward the center, as can be seen in Figures 2(a) and 2(c). The width of the coffee-ring is about 0.4 mm, which is more than half of the radius of the pattern. Radiating cracks distribute on the coffee-ring. In the center, some nanoparticles are scattered; however, at the center, because the thickness is smaller than the critical value [12], no crack emerges.

The coffee-ring effect is more remarkable on rougher substrates. The cross-section of the coffee-ring exhibits symmetrical hill-like shapes. The thickness of the shape reaches  $80 \mu\text{m}$  with a width of 0.2 mm. The width is about one-third of the radius. Cracks are distributed radially along the coffee-ring. The remainder of the pattern is covered by a few particles, which have not formed cracks yet.

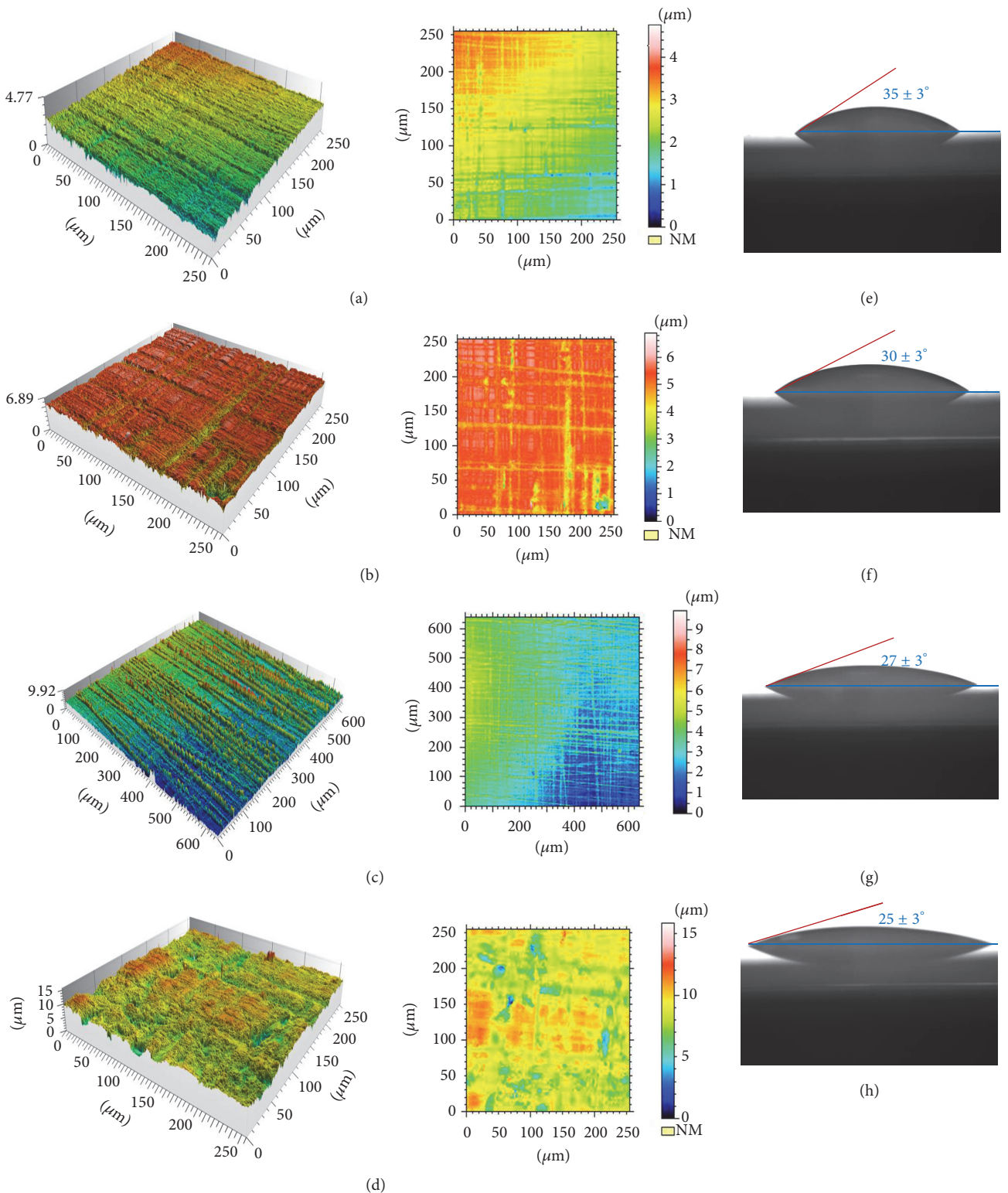


FIGURE 1: Surface roughness and contact angle of PTFE droplets on glass substrates. (a)–(d) Substrates with different roughness, polished using sandpaper with different mesh sizes. Larger sandpaper grain size increased the surface roughness. (e)–(h) Contact angle of the PTFE suspension on the substrate. The contact angle decreased as the substrate became rougher.

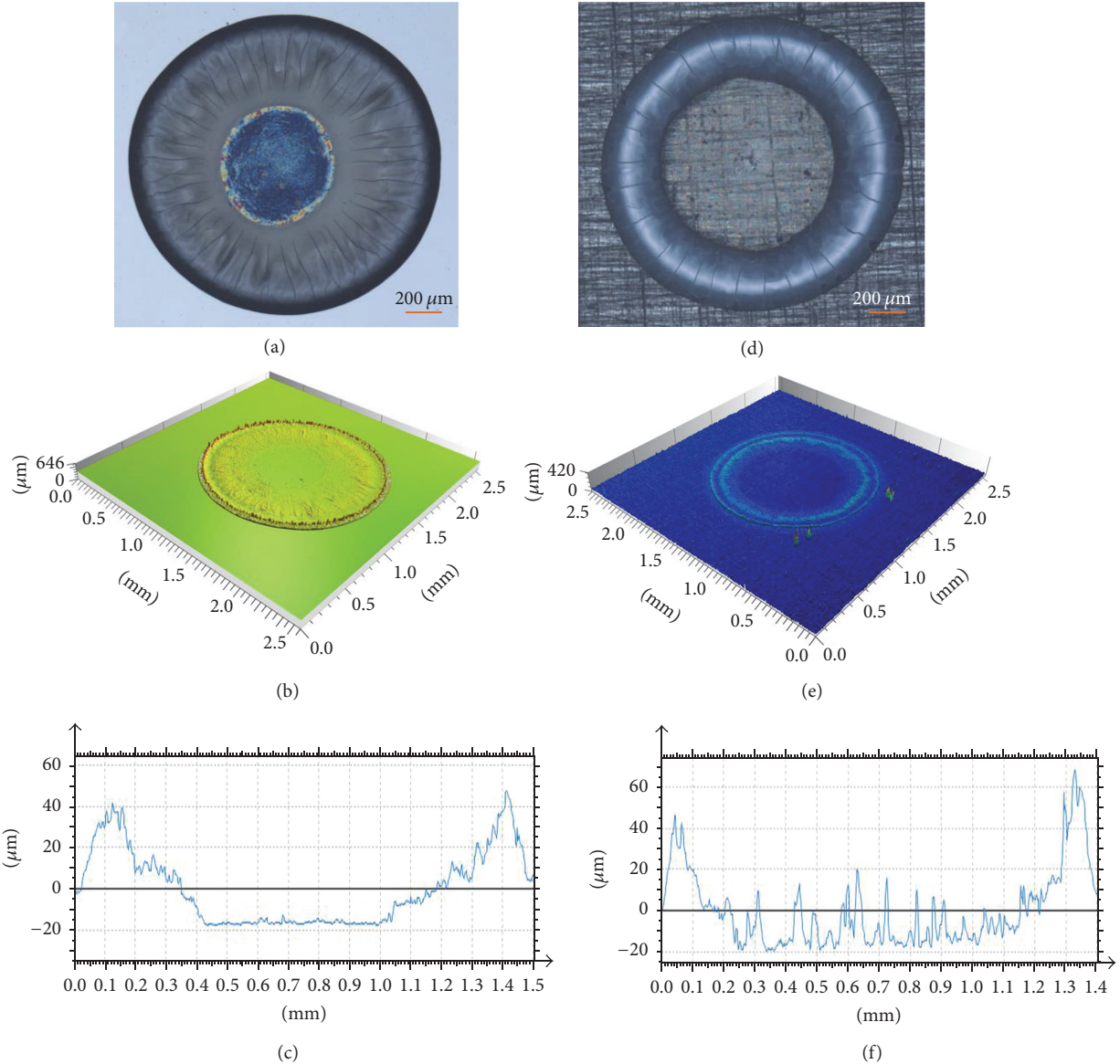


FIGURE 2: Evaporation patterns of PTFE colloidal droplets and their profiles on different substrates: (a)–(c) smooth substrate, (d)–(f) rough substrate.

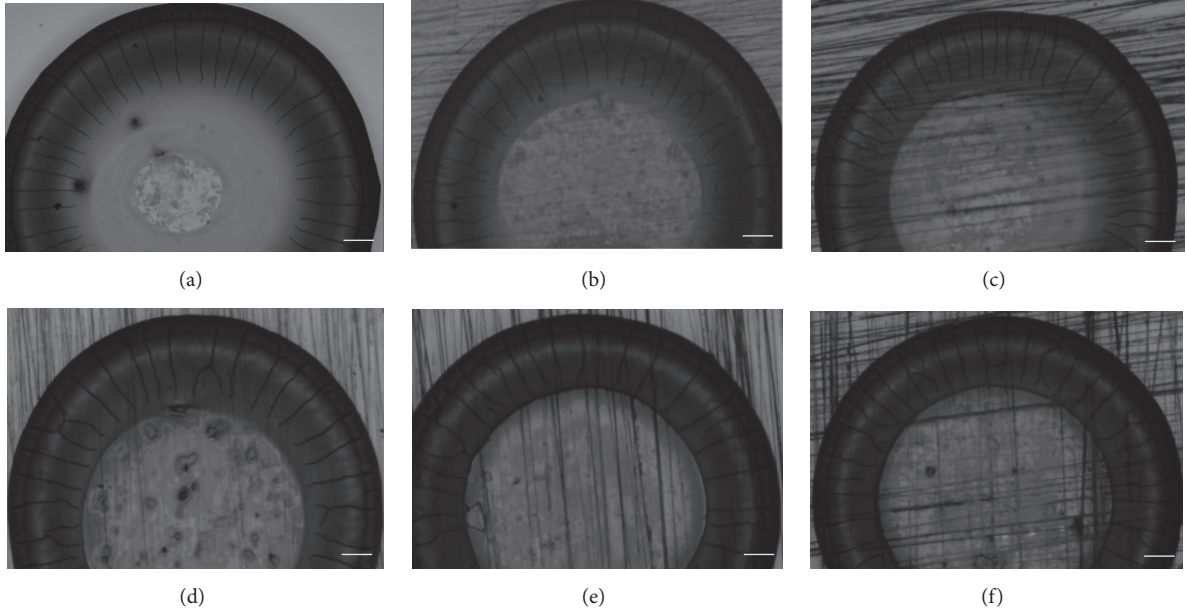
Figure 3 shows the evaporated patterns of the PTFE droplets deposited on smooth and rough substrates with different roughness. The pattern deposited on smooth glass clearly exhibits the widest coffee-ring. The cross-section is wedge-shaped, as can also be seen in Figures 2(b) and 2(c). With increasing roughness, the width of the coffee-ring decreased. The cross-section gradually changed from wedge- to hill-shaped, which is also exhibited in Figure 2. In addition, with increasing roughness, the total number of the crack decreases while the distance between adjacent cracks increases. The evaporation induced cracking is a competition between elastic energy stored and the surface energy of the newly produced area [16]. With the enhancement of coffee-ring effect due to increasing roughness, the cross-section area of the ring is increased. As a result, the total cracks

quantity decreases. Table 1 contains the parameters of the deposited patterns, including the width and height of the coffee-ring, number of cracks, and the distance between adjacent cracks. It should be noted that data listed in the table are average values, obtained at least 10 samples for each parameter.

**3.3. Dynamic Process of Colloid Droplets Evaporation.** To further reveal the mechanism by which substrate roughness affects pattern formation, we observed the process of droplet evaporation in real time. The evaporation process of PTFE colloid droplets on the smooth substrate is shown in Figure 4. The whole evaporation process lasts about 180 s, during which, cracks nucleate and grow within 3 s. Compared to the

TABLE 1: Parameters of evaporation patterns on different substrates.

Substrate roughness (mesh of sand paper)	Width of the coffee ring ( $\mu\text{m}$ )	Height of the coffee ring ( $\mu\text{m}$ )	Crack quantity	Crack distance ( $\mu\text{m}$ )
Smooth glass	$400 \pm 10$	$55 \pm 2$	$50 \pm 5$	$63 \pm 2$
1500	$250 \pm 6$	$60 \pm 2$	$48 \pm 4$	$65 \pm 2$
1000	$230 \pm 5$	$63 \pm 3$	$46 \pm 3$	$68 \pm 2$
800	$200 \pm 5$	$70 \pm 3$	$45 \pm 3$	$70 \pm 2$
400	$170 \pm 4$	$75 \pm 4$	$43 \pm 2$	$73 \pm 2$
200	$160 \pm 4$	$80 \pm 5$	$40 \pm 2$	$78 \pm 2$

FIGURE 3: Evaporation patterns of PTFE colloidal droplets on glass slides with different roughness: (a) smooth glass; (b)–(f) increasing surface roughness, achieved using sandpaper with mesh sizes of 1500, 1000, 800, 400, and 200, respectively (scale bars represent  $100 \mu\text{m}$ ).

droplet deposited on the rough substrate, the evaporation front of the droplet on the smooth substrate moves more slowly, probably because of the larger contact angle. At the same time, both the capillary flow and Marangoni flow are strong for the droplet on the smooth substrate. The move direction of the flows is reversed, slowing down the motion of the contact line. After formation of coffee-ring, radial cracks emerged. The cracks extend along the radial direction because evaporation of the outer rings causes cracks to be in a tangential tension state.

The evaporation process of PTFE colloidal droplets on a rough substrate is shown in Figure 5. In contrast to the smooth substrate, the whole evaporation process lasted less than 80 s. Crack formation and growth take just 1 s and the contact line moves more quickly than on the smooth surface. After 20 s, radial-shaped wrinkles emerged on the evaporation front. During the later stages of evaporation, the contact line moved more quickly, mainly because of the greatly reduced number of particles remaining in the colloidal suspension. Cracks form cores more easily and

grow far more rapidly on the rough substrate than on the smooth one, mainly because the rough substrate offers more nucleation sites, making it easier to form cracking cores. In addition, the thicker coffee-ring stored more energy, enhancing the expansion rate.

**3.4. Formation Mechanism of Evaporating Patterns.** The evaporation of PTFE colloid droplets is always accompanied by obvious coffee-ring effect on solid substrate (Figure 2), with the contact line of the droplet pinned during evaporation (Figures 4 and 5). As shown by Deegan et al. [5], the capillary compensating flow is caused by the pinning of the contact line and the evaporating heterogeneity of droplets, which also lead to the continuous accumulation of colloid particles at the contact line. Evaporating patterns are always ring-like stains on hydrophilic substrates [10]. However, the deposition morphology is different when the roughness changes. During our experiment, the cross-section changed from wedge- to hill-shaped with the width of the coffee-ring decreasing with increasing surface roughness.

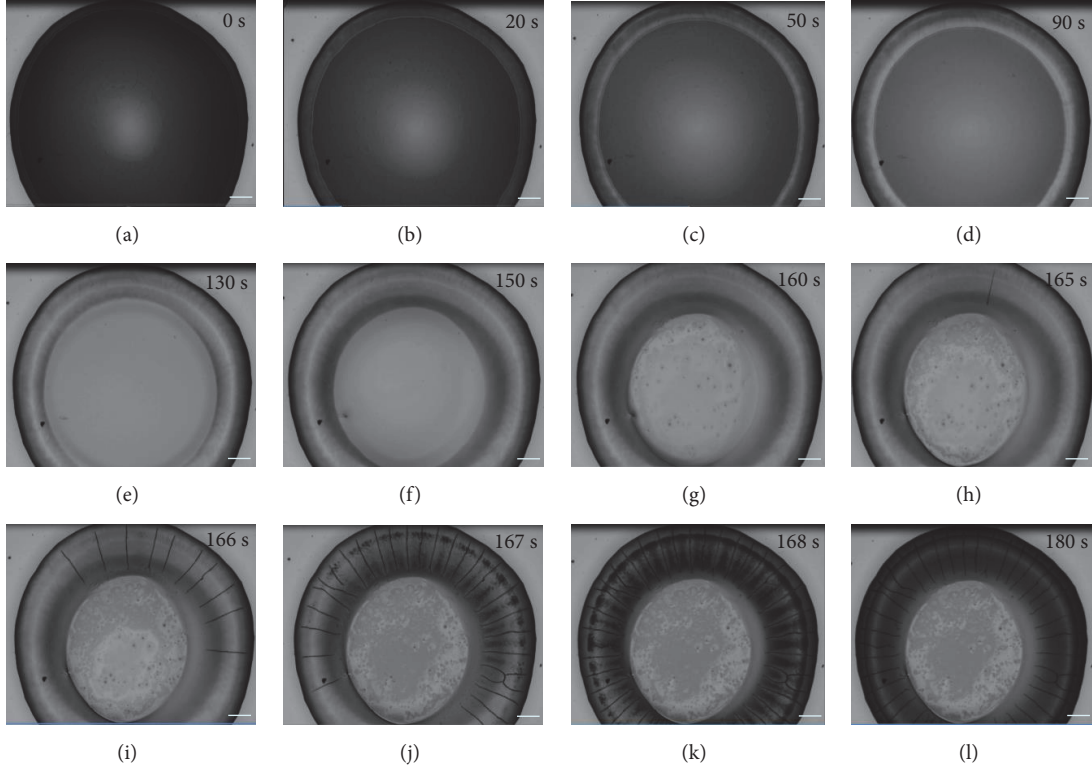


FIGURE 4: Evaporation dynamics of a PTFE droplet on a smooth substrate. Panels (a)–(l) correspond to different evaporation times (scale bars represent  $100 \mu\text{m}$ ).

Several factors contribute to these results, just as shown in Figure 6. The most important is that when the roughness of the substrate increases, the contact angle of the droplet decreases, which leads to an increased evaporation rate at the edges. Meanwhile, the wicking effect provides additional evaporation mass, strengthening the capillary flow. These factors result in many particles moving to the edge. In addition, the roughness of the substrate reinforces pinning of the contact line, intensifying contact angle hysteresis and thus helping particles move to and remain at the edge. In addition, the circumfluence which flows from the edge to the center is hindered by the roughness of the substrate. When the roughness increased to the critical value, the circumfluence along it is hindered, and the capillary compensation circulating current will not be established. Under these conditions, no particles can be brought back to the center. It is worth pointing out that the circumfluence is not hindered when evaporating on smooth substrate, such that it is possible to set up a capillary compensating circulating current. Some particles on the edge, which are transported by the capillary flow, are removed to the center by the circumfluence, resulting in the coffee-ring gradually extending from the edge to the center, as shown in Figure 6(c). Finally, during the evaporation process, helical corrugated wrinkles emerged on the evaporation front, as shown in Figure 5, which also prevent particles located on the edge from moving to the center.

On rough substrates, particles can be easily transported to the edge where they remain. This results in relatively few particles being located in the center after evaporation. The evaporation front moves more quickly during the final stages of evaporation because of the small number of particles in the center. These factors and those described above work together to strengthen the coffee-ring effect, decreasing the width and increasing the thickness of the coffee-ring.

In addition to difference in morphology, the dynamics of crack expansion is influenced by the roughness of the substrate. A greater number of nucleation sites on rougher substrate make crack formation easier. The crack expansion rate on rough substrates is much higher than that on a smooth substrate because the coffee-ring is thicker and stores more elastic energy during evaporation. However, because of the complexity of evaporation and the time variation of crack growth, it is still a great challenge to build a precise dynamic model to describe crack growth during evaporation.

#### 4. Conclusions

We draw conclusions from studying the evaporation and pattern formation of PTFE colloid droplets on smooth and rough substrates:

- (1) The coffee-ring effect emerged when PTFE colloid droplets evaporated on a smooth substrate. The cross-section

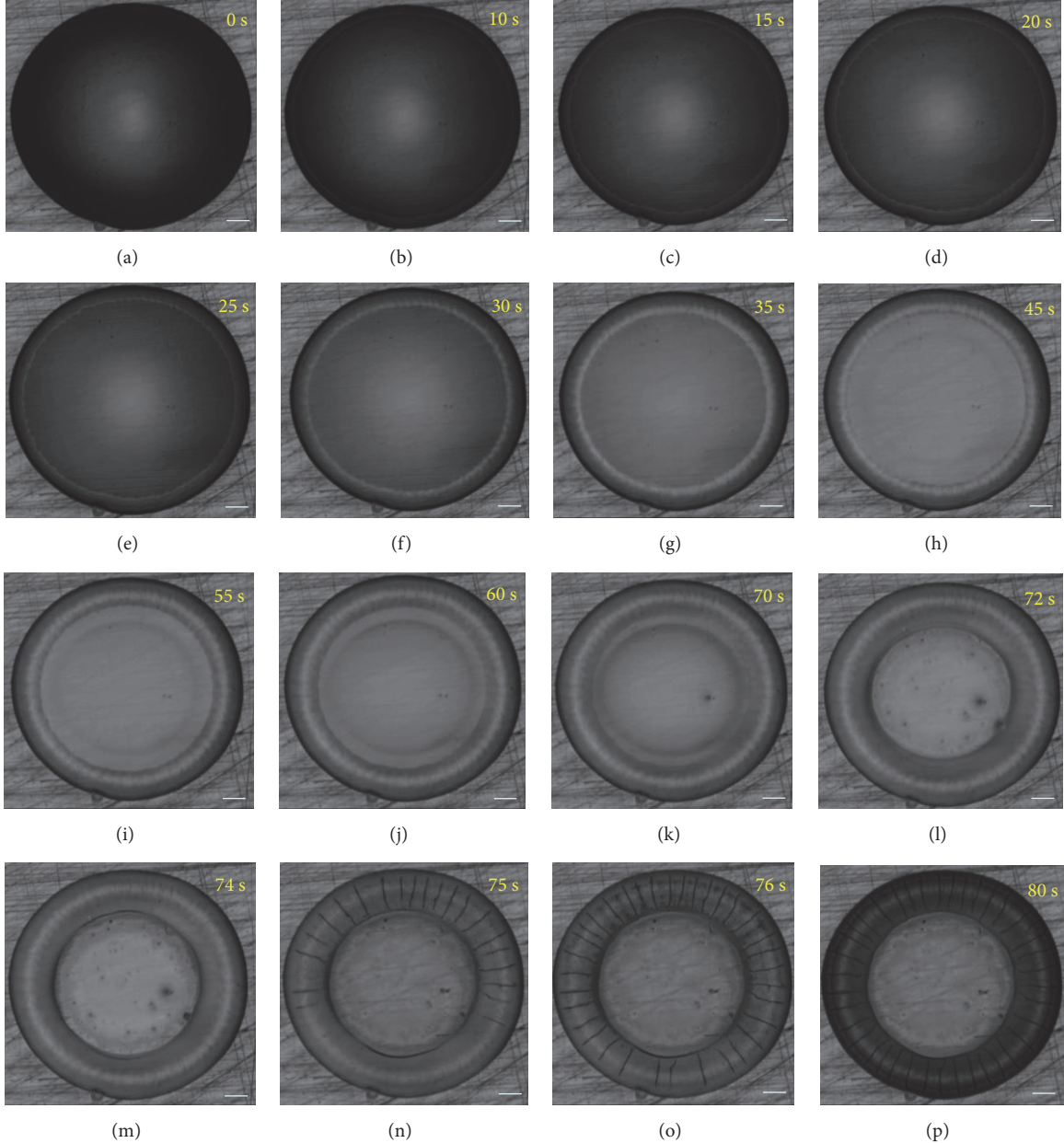


FIGURE 5: Evaporation dynamics of PTFE droplet on rough substrate, (a)–(p) correspond to different evaporation time. The mesh of sand paper used is 200 (scale bars represent 100  $\mu\text{m}$ ).

of the deposition was wedge-shaped. Coffee-ring effect was more pronounced when the droplets evaporate on rough substrates. With increasing substrate roughness, the cross-section of the deposition changed from wedge- to hill-shaped.

(2) The evaporation rate of droplets is far higher on rough substrates than on the smooth substrate. This is because of the smaller contact angle on the rough surface and the emergence of the wicking effect which produces additional evaporation mass. These two factors enhance the capillary flow, driving particles to the edge. Meanwhile, the roughness of the substrate helps the pinning of the contact line and increases contact angle hysteresis, which also helps to drive particles to the edge.

In addition, circular flow can not be established on the rough substrate and radial-shaped wrinkle form on the evaporation front, preventing the particles' move to the center. Thus, the rough substrate exhibits a more pronounced coffee-ring effect, with the width decreasing and the height increasing with increasing roughness.

(3) Crack nucleation is easier and the rate of crack expansion is higher for droplet evaporated on rough substrates than on smooth substrates. This is because of the large number of nucleation sites on rough substrates. Because of the thicker coffee-ring, more elastic energy is stored during evaporation, which also enhances the crack expansion rate.

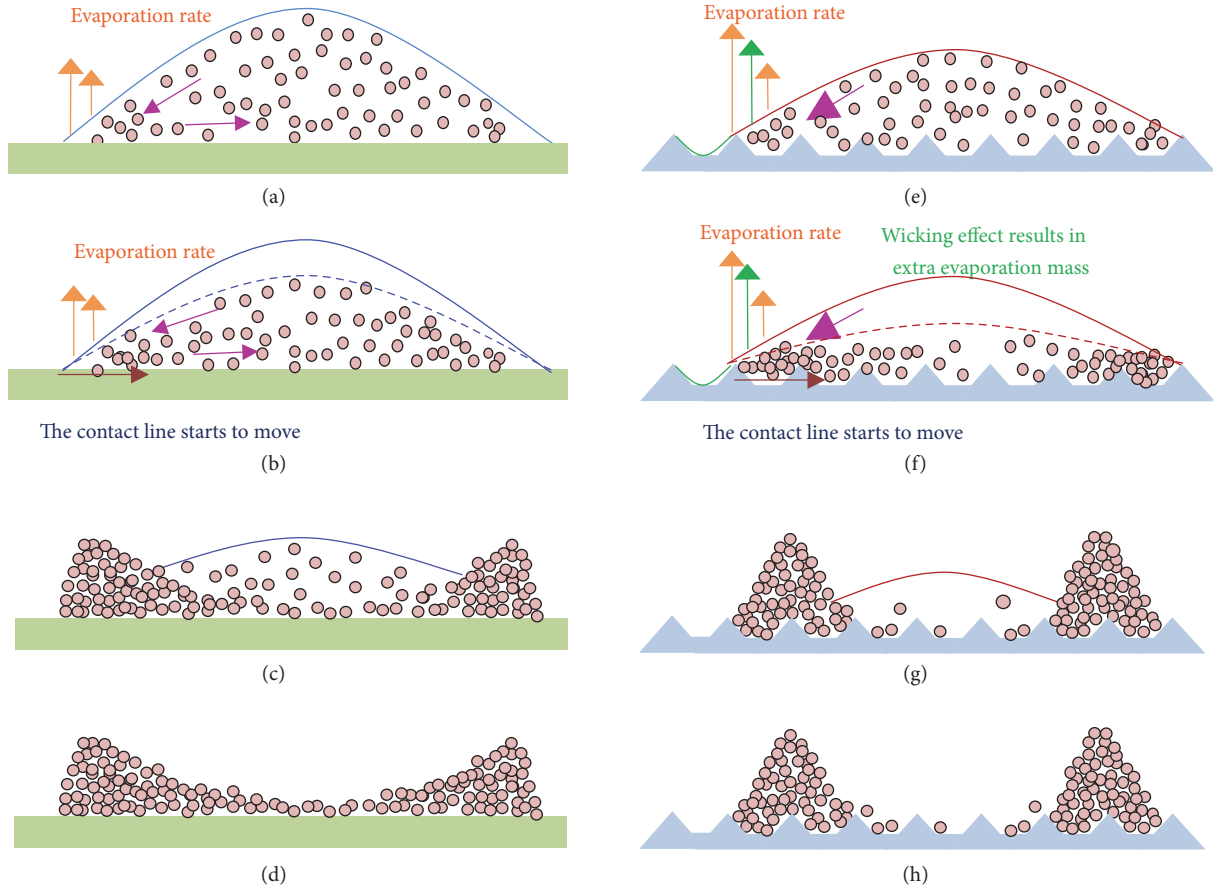


FIGURE 6: Formation mechanism of evaporation patterns on (a–d) a smooth substrate and (e–h) a rough substrate. (a) On a smooth substrate, the contact angle is larger and the evaporation rate is low; (b) recycling flow is constructed on the smooth substrate; (c) in the later stages of evaporation, many particles remain in the dispersion on the smooth substrate; (d) wedge-shaped cross-section of the deposition; (e) on a rough substrate, the contact angle decreases and the wicking effect emerges, leading to a higher evaporation rate; (f) there is no circumfluence on the rough substrate, with contact angle hysteresis being more evident; (g) almost no particles remain in the center; (h) high-shaped cross-section morphology.

## Conflicts of Interest

The authors declare no potential conflicts of interest.

## Acknowledgments

This work is supported by the Foundation of Shaanxi Provincial Education Department, China (17JK1123, 16JK2198) and the Xi'an Science and Technology Project (2017CGWL15).

## References

- [1] K. Sefiane, “Patterns from drying drops,” *Advances in Colloid and Interface Science*, vol. 206, pp. 372–381, 2014.
- [2] R. Chen, L. Zhang, D. Zang, and W. Shen, “Blood drop patterns: Formation and applications,” *Advances in Colloid and Interface Science*, vol. 231, pp. 1–14, 2016.
- [3] K. Keseroglu and M. Culha, “Assembly of nanoparticles at the contact line of a drying droplet under the influence of a dipped tip,” *Journal of Colloid and Interface Science*, vol. 360, no. 1, pp. 8–14, 2011.
- [4] H. Yoo and C. Kim, “Experimental studies on formation, spreading and drying of inkjet drop of colloidal suspensions,” *Colloids and Surfaces A: Physicochemical and Engineering Aspects*, vol. 468, pp. 234–245, 2015.
- [5] R. D. Deegan, O. Bakajin, T. F. Dupont, G. Huber, S. R. Nagel, and T. A. Witten, “Capillary flow as the cause of ring stains from dried liquid drops,” *Nature*, vol. 389, no. 6653, pp. 827–829, 1997.
- [6] Y. Li, C. Lv, Z. Li, D. Quéré, and Q. Zheng, “From coffee rings to coffee eyes,” *Soft Matter*, vol. 11, no. 23, pp. 4669–4673, 2015.
- [7] R. G. Larson, “Re-shaping the coffee ring,” *Angewandte Chemie International Edition*, vol. 51, no. 11, pp. 2546–2548, 2012.
- [8] L. Cui, J. Zhang, X. Zhang et al., “Avoiding coffee ring structure based on hydrophobic silicon pillar arrays during single-drop evaporation,” *Soft Matter*, vol. 8, no. 40, pp. 10448–10456, 2012.
- [9] P. J. Yunker, T. Still, M. A. Lohr, and A. G. Yodh, “Suppression of the coffee-ring effect by shape-dependent capillary interactions,” *Nature*, vol. 476, no. 7360, pp. 308–311, 2011.
- [10] Y. Zhang, Z. Liu, D. Zang, Y. Qian, and K.-J. Lin, “Pattern transition and sluggish cracking of colloidal droplet deposition with polymer additives,” *Science China Physics, Mechanics & Astronomy*, vol. 56, no. 9, pp. 1712–1718, 2013.

- [11] R. Adelung, O. Cenkaktas, J. Franc et al., “Strain-controlled growth of nanowires within thin-film cracks,” *Nature Materials*, vol. 3, no. 6, pp. 375–379, 2004.
- [12] R. C. Chiu, T. J. Garino, and M. J. Cima, “Drying of Granular Ceramic Films: I, Effect of Processing Variables on Cracking Behavior,” *Journal of the American Ceramic Society*, vol. 76, no. 9, pp. 2257–2264, 1993.
- [13] M. Sendova and K. Willis, “Spiral and curved periodic crack patterns in sol-gel films,” *Applied Physics A: Materials Science & Processing*, vol. 76, no. 6, pp. 957–959, 2003.
- [14] L. Goehring, W. J. Clegg, and A. F. Routh, “Wavy cracks in drying colloidal films,” *Soft Matter*, vol. 7, no. 18, pp. 7984–7987, 2011.
- [15] G. Jing and J. Ma, “Formation of circular crack pattern in deposition self-assembled by drying nanoparticle suspension,” *The Journal of Physical Chemistry B*, vol. 116, no. 21, pp. 6225–6231, 2012.
- [16] Y. Zhang, Y. Qian, Z. Liu, Z. Li, and D. Zang, “Surface wrinkling and cracking dynamics in the drying of colloidal droplets,” *The European Physical Journal E*, vol. 37, no. 9, article 84, 7 pages, 2014.
- [17] F. Boulogne, L. Pauchard, and F. Giorgiutti-Dauphiné, “Effect of a non-volatile cosolvent on crack patterns induced by desiccation of a colloidal gel,” *Soft Matter*, vol. 8, no. 32, pp. 8505–8510, 2012.
- [18] R. Chen, L. Zhang, D. Zang, and W. Shen, “Understanding desiccation patterns of blood sessile drops,” *Journal of Materials Chemistry B*, vol. 5, no. 45, pp. 8991–8998, 2017.
- [19] D. Zang, Y. Yu, Z. Chen, X. Li, H. Wu, and X. Geng, “Acoustic levitation of liquid drops: Dynamics, manipulation and phase transitions,” *Advances in Colloid and Interface Science*, vol. 243, pp. 77–85, 2017.
- [20] T. Liu, H. Luo, J. Ma, W. Xie, Y. Wang, and G. Jing, “Surface roughness induced cracks of the deposition film from drying colloidal suspension,” *European Physical Journal E*, vol. 39, no. 2, article no. 24, pp. 1–8, 2016.

## Research Article

# The Effect of Geometrical Parameters on Resonance Characteristics of Acoustic Metamaterials with Negative Effective Modulus

Xiao-Le Yan,<sup>1</sup> Li-Mei Hao<sup>ID</sup>,<sup>1</sup> Mei-Ling Men,<sup>1</sup> and Zhi Chen<sup>ID</sup><sup>2</sup>

<sup>1</sup>Department of Applied Physics, Xian University of Science and Technology, Xian 710054, China

<sup>2</sup>Department of Applied Physics, Northwestern Polytechnical University, Xian 710129, China

Correspondence should be addressed to Li-Mei Hao; haolm@xust.edu.cn and Zhi Chen; c2002z@nwpu.edu.cn

Received 24 November 2017; Revised 7 February 2018; Accepted 28 February 2018; Published 4 April 2018

Academic Editor: Liyuan Zhang

Copyright © 2018 Xiao-Le Yan et al. This is an open access article distributed under the Creative Commons Attribution License, which permits unrestricted use, distribution, and reproduction in any medium, provided the original work is properly cited.

There has been an explosion of interest in acoustic metamaterial in the last ten years. The tunable negative acoustic metamaterial is an important issue for designing metamaterials. The acoustic metamaterial is restricted by the narrow bandgap of sound waves for the local resonance of metamaterial unit cells. By shifting the sizes of the unit cell, the acoustic metamaterial could potentially overcome the limit of the narrow resonance frequency. In this research, we focus on the resonant behavior of split hollow sphere (SHS) in the waveguide. Firstly, we analyze the resonance characteristics of SHS and get an analytical formula for the effect of geometrical parameters on the resonance frequency. Furthermore, the resonance frequency of SHS is verified with finite-element method analysis based on COMSOL Multiphysics simulation. The results are in good agreement with theory model. It is observed that there is a blue shift of the resonance frequency with the gradual increase of the neck radius of SHS, a V-type response curve with the increase of inner radius of SHS, and a red shift with the increase of outer radius of SHS. Using the method of estimate of resonance, we could get a precisely controllable unit structure with negative effective modulus and offer a way to optimize the realization of double negative acoustic metamaterial.

## 1. Introduction

Acoustic metamaterial is a kind of man-made material that exhibit superior properties, and it is applied to control the direction of sound wave. The idea of negative effective density of acoustic metamaterial using local resonance unit was first proposed by Liu et al. in 2000 [1]. In this way, more researchers pay attention to local resonant acoustic metamaterial with negative effective density mass [2–10]. At the year of 2006, Fang et al. [11] designed a one-dimensional array consisted of split hollow cavity with subwavelength which is a new class of acoustic metamaterial with negative effective modulus at the ultrasonic frequency. Later on, Lee et al. [12] made a kind of one-dimensional acoustic metamaterial with splitting hollow on the side of hollow tube and confirmed that the acoustic metamaterial has the property of negative effective modulus at the frequency range of 0~450 Hz. A simpler version of two-dimensional negative

effective modulus based on SHS was prepared by Ding et al. [13]. By 2015, Jing et al. [14] proposed a new kind of monopole resonance characteristics of balloon soft resonator to realize negative effective modulus. However, the main disadvantage of the local resonant acoustic metamaterials is that the response frequencies of different units are different and the frequency bands are narrow. Therefore, similar to electromagnetic metamaterials, the tunable negative acoustic metamaterial is an important issue in the acoustic research. The tunable range of resonant frequency is one of the important parameters in the application of acoustic metamaterials.

At present, active and passive methods have been adopted to control the resonance frequency of metamaterials with negative modulus [15–17]. Akl and Baz [15] controlled the Helmholtz resonator with negative modulus with by coupling with piezoelectric film and applying the electric field. There are many factors that influence the resonance characteristics of acoustic metamaterial unit, such as the shape, size,

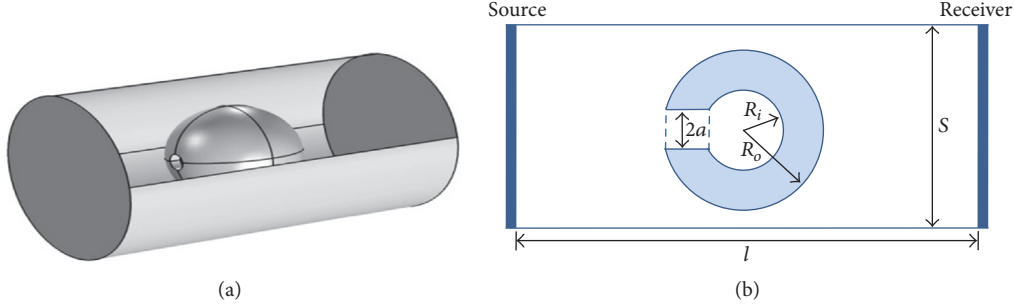


FIGURE 1: (a) The 3D scheme of the metamaterial unit cell. (b) The cross section of the cell.

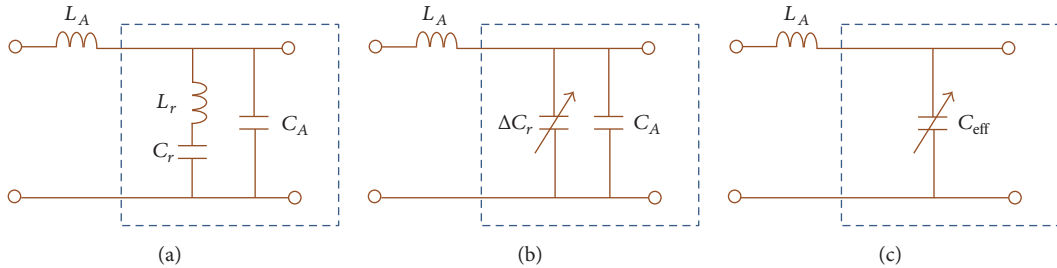


FIGURE 2: (a) An acoustic equivalent circuit using the impedance analogy. (b) The effective impedance circuit of SHS. (c) The effective impedance circuit of the two capacitors.

medium, and number of holes. Ding et al. [18] controlled the resonance frequency with negative modulus by shifting the hole size of SHS. Hao et al. [19] tuned the resonant frequency by changing the medium type of SHS. In addition, the resonant frequency can be controlled by multiple holes on the SHS [20]. At present, little attention has been paid to the precise relationship between the size of structure units and resonance frequency.

In this work, based on the Helmholtz theory and transmission line theory, the resonance characteristic of SHS was discussed. The effective bulk modulus and the amendment formula of resonance frequency were established. Furthermore, COMSOL Multiphysics with the finite-element method was used to design and simulate 3D structure of the acoustic metamaterials unit cell and to verify the effects of geometrical parameters on resonance characteristics consisting of size parameters of the neck radius, inner radius, and outer radius. This provides the basis and guidance for the design and fabrication of double negative acoustic metamaterials in arbitrary frequency by coupling structure units with negative mass density in the next step.

## 2. The Resonance Characteristics of SHS

**2.1. Resonant Metamaterial Unit Cell.** The Helmholtz resonators in [11] are arranged orthogonal to the propagation direction of the sound in the waveguide and the structure is successfully achieved negative effective bulk modulus. From transmission line concept, the equivalent circuit of a Helmholtz resonator is given by an LC circuit with no dissipation. And there is another LC section of the waveguide

which is connected in parallel with the LC circuit. Based on this idea, we place a SHS in the middle of the cylindrical waveguide in the proposed metamaterial unit cell, as shown in Figure 1(a). The SHS is a type of Helmholtz resonator, including the sphere cavity and the short-tube formed by split hole, also called the neck. Here, it will be shown that the structure can be also used to support negative effective bulk modulus of acoustic metamaterial.

In Figure 1(b) a cross section of the metamaterial unit cell is shown. The cylindrical waveguide is driven at left end by a sound source and is measured at right end by a receiver. The cross section area of the waveguide is  $S$ , and the length is  $l$ . The SHS (a spherical cavity with the inner radius  $R_i$  and the outer one  $R_o$ , and a narrow neck with the radius  $a$ ) is positioned at the source and levitated in the middle of the waveguide.

The equivalent circuit of the unit cell with lossless is given by an analogy circuit as Figure 2(a). In this model, the impedance of the waveguide is represented by the acoustic inertance  $L_A$  given by [21]

$$L_A = \frac{\rho l}{S} \quad (1)$$

and the acoustic compliance  $C_A$ , which is given by

$$C_A = \frac{V}{\rho v_s^2}, \quad (2)$$

where  $\rho$  is the density of air,  $v_s$  is the sound velocity, and  $V$  is the volume of the air in the waveguide except the SHS. Additionally, the SHS can be modeled with acoustic inertance

$$L_r = \frac{\rho L_p}{S_p} \quad (3)$$

and acoustic compliance

$$C_r = \frac{V_p}{\rho v_s^2}, \quad (4)$$

where  $L_p$  is the effective length of the neck,  $S_p$  is the cross-sectional area of the one, and  $V_p$  is the effective volume of cavity.

**2.2. The Effective Bulk Modulus of the Unit Cell.** It is well known that, according to the dynamical theory, the vibration system is characterized by its mechanical impedance. Similarly, acoustic impedance  $Z_a$  describes the relationship between the sound pressure and the particle velocity, which is given by

$$Z_a = R_a + jX_a, \quad (5)$$

where  $R_a$  is the acoustic resistance and  $X_a$  is the acoustic reactance. The acoustic resistance represents the energy losses and the acoustic reactance is a concentrated expression of the inertia and elasticity of the system.

Since the fluid medium is air in the waveguide, the shear viscosity and thermal conductivity of the gas are too small enough and can be neglected. Therefore, the acoustic resistance is equal to zero in the analog circuit.

In the case of the acoustic metamaterial unit cell, if the waveguide acts as a simple low-pass filter (LPF), the SHS can be viewed as an “internal heat” as shown in Figure 2(a). The resonance frequency of the SHS falls within the passband of the LPF. In the cylindrical waveguide, there is just one propagating acoustic mode below some cut-off frequency.

In order to simplify the question, the equivalent parameters method is used to the analysis of acoustic reactance. We use the effective acoustic compliance  $\Delta C_r$  representing the quantity of the inertia and elasticity of SHS which is connected in parallel with  $C_A$  as shown in Figure 2(b). Consequently, the parallel combination of the two capacitors has one all effective acoustic compliance  $C_{\text{eff}}$ , Figure 2(c).  $C_{\text{eff}}$  could vary in a large number for local resonance and plays a major role in the circuit.

In the context of acoustics, the bulk modulus of unit cell  $B_A$  is an important parameter of sound propagation [11]. Suppose that sound propagation is an isentropic process, for which  $v_s^2 = \partial p / \partial \rho = B_A / \rho$ ; bulk modulus  $B_A = \rho v_s^2$  is reciprocal to the acoustic compliance from (2) and can be expressed as follows:

$$B_A = \frac{V}{C_A}. \quad (6)$$

Because the gas acts like a spring in the waveguide, the acoustic compliance is written as

$$C_A = \frac{1}{K_A} = \frac{S^2}{K}, \quad (7)$$

where  $K$  is the mechanical stiffness of the spring. Since the waveguide is the host frame of unit cell, the effective bulk modulus  $B_{\text{eff}}$  is defined as

$$B_{\text{eff}} = \frac{V}{C_{\text{eff}}}. \quad (8)$$

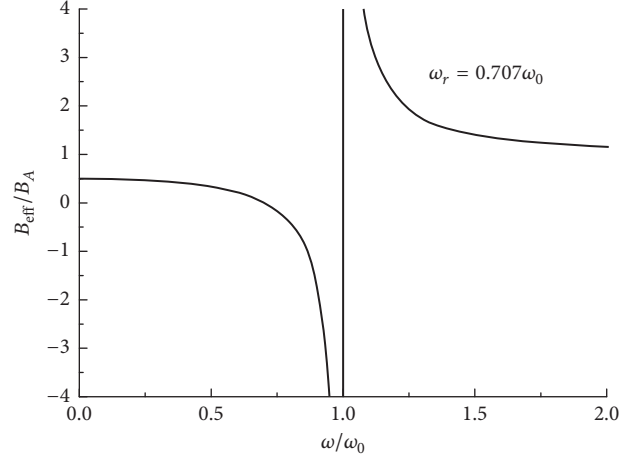


FIGURE 3: Effective bulk modulus of the unit cell obtained from the analytical expression.

Under the above assumption, acoustic impedance of the unit cell becomes

$$Z_a = j\omega L_A + \frac{1}{j\omega C_{\text{eff}}}. \quad (9)$$

Let us suppose that the waveguide has a larger cross section area and therefore the effective acoustic compliance  $C_{\text{eff}}$  is significantly greater than acoustic inertance  $L_A$  at near resonance frequency. Equation (9) is now

$$\begin{aligned} Z_a &\approx \frac{1}{j\omega C_{\text{eff}}} = \frac{(1/j\omega C_A)(j\omega L_r + 1/j\omega C_r)}{j\omega L_r + 1/j\omega C_A + 1/j\omega C_r} \\ &= \frac{1}{j\omega C_A} \frac{\omega^2 - \omega_r^2}{\omega^2 - \omega_0^2}, \end{aligned} \quad (10)$$

where  $\omega_0^2 = \omega_A^2 + \omega_r^2$ ,  $\omega_A = 1/\sqrt{L_r C_A}$ , and  $\omega_r = 1/\sqrt{L_r C_r}$ . The effective acoustic compliance and effective bulk modulus are determined by the following expressions, respectively:

$$C_{\text{eff}} = C_A \frac{\omega^2 - \omega_0^2}{\omega^2 - \omega_r^2}, \quad (11)$$

$$B_{\text{eff}} = B_A \frac{\omega^2 - \omega_r^2}{\omega^2 - \omega_0^2}. \quad (12)$$

From (12), it can be seen that the inclusion of SHS in the waveguide results in the variation of effect bulk modulus of unit cell with frequency, as shown in Figure 3.

It can be seen that effective bulk modulus between frequencies  $0 < \omega < \omega_r$  is greater than zero but is less than  $B_A$ . With the increasing of frequency, the effective bulk modulus is decreasing, because the acoustic inertance of SHS begins to take more effect. The frequency  $\omega_r$  is the series resonance frequency of SHS unit. At this frequency, acoustic impedance is equal to zero which means the sound wave is by-passed and the effective bulk modulus is also zero.

In the frequencies range  $\omega_r < \omega < \omega_0$ , the inertia of SHS is so big that the effective bulk modulus is negative. The effective

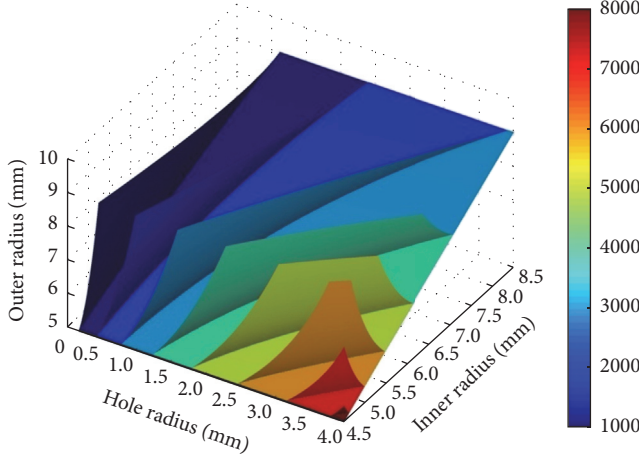


FIGURE 4: Relation between the parameters of SHS and the resonance frequency.

bulk modulus tends to minus infinity as frequency increases from  $\omega_r$  to  $\omega_0$ . It should be noted that the frequency  $\omega_0$  is the parallel resonance frequency of the  $\Delta C_r$  and  $C_A$  and is also antiresonance frequency. At the frequency, the acoustic impedance is equal to minus infinity.

The effective bulk modulus is greater than zero in the frequency range above  $\omega_0$  and is greater than  $B_A$ . With the increasing of frequency, the effective bulk modulus is decreasing to  $B_A$ . It is also because of the more influence of the acoustic inertance of SHS.

**2.3. The Resonance Frequency of SHS.** From the above analysis, we can see that the resonance of SHS plays an important role in the negative effective bulk modulus of unit cell. Based on Helmholtz theory [21], the resonance frequency of

$$f_r = \frac{\nu_s}{2\pi} \sqrt{\frac{\pi a^2}{\left( \sqrt{R_0^2 - a^2} - \sqrt{R_i^2 - a^2} + 0.61a + (8/3\pi)a \right) \left[ (4/3)\pi R_i^3 - \pi \left( R_i - \sqrt{R_i^2 - a^2} \right)^2 \left( R_i - (R_i - \sqrt{R_i^2 - a^2})/3 \right) \right]}}. \quad (17)$$

In order to analyze the influence of geometrical parameters of SHS on tunable frequency, the relation between the three parameters of SHS and the resonance frequency was shown in Figure 4 based on formula (17). It can be seen that there is a lower resonance frequency as the neck size is smaller, and there is a higher frequency as the neck size is larger. This provides us an important way to precisely control acoustic metamaterial with negative effective modulus.

**2.4. Simulation Results.** The acoustic field is simulated by COMSOL Multiphysics 4.3 and the pressure acoustic and solid mechanics are coupled in the acoustic model for the continuity. The model consists of a SHS unit and a waveguide. The plane sound wave was used as a sound source and the

SHS can be calculated by the similar LC circuit shown in Figure 1(a). The resonance frequency of SHS is

$$f_r = \frac{1}{2\pi \sqrt{L_r C_r}} = \frac{\nu_s}{2\pi} \sqrt{\frac{S_p}{L_p V_p}}. \quad (13)$$

The effective volume of cavity  $V_p$ , that is, the volume of inner sphere minus the volume of spherical crown as part of short-tube, is thus given by

$$\begin{aligned} V_p &= \frac{4}{3}\pi R_i^3 \\ &- \pi \left( R_i - \sqrt{R_i^2 - a^2} \right)^2 \left( R_i - \frac{R_i - \sqrt{R_i^2 - a^2}}{3} \right), \end{aligned} \quad (14)$$

where  $S_p = \pi a^2$  is the area of cross section of the short-tube.

The geometric length of the short-tube is

$$l_p = \sqrt{R_0^2 - a^2} - \sqrt{R_i^2 - a^2}. \quad (15)$$

Since the effective length of air in short-tube is longer than geometric length, we define it as the effective length  $L_p$ . In this model, the short-tube has two end corrections, where the outside of short-tube is considered as nonflange and the correction length is  $0.61a$ ; the inside is under the flange state and the correction length is  $(8/3\pi)a$  [22]. Thus, the effective length of short-tube is

$$L_p = \sqrt{R_0^2 - a^2} - \sqrt{R_i^2 - a^2} + 0.61a + \frac{8}{3\pi}a. \quad (16)$$

From the results given by (14) and (16), the amendment formula of resonance frequency is therefore

other open end of outlet waveguide was modeled with PML boundary condition. The remaining boundaries of waveguide are specified as sound hard condition for the sound waves reflecting from waveguide wall completely. The material of wall of SHS is polyethylene and the fluid domain is full of air. At standard temperature and pressure conditions, the bulk modulus  $B_o$  of air is  $1.42 \times 10^5$  Pa for an isentropic process. Suppose that  $l = 20.0$  mm,  $S = 225 \pi \text{mm}^2$ ,  $R_o = 5.0$  mm,  $R_i = 4.5$  mm, and  $a = 0.5$  mm to 2.5 mm (Figure 1(b)).

The results of the transmission spectrum are got and shown in Figure 5. Except that the curve of the radius of 0 mm has no transmission dip, there is a dip in every transmission curve. Furthermore, the blue shift of transmission dip occurs as the neck radius of SHS becomes bigger. According to (3),

TABLE 1: Relation between the neck radius and resonance frequency, ( $R_o = 5.0 \text{ mm}$ ,  $R_i = 4.5 \text{ mm}$ ).

The radius of neck/mm	0.5	1.0	1.5	2.0	2.5
Theoretical frequency/Hz	2200	3502	4602	5602	6491
Simulate frequency/Hz	2190	3514	4607	5594	6546

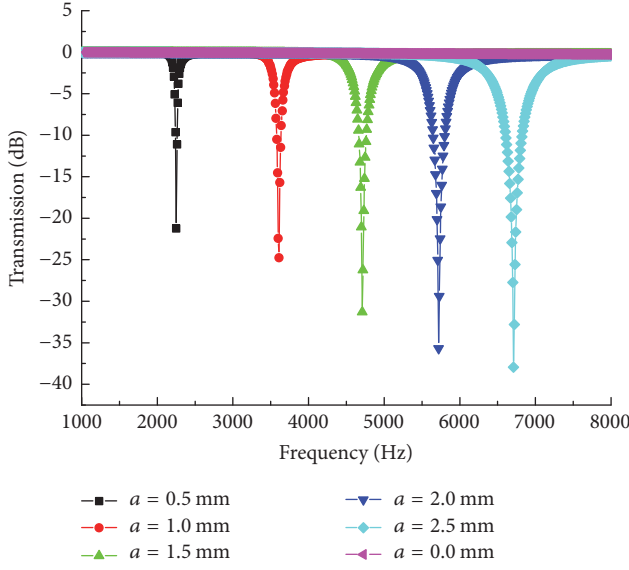


FIGURE 5: The transmission coefficients of Unit cell with different neck radius ( $R_o = 5.0 \text{ mm}$ ,  $R_i = 4.5 \text{ mm}$ ).

the increased quality of the air in the neck enhances its acoustic inertance, while the volume value of cavity has decreased slightly. In terms of the serial inductor-capacitor circuit, if the radius of cavity is constant, the inductance of the SHS decreases with increasing neck radius. Although the inner radius of SHS has not been changed, some volume of them becomes a part of the short-tube. The ability of storing energy of SHS gets weak and makes the capacitance of the resonator smaller. Hence, resonance frequency goes up with the increase of the neck radius of SHS.

The values of resonance frequency are shown in Table 1. For example, the SHS with 0.5 mm neck radius has phase reverse near the frequency of 2190 Hz for the local resonance. As is shown in Figure 6, the real part of effective modulus is negative near the resonance frequency of SHS, and it represents the character of the negative dynamic response. Similarly, effective modulus with different neck radius was obtained, and negative effective modulus near the resonance frequency is achieved individually (see Figure 6). This result is consistent with that described in [11].

For verifying the validity of formula (17), we calculate the values of resonance frequency with COMSOL method and amendment formula (17), and they were listed in Table 1. The simulated value of resonance frequency is in good agreement with the analysis results of the equivalent circuit. Thus, using formula (17), we can obtain the precise value and then control resonance frequency of SHS accurately.

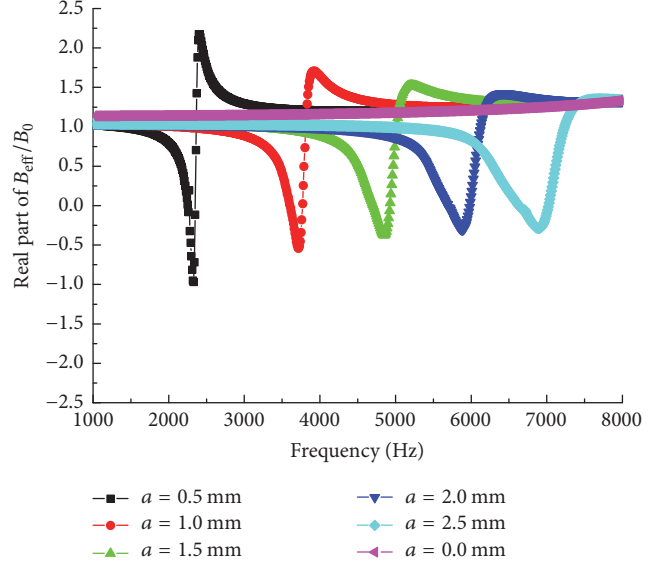


FIGURE 6: The effective modulus curves of unit cell with different neck radius ( $R_o = 5.0 \text{ mm}$ ,  $R_i = 4.5 \text{ mm}$ ).

### 3. Influence of Geometrical Parameters of SHS on Resonance Frequency

Similarly, the effects of other parameters on the tunable frequency of SHS were analyzed with COMSOL Multiphysics and formula (17) in the section. Formula (17) suggests that the tunable parameters of SHS include the hole radius, outer radius, inner radius of sphere cavity, and so on. Because the inner radius and neck radius affect the cavity volume, the difference between outer and inner radius acts as the length of short-tube, and the neck radius affects the area of cross section of short-tube. Thus, three characteristic parameters of SHS have a simultaneous influence on the tunable frequency. In this section, the effects of the inner and outer radius on the resonance frequency were mainly discussed.

**3.1. The Inner Radius of SHS.** Supposing that  $R_o = 9.0 \text{ mm}$ ,  $a = 0.5 \text{ mm}$ , and  $R_i = 4.5 \text{ mm}$  to  $8.5 \text{ mm}$ , the transmission spectrum are measured and shown in Figure 7. The resonance frequency decreases firstly and then increases with increasing the inner radius gradually. In addition, the negative modulus can be obtained near their respective resonance frequency. The results of formula calculation and the simulation agree well, which suggestss that we can obtain the precise resonance frequency by formula (17) and accurately control the AM with SHS.

There is a V-type character of the resonant frequency and the minimum frequency value is at the inner radius with 7.5 mm. This phenomenon explained that the acoustic inductance of SHS decreases with increasing the inner radius; on the other hand, the acoustic capacitance increases with increasing the volume of cavity. Under the influence of two opposite aspect, the resonance frequency decreases firstly and then increases with the increase of the inner radius.

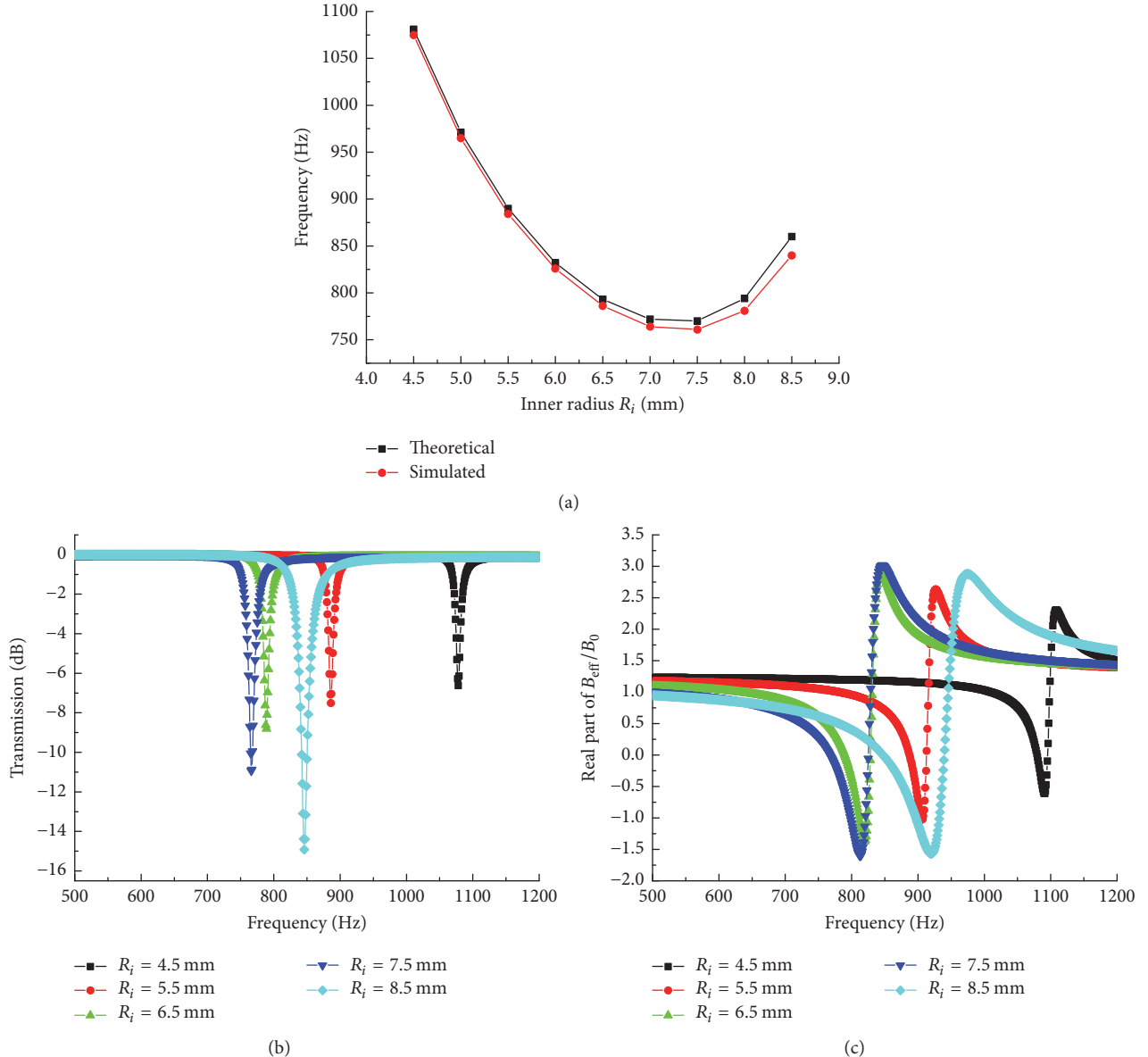


FIGURE 7: The relation curves present the relationship between the inner radius and related parameters ( $R_o = 9.0$  mm,  $a = 0.5$  mm). (a) The resonance frequency of SHS. (b) The transmission coefficient. (c) The effective modulus.

**3.2. The Outer Radius of SHS.** Supposing that  $R_i = 4.5$  mm,  $a = 0.5$  mm, and  $R_o = 5.0$  mm to 9.0 mm, Figure 8 is the relation curves between the outer radius and related parameters, and the resonance frequency has a red shift with increasing the outer radius of SHS. This simulated result is in agreement with Helmholtz theory as well. In addition, the negative modulus can also be achieved near their respective resonance frequency.

The red shift explained that when the inner radius of SHS unchanged and the capacitance is constant, the sound energies of SHS unit with different outer radius are the same. However, the acoustic inductance of SHS increases with the increase of length of short-tube acted as inductor. Hence, the resonant frequency has a red shift.

The results of formula calculation and the simulation agree well, which suggests that we can obtain the precise resonance frequency by formula (17) and accurately control the acoustic metamaterial of SHS with negative modulus.

The results of formula calculation and the simulation agree well, which suggests that we can obtain the precise resonance frequency by formula (17).

#### 4. Conclusion

Based on SHS unit, the tunable mechanism of structure size on controlling the resonance frequency of acoustic metamaterial with negative effective modulus was proposed from aspects of Helmholtz theory and the finite-element

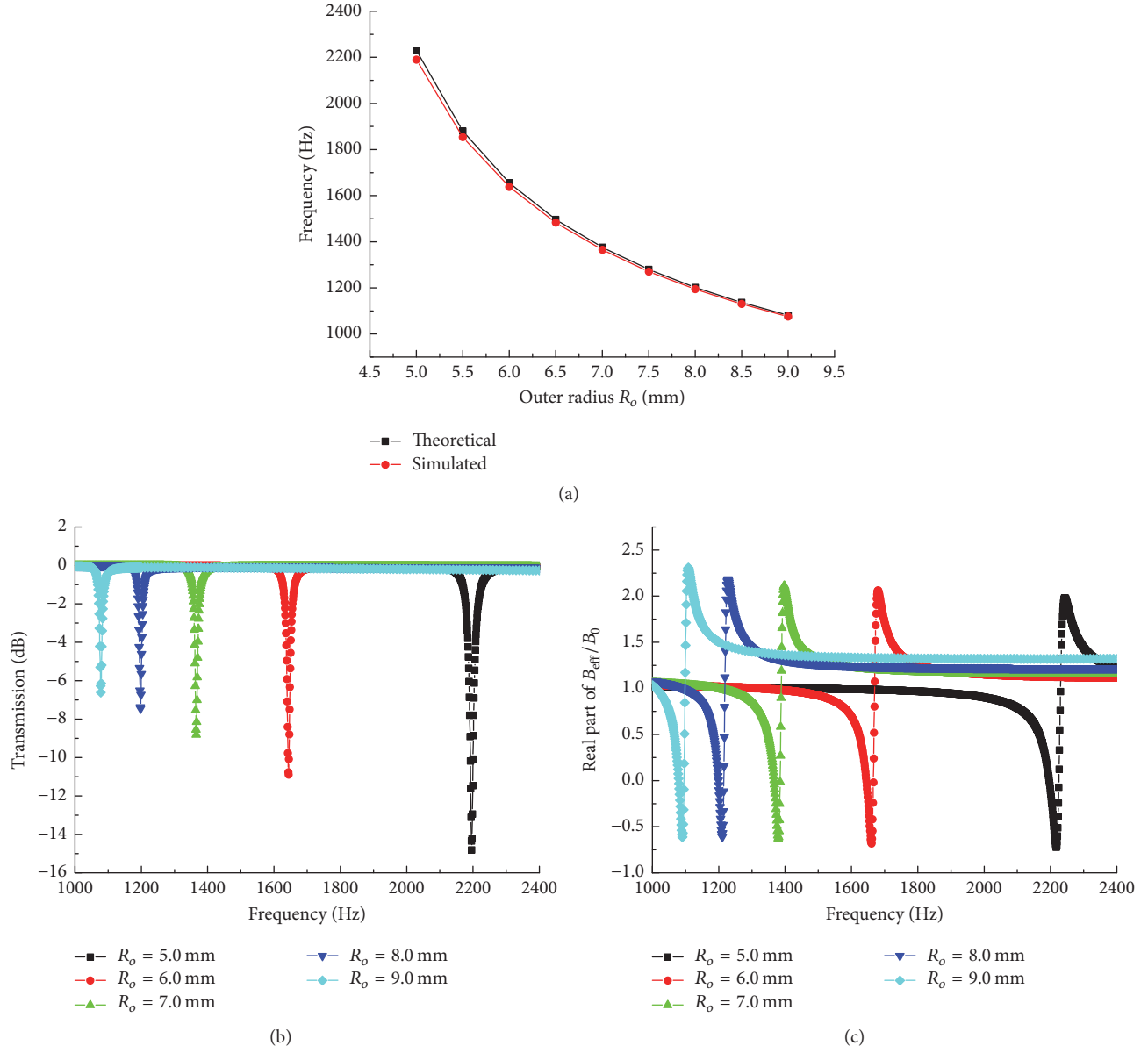


FIGURE 8: The relation curves present the relationship between the outer radius and related parameters ( $R_i = 4.5$  mm,  $a = 0.5$  mm). (a) The resonance frequency of SHS. (b) The transmission coefficient. (c) The effective modulus.

method. The amendment formula of resonance frequency of SHS was derived, and it can precisely describe the relation between resonance frequency and neck radius, inner radius and outer radius. Furthermore, COMSOL simulation was used to verify effectiveness of amendment formula, and it is revealed that simulated results of resonance frequency are in good agreement with theoretical results. The results indicate that the blue shift of resonance frequency occurs when the neck radius of SHS increases; the resonance frequency has a “V” change with the increase of inner radius of SHS; the resonance frequency has a red shift with increasing the outer radius of SHS. The method can precisely control the resonance frequency of acoustic metamaterial with negative effective modulus. There is a potential value on ultrasonic

imaging, underwater acoustic, architectural acoustic, and sound absorbing material, and so on.

## Conflicts of Interest

The authors declare that there are no conflicts of interest regarding the publication of this paper.

## Acknowledgments

This work was supported by the National Natural Science Foundation of China (Grant nos. 11102164 and 11304243), the Natural Science Foundation of Shaanxi Province, China (Grant no. 2014JQ1039), the Scientific Research Program

Funded by Shaanxi Provincial Education Department (Grant no. 15JK1485), the Program of New Staff and Research Area Project of NPU (Grant no. I3GH014602), and the Cultivation Fund of Xi'an University of Science and Technology (Grant no. 2009029).

## References

- [1] Z. Liu, X. Zhang, Y. Mao et al., "Locally resonant sonic materials," *Science*, vol. 289, no. 5485, pp. 1734–1736, 2000.
- [2] Z. Yang, J. Mei, M. Yang, N. H. Chan, and P. Sheng, "Membrane-type acoustic metamaterial with negative dynamic mass," *Physical Review Letters*, vol. 101, no. 20, Article ID 204301, 2008.
- [3] C.-L. Ding and X.-P. Zhao, "Audible sound metamaterial," *Acta Physica Sinica*, vol. 58, no. 9, pp. 6351–6355, 2009.
- [4] J. Pierre, B. Dollet, and V. Leroy, "Resonant acoustic propagation and negative density in liquid foams," *Physical Review Letters*, vol. 112, no. 14, Article ID 148307, 2014.
- [5] M. Yang, G. Ma, Z. Yang, and P. Sheng, "Coupled membranes with doubly negative mass density and bulk modulus," *Physical Review Letters*, vol. 110, no. 13, Article ID 134301, 2013.
- [6] J. J. Park, C. M. Park, K. J. B. Lee, and S. H. Lee, "Acoustic superlens using membrane-based metamaterials," *Applied Physics Letters*, vol. 106, no. 5, Article ID 051901, 2015.
- [7] K. Song, S.-H. Lee, K. Kim, S. Hur, and J. Kim, "Emission enhancement of sound emitters using an acoustic metamaterial cavity," *Scientific Reports*, vol. 4, article no. 4165, 2014.
- [8] J. Liu, Z. L. Hou, and X. J. Fu, "Mechanism for local resonant acoustic metamaterial," *Acta Physica Sinica*, vol. 64, no. 15, Article ID 154302, pp. 54302–154302, 2015.
- [9] X. W. Yang, J. S. Lee, and Y. Y. Kim, "Effective mass density based topology optimization of locally resonant acoustic metamaterials for bandgap maximization," *Journal of Sound and Vibration*, vol. 383, no. 11, pp. 89–107, 2016.
- [10] A. O. Krushynska, V. G. Kouznetsova, and M. G. Geers, "Viscoelastic effects on wave dispersion in three-phase acoustic metamaterials," *Journal of the Mechanics and Physics of Solids*, vol. 96, no. 11, pp. 29–47, 2014.
- [11] N. Fang, D. Xi, J. Xu et al., "Ultrasonic metamaterials with negative modulus," *Nature Materials*, vol. 5, no. 6, pp. 452–456, 2006.
- [12] S. H. Lee, C. M. Park, Y. M. Seo, Z. G. Wang, and C. K. Kim, "Acoustic metamaterial with negative modulus," *Journal of Physics: Condensed Matter*, vol. 21, no. 17, Article ID 175704, 2009.
- [13] C. Ding, L. Hao, and X. Zhao, "Two-dimensional acoustic metamaterial with negative modulus," *Journal of Applied Physics*, vol. 108, no. 7, Article ID 074911, 2010.
- [14] X. Jing, Y. Meng, and X. Sun, "Soft resonator of omnidirectional resonance for acoustic metamaterials with a negative bulk modulus," *Scientific Reports*, vol. 5, no. 11, Article ID 16110, 2015.
- [15] W. Akl and A. Baz, "Multi-cell active acoustic metamaterial with programmable bulk modulus," *Journal of Intelligent Material Systems and Structures*, vol. 21, no. 3, pp. 541–556, 2010.
- [16] X. Yu, Z. Lu, F. Cui, L. Cheng, and Y. Cui, "Tunable acoustic metamaterial with an array of resonators actuated by dielectric elastomer," *Extreme Mechanics Letters*, vol. 12, pp. 37–40, 2017.
- [17] B. Xia, N. Chen, L. Xie, Y. Qin, and D. Yu, "Temperature-controlled tunable acoustic metamaterial with active band gap and negative bulk modulus," *Applied Acoustics*, vol. 112, no. 11, pp. 1–9, 2016.
- [18] C. L. Ding, X. P. Zhao, L. M. Hao, and W. R. Zhu, "Acoustic metamaterial with split hollow spheres," *Acta Physica Sinica*, vol. 60, no. 4, Article ID 044301, 2011.
- [19] L.-M. Hao, C.-L. Ding, and X.-P. Zhao, "Tunable acoustic metamaterial with negative modulus," *Applied Physics A: Materials Science & Processing*, vol. 106, no. 4, pp. 807–811, 2012.
- [20] L.-M. Hao, C.-L. Ding, and X.-P. Zhao, "Design of a passive controllable negative modulus metamaterial with a split hollow sphere of multiple holes," *Journal of Vibration and Acoustics*, vol. 135, no. 4, Article ID 041008, 2013.
- [21] G. H. Du, *Fundamentals of Acoustics*, Nanjing University Press, Nanjing, China, 2012.
- [22] D. T. Blackstock, *Fundamentals of Physical Acoustics*, John Wiley & Sons, NJ, USA, 2000.

## Review Article

# Droplet Drying Patterns on Solid Substrates: From Hydrophilic to Superhydrophobic Contact to Levitating Drops

Sujata Tarafdar ,<sup>1</sup> Yuri Yu. Tarasevich ,<sup>2</sup>  
Moutushi Dutta Choudhury,<sup>3</sup> Tapati Dutta,<sup>1,4</sup> and Duyang Zang<sup>5</sup>

<sup>1</sup>Condensed Matter Physics Research Center (CMPRC), Physics Department, Jadavpur University, Kolkata 700 032, India

<sup>2</sup>Laboratory of Mathematical Modeling, Astrakhan State University, Astrakhan 414056, Russia

<sup>3</sup>Centre for Advanced Studies in Condensed Matter and Solid State Physics, Department of Physics,  
Savitribai Phule Pune University, Pune 411 007, India

<sup>4</sup>Physics Department, St. Xavier's College, Kolkata 700 016, India

<sup>5</sup>Functional Soft Matter and Materials Group (FS2M), Key Laboratory of Material Physics and Chemistry under Extraordinary Conditions, School of Science, Northwestern Polytechnical University, Xi'an, Shaanxi 710129, China

Correspondence should be addressed to Sujata Tarafdar; sujata\_tarafdar@hotmail.com

Received 19 December 2017; Accepted 12 February 2018; Published 3 April 2018

Academic Editor: Charles Rosenblatt

Copyright © 2018 Sujata Tarafdar et al. This is an open access article distributed under the Creative Commons Attribution License, which permits unrestricted use, distribution, and reproduction in any medium, provided the original work is properly cited.

This review is devoted to the simple process of drying a multicomponent droplet of a complex fluid which may contain salt or other inclusions. These processes provide a fascinating subject for study. The explanation of the rich variety of patterns formed is not only an academic challenge but also a problem of practical importance, as applications are growing in medical diagnosis and improvement of coating/printing technology. The fundamental scientific problem is the study of the mechanism of micro- and nanoparticle self-organization in open systems. The specific fundamental problems to be solved, related to this system, are the investigation of the mass transfer processes, the formation and evolution of phase fronts, and the identification of mechanisms of pattern formation. The drops of liquid containing dissolved substances and suspended particles are assumed to be drying on a horizontal solid insoluble smooth substrate. The chemical composition and macroscopic properties of the complex fluid, the concentration and nature of the salt, the surface energy of the substrate, and the interaction between the fluid and substrate which determines the wetting all affect the final morphology of the dried film. The range of our study encompasses the fully wetting case with zero contact angle between the fluid and substrate to the case where the drop is levitated in space, so there is no contact with a substrate and angle of contact can be considered as 180°.

## 1. Introduction

The study of drying droplets, especially those containing colloidal particles or salts, has become a topic of wide interest in recent years. This is evident from the fact that international conferences on droplets are regularly organized (Droplets Conferences and EMN Droplets) and books exclusively devoted to this subject have been published [1–8]. There are, in addition, several excellent review articles on droplets [9–21]. Different features of this problem, such as the rate of drying, evolution of the drop geometry, and the final pattern formed, depend on a number of parameters, notably the

composition of the drying fluid, ambient conditions during drying, and the substrate which supports the drop.

The widespread interest in the drying droplets with inclusions stems from important and innovative applications, mainly in medical science and in technology. When the fluid in the droplet evaporates, the solid material left behind can be distributed in a wide variety of patterns on the substrate. Inclusions may be salts, nanoparticles in the form of nanorods, nanotubes, or any other shape, starches, proteins, and so on. Patterns formed can range from a simple ring at the periphery of the droplet, the so-called coffee ring [22, 23], to multiple rings forming bands, fractal and

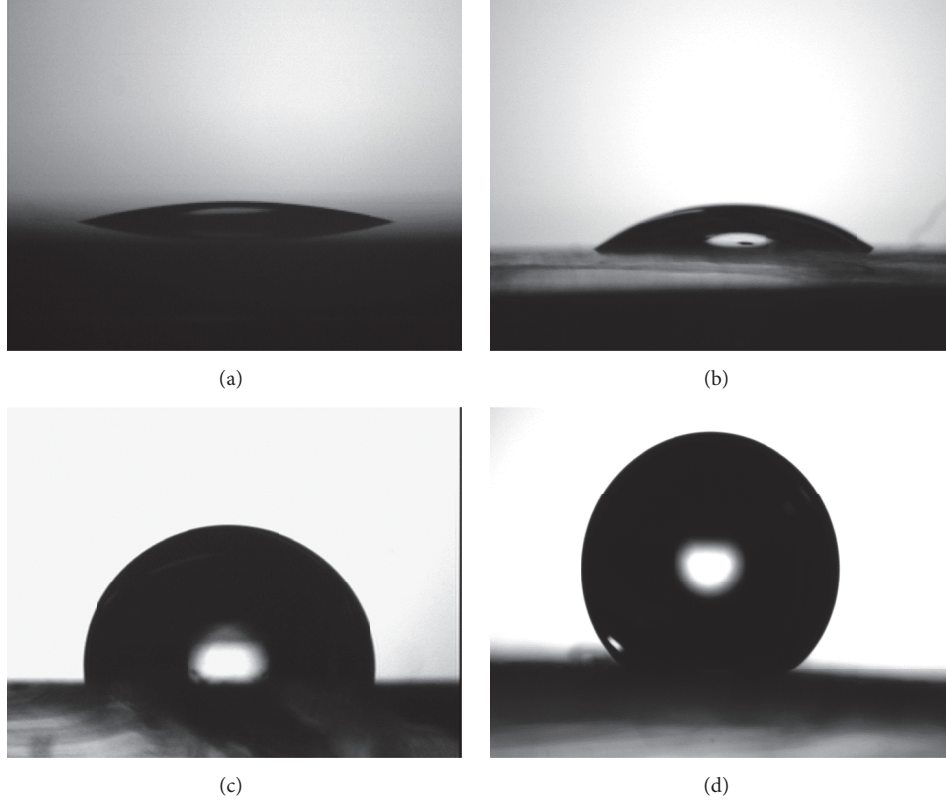


FIGURE 1:  $5\text{ }\mu\text{l}$  drop of water (a) on glass substrate (treated with Piranha solution), (b) on nontreated glass substrate, (c) on polystyrene (PS) substrate, and (d) on hydrophobic TEFLOON substrate.

multiparticle aggregates of salt crystals, or nanoparticles [24–27]. In addition, the dried drop may develop crack patterns [8, 28–43], which can also be induced by external fields [35, 44]. It is important to realize that the shape of the droplet plays a crucial role in generating these patterns. Unless the drop is too large, its shape may be roughly approximated by a section of a sphere or a spherical cap. In some cases, when a crust or skin forms on the free surface [45], buckling instability may develop [46–49]. Nonuniform evaporation over different regions of the drop surface generates convection currents that determine mass transfer. Temperature and concentration gradients also develop [50–53], leading to surface tension gradients, resulting in thermal Marangoni flow [54–59] or/and solutal Marangoni flow [60]. Obviously, drying out of a large flat film of fluid would lead to a different situation. Figure 1 presents sessile droplets on hydrophilic and hydrophobic surfaces. A thin section of a sphere, where the height at the center is small compared to the lateral dimension, represents a sessile drop that wets the surface well (Figure 1(a)). Here, the angle of contact is very small. On the other hand, a section much larger than a hemisphere represents a strongly hydrophobic contact (Figure 1(d)).

Another possible geometry of a drop in contact with a solid surface is the *pendant drop*, which is suspended from a support *above* it, like a rain drop hanging from a leaf. The pendant drop has also been studied [69], but we do not discuss it further in the present article.

To eliminate the effect of substrate, one may turn to the pendant drop hung by a thin needle or nonwetting drop supported by a superhydrophobic surface. In this case, though its shape was quasi-spherical, the boundary condition for evaporation was, however, influenced by the contact points, thus in turn influencing the evaporation flux. Via levitation techniques, for instance, electrostatic, magnetic, and acoustic levitation, the contact of solid substrate can be completely avoided; thus it somewhat can provide a more uniform evaporation flux along the drop surface. But for most of levitation techniques, the levitation force to balance gravity is surface force, not body force; therefore, the natural convection cannot be suppressed. To further study evaporation without the influence of natural convection, experiments under microgravity, that is, levitation experiments in space, are expected.

Recent experiments on levitated droplets [70] represent the extreme case of a spherical drop with no contact to a substrate. This situation is relevant in space research. In the present review, we aim to discuss the whole range of contact angles and how it affects the morphology of the dried residue. Interplay of related factors such as the chemistry of the materials, interface tensions involved, and physical properties such as elastic or viscoelastic moduli and ambient drying conditions all need to be taken into consideration [71]. There can also be external perturbations such as electric/magnetic fields, heating/cooling of the substrate, or mechanical

perturbations. We try to discuss these factors and their contribution as far as possible within the brief span of this review.

We excluded from our consideration some specific topics such as evaporation of sessile droplets on inclined (including vertical), patterned (textured), dissolvable, and porous substrates. To obtain some information about these topics, we can refer the reader to [72–76]. Besides, we omitted all effects connected with artificially inhomogeneous evaporation such as obstacles [77], masks [78], modulated gas phase convection [79], and infrared heating [80], which can force or impede evaporation at particular parts of the free surface of the drop.

The medical science application of the droplet problem utilizes characteristics of the droplet patterns found in dried body fluids, such as blood, serum, tear drops, saliva, and cervical fluid, for identifying diseases in patients. The technique offers a simple and inexpensive method in pathological diagnostics, which has been in use for several decades [3, 81].

A more recent technological innovation is the use of dried droplets with conducting inclusions such as silver nanoparticles or carbon nanotubes (CNT) to create a nearly invisible but connected conducting network on a transparent surface [27, 82, 83]. The demand for such transparent conductors is extremely high in photovoltaic devices of everyday use. The droplet method has a potential to fabricate such surfaces easily and inexpensively. There are other applications related to, for example, ink-jet printing [84] and high throughput drug screening [60].

## 2. Experimental Studies

In this section, we give an overview of experimental studies on evaporating droplets. We have tried to classify the large body of earlier work into subsections to facilitate the discussion. However, separating the experiments into clear-cut nonoverlapping sections is not always possible. We hope the reader will bear with us in this attempt to present an array of a colourful mass of tangled threads, sorted out as far as possible.

**2.1. Evaporation of a Pure Fluid.** A sessile drop of a pure liquid, such as water or methanol, when placed on a solid substrate evaporates completely without leaving any residue. The points of interest here are the spreading rate of the drop, the equilibrium shape reached, and how it evolves with time up to complete evaporation. These observations help in understanding the more complicated situations that follow. Obviously, the nature of fluid and ambient are important as well as the properties of the substrate and interaction between fluid and substrate [85]. So we have to consider the substrate here as well, but we leave situations where the substrate (or its absence) has a crucial role to Section 2.2.1.

A liquid drop on a solid surface evolves spontaneously until it reaches its equilibrium with minimum surface area consistent with Laplace's equation (see, e.g., [86]). The shape of the drop on a surface depends on the surface energy of the substrate and the liquid drop, as well as the interface energies between different phases. An additional energy is needed to create an interface between the liquid and solid; this is called

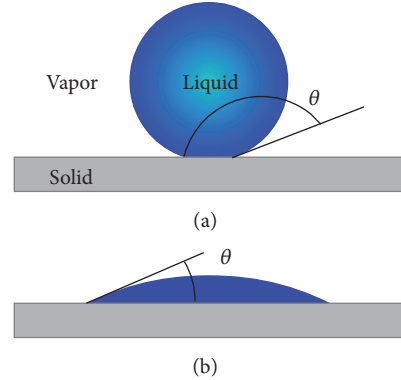


FIGURE 2: Contact angle between a drop and a substrate: (a) nonwettable substrate and (b) a partially wetted substrate.

the interface free energy. In equilibrium, a liquid drop satisfies Young's equation (see, e.g., [86]).

$$\gamma_s = \gamma_{sl} + \gamma_l \cos \theta, \quad (1)$$

where  $\gamma_s$ ,  $\gamma_{sl}$ , and  $\gamma_l$  represent the energy of the surface, solid-liquid interface, and the liquid-vapor interface, respectively.  $\theta$  is the contact angle between liquid and the surface (Figure 2).

The effects of vapor adsorption and spreading pressure are not considered here. Further, the drop is considered to be much smaller than the capillary length  $l_c$ , which is defined as

$$l_c = \sqrt{\frac{\gamma_s}{\rho g}}; \quad (2)$$

here,  $\rho$  is the density of the liquid and  $g$  is the acceleration due to gravity [1, 86]. Conventionally, the term “drop” is used when the volume of the liquid drop is more than  $100 \mu\text{l}$  and for lower volumes the term “droplet” is used [87].

Assuming the drop to be a spherical cap, the drop boundary on the substrate, that is, the three-phase contact line (TPCL), where solid, liquid, and vapor meet, has the shape of a perfect circle, for an ideal smooth surface. In this article, we do not elaborate on rough or prepatterned surfaces, where there may be interesting deviations [88, 89]. We also leave out from our discussion sessile drops describing works on soft or liquid surfaces.

As the liquid evaporates with time, the drop can shrink in two ways [90] (Figure 3):

- (1) The TPCL remains “pinned” to the substrate, leaving the circular solid-liquid contact surface constant; this is referred to as the “Constant Contact Radius (CCR) mode” of drying. Obviously, the angle of contact will decrease with time in this case.
- (2) Alternatively, the radius of the TPCL can decrease, while the angle of contact remains constant. This is called the “Constant Contact Angle (CCA) mode.”

These are two extreme cases but many real experiments show mixed behavior, where both the contact angle and the contact radius vary (so-called stick-and-slip mode; see, e.g., [91]).

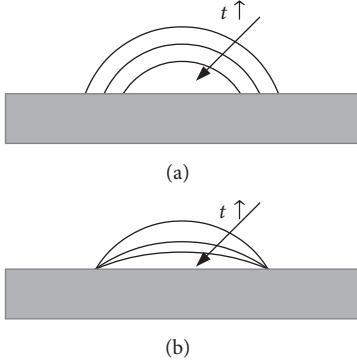


FIGURE 3: (a) Constant Contact Angle (CCA) mode and (b) Constant Contact Radius (CCR) mode.

CCR is the favored mode for drying on high energy surfaces. For example, in case of Piranha treated glass substrate, the contact angle of a water droplet is less than  $15^\circ$  and it is pinned during drying [92, 93]. On the other hand, in the case of low energy surfaces, for example, a TEFLON coated substrate, the contact angle is more than  $150^\circ$  and the mode of drying is CCA. However, things get complicated in the case of liquid drying on a PMMA or polystyrene substrate. The equilibrium contact angles are  $70^\circ$  and  $90^\circ$ , respectively, but the drying mode switches from CCR to CCA mode with time (Figure 4) [94]. Yu et al. [95] explain the switching from CCR to CCA mode from a thermodynamic point of view. Since we are not discussing rough or patterned surfaces, we refer the interested reader to relevant literature in this area. Modifications of Young's equation required for such problems are discussed in [96–99]. The question of contact angle hysteresis (CAH) also needs to be addressed here [100]. The effect of CAH on pattern formation is discussed in [101].

**2.2. Evaporation of a Mixture.** In Section 2.1, we discussed how the shape and size of an evaporating drop of pure liquid change during drying. However, once the liquid evaporates completely, no trace of the drop is left, if the substrate is hard and inert. In this section, we come to more interesting observations. What happens when a drop of a solid-liquid suspension or a salt solution evaporates? What pattern does the solid residue leave on the substrate? Study of this phenomenon as a physics problem started with Deegan et al.'s [22] work on the "coffee stain." Noticeably, at the same time, similar independent researches have been published by Parisse and Allain [90, 102]. Moreover, pattern formation in desiccated drops of biological fluids has been known in medical community even several decades earlier [103, 104].

**2.2.1. Evaporation of a Suspension of Micro- or Nanoparticles.** It is a common observation that when a spilt drop of coffee dries, it leaves a dark ring along the periphery of the droplet, the so-called *coffee-stain* pattern. Initially, the drop looked uniform, so why do the microscopic grains of coffee crowd along the edge during drying, leaving the central portion nearly clean?

Deegan et al. [22, 23] explained that this happens for a pinned boundary (CCR mode). This causes "capillary flow" internal currents from the center towards the TPCL, carrying the suspended solid particles to the boundary, where they get deposited in the form of a ring.

The necessary conditions for formation of the coffee stain are (i) evaporation and (ii) the fact that the drop should be pinned to the substrate during evaporation (Figure 5). Note that an alternative mechanism for coffee-ring deposition based on convection [105] and on active role of free surface [106] has been proposed.

Different patterns of drying are noted when the above conditions are not satisfied. If the TPCL does not remain pinned to the substrate but slips and sticks during drying, a series of concentric rings with varying radius are formed [91, 107, 108].

There is another important effect that competes with the capillary flow causing "coffee-ring effect" and leads to deposition of the suspended particles near the center of the drop. On the other hand, in some cases, the whole solid is deposited near the center of the drop [13, 23, 109]. This is more prominent when the angle of contact is large and is named the *Marangoni effect* [54, 110–112]. It arises due to a gradient in surface tension. There are two sources of such a gradient. First of all, a gradient in surface tension can be produced by a temperature gradient created by different rates of evaporation along the surface of the drop (thermal Marangoni effect). Since evaporation absorbs latent heat, regions near the TPCL cool more than the surface near the top of the drop. This leads to a convection current from the center of the drop surface to the periphery then to center of the bottom of the drop and again to the center of the surface. The temperature gradient in turn produces a gradient in surface tension. This drives the suspended particles along with the fluid in circulating paths from the top of the drop downward towards the center (Figure 6). Here they may get adsorbed on the surface or move towards the periphery and recirculate with the vortex formed. Notice that direction of the Marangoni flow depends on the relative thermal conductivities of the substrate and liquid,  $k_R \equiv k_S/k_L$ , reversing direction at a critical contact angle over the range  $1.45 < k_R < 2$  [85]. It is important to note that a *single* circular flow or vortex is not the only possibility. It has been demonstrated that Marangoni convection induced by thermal conduction in the drop and the substrate can result in multiple vortices, depending on the ratio of substrate to fluid thermal conductivities, the substrate thickness, and the contact angle [113]. The Marangoni effect has been clearly demonstrated in organic liquids. Hu and Larson [111] show that, during evaporation, PMMA microparticles suspended in octane collect near the center of the drop. In water, however, the coffee-ring is observed. Another origin of a Marangoni flow is concentration gradient. Thermal and solutal Marangoni effects may compete with one another [60].

Marangoni effect should always be present in clean fluids but is suppressed in water if surfactants are present. According to Hu and Larson [111], it is difficult to avoid presence of trace surfactants even in "pure" water, so the coffee ring dominates.

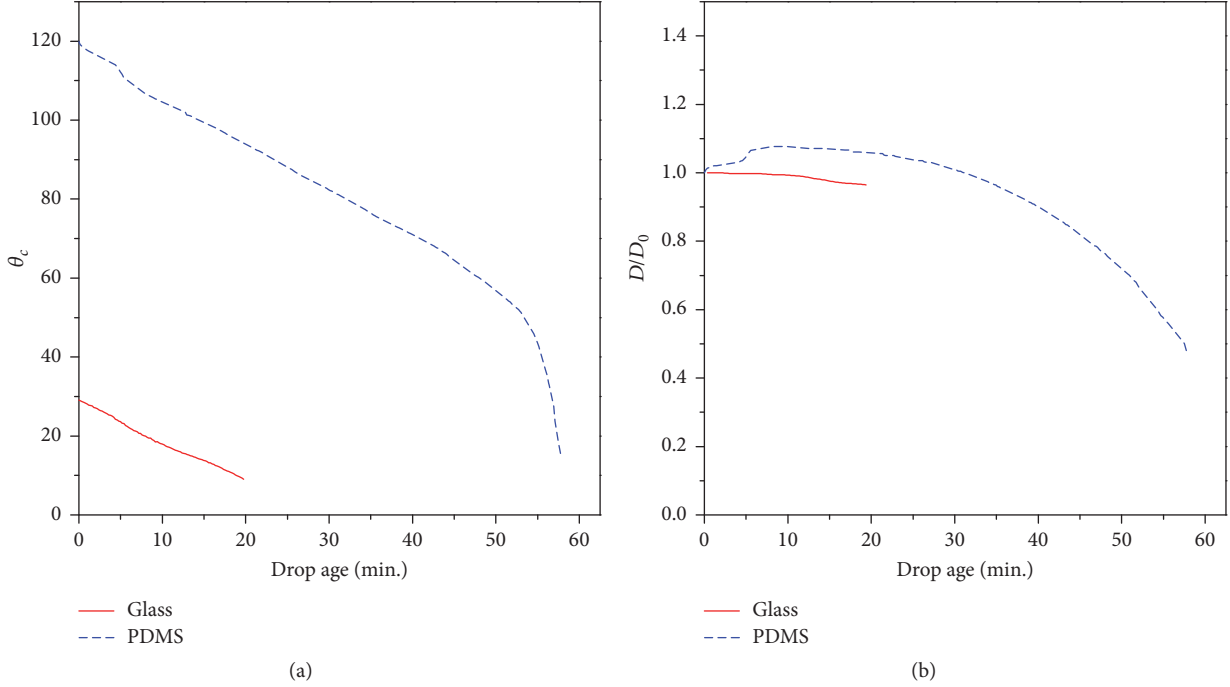


FIGURE 4: (a) Contact angle variations for a water droplet on nontreated glass substrate (red solid curve) and PDMS substrate (blue-dashed curve); (b) normalized diameter of same drops on glass substrate (red solid curve) and PDMS substrate (blue-dashed curve).

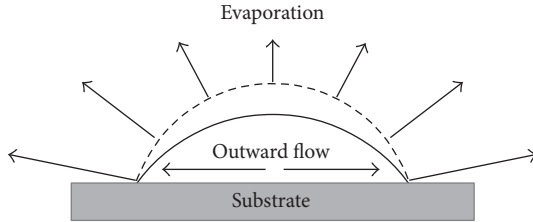


FIGURE 5: Evaporation and TPCL pinning as the origin of outward flow inside evaporating sessile droplet [22]. Initial position of the free surface is shown as the dashed line, whereas its new position due to evaporation is shown as the solid line.

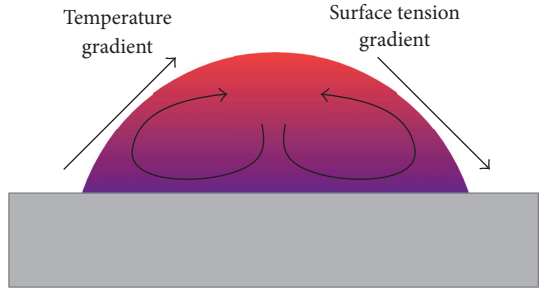


FIGURE 6: Thermal Marangoni effect is produced by inhomogeneous cooling of the free surface due to evaporation. The temperature gradient in turn causes a surface tension gradient.

The competition between the capillary effect leading to the coffee ring and Marangoni effect is decided by several parameters including the thermal conductivities of the substrate and fluid [85, 113–117] and a Marangoni number (thermal) (Ma) has been defined to characterize this [54, 118]:

$$Ma = -\frac{\partial \gamma}{\partial T} \frac{H \Delta T}{\mu \kappa}. \quad (3)$$

Here,  $\Delta T$  is the temperature gradient,  $\mu$  is the viscosity of the fluid,  $\kappa$  is the thermal diffusivity, the surface tension of the fluid is  $\gamma$ , and  $H$  is the height of the drop. So, hydrophobicity or high contact angle of the liquid on the substrate is needed for getting higher  $H$  to induce stronger Marangoni flow inside the droplet.

Once the factors deciding the dominance of capillary flow or Marangoni effect have been identified, it becomes possible to control the deposition pattern and choose whether a thin

ring or a uniformly covered circular patch or a small spot at the center of the drop is desired. Besides physical and chemical properties of the fluid and substrate, manipulating the temperature distribution using heated/cooled substrates or microheaters has also been used to tailor the deposition pattern [119–121] for various applications. The effect of particle shape has also been found to play a role in the final desiccation pattern; ellipsoid-shaped particles suppress the coffee-ring effect as shown in several works [109, 117].

**2.2.2. Evaporation of a Salt Solution.** In Section 2.2.1, we considered a fluid drop containing suspended solid particles of nm to  $\mu\text{m}$  size, which do not interact with each other. Now we discuss the case of a *dissolved salt* in a suitable liquid. So here we have dissociated ions uniformly distributed in a liquid drop. Unlike the colloid particles in Section 2.2.1,

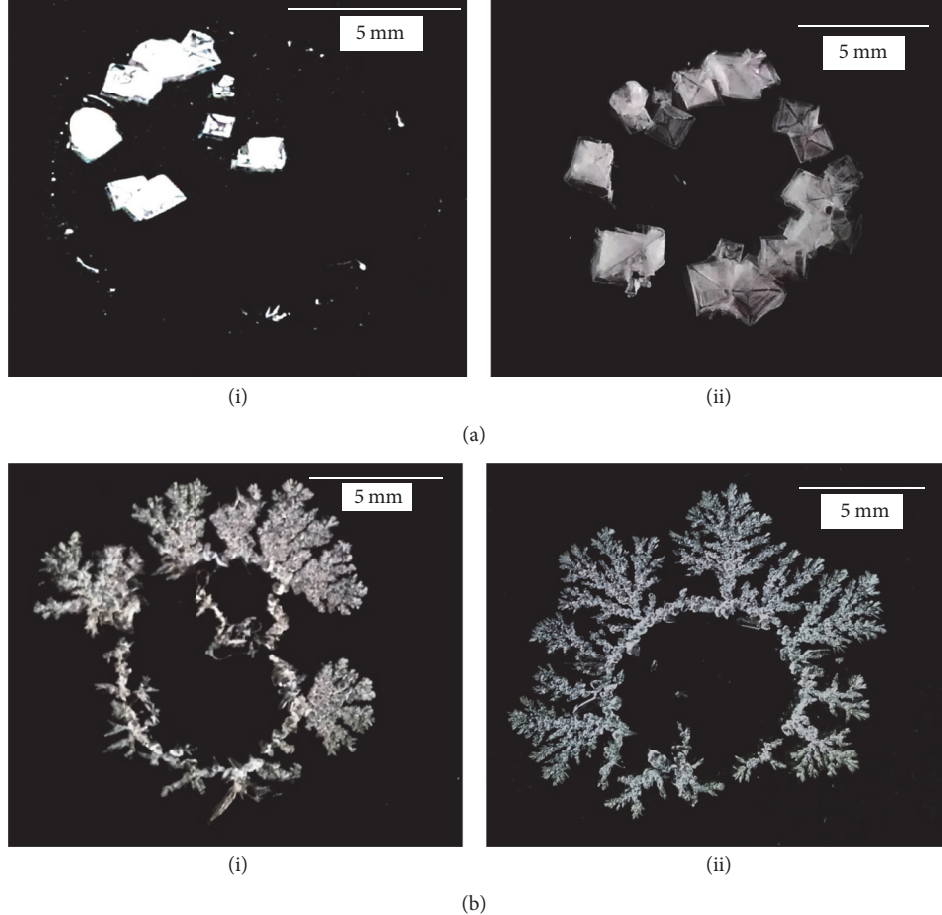


FIGURE 7: (a) and (b) are dried drops ( $50 \mu\text{l}$ ) of NaCl and Na<sub>2</sub>SO<sub>4</sub> solutions on Piranha treated glass substrates. (i) and (ii) represent different concentrations (0.05 M and 0.1 M, resp.) of salts in the solutions.

the ions tend to form *crystals* as the drop dries and salt concentration increases.

Dutta Choudhury et al. [24, 26] evaporated droplets of aqueous NaCl solution of different concentrations on a hydrophilic substrate. They found that the capillary flow dominates here and the salt collects along the pinned TPCL in the form of a ring of cubic crystals. The size and structure of the crystals depend on salt concentration and evaporation rate. For large concentrations, there is a tendency to form *hopper crystals*. Hopper crystals [122, 123] are somewhat like empty boxes and form when growth at the corners and edges is faster compared to the faces (Figure 7(a)). Droplets of aqueous copper sulphate solutions also display the coffee-ring effect, with crystals forming along the periphery of the drop [124–126]. However, Shahidzadeh et al. [124] did not find coffee rings on drying aqueous NaCl. Rather they found that the salt accumulates near the center of the dried drop. In their experiments, the crystals formed initially at the periphery but were later pushed towards the center. The conflicting findings of Dutta Choudhury et al. [24] and Shahidzadeh et al. may be due to finer details of the experiment. It is possible that fine imperfections/roughness on the surface in the case of the former group pinned the NaCl crystals

at the drop periphery, without allowing them to be pushed inward.

Other interesting forms of crystallization have been reported as well. Sodium sulphate crystallizes in two forms—thenardite and mirabilite. At high relative humidity (RH), a drop of aqueous sodium sulphate shows on drying tree-like growth of mirabilite on the substrate *outside the drop* in addition to crystal formation within the drop boundary (Figure 7(b)). This peculiar growth has been explained as follows: crystals formed along the TPCL release water of crystallization which seeps out from the drying droplet and the dendritic trees grow from these. At low RH, thenardite crystals grow within the drop boundary [125, 127].

**2.2.3. Evaporation of a Complex Fluid Drop Containing Salt.** If the host liquid is a complex non-Newtonian fluid and salt is added to it, the solid residue after evaporation exhibits most beautiful patterns. Such patterns on dried biological fluids have long been studied [103, 104, 128–137], particularly as a tool for diagnosis of certain diseases [3, 62, 138–141]. Before discussing the salt added complex fluid, we should examine what happens in absence of the salt.

If a drop of gelatinized starch or gelatin or an aqueous solution of a polymer like polyethylene oxide is allowed to dry, usually a uniform circular film is produced. Depending on the nature of the fluid and substrate, the film either sticks to the substrate or can be cleanly pulled off [142].

Gelatin, starch, or a similar medium which increases the viscosity of the solution by orders of magnitude can change pattern formation of salts drastically. The flow fields within the drop get suppressed and salt crystals no longer show their normal morphology. The role of gelatin in tuning crystal growth has been known for a long time [26]. Goto et al. [143] demonstrate how tuning concentration of a drying gelatin and NaCl drop and manipulating concentration gradients create unique morphologies such as orthogonal or oblique lattices and curving patterns. They show that nonequilibrium growth conditions lead to various dendritic patterns.

If salts are present in the droplet, they usually crystallize during drying. Morphology of the salt crystals is very sensitive to the kind of salt, concentration, and type of colloidal particles, as well as the rate of evaporation [24–26, 29, 142, 144–148]. This sensitiveness allows using the morphology of salt crystals as an indicator, for example, to diagnose different diseases by drying drops of biological fluids [139, 149].

On addition of a salt, the salt crystallizes in different forms, often several different crystallization modes appear as drying proceeds, and video recordings observed under an optical microscope are fascinating to watch (see videos; a drop of aqueous gelatin solution with a little NaCl salt is allowed to dry; large crystals of salt form, followed by multifractal dendrites in-between and a drop of gelatin containing sodium sulfate forms patterns on drying; concentric rings and dendrites growing from them can be seen). Sodium chloride in gelatinized potato starch solution forms dendrites or hopper crystals of different morphology, depending on experimental conditions [24]. In gelatin, two distinct modes of pattern formation were observed [26, 142]. Formation of initial faceted rectilinear crystals of macroscopic dimensions (of  $\sim$ mm) size was followed by a fine dendritic network observable only under a microscope. The faceted crystals appear to consist of NaCl only, while the dendrites may be a composite; further analysis is needed here. The dendritic pattern consists of fine self-similar branches meeting at right angles and has been shown to be multifractal [26]. Other salts also form interesting patterns when dried in a gelatin drop. Sodium sulphate forms a series of rings, which are grouped in bands, and dendritic crystals grow from the rings [126]. Copper sulphate forms feather-like patterns, with anisotropy evident from images under crossed polarizers [126]. These patterns also reveal fractal characteristics [150]. Effect of albumin concentrations on sodium chloride crystallization from drying drops of albumin-salt solutions has been experimentally investigated [147].

The processes occurring during the desiccation of the sessile colloidal droplets and morphology of the resulting precipitate depend on many different factors, for example, the nature and shape of the colloidal particles [109] and their initial volume fraction [147], the presence of admixtures (e.g., surfactants) in the solution [50, 107, 151, 152], ionic strength and pH of the solution [28], the properties of substrate

(thermal conductivity, whether hydrophilic/hydrophobic) [24, 85, 153, 154], and evaporation mode [32, 36, 155–157].

Surfactants have a strong effect on Marangoni flow as already discussed. A particle-surfactant mixture thus can modulate the capillary flow [18, 107, 152]. Colloidal sulphur with salt self-assembles into a wide variety of patterns, depending on conditions [158]. Different sodium salts are formed in situ, using different acids—monobasic, dibasic, and tribasic. For HCl, the typical NaCl aggregation pattern was observed (similar to [26]). For dibasic sulphuric acid, morphology similar to the two crystalline forms of sodium sulphate was observed and tribasic, citric acid produced a uniform deposition without any definite pattern.

Classification of possible desiccation modes may be done using two characteristic times, namely, the drying time,  $t_d$ , and the gelation time,  $t_g$  [28]. There are three different modes of colloidal sessile droplet desiccation [28]:

- (1)  $t_g \gg t_d$ , where  $t_g$  is the gelation time and  $t_d$  is the desiccation time. The gelled phase occurs near the droplet edge and moves inward, while the central area of the droplet remains liquid.
- (2)  $t_g \approx t_d$ . The gelled skin covers the free droplet surfaces. This thin shell cannot prevent evaporation of the solvent. The buckling instability occurs [48].
- (3)  $t_g \ll t_d$ . The phase transition from sol to gel in the whole bulk of the droplet is almost instantaneous. The gelled droplet loses solvent via evaporation very slowly.

When  $t_g \gg t_d$ , the desiccation process can be divided into several stages (see, e.g., [63, 159, 160]):

- (1) Initial single-phase liquid stage: the whole droplet is a sol. The outward flow carries suspended particles to the droplet edge until the volume fraction of the suspended particles,  $\Phi$ , reaches the critical value,  $\Phi_g$ . Note that particle-enriched region is extremely narrow, whereas the particle volume fraction in the central area of the droplet is almost constant along its radius. This stage was simulated in [161–163] and in [159].
- (2) Intermediate two-phase stage: a gelled ring appears near the droplet edge and grows towards the droplet center. The volume fraction of the colloidal particles is constant inside the *foot*, that is, the outer gelled band,  $\Phi_g$ , and almost constant in the sol,  $\Phi$ , except for a rather narrow area near the phase front. This stage was simulated in [164–166] and in [159, 167].
- (3) Final single-phase solid stage: the gelled deposit loses the remaining moisture very slowly. Some real fluids of interest (e.g., biological fluids) can contain both suspended particles and dissolved substances. In this case, the dendritic crystals can occur in the central area of a sample [25, 29, 60]. Finally, the desiccation crack patterns appear [8, 28–31, 33, 36, 38].

**2.2.4. Biological Fluids.** Most biological fluids can be regarded as a complex fluid containing salts. But we devote a

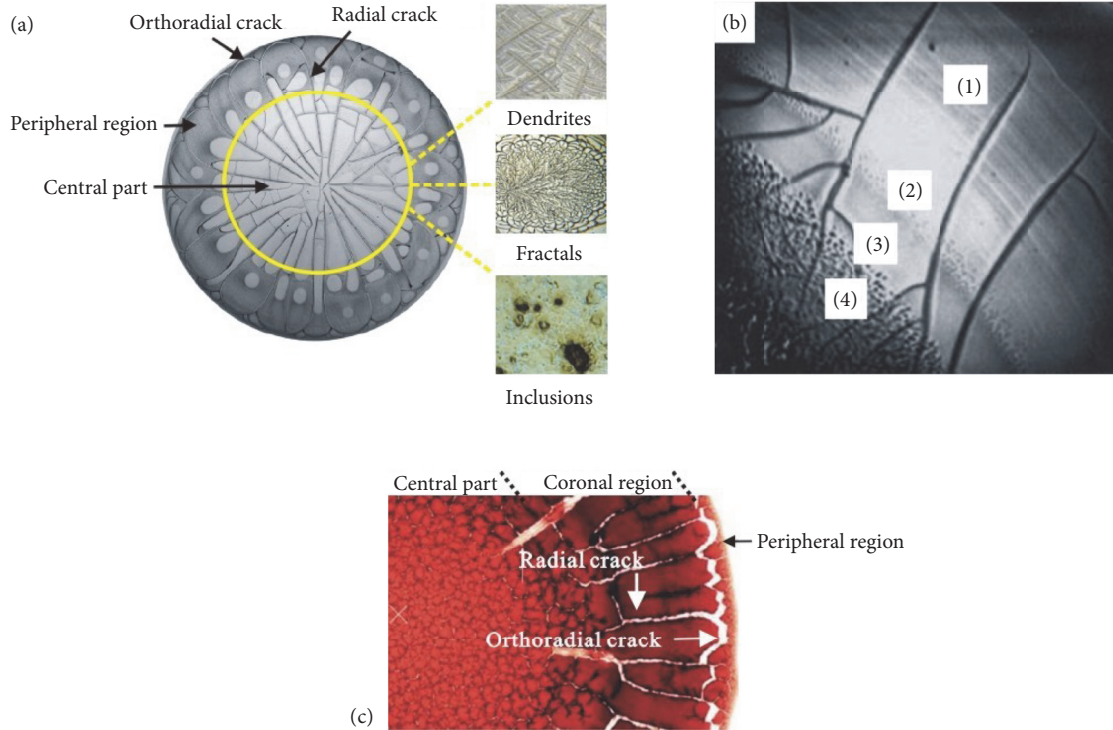


FIGURE 8: Desiccation patterns in the sessile drop of (a) blood plasma from a healthy adult (adopted from [61] with the permission of Springer and from [62] with the permission of Hindawi); (b) morphological details of four regional patterns in the sessile drop of BSA saline solution: (1) homogeneous protein film, (2) protein precipitates, (3) protein gel, and (4) salt crystal [63] (reproduced with permission of Elsevier); (c) whole blood droplet drying on a glass substrate (adopted from [64] with the permission of Cambridge University Press). The whole figure is reproduced from [65].

separate section to these liquids, because the complexity in composition and the bioactive nature of the constituents of body fluids make the evaporation of such liquid drops quite different from laboratory prepared micro or nanofluid drops.

Although pattern formation can be observed during drying of both inorganic and organic colloids, the case of biological fluids is increasingly attracting attention from the scientific community in recent years [64, 168, 169] as this study promises to be a simple and cost-effective technique for diagnosis [20]. We shall discuss further details of application in medicine in Section 4. In this section, we will review some of the experimental observations of drying on drops of human blood serum, whole blood, and other biofluids such as urine, saliva, and tears.

While performing the experiments seems very simple (table top experiments producing interesting patterns can be done even at home), understanding the physics behind the pattern formation phenomena turns out to be extremely complicated and involves a number of interrelated processes of different nature [10, 12]. During desiccation of biological fluids, a sequence of various physical and physicochemical processes can be observed [63, 170]. For example, redistribution of the components occurs. Protein molecules are carried by flows to the edge of the droplet and accumulate to form a gel. The salt is distributed over the whole area of the droplet almost uniformly. After complete drying of the droplet, a protein precipitate remains on the substrate in the form of a

ring; the width of the ring depends on concentrations of the protein and the salt [3, 171, 172]. Salt crystals can form fractal (dendritic) structures [24, 29, 142, 173, 174]. In the later stages of drying, a sample may crack [8, 28, 29]; the characteristic pattern of the cracks also helps in diagnosing diseases from which the subject may be suffering [175].

Blood serum mainly contains 90% (by mass) of water, 6% of macromolecular proteins, 1% of inorganic electrolytes, and other minor components [20]. Although its composition is complicated, blood serum behaves like a Newtonian fluid. Desiccation patterns of a sessile drop of blood serum drying on a solid substrate are generally characterized by two distinguishable regions: a peripheral region and a central part. Cracking patterns in orthoradial and radial directions are observed throughout the whole sessile drop, and crystal patterns with different morphologies accumulate in the central part [61], as shown in Figure 8(a).

Three major factors influence the morphologies of these serum patterns: concentration of inorganic salts, concentration of macromolecular proteins, and the wettability of the droplet on the substrate. Inorganic salts are essential for formation of crystal patterns in the central part [50]. High concentration of salts promotes the aggregation of macromolecular proteins, thus changing the morphologies of crystal patterns [176]. The wettability of the substrate plays an important role in determining the apparent contact angle of the sessile drop [177]. This may further influence the TPCL

motion and the mass transportation during drying and in turn the desiccation patterns.

Whole human blood behaves like a non-Newtonian fluid unlike blood serum. It is composed of plasma (55% by volume) and cellular components (45% by volume) (i.e., red blood cells (RBCs), white blood cells (WBCs), and platelets); RBCs, WBCs, and platelets represent 97%, 2%, and 1% of the total volume of these cellular components, respectively. Desiccation patterns in the dried sessile drop of whole human blood are significantly different from those of blood plasma without cellular components [64, 153]. Patterns in the blood droplet from healthy adults dried on glass substrates consist of three distinct zones with different characteristic cracking patterns (Figure 8(b)), namely, a fine peripheral region adhering to the substrates, a coronal region with regularly ordered radial cracks and large-sized deposit plaques, and a central part with disordered chaotic cracks and small-sized deposit plaques [64]. Desiccation patterns of the blood droplet are significantly influenced by the external drying conditions, such as the RH and the wettability of the blood droplet on the substrates [36, 38, 157].

Characteristic desiccation patterns are also formed in the sessile drops of other biofluids (e.g., urine, saliva, and tear fluids) [11, 178, 179]. Yakhno et al. investigated the drying of sessile drops of urine and saliva from the healthy adults and divided it into three stages: the redistribution of materials leads to the continuous flattening of the droplet; the deposited macromolecular proteins aggregate to form the gel matrix; the inorganic salts induce phase transition of macromolecular proteins to form desiccation patterns [11]. The desiccation patterns of the tear droplet are characterized by a thin amorphous film in the peripheral region, with fern-like patterns in the central part. The thin amorphous film in the peripheral region has crack patterns as observed by SEM. The fern-like patterns in the central part are composed of cubic crystals and dendritic patterns adjacent to them. Energy dispersive X-ray analysis (EDXA) results revealed that dendritic patterns were predominantly made up of sodium and chloride, while cubic crystals were potassium and chloride [180].

Despite the application of the phenomena for practical purposes and considerable progress in understanding of the phenomena [10, 12], the theoretical description of the pattern formation in desiccating biological fluids is still incomplete. The physical, biophysical, biochemical, biological, and physicochemical processes occurring in the dehydration of biological fluids remain largely to be clarified.

Analysis based on a visual comparison of the structures formed by drying a liquid drop [3, 4, 81, 181, 182] has significant drawbacks. Conclusions are liable to be subjective, without techniques for defining quantitative parameters to characterize the structures. Computer pattern recognition may be tried to eliminate this shortcoming [36, 61, 183].

Other samples of biological origin which form liquid crystal phases have shown interesting patterns on drying droplets. For example, DNA [184] forms a ring-like deposit with zigzag patterns [185]. Cetyltrimethylammonium Bromide drops with salt were also found to form concentric rings and crystalline aggregates near the center [186].

**2.3. Evaporation of Drops under Levitation.** So far we discussed sessile droplets that sit on a solid substrate during drying. Even for the superhydrophobic case with contact angles approaching  $180^\circ$ , the dried pattern left on the substrate is two-dimensional or quasi-two-dimensional (when the deposits pile up forming rings or aggregates). The aspect ratio of the deposit, that is, the maximum height, divided by the drop radius is much less than 1. Is it possible for a drying drop to reduce to a spherical shell after evaporation? It turns out that this can be achieved by drying a levitated drop floating in air with zero contact to any surface. Suspending the drop by properly adjusted acoustic fields is the most convenient technique for this study. Radiative heating leads to evaporation of the solvent.

Tijerino et al. [66] evaporated droplets with nanosilica suspensions under different conditions of acoustic amplitudes and solid concentration to obtain residues with varied shapes like rings, bowls, and spheroids (Figure 9). Wulsten et al. [70] used acoustic levitation to investigate the effect of a solvent containing different polymers and the drug itraconazole on drying. The morphology of the residue was found to depend on the drug, while the polymer determined the drying rate. Single-phase droplets [70, 187] and binary or multiphase droplet [188, 189] have been studied using similar techniques.

Although liquid drops can be levitated by various levitation techniques ranging from electrostatic to diamagnetic [190], the acoustic technique is more suitable for evaporation experiments as the electromagnetic properties of the materials are not relevant here. The drying patterns of colloidal droplets depend on the particle-particle interactions and are significantly affected by the substrates as well. With the increase of substrate contact angle, the final residue pattern can be coffee-ring-like stains (Figure 10(a)) on hydrophilic substrate [37] and bowl-shaped residue (Figure 10(b)) on a hydrophobic substrate ( $\Theta \sim 90^\circ$ ) [67]. Under acoustic levitation, a ring-shaped residue has been obtained (Figure 10(c)) [68], which exhibits a geometrical similarity with the initial dog-bone shape of the acoustically levitated droplet [191]. These results highlight the important role played by the drop profile in drying pattern formation, and acoustic levitation provides the possibility to study drop evaporation at zero-contact condition for different initial shapes.

**2.4. Desiccation Crack Patterns on Drying Drops.** As a colloidal drop dries, viscosity increases and a sol-gel transition may occur. Stress accumulates nonuniformly due to the droplet shape and inhomogeneity of the fluid. This often leads to formation of cracks with characteristic patterns. In addition to the *crack patterns*, other quasi-3D effects are of interest such as wrinkling, buckling, and skin formation.

Desiccation crack patterns have been intensively investigated both experimentally and theoretically [28–32, 34, 36–41, 192]. State of the art may be found in the recently published book [8]. We discuss here some studies on crack formation in drying drops [16, 24, 29, 193].

The final drying pattern and crack nucleation vary with the kinetics of the evaporation rate. During solvent evaporation, curvature of the solvent-air meniscus is responsible for

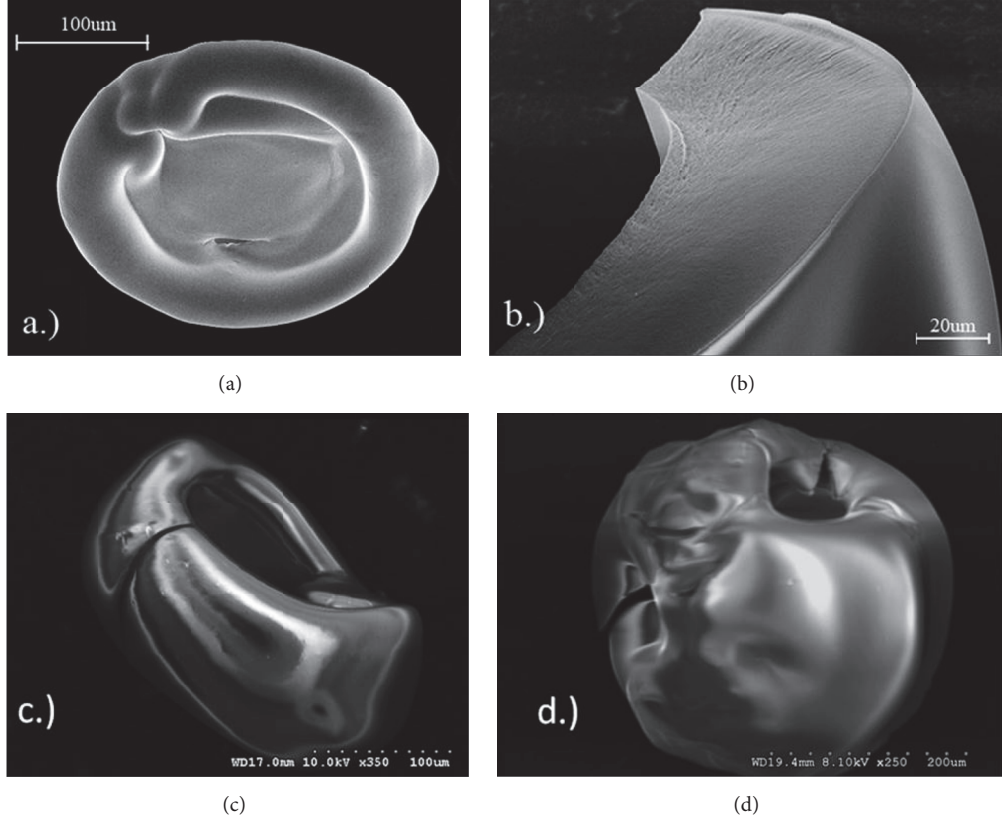


FIGURE 9: Different residues obtained from levitating droplets (reproduced from [66], with the permission of AIP Publishing).

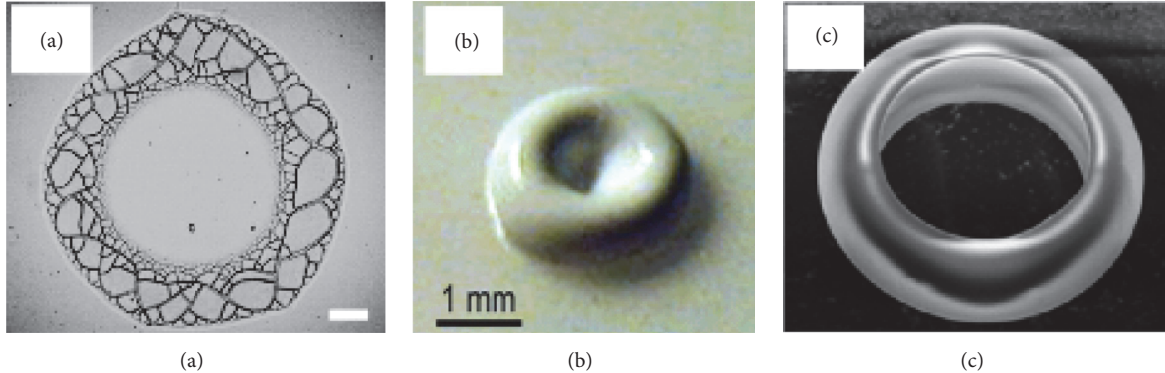


FIGURE 10: Different drying patterns obtained from varied conditions. (a) Coffee ring-like stain on hydrophilic substrate, reprinted with permission from [37]; (b) bowl-shaped relic on hydrophobic surface, reprinted with permission from [67]; (c) ring-shaped residue obtained from acoustic levitation, reprinted with permission from [68].

a capillary pressure in the liquid phase. The capillary pressure induces shrinkage of the porous matrix, which is constrained by the adhesion of the deposit to the glass substrate. As tensile stresses build up, the internal stresses become too great and fractures appear to release mechanical energy. The differences in pattern formation arise due to the competition between the drying process and the adhesion of the matrix on the substrate.

Annarelli et al. [29] worked on the evaporation, gelling, and the cracking behavior of a deposited drop of protein

solution, bovine serum albumin. They observed that the cracks appearing at the gelling edge were regularly spaced and were a result of the competition between evaporation-induced evolution and relaxation-induced evolution. When the crack evolution is only evaporation-induced, the mean crack spacing is proportional to the layer thickness. However, in the case of a drop of bovine serum albumin, the evolution of cracks has been described in relation to the change with time of the average shrinkage stress. In this case, the mean crack spacing was observed to be inversely proportional to

the deposit thickness. This is unexpected as normally crack spacing increases with thickness.

Brutin and his group worked on the pattern formation of desiccating droplets of human blood from which the coagulation protein had been removed [7, 64]. They studied the dynamics of the process of evaporation of a blood droplet using top-view visualization and the drop mass evolution during the drying process. Brutin et al. [64] showed that there are two distinct regimes of evaporation during the drying of whole blood. The first regime is driven by convection, diffusion, and gelation, while the second regime is only diffusive in nature. A diffusion model of the drying process allows a prediction of the transition between these two regimes of evaporation. Concentration of the solid mass in the drop was important and fracture occurred at a critical mass concentration of solid in a drying drop of blood. They showed that the final crack patterns formed on drying droplets of blood collected from a healthy person, anemic person, and hyperlipidemic person are quite different. But drawing conclusions for definite diagnosis is not so straightforward as the crack patterns are strongly affected by external conditions such as the ambient relative humidity and the nature of the substrate.

Brutin et al. [64] conclude that the final drying pattern and crack nucleation vary with the kinetics of the evaporation rate. The transfer of water to air is limited by diffusion and is controlled by the relative humidity in the surrounding air. The drying process of a sessile drop of blood is characterized by an evolution of the solution into a gel saturated with solvent. When the gel is formed, the new porous matrix formed by the aggregation of particles continues to dry by evaporation of the solvent, which causes the gel to consolidate.

Carle and Brutin [154] studied the influence of surface functional groups and substrate surface energy on the formation of crack patterns and on the dry-out shape in drying a water-based droplet of nanofluid. They have also studied desiccation of blood droplets [153] on different substrates such as glass and glass coated with gold or aluminium. They measured the rate of heat transfer from the substrate to the fluid drop. They show that wettability of the substrate by the fluid is the decisive factor, which can account for the differences in the morphology of the desiccated blood drop on different surfaces, rather than the thermal diffusivity which determines rate of heat transfer from the substrate to the drop. On metallic surfaces, where the drop is nearly hemispherical and a glassy skin forms on the fluid-air interface, there are hardly any cracks. On a glass surface, on the other hand, where the drop is more or less flat, an intricate pattern of cracks form. Figure 11 shows spiral cracks typical of albumin; these can be easily observed by drying egg white [8].

The study of desiccation crack patterns on clay-gel droplets dried in a static electric field [35] led to some interesting results. The number of cracks formed and the time of first appearance of the cracks could be related to the field strength through exponential relations. In a further set of observations, the field was applied for a very short finite duration and then switched off. Now the time required for crack appearance after switching off could be related to the

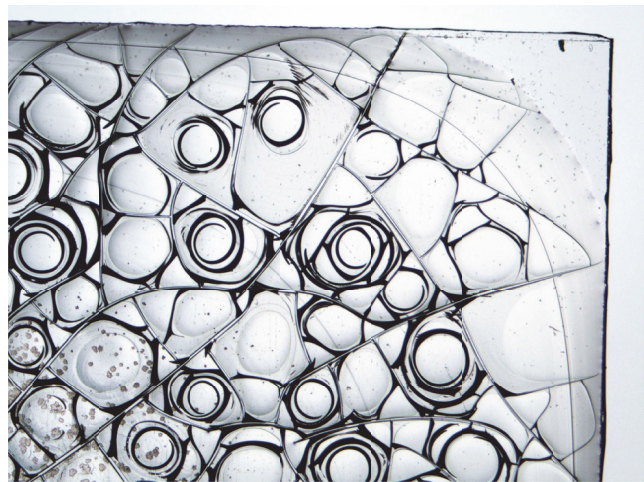


FIGURE 11: Crack patterns in a dried sample of albumin (courtesy of N.A. Koltovoi).

field strength and exposure time, when all quantities were appropriately scaled.

In a follow-up of this work [194], where platinum electrodes were used to avoid chemical interactions during drying, it was shown that the clay drop behaves like a leaky capacitor and could be modelled using methods of generalized calculus [195].

Effect of the drop constituents on *crack speed* has also been studied. Zhang et al. show that a colloidal solution of polytetrafluoroethylene particles cracks radially as it dries [196]. Crack speed varies as a power law with thickness and surfactants such as sodium dodecyl sulfate can be used to tune the cracking.

**2.5. Desiccation under Perturbation.** While there are several works on desiccating droplets done by different groups, there are very few studies on drying droplets in the presence of a perturbation. The contact angle of a conductive aqueous laden drop with organic or inorganic solutes or ambient oils changes with the application of alternating current (AC) voltage during drying. Banpurkar et al. [197] studied the above effects in experiments to demonstrate the potential of electrowetting-based tensiometry. Contact angle ( $\theta$ ) decreases with increasing amplitude ( $V_{AC}$ ) of AC voltage following the linear relation of  $\cos \theta$  with  $V_{AC}$ . They applied low frequency AC voltage and obtained interfacial tensions from  $5 \text{ mJ/m}^2$  to  $72 \text{ mJ/m}^2$ , in close agreement with the macroscopic tensiometry for drop volumes between 20 and 2000 nL. Vancauwenbergh et al. [198] reviewed the effect of an electric field on a sessile drop. They observed that an external electric field can change the contact angle and shape of a droplet. The electric field also affects the evaporation rate during drying. The contact angle is not always an increasing function of the magnitude of the applied electric field but may be a decreasing function for some liquid droplets as well.

Studies have also been done on the effect of external perturbations during drying. The effect of electric fields has been studied on cracks formed in drops of drying clay gels

[35, 194]. Khatun et al. [35] and Hazra et al. [194] investigated desiccation cracks on drying droplets of aqueous Laponite solution in the presence of a static electric field (DC). The electric field had cylindrical geometry, with the peripheral electrode being an aluminium wire [35] or platinum wire [194] bent into a circular form with diameter of  $\sim 1.8$  cm. A drop of Laponite gel was deposited inside this wire loop. Another aluminium/platinum wire with its tip touching the lower substrate through the centre of the drop acted as the central electrode. Typical cracks had radial symmetry and were found to emerge always from the positive electrode. The cracks formed even when the field was applied for a few seconds and then switched off; this was interpreted as a *memory effect*.

Sanyal et al. [199] experimentally investigated nanoparticle aggregation and structure alteration of evaporating sessile colloidal droplets when subjected to low frequency vibrations of the substrate. Low frequencies perturbed the droplet when the corresponding vibrational wavelength was comparable to the size. For forcing frequencies in the resonance band of lowest allowable mode, the change in the overall morphology of the deposit structure from natural droplet drying was pronounced, with a sharper wedge at the periphery. Recirculation and subsequent outer flow near the droplet edges created higher particle concentration, leading to faster growth of the peripheral wedge. For frequencies away from resonance, the internal flow was mostly uniform, leading to less enhanced wedge structure, similar in appearance to the case of natural evaporation. They demonstrated that, by using forced vibration, desired control of particle deposition could be achieved for various applications.

**2.6. Interacting Droplets.** We briefly mention another recent interesting line of research here. There are studies showing that a drying drop influences the pattern formation on another drying drop, provided that the distance between them does not exceed a certain limit. This is because the presence of another drop enhances the RH on the side nearer the other drop. So evaporation at the near side is less than that at the far side when two drops are placed side by side. Pradhan and Panigrahi [200] give an experimental as well as a simulation study of this problem.

Cira et al. [201] showed experimentally that two-component droplets of well-chosen miscible liquids such as propylene glycol and water deposited on clean glass at distances of up to several radii apart moved towards each other. This occurred over a wide range of concentrations and even when both droplets had the same concentration. The droplets increased speed as they approached each other. These long-range interactions were preserved even across a break in the glass slide. They explained that the two neighbouring droplets each lie in a gradient of water vapor produced by the other. This gradient causes a local increase in RH and thus decreased evaporation of the thin film on the adjacent portions of the droplets, breaking symmetry. The decreased evaporation leads to an increased water fraction in the thin film, hence increasing the interface tension between liquid and vapor for the film, denoted by  $\gamma_{LV,film}$  locally. Asymmetric  $\gamma_{LV,film}$  around the droplet causes a net force that drives the

droplets towards each other. Cira et al. [201] proposed a mathematical model to obtain the net force acting on each droplet as follows:

$$F = 2\gamma_{LV,droplets}mR \int_0^\pi \frac{(1 - RH_{room}) R \cos \psi}{\sqrt{d^2 + R^2 + 2Rd \cos \psi}} d\psi, \quad (4)$$

where  $m$  is the slope of a plot of apparent contact angle versus the relative humidity, RH;  $d$  is the distance between the droplets;  $\psi$  is a parameter of integration;  $RH_{room}$  is the ambient humidity far from the droplets. This net force causes droplet motion and is balanced by a viscous drag.

If droplets of different surface tension but equal concentration coalesce upon contact, fluid is directly exchanged between the droplets. This exchange of fluid leads to a surface tension gradient and Marangoni flow across both droplets, where the droplet of lower surface tension chases the droplet of higher surface tension, which in turn flees away. They explained the observed phenomena of droplets of sufficiently different concentrations exhibiting a “chasing phase” indicative of a repulsive force that comes into play as the gradient of the vapor pressure decreases  $\gamma_{LV,film}$  around the droplets causing them to move away.

Using their understanding of “self-fuelled surface tension driven fluidic machines,” the authors have explored several applications in food coloring, glass slides, and permanent Sharpie markers.

### 3. Theoretical Description and Modelling

**3.1. Models of Evaporation.** Any model of mass and heat transfer inside an evaporating drop and any model of deposit pattern formation are based on models of evaporation from free surface of the drop. The functional form of the evaporation rate depends on the rate-limiting step, which can be either the transfer rate across the liquid-vapor interface or the diffusive relaxation of the saturated vapor layer immediately above the free surface of the drop [202]. Hence, two main approaches should be mentioned.

The first one is based on the assumption that evaporation from free surface of the drop is steady-state and diffusion-limited. Analysis of this assumption validity can be performed in detail by Popov [202]. In the case of diffusion-limiting quasi-steady process, the vapor density above the liquid-vapor interface obeys the Laplace equation. When droplet shape is governed by surface tension, it can be treated as a spherical cap (see Section 1) and Laplace equation can be solved analytically. This solution has one essential drawback; namely, vapor flux is singular at TPCL. To suppress this physically senseless singularity, a correcting factor may be introduced [203–205].

The second one is based on the assumption that the rate-limiting factor is heat transfer [206]. In this case, a singularity is missing in analytical formula for the vapor rate except for the case of highly volatile droplet.

**3.2. 2D Models of Mass Transfer.** Modelling of the processes occurring during the drying of colloidal droplet solutions is

very complicated, because these processes are extraordinarily varied and complex [63]. The authors have different views about the driving mechanisms that lead to the formation of the solid phase [22, 23, 90, 91, 202, 207]. For example, [208] considered competition of convection and sedimentation, but [159] considered competition of convection and diffusion. Numerous models were proposed during the last two decades. Several models describe some particular processes occurring during the colloidal droplet desiccation (e.g., capillary flow and mass transport processes) [23, 90, 105, 167, 202, 207–215]. Generally, models are developed for systems with low concentrations of the colloidal particles.

Two very different situations are possible when a colloidal sessile droplet desiccates. In the first case, the particles inside a droplet can interact with each other only mechanically (impacts). In this case, the deposit forms a porous medium. Such a medium prevents neither bulk flow inside it nor evaporation from its surface. Moreover, such a porous medium can enhance evaporation from its surface due to drainage effect [209]. In the second case, the colloidal particles can form strong interparticle bonds. In this case, hydrodynamic flows, particle diffusion, and solvent evaporation are restricted. The proposed theoretical models mainly deal with the first situation [23, 90, 105, 167, 202, 207–214]. Only a few models treat the deposit as impenetrable for flows and preventing evaporation [159, 165–167]. Nevertheless, the simulation of desiccated colloidal droplets with phase transition is extremely important for high-throughput drug screening [60], biostabilization [216], identification of fluids [183], and medical tests [139, 217–219]. The models in [159, 165–167] utilize sets of rather complicated partial differential equations (PDE).

Other approaches for simulating pattern formation in drying drops have also been tried. A simple Monte Carlo algorithm for evaporation and pattern formation has been developed by Dutta Choudhury et al. to reproduce the formation of faceted salt crystals and dendritic aggregates in drying droplets of aqueous gelatin containing NaCl [142]. The pattern formation can be correlated to the topological concept of the Euler number [220].

Several models describing desiccated sessile colloidal droplets have been reported recently [117, 159, 165, 167, 221]. They are based on the lubrication approximation [222]. This approach has several serious shortcomings [223] as enumerated below:

- (1) Only thin films can be considered; all quantities are supposed to be dependent only on one radial coordinate.
- (2) In fact, a two-phase system is considered as one-phase system; the gel is assumed to be a liquid with very high viscosity; the hydrodynamic equations are written for the whole droplet desiccation.
- (3) The mathematical expression for evaporation flux above the free surface is speculative rather than being supported by experiments. To the best of our knowledge, measurements of the vapor flux above a system with sol-gel phase transition are not published yet.

(4) Knowledge of the effect of particle concentration on viscosity is needed for calculations. This dependence can be obtained from experiments with rather large volumes of colloid. Viscosity of a small droplet with a large free surface and large contact area with a substrate can deviate from this in a rather complex manner.

(5) It is assumed that all the molecules that get to the edge of the droplet pass into the solid phase. Generally, this assumption can be wrong in the presence of convection of any nature in a droplet. An inward flux of particles due to diffusion may also exist.

To overcome the limitations of the listed models, three-dimensional (3D) models need to be developed and utilized.

**3.3. Modelling Flow in 3 Dimensions.** A number of papers devoted to 3D models of processes inside evaporating droplets were published during the last few years. Mostly, the articles consider droplets of pure liquids and simulate flows within them [114, 224–229]. The analytical solutions of the Laplace equation which describe the velocity field inside evaporating droplets of a nonviscous liquid were obtained for the contact angle of 90° by Tarasevich [226] and for a case of arbitrary contact angle by Masoud and Felske [230].

Flow inside the boundary line of an evaporating liquid for any contact angle was found using Stokes approach [231]. Numerical calculations of the velocity field within evaporating droplets were performed using finite element method [54, 110, 225]. Presence of dissolved substances or suspended particles inside the droplets and deposit formation were not taken into account in these models.

**3.4. 3D Models of Mass Transfer.** 3D models describing the processes inside the particle-laden droplets were developed using both the continuum and discrete approaches. Development of discrete models was initiated by the requirements of modelling of evaporation-driven self-assembly (EDSA) or evaporation-induced self-assembly (EISA) [214, 232–239]. Additional references can be found in [240]. Recently published models considered the Brownian motion of particles inside the droplets. For instance, in the work of Petsi et al. [213], the Brownian motion of the particles is superimposed on the hydrodynamic flow calculated previously [231]. A continuum approach has also been applied in some works [59, 208, 209].

Conflicting results from experiments imply that available models may be too simplistic and more realistic theories need to be developed. For example, some experimental data indicate that transfer of the suspended particles to the edge of the drying droplets is possible only when the Marangoni effect is suppressed [111]. However, other experimental studies consider the Marangoni effect to be the driving force for the formation of a new phase on the edge of a drop. It appears therefore that the theoretical models are incomplete, or too drastic approximations/assumptions have been made while formulating them.

There is also some confusion due to nonuniform terminology used by different research groups. For example, [209]

reports *depinning* for large contact angle and no depinning for small contact angle. But it refers to receding of the fluid from the solid deposited at the TPCL as “depinning.” But many other researchers use the term “depinning” as the inward motion of the TPLC as a whole, leaving no deposit behind.

Another such instance is the fact that the direction of flow can be opposite to a direction that is predicted by calculations for the pure solvent [241]. Independent experiments confirmed that the flows in pure liquids and in liquids with admixtures go in different directions [242, 243]. In the multicomponent liquids of biological origin, the thermocapillary and solutocapillary effects can eliminate each other [60]. Calculations of various research groups have shown that during evaporation of the droplet of a pure liquid there are circular flows caused by the Marangoni stress. The flow is directed along the droplets base to its edge and along its surface towards to the center of the drop [54, 114, 225, 228, 244]. At the same time, experiments conducted with biological fluids exhibit opposite direction of flow [241–243]. According to Kistovich et al., Marangoni flow cannot generally occur during drying of the droplets of biological fluids; they suggest that the observed circular currents are caused by buoyant convection [105].

Most of the earlier models for simulating evaporation of droplets have been developed for single solvent droplets. Recently, a finite element model has been formulated by Diddens et al. [245, 246], which explains results of interesting experimental phenomena such as self-wrapping of ouzo drops on a superamphiphobic substrate [247].

Evaporation of a multicomponent drop is interesting because the solvent contains different liquids with different volatility, so the composition changes during evaporation. For example, in a water-glycerol mixture, where evaporation of glycerol can be neglected compared to water, a large contact angle is shown to lead to a reversed Marangoni flow. If the relative humidity is high, when water content of the drop is reduced due to evaporation, water vapor from the surroundings condenses onto the drop. The problem now becomes nonlinear and chaotic vortices form [246]. This has been observed experimentally as well [248].

On the other hand, for a water-ethanol mixture, where both components evaporate fast, the substrate cools rapidly and thermal transport has to be taken into account. Chaotic behavior is predicted by the model [246] and has also been observed experimentally [249–251]. There are, in addition, models focusing on a particular aspect of desiccation such as skin formation [252, 253].

**3.5. Crystal Growth.** The sensitivity of crystal morphology on various parameters impedes modelling because a lot of different effects have to be taken into account. In fact, all used models should be treated as semiempirical. The models often utilize the lattice approach [142, 254–257] and diffusion equation [25, 258]. Adequacy of some models [254–256] has been questioned [258]. Mainly, dendritic crystal growth can be observed at the final stages of drop desiccation. Both nonequilibrium growth and presence of impurities may produce dendritic shape of crystals [259]; these effects can

be reproduced in a simple model [260]. The semiempirical Monte Carlo approach by Dutta Choudhury et al. [142] qualitatively reproduces the crossover in faceted and dendritic crystal growth and shows the relevance of statistical methods in this problem through the Euler number [220].

The phase-field method [261] looks extremely promising for modelling crystal growth in desiccated colloidal droplets with salt admixtures, but it requires a lot of additional information, which is difficult to obtain experimentally.

## 4. Applications and Perspectives

Initially, the negative effect of the coffee ring was of concern to scientists and engineers, since it precludes uniform deposition in processes such as ink-jet printing. So methods to reverse it were in demand. We have discussed in Section 2.2.1 that this is possible by enhancing Marangoni flow or imposing temperature gradients. Another method is to use electrowetting [96, 262, 263]. This can be done by applying voltage though the drop by the technique known as eMALDI, introduced by Eral et al. [96]. Varying voltages give different deposition of salt patterns on substrates [262].

In recent times, however, the picture has changed; increasingly various patterns formed by evaporating drops are being put to good use, instead of being considered a hindrance. We briefly mention below some fields where the *nonuniform distribution* of solute in the drying drop has been helpful.

**4.1. Application in Functional Materials.** The group led by Shimoni et al. [264] created a connected network of coffee rings by deposition of conducting micro/nanoparticles on a transparent substrate. This produces a transparent conductor that is extremely important in today’s technology for various photovoltaic devices. The droplet technique provides a much cheaper alternative to indium tin oxide or indium tin fluoride coated glass, traditionally used as transparent conducting material. Drying a drop of some specific solvents with CNT (carbon nanotubes) on a cooled substrate similarly produces a polygonal connected, self-assembled network, which is transparent as well as conducting [27]. Moreover, the coffee-ring effect is used for the separation of two different sized particles [265, 266].

**4.2. Biomedical Application.** The utility of studying patterns of dried biological fluids has been well known in medical diagnosis [138]. The structures observed after drying biological fluids on a horizontal impenetrable substrate attracted the attention of researchers as early as the 1950s [103, 104, 128–132, 134–137]. In the 1980s–1990s, doctors of the former Soviet Union began to use the appearance of structures formed by drying droplets of biological fluids for the diagnosis of various diseases [3, 4, 81, 181, 267]. Unfortunately, very few of these articles were published in English [62, 138, 140, 149, 182, 217].

Many constituents of biological fluids crystallize on drying. The presence of these crystals, their morphology, size, and abundance are of great help in pathological investigations. Denisov describes crystallization patterns observed in saliva of patients with gastrointestinal diseases [268]. He

shows that box-shaped, cross-shaped, and dendritic crystals with multiple-level branching are observed in various samples. The shapes can be classified in a phase diagram with nonoverlapping groups to identify problems such as peptic ulcer, chronic gastritis, and other such diseases in patients.

The potential for diagnosis by using the evaporation patterns of whole blood or blood serum lies in the fact that blood composition may vary due to diseases, which in turn results in changes in the evaporation patterns. Researchers had used dried human serum patterns to diagnose metastatic carcinoma [269] and also found that various interesting patterns could be used to reveal different pathological information [61]. The dried drop patterns of blood serum were also suggested to be useful for disease diagnosis because some featured morphologies of blood serum patterns could be used to acquire information about the health state of human organisms [138]. However, the use of whole blood patterns for medical diagnosis was rarely reported [42, 153], and more systematic experiments are expected.

The coffee-ring effect has been used as low-resource diagnostics for detection of the malarial biomarker *Plasmodium falciparum* [270] and also as a biomarker elsewhere [138, 271–273]. Blood drop patterns are used extensively for diagnostic purposes [20]. Crack patterns in dried drops of biofluids are also used to extract valuable information in medical diagnosis. Dried droplets of blood and blood serum show characteristic crack patterns for patients suffering from anemia, hyperlipidemia, and other disorders [7, 21]. A related field where droplet patterns are of importance is forensics related to crime investigation [7]. More such areas are bio-preservation [216, 274] and high-throughput drug screening, where pattern formation in the drying sample is not desirable [60].

Some other applications have come up too; patterns on dried droplets may be used for quality analysis of food grains [275], as well as alcoholic drinks [276], fast identification of fluid and substrate chemistry based on automatic pattern recognition of stains [183], assessment of quality of products [275], and Raman spectroscopy [180, 277–286].

**4.3. Droplet Levitation.** The idea behind drying a droplet under levitation is to eliminate the effect of gravity during drying and observe desiccation under *no contact* condition. However, the droplet levitation technology is a promising candidate for generating novel applications. For example, the technique of manipulating levitated drops used on liquid marbles [287] may be applied to insert desired components in dried shell structures [66] for drug delivery or other applications.

There is, however, one concern with evaporation under levitation. This is that although one can avoid substrate contact and maintain the evaporating drops in a quasi-spherical shape, the levitation techniques, for instance, acoustic levitation, often lead to an additional boundary layer to the levitated drop, which may influence the evaporation process. In addition, the levitation force could also influence the morphology of dried residues. To investigate the mass transfer and evaporation-driven assembly in a truly undisturbed manner, drop evaporation in a space station is highly

desirable. This will be of great help in understanding the emergence of crust, formation of cavity, buckling of crust, and elucidating the effect of gravity on these processes.

## 5. Conclusion

There obviously remains much more work to be done in this interesting and useful area of research. At this juncture, some tasks can be specially emphasized:

- (i) Obtaining new experimental data critically needed for the design and development of adequate models
- (ii) The development of 3D models describing the redistribution of the components, the movement of the phase front, and the evolution of the profile of the drying colloidal droplets with salt admixtures. In these systems, phase transition from sol to gel is concentration-driven. The thermal phase transition from liquid to vapor also takes place in this system. This phase transition leads to a movement of the liquid-vapor phase boundary (i.e., the droplet volume decreases and droplet profile changes)
- (iii) Considering additional effects that may be crucial to understanding the processes of pattern formation but have not yet been included in the models (e.g., variations of the viscosity of a colloid with time and concentration of salts and changes of the vapor flux above the free surface of the droplets when the phase boundary (sol-gel) is moving). Time-varying interactions between the components of the droplet (e.g., particles and ions) also need to be considered
- (iv) Studying the effect of external fields such as electromagnetic and acoustic fields on the droplet evaporation process
- (v) Analyzing the final pattern through tools such as fractal and multifractal characterization

To conclude, the simple but effective process of drying a fluid drop and observing it under a microscope (preferably with video recording) is rapidly developing into a new and exciting field of research. Several reviews [15–17, 20, 288, 289] and books [5–8] based on pattern formation during desiccation published within the short span of just four years confirm the intensely growing interest in this subject. Exploiting the full potential of this topic in basic science research and applications needs involvement and interaction between scientists and engineers from disciplines of physics, chemistry, biology, medicine, and other related fields.

## Conflicts of Interest

The authors declare that there are no conflicts of interest regarding the publication of this paper.

## Acknowledgments

Yuri Yu. Tarasevich acknowledges the funding from the Ministry of Education and Science of the Russian Federation

(Project no. 3.959.2017/4.6). Duyang Zang acknowledges the National Natural Science Foundation of China (Grant no. U1732129). Moutushi Dutta Choudhury acknowledges SERB, India, for providing financial support through NPDF (PDF/2016/001151/PMS).

## References

- [1] P. G. de Gennes, F. Brochard-Wyart, and D. Quéré, *Capillarity and Wetting Phenomena*, Springer, New York, NY, USA, 2004.
- [2] D. J. Wedlock, *Controlled Particle, Droplet and Bubble Formation*, Butterworth-Heinemann, 1994.
- [3] V. N. Shabalin and S. N. Shatohina, *Morphology of Human Biological Fluids*, Khrizostom, Moscow, Russia, (Russian) 2001.
- [4] E. Rapis, *Protein and Life (Self-Assembling and Symmetry of Protein Nanostructures)*, Philobiblion, Jerusalem, Israel; Miltap-KPGIT, Moscow, Rusiia, (Russian) 2003.
- [5] Z. Lin, Ed., *Evaporative Self-Assembly of Ordered Complex Structures*, World Scientific Publishing Company, 2010.
- [6] P. Innocenzi, L. Malfatti, and P. Falcaro, *Water Droplets to Nanotechnology*, The Royal Society of Chemistry, 2013.
- [7] D. Brutin, Ed., *Droplet Wetting and Evaporation*, Academic Press, Oxford, UK, 2015.
- [8] L. Goehring, A. Nakahara, T. Dutta, S. Kitsunezaki, and S. Tarafdar, *Desiccation Cracks and Their Patterns: Formation and Modelling in Science and Nature, Statistical Physics of Fracture and Breakdown*, Wiley, 2015.
- [9] S. K. Aggarwal and F. Peng, "A review of droplet dynamics and vaporization modeling for engineering calculations," *Journal of Engineering for Gas Turbines and Power*, vol. 117, no. 3, pp. 453–461, 1995.
- [10] Yu. Y. Tarasevich, "Mechanisms and models of the dehydration self-organization in biological fluids," *Physics-Uspekhi*, vol. 47, no. 7, pp. 717–728, 2004.
- [11] T. A. Yakhno, V. G. Yakhno, A. G. Sanin, O. A. Sanina, and A. S. Pelyushenko, "Protein and salt: Spatiotemporal dynamics of events in a drying drop," *Technical Physics*, vol. 49, no. 8, pp. 1055–1063, 2004.
- [12] T. A. Yakhno and V. G. Yakhno, "Structural evolution of drying drops of biological fluids," *Technical Physics*, vol. 54, no. 8, pp. 1219–1227, 2009.
- [13] Y. Choi, J. Han, and C. Kim, "Pattern formation in drying of particle-laden sessile drops of polymer solutions on solid substrates," *Korean Journal of Chemical Engineering*, vol. 28, no. 11, pp. 2130–2136, 2011.
- [14] H. Y. Erbil, "Evaporation of pure liquid sessile and spherical suspended drops: A review," *Advances in Colloid and Interface Science*, vol. 170, no. 1-2, pp. 67–86, 2012.
- [15] K. Sefiane, "Patterns from drying drops," *Advances in Colloid and Interface Science*, vol. 206, pp. 372–381, 2014.
- [16] A. F. Routh, "Drying of thin colloidal films," *Reports on Progress in Physics*, vol. 76, no. 4, Article ID 046603, 2013.
- [17] R. G. Larson, "Transport and deposition patterns in drying sessile droplets," *AIChE Journal*, vol. 60, no. 5, pp. 1538–1571, 2014.
- [18] N. M. Kovalchuk, A. Trybala, and V. M. Starov, "Evaporation of sessile droplets," *Current Opinion in Colloid & Interface Science*, vol. 19, no. 4, pp. 336–342, 2014.
- [19] M. Anyfantakis and D. Baigl, "Manipulating the coffee-ring effect: interactions at work," *ChemPhysChem*, vol. 16, no. 13, pp. 2726–2734, 2015.
- [20] R. Chen, L. Zhang, D. Zang, and W. Shen, "Blood drop patterns: Formation and applications," *Advances in Colloid and Interface Science*, vol. 231, pp. 1–14, 2016.
- [21] D. Brutin and V. Starov, "Recent advances in droplet wetting and evaporation," *Chemical Society Reviews*, vol. 47, no. 2, pp. 558–585, 2018.
- [22] R. D. Deegan, O. Bakajin, T. F. Dupont, G. Huber, S. R. Nagel, and T. A. Witten, "Capillary flow as the cause of ring stains from dried liquid drops," *Nature*, vol. 389, no. 6653, pp. 827–829, 1997.
- [23] R. D. Deegan, O. Bakajin, T. F. Dupont, G. Huber, S. R. Nagel, and T. A. Witten, "Contact line deposits in an evaporating drop," *Physical Review E: Statistical, Nonlinear, and Soft Matter Physics*, vol. 62, no. 1, pp. 756–765, 2000.
- [24] M. Dutta Choudhury, T. Dutta, and S. Tarafdar, "Pattern formation in droplets of starch gels containing NaCl dried on different surfaces," *Colloids and Surfaces A: Physicochemical and Engineering Aspects*, vol. 432, pp. 110–118, 2013.
- [25] T. Dutta, A. Giri, M. D. Choudhury, and S. Tarafdar, "Experiment and simulation of multifractal growth of crystalline NaCl aggregates in aqueous gelatin medium," *Colloids and Surfaces A: Physicochemical and Engineering Aspects*, vol. 432, pp. 127–131, 2013.
- [26] A. Giri, M. Dutta Choudhury, T. Dutta, and S. Tarafdar, "Multifractal growth of crystalline NaCl aggregates in a gelatin medium," *Crystal Growth and Design*, vol. 13, no. 1, pp. 341–345, 2013.
- [27] B. Roy, S. Karmakar, and S. Tarafdar, "Self assembled transparent conducting network of multi-walled carbon nanotubes formed by evaporation," *Materials Letters*, vol. 207, pp. 86–88, 2017.
- [28] L. Pauchard, F. Parisse, and C. Allain, "Influence of salt content on crack patterns formed through colloidal suspension desiccation," *Physical Review E: Statistical Physics, Plasmas, Fluids, and Related Interdisciplinary Topics*, vol. 59, no. 3, pp. 3737–3740, 1999.
- [29] C. C. Annarelli, J. Fornazero, J. Bert, and J. Colombani, "Crack patterns in drying protein solution drops," *European Physical Journal E*, vol. 5, no. 5, pp. 599–603, 2001.
- [30] K.-T. Leung, L. Józsa, M. Ravasz, and Z. Néda, "Pattern formation: spiral cracks without twisting," *Nature*, vol. 410, no. 6825, p. 166, 2001.
- [31] Z. Néda, K.-T. Leung, L. Józsa, and M. Ravasz, "Spiral cracks in drying precipitates," *Physical Review Letters*, vol. 88, no. 9, Article ID 095502, 2002.
- [32] B. D. Caddock and D. Hull, "Influence of humidity on the cracking patterns formed during the drying of sol-gel drops," *Journal of Materials Science*, vol. 37, no. 4, pp. 825–834, 2002.
- [33] E. Golbraikh, E. G. Rapis, and S. S. Moiseev, "On the crack pattern formation in a freely drying protein film," *Technical Physics*, vol. 48, no. 10, pp. 1333–1337, 2003.
- [34] G. Jing and J. Ma, "Formation of circular crack pattern in deposition self-assembled by drying nanoparticle suspension," *The Journal of Physical Chemistry B*, vol. 116, no. 21, pp. 6225–6231, 2012.
- [35] T. Khatun, T. Dutta, and S. Tarafdar, "Crack formation under an electric field in droplets of laponite gel: Memory effect and scaling relations," *Langmuir*, vol. 29, no. 50, pp. 15535–15542, 2013.
- [36] W. Bou Zeid, J. Vicente, and D. Brutin, "Influence of evaporation rate on cracks' formation of a drying drop of whole blood," *Colloids and Surfaces A: Physicochemical and Engineering Aspects*, vol. 432, pp. 139–146, 2013.

- [37] Y. Zhang, Z. Liu, D. Zang, Y. Qian, and K.-J. Lin, "Pattern transition and sluggish cracking of colloidal droplet deposition with polymer additives," *Science China Physics, Mechanics & Astronomy*, vol. 56, no. 9, pp. 1712–1718, 2013.
- [38] B. Sobac and D. Brutin, "Desiccation of a sessile drop of blood: Cracks, folds formation and delamination," *Colloids and Surfaces A: Physicochemical and Engineering Aspects*, vol. 448, no. 1, pp. 34–44, 2014.
- [39] F. Giorgiutti-Dauphiné and L. Pauchard, "Striped patterns induced by delamination of drying colloidal films," *Soft Matter*, vol. 11, no. 7, pp. 1397–1402, 2015.
- [40] U. U. Ghosh, M. Chakraborty, A. B. Bhandari, S. Chakraborty, and S. DasGupta, "Effect of surface wettability on crack dynamics and morphology of colloidal films," *Langmuir*, vol. 31, no. 22, pp. 6001–6010, 2015.
- [41] J. Y. Kim, K. Cho, S.-A. Ryu, S. Y. Kim, and B. M. Weon, "Crack formation and prevention in colloidal drops," *Scientific Reports*, vol. 5, Article ID 13166, 2015.
- [42] R. Chen, L. Zhang, D. Zang, and W. Shen, "Understanding desiccation patterns of blood sessile drops," *Journal of Materials Chemistry B*, vol. 5, no. 45, pp. 8991–8998, 2017.
- [43] H. Lama, M. G. Basavaraj, and D. K. Satapathy, "Tailoring crack morphology in coffee-ring deposits via substrate heating," *Soft Matter*, vol. 13, no. 32, pp. 5445–5452, 2017.
- [44] Y. Men, W. Wang, P. Xiao et al., "Controlled evaporative self-assembly of  $\text{Fe}_3\text{O}_4$  nanoparticles assisted by an external magnetic field," *RSC Advances*, vol. 5, pp. 31519–31524, 2015.
- [45] Y. Li, Q. Yang, M. Li, and Y. Song, "Rate-dependent interface capture beyond the coffee-ring effect," *Scientific Reports*, vol. 6, Article ID 24628, 2016.
- [46] L. Pauchard and C. Allain, "Buckling instability induced by polymer solution drying," *EPL (Europhysics Letters)*, vol. 62, no. 6, pp. 897–903, 2003.
- [47] L. Pauchard and C. Allain, "Stable and unstable surface evolution during the drying of a polymer solution drop," *Physical Review E: Statistical, Nonlinear, and Soft Matter Physics*, vol. 68, no. 5, Article ID 052801, 2003.
- [48] L. Pauchard and C. Allain, "Mechanical instability induced by complex liquid desiccation," *Comptes Rendus Physique*, vol. 4, no. 2, pp. 231–239, 2003.
- [49] Y. Gorand, L. Pauchard, G. Calligari, J. P. Hulin, and C. Allain, "Mechanical instability induced by the desiccation of sessile drops," *Langmuir*, vol. 20, no. 12, pp. 5138–5140, 2004.
- [50] T. A. Yakhno, V. V. Kazakov, O. A. Sanina, A. G. Sanin, and V. G. Yakhno, "Drops of biological fluids drying on a hard substrate: Variation of the morphology, weight, temperature, and mechanical properties," *Technical Physics*, vol. 55, no. 7, pp. 929–935, 2010.
- [51] F. Girard, M. Antoni, and K. Sefiane, "Infrared thermography investigation of an evaporating sessile water droplet on heated substrates," *Langmuir*, vol. 26, no. 7, pp. 4576–4580, 2010.
- [52] T. A. Yakhno, O. A. Sanina, M. G. Volovik, A. G. Sanin, and V. G. Yakhno, "Thermographic investigation of the temperature field dynamics at the liquid-air interface in drops of water solutions drying on a glass substrate," *Technical Physics*, vol. 57, no. 7, pp. 915–922, 2012.
- [53] Y. Tsoumpas, S. Dehaeck, A. Rednikov, and P. Colinet, "Effect of Marangoni flows on the shape of thin sessile droplets evaporating into air," *Langmuir*, vol. 31, no. 49, pp. 13334–13340, 2015.
- [54] H. Hu and R. G. Larson, "Analysis of the effects of Marangoni stresses on the microflow in an evaporating sessile droplet," *Langmuir*, vol. 21, no. 9, pp. 3972–3980, 2005.
- [55] D. J. Harris and J. A. Lewis, "Marangoni effects on evaporative lithographic patterning of colloidal films," *Langmuir*, vol. 24, no. 8, pp. 3681–3685, 2008.
- [56] H. Bodiguel and J. Leng, "Imaging the drying of a colloidal suspension," *Soft Matter*, vol. 6, no. 21, pp. 5451–5460, 2010.
- [57] X. Xu, J. Luo, and D. Guo, "Radial-velocity profile along the surface of evaporating liquid droplets," *Soft Matter*, vol. 8, no. 21, pp. 5797–5803, 2012.
- [58] Y.-C. Hu, Q. Zhou, H.-M. Ye, Y.-F. Wang, and L.-S. Cui, "Peculiar surface profile of poly(ethylene oxide) film with ring-like nucleation distribution induced by Marangoni flow effect," *Colloids and Surfaces A: Physicochemical and Engineering Aspects*, vol. 428, pp. 39–46, 2013.
- [59] G. Son, "Numerical simulation of particle-laden droplet evaporation with the Marangoni effect," *The European Physical Journal Special Topics*, vol. 224, no. 2, pp. 401–413, 2015.
- [60] P. Takhistov and H.-C. Chang, "Complex stain morphologies," *Industrial & Engineering Chemistry Research*, vol. 41, no. 25, pp. 6256–6269, 2002.
- [61] M. E. Buzovsky, Yu. P. Shcherbak, and I. V. Shishpor, "Quantitative estimation of the microstructural inhomogeneity of biological fluid facies," *Technical Physics*, vol. 59, no. 10, pp. 1550–1555, 2014.
- [62] S. N. Shatokhina, V. N. Shabalin, M. E. Buzovsky, and V. T. Punin, "Bio-liquid morphological analysis," *The Scientific World-JOURNAL*, vol. 4, pp. 657–661, 2004.
- [63] T. Yakhno, "Salt-induced protein phase transitions in drying drops," *Journal of Colloid and Interface Science*, vol. 318, no. 2, pp. 225–230, 2008.
- [64] D. Brutin, B. Sobac, B. Loquet, and J. Sampol, "Pattern formation in drying drops of blood," *Journal of Fluid Mechanics*, vol. 667, pp. 85–95, 2011.
- [65] R. Chen, L. Zhang, D. Zang, and W. Shen, "Wetting and drying of colloidal droplets: physics and pattern formation," in *Advances in Colloid Science*, InTech, 2016.
- [66] E. Tijerino, S. Basu, and R. Kumar, "Nanoparticle agglomeration in an evaporating levitated droplet for different acoustic amplitudes," *Journal of Applied Physics*, vol. 113, no. 3, Article ID 034307, 2013.
- [67] L. Chen and J. R. G. Evans, "Drying of colloidal droplets on superhydrophobic surfaces," *Journal of Colloid and Interface Science*, vol. 351, no. 1, pp. 283–287, 2010.
- [68] S. Basu, E. Tijerino, and R. Kumar, "Insight into morphology changes of nanoparticle laden droplets in acoustic field," *Applied Physics Letters*, vol. 102, no. 14, Article ID 141602, 2013.
- [69] R. G. Picknett and R. Bexon, "The evaporation of sessile or pendant drops in still air," *Journal of Colloid and Interface Science*, vol. 61, no. 2, pp. 336–350, 1977.
- [70] E. Wulsten, F. Kiekens, F. van Dycke, J. Voorspoels, and G. Lee, "Levitated single-droplet drying: Case study with itraconazole dried in binary organic solvent mixtures," *International Journal of Pharmaceutics*, vol. 378, no. 1-2, pp. 116–121, 2009.
- [71] R. Mukherjee, R. Pangule, A. Sharma, and G. Tomar, "Contact instability of elastic bilayers: Miniaturization of instability patterns," *Advanced Functional Materials*, vol. 17, no. 14, pp. 2356–2364, 2007.
- [72] U. Thiele and E. Knobloch, "Thin liquid films on a slightly inclined heated plate," *Physica D: Nonlinear Phenomena*, vol. 190, no. 3-4, pp. 213–248, 2004.

- [73] D. I. Yu, H. J. Kwak, S. W. Doh et al., "Wetting and evaporation phenomena of water droplets on textured surfaces," *International Journal of Heat and Mass Transfer*, vol. 90, pp. 191–200, 2015.
- [74] N. Anantharaju, M. Panchagnula, and S. Neti, "Evaporating drops on patterned surfaces: Transition from pinned to moving triple line," *Journal of Colloid and Interface Science*, vol. 337, no. 1, pp. 176–182, 2009.
- [75] S. K. Singh, S. Khandekar, D. Pratap, and S. A. Ramakrishna, "Wetting dynamics and evaporation of sessile droplets on nanoporous alumina surfaces," *Colloids and Surfaces A: Physicochemical and Engineering Aspects*, vol. 432, pp. 71–81, 2013.
- [76] M. Gonuguntla and A. Sharma, "Polymer patterns in evaporating droplets on dissolving substrates," *Langmuir*, vol. 20, no. 8, pp. 3456–3463, 2004.
- [77] C. Parneix, P. Vandoolaeghe, V. S. Nikolayev, D. Quéré, J. Li, and B. Cabane, "Dips and rims in dried colloidal films," *Physical Review Letters*, vol. 105, no. 26, Article ID 266103, 2010.
- [78] D. J. Harris, H. Hu, J. C. Conrad, and J. A. Lewis, "Patterning colloidal films via evaporative lithography," *Physical Review Letters*, vol. 98, no. 14, Article ID 148301, 2007.
- [79] H. M. J. M. Wedershoven, K. R. M. Deuss, C. Fantin, J. C. H. Zeegers, and A. A. Darhuber, "Active control of evaporative solution deposition by means of modulated gas phase convection," *International Journal of Heat and Mass Transfer*, vol. 117, pp. 303–312, 2018.
- [80] A. Georgiadis, F. N. Muhamad, A. Utgenannt, and J. L. Keddie, "Aesthetically textured, hard latex coatings by fast IR-assisted evaporative lithography," *Progress in Organic Coatings*, vol. 76, no. 12, pp. 1786–1791, 2013.
- [81] L. V. Savina, *Crystalloscopic Structures of Blood Serum of Healthy People and Patients*, Sov. Kuban, Krasnodar, Russia, 1999 (Russian).
- [82] J. Gao, K. Kempa, M. Giersig, E. M. Akinoglu, B. Han, and R. Li, "Physics of transparent conductors," *Advances in Physics*, vol. 65, no. 6, pp. 553–617, 2016.
- [83] A. Kumar and G. U. Kulkarni, "Evaluating conducting network based transparent electrodes from geometrical considerations," *Journal of Applied Physics*, vol. 119, no. 1, Article ID 015102, 2016.
- [84] Z. Zhan, J. An, Y. Wei, V. T. Tran, and H. Du, "Inkjet-printed optoelectronics," *Nanoscale*, vol. 9, no. 3, pp. 965–993, 2017.
- [85] W. D. Ristenpart, P. G. Kim, C. Domingues, J. Wan, and H. A. Stone, "Influence of substrate conductivity on circulation reversal in evaporating drops," *Physical Review Letters*, vol. 99, no. 23, Article ID 234502, 2007.
- [86] L. D. Landau and E. M. Lifshitz, "Surface phenomena," in *Fluid Mechanics*, chapter 7, pp. 230–244, Pergamon Press, 1st edition, 1959.
- [87] W. A. Sirignano, "Introduction," in *Fluid Dynamics and Transport of Droplets and Sprays*, pp. 1–6, Cambridge University Press, Cambridge, UK, 1999.
- [88] R. Mukherjee, D. Bandyopadhyay, and A. Sharma, "Control of morphology in pattern directed dewetting of thin polymer films," *Soft Matter*, vol. 4, no. 10, pp. 2086–2097, 2008.
- [89] R. Mukherjee, M. Gonuguntla, and A. Sharma, "Meso-patterning of thin polymer films by controlled dewetting: From nano-droplet arrays to membranes," *Journal of Nanoscience and Nanotechnology*, vol. 7, no. 6, pp. 2069–2075, 2007.
- [90] F. Parisse and C. Allain, "Shape changes of colloidal suspension droplets during drying," *Journal de Physique II*, vol. 6, no. 7, pp. 1111–1119, 1996.
- [91] R. D. Deegan, "Pattern formation in drying drops," *Physical Review E: Statistical Physics, Plasmas, Fluids, and Related Interdisciplinary Topics*, vol. 61, no. 1, pp. 475–485, 2000.
- [92] A. Lazauskas and V. Grigaliūnas, "Float glass surface preparation methods for improved chromium film adhesive bonding," *Medziagotyra*, vol. 18, no. 2, pp. 181–186, 2012.
- [93] J. Canning, I. Petermann, and K. Cook, "Surface treatment of silicate based glass: base Piranha treatment versus 193 nm laser processing," in *3rd Asia Pacific Optical Sensors Conference*, J. Canning and G. Peng, Eds., vol. 8351 of *Proceedings of SPIE*, Sydney, Australia, February 2012.
- [94] Y. Ma, X. Cao, X. Feng, and H. Zou, "Fabrication of superhydrophobic film from PMMA with intrinsic water contact angle below 90°," *Polymer Journal*, vol. 48, no. 26, pp. 7455–7460, 2007.
- [95] D. I. Yu, H. J. Kwak, S. W. Doh et al., "Dynamics of contact line depinning during droplet evaporation based on thermodynamics," *Langmuir*, vol. 31, no. 6, pp. 1950–1957, 2015.
- [96] H. B. Eral, D. Mampallil Augustine, M. H. G. Duits, and F. Mugele, "Suppressing the coffee stain effect: How to control colloidal self-assembly in evaporating drops using electrowetting," *Soft Matter*, vol. 7, no. 10, pp. 4954–4958, 2011.
- [97] H. B. Eral, D. van den Ende, and F. Mugele, "Say goodbye to coffee stains," *Physics World*, vol. 25, no. 4, pp. 33–37, 2012.
- [98] D. Mampallil, H. B. Eral, D. van den Ende, and F. Mugele, "Control of evaporating complex fluids through electrowetting," *Soft Matter*, vol. 8, no. 41, pp. 10614–10617, 2012.
- [99] F.-C. Wang and H.-A. Wu, "Pinning and depinning mechanism of the contact line during evaporation of nano-droplets sessile on textured surfaces," *Soft Matter*, vol. 9, no. 24, pp. 5703–5709, 2013.
- [100] A. Zigelman and O. Manor, "A model for pattern deposition from an evaporating solution subject to contact angle hysteresis and finite solubility," *Soft Matter*, vol. 12, no. 26, pp. 5693–5707, 2016.
- [101] C. W. Extrand and Y. Kumagai, "Contact angles and hysteresis on soft surfaces," *Journal of Colloid and Interface Science*, vol. 184, no. 1, pp. 191–200, 1996.
- [102] F. Parisse and C. Allain, "Drying of colloidal suspension droplets: Experimental study and profile renormalization," *Langmuir*, vol. 13, no. 14, pp. 3598–3602, 1997.
- [103] C. Koch, "Feinbau und Entstehungsweise von Kristallstrukturen in getrockneten Tropfen hochmolekulär salzhaltiger Flüssigkeiten," *Kolloid-Zeitschrift*, vol. 138, no. 2, pp. 81–86, 1954.
- [104] A. Solé, "Die rhythmischen Kristallisierungen im Influenzstrogramm," *Kolloid-Zeitschrift*, vol. 137, no. 1, pp. 15–19, 1954.
- [105] A. V. Kistovich, Yu. D. Chashechkin, and V. V. Shabalin, "Formation mechanism of a circumferential roller in a drying biofluid drop," *Technical Physics*, vol. 55, no. 4, pp. 473–478, 2010.
- [106] S. Jafari Kang, V. Vandadi, J. D. Felske, and H. Masoud, "Alternative mechanism for coffee-ring deposition based on active role of free surface," *Physical Review E: Statistical, Nonlinear, and Soft Matter Physics*, vol. 94, no. 6, Article ID 063104, 2016.
- [107] M. Anyfantakis, Z. Geng, M. Morel, S. Rudiuk, and D. Baigl, "Modulation of the coffee-ring effect in particle/surfactant mixtures: The importance of particle-interface interactions," *Langmuir*, vol. 31, no. 14, pp. 4113–4120, 2015.
- [108] W. Zhang, T. Yu, L. Liao, and Z. Cao, "Ring formation from a drying sessile colloidal droplet," *AIP Advances*, vol. 3, no. 10, Article ID 102109, 2013.

- [109] P. J. Yunker, T. Still, M. A. Lohr, and A. G. Yodh, "Suppression of the coffee-ring effect by shape-dependent capillary interactions," *Nature*, vol. 476, no. 7360, pp. 308–311, 2011.
- [110] H. Hu and R. G. Larson, "Analysis of the microfluid flow in an evaporating sessile droplet," *Langmuir*, vol. 21, no. 9, pp. 3963–3971, 2005.
- [111] H. Hu and R. G. Larson, "Marangoni effect reverses coffee-ring depositions," *The Journal of Physical Chemistry B*, vol. 110, no. 14, pp. 7090–7094, 2006.
- [112] H. Kim, F. Boulogne, E. Um, I. Jacobi, E. Button, and H. A. Stone, "Controlled uniform coating from the interplay of Marangoni flows and surface-adsorbed macromolecules," *Physical Review Letters*, vol. 116, no. 12, Article ID 124501, 2016.
- [113] L. Yu. Barash, "Marangoni convection in an evaporating droplet: analytical and numerical descriptions," *International Journal of Heat and Mass Transfer*, vol. 102, pp. 445–454, 2016.
- [114] L. Yu. Barash, T. P. Bigioni, V. M. Vinokur, and L. N. Shchur, "Evaporation and fluid dynamics of a sessile drop of capillary size," *Physical Review E: Statistical, Nonlinear, and Soft Matter Physics*, vol. 79, no. 4, Article ID 046301, 2009.
- [115] L. Yu. Barash, "Dependence of fluid flows in an evaporating sessile droplet on the characteristics of the substrate," *International Journal of Heat and Mass Transfer*, vol. 84, pp. 419–426, 2015.
- [116] Y. H. Chen, W. N. Hu, J. Wang, F. J. Hong, and P. Cheng, "Transient effects and mass convection in sessile droplet evaporation: The role of liquid and substrate thermophysical properties," *International Journal of Heat and Mass Transfer*, vol. 108, pp. 2072–2087, 2017.
- [117] A. D. Eales, A. F. Routh, N. Dartnell, and G. Simon, "Evaporation of pinned droplets containing polymer—an examination of the important groups controlling final shape," *AICHE Journal*, vol. 61, no. 5, pp. 1759–1767, 2015.
- [118] D. Schwabe and A. Scharmann, "Some evidence for the existence and magnitude of a critical marangoni number for the onset of oscillatory flow in crystal growth melts," *Journal of Crystal Growth*, vol. 46, no. 1, pp. 125–131, 1979.
- [119] S. Chavan, H. Cha, D. Orejon et al., "Heat transfer through a condensate droplet on hydrophobic and nanostructured superhydrophobic surfaces," *Langmuir*, vol. 32, no. 31, pp. 7774–7787, 2016.
- [120] X. Zhong and F. Duan, "Disk to dual ring deposition transformation in evaporating nanofluid droplets from substrate cooling to heating," *Physical Chemistry Chemical Physics*, vol. 18, no. 30, pp. 20664–20671, 2016.
- [121] N. D. Patil, P. G. Bange, R. Bhardwaj, and A. Sharma, "Effects of substrate heating and wettability on evaporation dynamics and deposition patterns for a sessile water droplet containing colloidal particles," *Langmuir*, vol. 32, no. 45, pp. 11958–11972, 2016.
- [122] J.-N. Tisserant, G. Wicht, O. F. Göbel et al., "Growth and alignment of thin film organic single crystals from dewetting patterns," *ACS Nano*, vol. 7, no. 6, pp. 5506–5513, 2013.
- [123] S. Wolfram, *A New Kind of Science*, Wolfram Media, Champaign, Ill, USA, 2002.
- [124] N. Shahidzadeh, M. F. L. Schut, J. Desarnaud, M. Prat, and D. Bonn, "Salt stains from evaporating droplets," *Scientific Reports*, vol. 5, Article ID 10335, 2015.
- [125] N. Shahidzadeh-Bonn, S. Rafai, D. Bonn, and G. Wegdam, "Salt crystallization during evaporation: Impact of interfacial properties," *Langmuir*, vol. 24, no. 16, pp. 8599–8605, 2008.
- [126] S. Bhattacharyya, B. Roy, and M. Dutta Choudhury, "Pattern formation in drying drops of colloidal copper sulphate solution on glass surface," *Journal of Surface Science and Technology*, vol. 32, pp. 79–84, 2017.
- [127] C. Rodriguez-Navarro and E. Doehe, "Salt weathering: influence of evaporation rate, supersaturation and crystallization pattern," *Earth Surface Processes and Landforms*, vol. 24, no. 2-3, pp. 191–209, 1999.
- [128] C. Koch, "Über Austrocknungssprünge," *Colloid and Polymer Science*, vol. 145, no. 1, pp. 7–14, 1956.
- [129] C. Koch, "Periodische Erscheinungen an trocknenden Tropfen hochmolekularer Flüssigkeiten," *Kolloid-Zeitschrift*, vol. 150, no. 1, pp. 80–83, 1957.
- [130] C. Koch, "Über Doppelbildungen (Dubletten) und gleichartige Erscheinungen in trockenen Tropfen hochmolekularer Flüssigkeiten (Dextran, Polyvinylpyrrolidon)," *Kolloid-Zeitschrift*, vol. 151, no. 1, pp. 62–66, 1957.
- [131] C. Koch, "Über Polyvinylpyrrolidonkristallverbände," *Kolloid-Zeitschrift*, vol. 151, no. 2, pp. 122–126, 1957.
- [132] C. Koch, "Kristallstrukturen und verwandte erscheinungen in getrockneten tropfen hochmolekular-salzhaltiger Flüssigkeiten (Kammerwasser)," *Documenta Ophthalmologica*, vol. 11, no. 1, pp. 182–189, 1957.
- [133] A. Solé, "Vergleichende Stagoskopie des Blutserums," *Österreichische Zoologische Zeitschrift*, vol. 5, pp. 366–376, 1954.
- [134] A. Solé, "Die Rhythmisierung im Influenzstagogramm," *Kolloid-Zeitschrift*, vol. 143, no. 2, pp. 73–83, 1955.
- [135] A. Solé, "Untersuchung über die Bewegung der Teilchen im Stagogramm und Influenzstagogramm," *Kolloid-Zeitschrift*, vol. 151, no. 1, pp. 55–62, 1957.
- [136] A. Solé, "Stagoskopische Untersuchungen über die Rhythmisierung einiger Aminosäuren sowie anderer organischer Verbindungen," *Kolloid-Zeitschrift*, vol. 151, no. 2, pp. 126–136, 1957.
- [137] A. Solé, *Stagoskopie: Einführung in Methodik, Theorie und Praxis für Ärzte und Naturforscher*, Franz Deuticke, Wien, Austria, 1960.
- [138] V. N. Shabalina and S. N. Shatokhina, "Diagnostic markers in the structures of human biological liquids," *Singapore Medical Journal*, vol. 48, no. 5, pp. 440–446, 2007.
- [139] A. K. Martusevich, Y. Zimin, and A. Bochkareva, "Morphology of dried blood serum specimens of viral hepatitis," *Hepatitis Monthly*, vol. 7, no. 4, pp. 207–210, 2007.
- [140] T. A. Yakhno, A. A. Sanin, R. G. Ilyazov et al., "Drying drop technology as a possible tool for detection leukemia and tuberculosis in cattle," *Journal of Biomedical Science and Engineering*, vol. 8, no. 1, pp. 1–23, 2015.
- [141] M. T. A. Rajabi and M. Sharifzadeh, "'Coffee ring effect' in ophthalmology: 'anionic dye deposition' hypothesis explaining normal lid margin staining," *Medicine*, vol. 95, no. 14, p. e3137, 2016.
- [142] M. Dutta Choudhury, T. Dutta, and S. Tarafdar, "Growth kinetics of NaCl crystals in a drying drop of gelatin: Transition from faceted to dendritic growth," *Soft Matter*, vol. 11, no. 35, pp. 6938–6947, 2015.
- [143] M. Goto, Y. Oaki, and H. Imai, "Dendritic growth of NaCl crystals in a gel matrix: Variation of branching and control of bending," *Crystal Growth and Design*, vol. 16, no. 8, pp. 4278–4284, 2016.
- [144] C. C. Annarelli, L. Reyes, J. Fornazero, J. Bert, R. Cohen, and A. W. Coleman, "Ion and molecular recognition effects on the crystallization of bovine serum albumin-salt mixtures," *Crystal Engineering*, vol. 3, no. 3, pp. 173–194, 2000.

- [145] T. Basu, M. M. Goswami, T. R. Middya, and S. Tarafdar, "Morphology and ion-conductivity of gelatin-LiClO<sub>4</sub> films: fractional diffusion analysis," *The Journal of Physical Chemistry B*, vol. 116, no. 36, pp. 11362–11369, 2012.
- [146] B. Roy, M. D. Choudhuri, T. Dutta, and S. Tarafdar, "Multi-scale patterns formed by sodium sulphate in a drying droplet of gelatin," *Applied Surface Science*, vol. 357, pp. 1000–1006, 2015.
- [147] T. A. Yakhno, "Sodium chloride crystallization from drying drops of albumin–salt solutions with different albumin concentrations," *Technical Physics*, vol. 60, no. 11, pp. 1601–1608, 2015.
- [148] G. Glibitskiy, D. Glibitskiy, O. Gorobchenko et al., "Textures on the surface of BSA films with different concentrations of sodium halides and water state in solution," *Nanoscale Research Letters*, vol. 10, no. 1, p. 155, 2015.
- [149] A. K. Martusevich and N. F. Kamakin, "Crystallography of biological fluid as a method for evaluating its physicochemical characteristics," *Bulletin of Experimental Biology and Medicine*, vol. 143, no. 3, pp. 385–388, 2007.
- [150] S. Bhattacharyya, B. Roy, and S. Tarafdar, "Aggregation of crystalline copper sulphate salt in a gelatin medium," *Fractals*, vol. 25, no. 5, Article ID 1750038, 2017.
- [151] T. A. Yahno, V. G. Yahno, A. G. Sanin, A. S. Pelyushenko, O. B. Shaposhnikova, and A. S. Chernov, "The phenomenon of drying drops and the possibility of its practical use," *Nonlinear World*, vol. 5, pp. 54–65, 2007 (Russian).
- [152] T. Still, P. J. Yunker, and A. G. Yodh, "Surfactant-induced Marangoni eddies alter the coffee-rings of evaporating colloidal drops," *Langmuir*, vol. 28, no. 11, pp. 4984–4988, 2012.
- [153] D. Brutin, B. Sobac, and C. Nicloux, "Influence of substrate nature on the evaporation of a sessile drop of blood," *Journal of Heat Transfer*, vol. 134, no. 6, Article ID 061101, 2012.
- [154] F. Carle and D. Brutin, "How surface functional groups influence fracturation in nanofluid droplet dry-outs," *Langmuir*, vol. 29, no. 32, pp. 9962–9966, 2013.
- [155] V. H. Chhasatia, A. S. Joshi, and Y. Sun, "Effect of relative humidity on contact angle and particle deposition morphology of an evaporating colloidal drop," *Applied Physics Letters*, vol. 97, no. 23, Article ID 231909, 2010.
- [156] W. Bou-Zeid and D. Brutin, "Effect of relative humidity on the spreading dynamics of sessile drops of blood," *Colloids and Surfaces A: Physicochemical and Engineering Aspects*, vol. 456, no. 1, pp. 273–285, 2014.
- [157] W. Bou Zeid and D. Brutin, "Influence of relative humidity on spreading, pattern formation and adhesion of a drying drop of whole blood," *Colloids and Surfaces A: Physicochemical and Engineering Aspects*, vol. 430, pp. 1–7, 2013.
- [158] S. Paria, R. Ghosh Chaudhuri, and N. N. Jason, "Self-assembly of colloidal sulfur particles on a glass surface from evaporating sessile drops: Influence of different salts," *New Journal of Chemistry*, vol. 38, no. 12, pp. 5943–5951, 2014.
- [159] T. Okuzono, M. Kobayashi, and M. Doi, "Final shape of a drying thin film," *Physical Review E: Statistical, Nonlinear, and Soft Matter Physics*, vol. 80, no. 2, Article ID 021603, 2009.
- [160] Y. Jung, T. Kajiya, T. Yamaue, and M. Doi, "Film formation kinetics in the drying process of polymer solution enclosed by bank," *Japanese Journal of Applied Physics*, vol. 48, no. 3, p. 031502, 2009.
- [161] Yu. Yu. Tarasevich and D. M. Pravoslavnova, "Drying of a multi-component solution drop on a solid substrate: qualitative analysis," *Technical Physics*, vol. 52, no. 2, pp. 159–163, 2007.
- [162] Yu. Yu. Tarasevich and D. M. Pravoslavnova, "Segregation in desiccated sessile drops of biological fluids," *The European Physical Journal E*, vol. 22, no. 4, pp. 311–314, 2007.
- [163] Yu. Yu. Tarasevich, O. P. Isakova, V. V. Kondukhov, and A. V. Savitskaya, "Effect of evaporation conditions on the spatial redistribution of components in an evaporating liquid drop on a horizontal solid substrate," *Technical Physics*, vol. 55, no. 5, pp. 636–644, 2010.
- [164] I. V. Vodolazskaya, Yu. Yu. Tarasevich, and O. P. Isakova, "The model of phase boundary motion in drying sessile drop of colloidal solution," *Nonlinear World*, vol. 8, pp. 142–150, 2010 (Russian).
- [165] Yu. Yu. Tarasevich, I. V. Vodolazskaya, and O. P. Isakova, "Desiccating colloidal sessile drop: dynamics of shape and concentration," *Colloid & Polymer Science*, vol. 289, no. 9, pp. 1015–1023, 2011.
- [166] I. V. Vodolazskaya and Yu. Yu. Tarasevich, "The model of drying sessile drop of colloidal solution," *Modern Physics Letters B*, vol. 25, no. 15, pp. 1303–1310, 2011.
- [167] K. Ozawa, E. Nishitani, and M. Doi, "Modeling of the drying process of liquid droplet to form thin film," *Japanese Journal of Applied Physics*, vol. 44, no. 6, pp. 4229–4234, 2005.
- [168] B. Sobac and D. Brutin, "Structural and evaporative evolutions in desiccating sessile drops of blood," *Physical Review E: Statistical, Nonlinear, and Soft Matter Physics*, vol. 84, no. 1, Article ID 011603, 2011.
- [169] K. Sefiane, "On the formation of regular patterns from drying droplets and their potential use for bio-medical applications," *Journal of Bionic Engineering*, vol. 7, supplement 1, pp. S82–S93, 2010.
- [170] T. A. Yakhno, A. G. Sanin, O. A. Sanina, and V. G. Yakhno, "Dynamics of mechanical properties of drying drops of biological liquids as a reflection of the features of self-organization of their components from nano- to microlevel," *Biophysics*, vol. 56, no. 6, pp. 1005–1010, 2011.
- [171] V. E. Prokhorov, "Some features of the biological liquid droplet revealed from its dehydrated phase structure analysis," in *Proceedings of the 15th International Conference "Fluxes and Structures in Fluids: Physics of Geospheres"*, abstracts 2, p. 187, 2009.
- [172] Y. J. P. Carreón, J. González-Gutiérrez, M. I. Pérez-Camacho, and H. Mercado-Uribe, "Patterns produced by dried droplets of protein binary mixtures suspended in water," *Colloids and Surfaces B: Biointerfaces*, vol. 161, pp. 103–110, 2018.
- [173] Yu. Yu. Tarasevich and A. K. Ayupova, "Effect of diffusion on the separation of components in a biological fluid upon wedge-shaped dehydration," *Technical Physics*, vol. 48, no. 5, pp. 535–540, 2003.
- [174] H. M. Gorr, J. M. Zueger, D. R. McAdams, and J. A. Barnard, "Salt-induced pattern formation in evaporating droplets of lysozyme solutions," *Colloids and Surfaces B: Biointerfaces*, vol. 103, pp. 59–66, 2013.
- [175] T. A. Yakhno, V. G. Yakhno, and A. V. Sokolov, "Shaping processes in drying drops of serum in norm and pathology," *Biophysics*, vol. 50, no. 4, pp. 638–645, 2005.
- [176] G. Chen and G. J. Mohamed, "Complex protein patterns formation via salt-induced self-assembly and droplet evaporation," *European Physical Journal E*, vol. 33, no. 1, pp. 19–26, 2010.
- [177] K. A. Esmonde-White, F. W. L. Esmonde-White, M. D. Morris, and B. J. Roessler, "Characterization of biofluids prepared by sessile drop formation," *The Analyst*, vol. 139, no. 11, pp. 2734–2741, 2014.

- [178] R. López Solís, L. T. Castro, D. S. Toro, M. Srur, and H. T. Araya, “Microdesiccates produced from normal human tears display four distinctive morphological components,” *Biological Research*, vol. 46, no. 3, pp. 299–305, 2013.
- [179] L. Traipe-Castro, D. Salinas-Toro, D. López et al., “Dynamics of tear fluid desiccation on a glass surface: a contribution to tear quality assessment,” *Biological Research*, vol. 47, no. 1, article 25, 2014.
- [180] E. I. Pearce and A. Tomlinson, “Spatial location studies on the chemical composition of human tear ferns,” *Ophthalmic and Physiological Optics*, vol. 20, no. 4, pp. 306–313, 2000.
- [181] E. G. Rapis, “Formation of an ordered structure upon drying of the protein film,” *Soviet Technical Physics Letters*, vol. 14, p. 679, 1988.
- [182] T. A. Yakhno, O. A. Sedova, A. G. Sanin, and A. S. Pelyushenko, “On the existence of regular structures in liquid human blood serum (plasma) and phase transitions in the course of its drying,” *Technical Physics*, vol. 48, no. 4, pp. 399–403, 2003.
- [183] N. Kim, Z. Li, C. Hurth, F. Zenhausern, S.-F. Chang, and D. Attinger, “Identification of fluid and substrate chemistry based on automatic pattern recognition of stains,” *Analytical Methods*, vol. 4, no. 1, pp. 50–57, 2012.
- [184] I. I. Smalyukh, O. V. Zribi, J. C. Butler, O. D. Lavrentovich, and G. C. L. Wong, “Structure and dynamics of liquid crystalline pattern formation in drying droplets of DNA,” *Physical Review Letters*, vol. 96, no. 17, Article ID 177801, 2006.
- [185] H. Maeda, “Observation of spatially rhythmic patterns from evaporating collagen solution droplets,” *Langmuir*, vol. 16, no. 26, pp. 9977–9982, 2000.
- [186] B. Roy, S. Karmakar, A. Giri, and S. Tarafdar, “Pattern formation of drying lyotropic liquid crystalline droplet,” *RSC Advances*, vol. 6, no. 113, pp. 112695–112703, 2016.
- [187] R. Mondragon, L. Hernandez, J. E. Julia et al., “Study of the drying behavior of high load multiphase droplets in an acoustic levitator at high temperature conditions,” *Chemical Engineering Science*, vol. 66, no. 12, pp. 2734–2744, 2011.
- [188] A. L. Yarin, G. Brenn, and D. Rensink, “Evaporation of acoustically levitated droplets of binary liquid mixtures,” *International Journal of Heat and Fluid Flow*, vol. 23, no. 4, pp. 471–486, 2002.
- [189] G. Brenn, L. J. Deviprasath, F. Durst, and C. Fink, “Evaporation of acoustically levitated multi-component liquid droplets,” *International Journal of Heat and Mass Transfer*, vol. 50, no. 25–26, pp. 5073–5086, 2007.
- [190] E. H. Brandt, “Levitation in physics,” *Science*, vol. 243, no. 4889, pp. 349–355, 1989.
- [191] C. P. Lee, A. V. Anilkumar, and T. G. Wang, “Static shape and instability of an acoustically levitated liquid drop,” *Physics of Fluids*, vol. 3, no. 11, pp. 2497–2515, 1991.
- [192] F. Giorgiutti-Dauphiné and L. Pauchard, “Elapsed time for crack formation during drying,” *European Physical Journal E*, vol. 37, no. 5, article 39, 2014.
- [193] N. Tsapis, E. R. Dufresne, S. S. Sinha et al., “Onset of buckling in drying droplets of colloidal suspensions,” *Physical Review Letters*, vol. 94, no. 1, Article ID 018302, 2005.
- [194] S. Hazra, T. Dutta, S. Das, and S. Tarafdar, “Memory of electric field in laponite and how it affects crack formation: modeling through generalized calculus,” *Langmuir*, vol. 33, no. 34, pp. 8468–8475, 2017.
- [195] S. Das, *Functional Fractional Calculus*, Springer, New Delhi, India, 2011.
- [196] Y. Zhang, Y. Qian, Z. Liu, Z. Li, and D. Zang, “Surface wrinkling and cracking dynamics in the drying of colloidal droplets,” *The European Physical Journal E*, vol. 37, no. 9, article 84, 7 pages, 2014.
- [197] A. G. Banpurkar, K. P. Nichols, and F. Muggele, “Electrowetting-based microdrop tensiometer,” *Langmuir*, vol. 24, no. 19, pp. 10549–10551, 2008.
- [198] V. Vancauwenberghe, P. Di Marco, and D. Brutin, “Wetting and evaporation of a sessile drop under an external electrical field: A review,” *Colloids and Surfaces A: Physicochemical and Engineering Aspects*, vol. 432, pp. 50–56, 2013.
- [199] A. Sanyal, S. Basu, S. Chowdhuri, P. Kabi, and S. Chaudhuri, “Precision control of drying using rhythmic dancing of sessile nanoparticle laden droplets,” *Applied Physics Letters*, vol. 104, no. 16, Article ID 163108, 2014.
- [200] T. K. Pradhan and P. K. Panigrahi, “Deposition pattern of interacting droplets,” *Colloids and Surfaces A: Physicochemical and Engineering Aspects*, vol. 482, pp. 562–567, 2015.
- [201] N. J. Cira, A. Benusiglio, and M. Prakash, “Vapour-mediated sensing and motility in two-component droplets,” *Nature*, vol. 519, no. 7544, pp. 446–450, 2015.
- [202] Y. O. Popov, “Evaporative deposition patterns: Spatial dimensions of the deposit,” *Physical Review E: Statistical, Nonlinear, and Soft Matter Physics*, vol. 71, no. 3, Article ID 036313, 2005.
- [203] M. Cachile, O. Bénichou, and A. M. Cazabat, “Evaporating droplets of completely wetting liquids,” *Langmuir*, vol. 18, no. 21, pp. 7985–7990, 2002.
- [204] M. Cachile, O. Bénichou, C. Poulard, and A. M. Cazabat, “Evaporating droplets,” *Langmuir*, vol. 18, no. 21, pp. 8070–8078, 2002.
- [205] C. Poulard, O. Bénichou, and A. M. Cazabat, “Freely receding evaporating droplets,” *Langmuir*, vol. 19, no. 21, pp. 8828–8834, 2003.
- [206] J. P. Burelbach, S. G. Bankoff, and S. H. Davis, “Nonlinear stability of evaporating/condensing liquid films,” *Journal of Fluid Mechanics*, vol. 195, pp. 463–494, 1988.
- [207] B. J. Fischer, “Particle convection in an evaporating colloidal droplet,” *Langmuir*, vol. 18, no. 1, pp. 60–67, 2002.
- [208] E. Widjaja and M. T. Harris, “Particle deposition study during sessile drop evaporation,” *AIChE Journal*, vol. 54, no. 9, pp. 2250–2260, 2008.
- [209] R. Bhardwaj, X. Fang, and D. Attinger, “Pattern formation during the evaporation of a colloidal nanoliter drop: A numerical and experimental study,” *New Journal of Physics*, vol. 11, Article ID 075020, 2009.
- [210] R. Zheng, “A study of the evaporative deposition process: pipes and truncated transport dynamics,” *The European Physical Journal E: Soft Matter and Biological Physics*, vol. 29, no. 2, pp. 205–218, 2009.
- [211] T. A. Witten, “Robust fadeout profile of an evaporation stain,” *EPL (Europhysics Letters)*, vol. 86, no. 6, Article ID 64002, 2009.
- [212] R. V. Craster, O. K. Matar, and K. Sefiane, “Pinning, retraction and terracing of evaporating droplets containing nanoparticles,” *Langmuir*, vol. 25, no. 6, pp. 3601–3609, 2009.
- [213] A. J. Petsi, A. N. Kalarakis, and V. N. Burganos, “Deposition of Brownian particles during evaporation of two-dimensional sessile droplets,” *Chemical Engineering Science*, vol. 65, no. 10, pp. 2978–2989, 2010.
- [214] H.-S. Kim, S. S. Park, and F. Hagelberg, “Computational approach to drying a nanoparticle-suspended liquid droplet,” *Journal of Nanoparticle Research*, vol. 13, no. 1, pp. 59–68, 2011.

- [215] A. Zigelman and O. Manor, "The deposition of colloidal particles from a sessile drop of a volatile suspension subject to particle adsorption and coagulation," *Journal of Colloid and Interface Science*, vol. 509, pp. 195–208, 2018.
- [216] V. Ragoonanan and A. Aksan, "Heterogeneity in desiccated solutions: Implications for biostabilization," *Biophysical Journal*, vol. 94, no. 6, pp. 2212–2227, 2008.
- [217] V. N. Shabalin and S. N. Shatokhina, "Autogenous rhythms and self-organization of biological fluids," *Bulletin of Experimental Biology and Medicine*, vol. 122, no. 10, pp. 967–973, 1996.
- [218] T. Yakhno, V. Yakhno, A. Sanin, O. Sanina, and A. Pelyushenko, "Dynamics of phase transitions in drying drops as an information parameter of liquid structure," *Nonlinear Dynamics*, vol. 39, no. 4, pp. 369–374, 2005.
- [219] A. A. Killeen, N. Ossina, R. C. McGlennen et al., "Protein self-organization patterns in dried serum reveal changes in B-cell disorders," *Molecular Diagnosis & Therapy*, vol. 10, no. 6, pp. 371–380, 2006.
- [220] T. Khatun, T. Dutta, and S. Tarafdar, "Islands in sea" and "lakes in Mainland" phases and related transitions simulated on a square lattice," *The European Physical Journal B*, vol. 90, no. 11, p. 213, 2017.
- [221] A. D. Eales, N. Dartnell, S. Goddard, and A. F. Routh, "The impact of trough geometry on film shape. A theoretical study of droplets containing polymer, for P-OLED display applications," *Journal of Colloid and Interface Science*, vol. 458, pp. 53–61, 2015.
- [222] D. M. Anderson and S. H. Davis, "The spreading of volatile liquid droplets on heated surfaces," *Physics of Fluids*, vol. 7, no. 2, pp. 248–265, 1995.
- [223] N. I. Lebovka, V. A. Gigiberiya, O. S. Lytvyn, Yu. Yu. Tarasevich, I. V. Vodolazskaya, and O. P. Bondarenko, "Drying of sessile droplets of laponite-based aqueous nanofluids," *Colloids and Surfaces A: Physicochemical and Engineering Aspects*, vol. 462, pp. 52–63, 2014.
- [224] H. Hu and R. G. Larson, "Evaporation of a sessile droplet on a substrate," *The Journal of Physical Chemistry B*, vol. 106, no. 6, pp. 1334–1344, 2002.
- [225] R. Mollaret, K. Sefiane, J. R. E. Christy, and D. Veyret, "Experimental and numerical investigation of the evaporation into air of a drop on a heated surface," *Chemical Engineering Research and Design*, vol. 82, no. 4, pp. 471–480, 2004.
- [226] Yu. Yu. Tarasevich, "Simple analytical model of capillary flow in an evaporating sessile drop," *Physical Review E: Statistical, Nonlinear, and Soft Matter Physics*, vol. 71, no. 2, Article ID 027301, 2005.
- [227] E. Widjaja and M. T. Harris, "Numerical study of vapor phase-diffusion driven sessile drop evaporation," *Computers & Chemical Engineering*, vol. 32, no. 10, pp. 2169–2178, 2008.
- [228] G. J. Dunn, S. K. Wilson, B. R. Duffy, S. David, and K. Sefiane, "A mathematical model for the evaporation of a thin sessile liquid droplet: Comparison between experiment and theory," *Colloids and Surfaces A: Physicochemical and Engineering Aspects*, vol. 323, no. 1-3, pp. 50–55, 2008, Bubble and Drop Interfaces—Selected papers from the International Workshop on Bubble and Drop Interfaces, 25–28 March 2007, Granada, Spain.
- [229] L. Yu. Barash, "Influence of gravitational forces and fluid flows on the shape of surfaces of a viscous fluid of capillary size," *Physical Review E: Statistical, Nonlinear, and Soft Matter Physics*, vol. 79, no. 2, Article ID 025302, 2009.
- [230] H. Masoud and J. D. Felske, "Analytical solution for inviscid flow inside an evaporating sessile drop," *Physical Review E: Statistical, Nonlinear, and Soft Matter Physics*, vol. 79, no. 1, Article ID 016301, 2009.
- [231] A. J. Petsi and V. N. Burganos, "Stokes flow inside an evaporating liquid line for any contact angle," *Physical Review E: Statistical, Nonlinear, and Soft Matter Physics*, vol. 78, no. 3, Article ID 036324, 2008.
- [232] C.-L. Hsu, S.-M. Chu, K. Wood, and Y.-R. Yang, "Percolation in two-dimensional nanoparticle films from colloidal self-assembly," *Physica Status Solidi (a)*, vol. 204, no. 6, pp. 1856–1862, 2007.
- [233] W. Chen, J. Koplik, and I. Kretzschmar, "Molecular dynamics simulations of the evaporation of particle-laden droplets," *Physical Review E: Statistical, Nonlinear, and Soft Matter Physics*, vol. 87, no. 5, Article ID 052404, 2013.
- [234] A. Crivoi and F. Duan, "Fingering structures inside the coffee-ring pattern," *Colloids and Surfaces A: Physicochemical and Engineering Aspects*, vol. 432, pp. 119–126, 2013.
- [235] P. Lebedev-Stepanov and K. Vlasov, "Simulation of self-assembly in an evaporating droplet of colloidal solution by dissipative particle dynamics," *Colloids and Surfaces A: Physicochemical and Engineering Aspects*, vol. 432, pp. 132–138, 2013.
- [236] N. I. Lebovka, S. Khrapatiy, R. Melnyk, and M. Vygorntskii, "Effects of hydrodynamic retardation and interparticle interactions on the self-assembly in a drying droplet containing suspended solid particles," *Physical Review E: Statistical, Nonlinear, and Soft Matter Physics*, vol. 89, no. 5, Article ID 052307, 2014.
- [237] A. Crivoi and F. Duan, "Three-dimensional Monte Carlo model of the coffee-ring effect in evaporating colloidal droplets," *Scientific Reports*, vol. 4, article 4310, pp. 1–6, 2014.
- [238] M. Fujita, O. Koike, and Y. Yamaguchi, "Direct simulation of drying colloidal suspension on substrate using immersed free surface model," *Journal of Computational Physics*, vol. 281, pp. 421–448, 2015.
- [239] H. Hwang and G. Son, "A level-set method for the direct numerical simulation of particle motion in droplet evaporation," *Numerical Heat Transfer, Part B: Fundamentals*, vol. 68, no. 6, pp. 479–494, 2015.
- [240] M. Fujita and Y. Yamaguchi, "Mesoscale modeling for self-organization of colloidal systems," *Current Opinion in Colloid & Interface Science*, vol. 15, no. 1-2, pp. 8–12, 2010.
- [241] M. G. Zaleski, V. L. Emanuél', and M. V. Krasnova, "Physical and chemical characteristics of structurization of a biological fluid drop as exemplified by the 'LITOS-system' diagnosticum," *Klinicheskaiia Laboratornaia Diagnostika*, no. 8, pp. 20–24, 2004 (Russian).
- [242] R. N. Bardakov, Yu. D. Chashechkin, and V. V. Shabalin, "Hydrodynamics of a drying multicomponent liquid droplet," *Journal of Fluid Dynamics*, vol. 45, no. 5, pp. 803–816, 2010.
- [243] Y. D. Chashechkin and R. N. Bardakov, "Formation of texture in residue of a drying drop of a multicomponent fluid," *Doklady Physics*, vol. 55, no. 2, pp. 68–72, 2010.
- [244] F. Girard, M. Antoni, A. Steinchen, and S. Faure, "Numerical study of the evaporating dynamics of a sessile water droplet," *Microgravity Science and Technology*, vol. 18, no. 3-4, pp. 42–46, 2006.
- [245] C. Diddens, J. G. M. Kuerten, C. W. M. van der Geld, and H. M. A. Wijshoff, "Modeling the evaporation of sessile multi-component droplets," *Journal of Colloid and Interface Science*, vol. 487, pp. 426–436, 2017.
- [246] C. Diddens, "Detailed finite element method modeling of evaporating multi-component droplets," *Journal of Computational Physics*, vol. 340, pp. 670–687, 2017.

- [247] H. Tan, C. Diddens, M. Versluis, H.-J. Butt, D. Lohse, and X. Zhang, "Self-wrapping of an ouzo drop induced by evaporation on a superamphiphobic surface," *Soft Matter*, vol. 13, no. 15, pp. 2749–2759, 2017.
- [248] S. Shin, I. Jacobi, and H. A. Stone, "Bénard-Marangoni instability driven by moisture absorption," *EPL (Europhysics Letters)*, vol. 113, no. 2, Article ID 24002, 2016.
- [249] J. R. E. Christy, Y. Hamamoto, and K. Sefiane, "Flow transition within an evaporating binary mixture sessile drop," *Physical Review Letters*, vol. 106, no. 20, Article ID 205701, 2011.
- [250] R. Bennacer and K. Sefiane, "Vortices, dissipation and flow transition in volatile binary drops," *Journal of Fluid Mechanics*, vol. 749, no. 5, pp. 649–665, 2014.
- [251] X. Zhong and F. Duan, "Flow regime and deposition pattern of evaporating binary mixture droplet suspended with particles," *The European Physical Journal E*, vol. 39, no. 2, article 18, pp. 1–6, 2016.
- [252] T. Okuzono, K. Ozawa, and M. Doi, "Simple model of skin formation caused by solvent evaporation in polymer solutions," *Physical Review Letters*, vol. 97, no. 13, Article ID 136103, 2006.
- [253] M. G. Hennessy, G. L. Ferretti, J. T. Cabral, and O. K. Matar, "A minimal model for solvent evaporation and absorption in thin films," *Journal of Colloid and Interface Science*, vol. 488, pp. 61–71, 2017.
- [254] L. M. Martyushev, V. D. Seleznev, and S. A. Skopinov, "Reentrant kinetic phase transitions during dendritic growth of crystals in a two-dimensional medium with phase separation," *Technical Physics Letters*, vol. 23, no. 7, pp. 495–497, 1997.
- [255] L. M. Martiouchiev, V. D. Seleznev, and S. A. Skopinov, "Computer simulation of nonequilibrium growth of crystals in a two-dimensional medium with a phase-separating impurity," *Journal of Statistical Physics*, vol. 90, no. 5-6, pp. 1413–1427, 1998.
- [256] L. M. Martyushev and V. D. Seleznev, "Self-similarity in the kinetic growth regime of a crystal in a phase-separating medium," *Technical Physics Letters*, vol. 25, no. 10, pp. 833–835, 1999.
- [257] A. Crivoi and F. Duan, "Evaporation-induced formation of fractal-like structures from nanofluids," *Physical Chemistry Chemical Physics*, vol. 14, no. 4, pp. 1449–1454, 2012.
- [258] Yu. Yu. Tarasevich, "Computer simulation of crystal growth from solution," *Technical Physics*, vol. 46, no. 5, pp. 627–629, 2001.
- [259] J. S. Langer, "Instabilities and pattern formation in crystal growth," *Reviews of Modern Physics*, vol. 52, no. 1, pp. 1–28, 1980.
- [260] Yu. Yu. Tarasevich, V. O. Konstantinov, and A. K. Ayupova, "Simulation of dendritic growth of salt crystals in biological fluids," in *Izvestija vuzov. Severo-Kavkazskij Region, Estestvennye nauki Special Issue. Math. Mod.*, pp. 147–149, (Russian) 2001.
- [261] J. A. Warren and W. J. Boettinger, "Prediction of dendritic growth and microsegregation patterns in a binary alloy using the phase-field method," *Acta Metallurgica et Materialia*, vol. 43, no. 2, pp. 689–703, 1995.
- [262] J. Zhang, M. K. Borg, K. Ritos, and J. M. Reese, "Electrowetting controls the deposit patterns of evaporated salt water nanodroplets," *Langmuir*, vol. 32, no. 6, pp. 1542–1549, 2016.
- [263] X. Li, K. L. Maki, and M. J. Schertzer, "A low cost fabrication method for electrowetting assisted desiccation of colloidal droplets," in *Symposia: Fluid Measurement and Instrumentation; Fluid Dynamics of Wind Energy; Renewable and Sustainable Energy Conversion; Energy and Process Engineering; Microfluidics and Nanofluidics; Development and Applications in Computational Fluid Dynamics; DNSLES and Hybrid RANSLES Methods*, vol. 1B, ASME, 2017.
- [264] A. Shimoni, S. Azoubel, and S. Magdassi, "Inkjet printing of flexible high-performance carbon nanotube transparent conductive films by "coffee ring effect"," *Nanoscale*, vol. 6, no. 19, pp. 11084–11089, 2014.
- [265] N. R. Devlin, K. Loehr, and M. T. Harris, "The separation of two different sized particles in an evaporating droplet," *AICHE Journal*, vol. 61, no. 10, pp. 3547–3556, 2015.
- [266] T.-S. Wong, T.-H. Chen, X. Shen, and C.-M. Ho, "Nanochromatography driven by the coffee ring effect," *Analytical Chemistry*, vol. 83, no. 6, pp. 1871–1873, 2011.
- [267] A. V. Vorobiev, A. K. Martusevich, and S. P. Peretyagin, *Crystallogenesis Biological Fluids and Substrates in Assessing the State of the Organism*, FGU "NNIITO Rosmedtechnology", Nizhny Novgorod, Russia, (Russian) 2008.
- [268] I. G. Denisov, Y. V. Grinkova, A. A. Lazarides, and S. G. Sligar, "Directed self-assembly of monodisperse phospholipid bilayer nanodiscs with controlled size," *Journal of the American Chemical Society*, vol. 126, no. 11, pp. 3477–3487, 2004.
- [269] E. Rapis, "A change in the physical state of a nonequilibrium blood plasma protein film in patients with carcinoma," *Technical Physics*, vol. 47, no. 4, pp. 510–512, 2002.
- [270] C. P. Gulka, J. D. Swartz, J. R. Trantum et al., "Coffee rings as low-resource diagnostics: Detection of the malaria biomarker plasmodium falciparum histidine-rich protein-II using a surface-coupled ring of Ni(II)NTA gold-plated polystyrene particles," *ACS Applied Materials & Interfaces*, vol. 6, no. 9, pp. 6257–6263, 2014.
- [271] J. R. Trantum, D. W. Wright, and F. R. Haselton, "Biomarker-mediated disruption of coffee-ring formation as a low resource diagnostic indicator," *Langmuir*, vol. 28, no. 4, pp. 2187–2193, 2012.
- [272] J. R. Trantum, M. L. Baglia, Z. E. Eagleton, R. L. Mernaugh, and F. R. Haselton, "Biosensor design based on Marangoni flow in an evaporating drop," *Lab on a Chip*, vol. 14, no. 2, pp. 315–324, 2014.
- [273] L. Bahmani, M. Neysari, and M. Maleki, "The study of drying and pattern formation of whole human blood drops and the effect of thalassaemia and neonatal jaundice on the patterns," *Colloids and Surfaces A: Physicochemical and Engineering Aspects*, vol. 513, pp. 66–75, 2017.
- [274] R. Less, K. L. M. Boylan, A. P. N. Skubitz, and A. Aksan, "Isothermal vitrification methodology development for non-cryogenic storage of archival human sera," *Cryobiology*, vol. 66, no. 2, pp. 176–185, 2013.
- [275] M. O. Kokornaczyk, G. Dinelli, I. Marotti, S. Benedettelli, D. Nani, and L. Betti, "Self-organized crystallization patterns from evaporating droplets of common wheat grain leakages as a potential tool for quality analysis," *TheScientificWorldJOURNAL*, vol. 11, pp. 1712–1725, 2011.
- [276] J. González-Gutiérrez, R. Pérez-Isidoro, and J. C. Ruiz-Suárez, "A technique based on droplet evaporation to recognize alcoholic drinks," *Review of Scientific Instruments*, vol. 88, no. 7, Article ID 074101, 2017.
- [277] K. A. Esmonde-White, S. V. Le Clair, B. J. Roessler, and M. D. Morris, "Effect of conformation and drop properties on surface-enhanced Raman spectroscopy of dried biopolymer drops," *Applied Spectroscopy*, vol. 62, no. 5, pp. 503–511, 2008.
- [278] K. A. Esmonde-White, G. S. Mandair, F. Raaij, B. J. Roessler, and M. D. Morris, "Raman spectroscopy of dried synovial fluid droplets as a rapid diagnostic for knee joint damage," in *Biomedical Optical Spectroscopy, 68530Y*, vol. 6853 of *Proceedings of SPIE*, San Jose, Calif, USA, January 2008.

- [279] K. A. Esmonde-White, G. S. Mandair, F. Raaij et al., "Raman spectroscopy of synovial fluid as a tool for diagnosing osteoarthritis," *Journal of Biomedical Optics*, vol. 14, no. 3, Article ID 034013, 2009.
- [280] K. A. Esmonde-White, G. S. Mandair, F. W. L. Esmonde-White, F. Raaij, B. J. Roessler, and M. D. Morris, "Osteoarthritis screening using raman spectroscopy of dried humansynovial fluid drops," in *Optics in Bone Biology and Diagnostics, 71660J*, vol. 7166 of *Proceedings of SPIE*, San Jose, Calif, USA, January 2009.
- [281] J. Filik and N. Stone, "Drop coating deposition Raman spectroscopy of protein mixtures," *Analyst*, vol. 132, no. 6, pp. 544–550, 2007.
- [282] J. Filik and N. Stone, "Raman point mapping of tear ferning patterns," in *Biomedical Optical Spectroscopy, 685309*, vol. 6853 of *Proceedings of SPIE*, San Jose, Calif, USA, January 2008.
- [283] J. Filik and N. Stone, "Investigation into the protein composition of human tear fluid using centrifugal filters and drop coating deposition Raman spectroscopy," *Journal of Raman Spectroscopy*, vol. 40, no. 2, pp. 218–224, 2009.
- [284] D. Zhang, K. Vangala, D. Jiang, S. Zou, and T. Pechan, "Drop coating deposition raman spectroscopy of fluorescein isothiocyanate labeled protein," *Applied Spectroscopy*, vol. 64, no. 10, pp. 1078–1085, 2010.
- [285] N. C. Dingari, G. L. Horowitz, J. W. Kang, R. R. Dasari, and I. Barman, "Raman spectroscopy provides a powerful diagnostic tool for accurate determination of albumin glycation," *PLoS ONE*, vol. 7, no. 2, Article ID e32406, 2012.
- [286] E. Kočišová, A. Vodáková, and M. Procházka, "DCDR spectroscopy as efficient tool for liposome studies: aspect of preparation procedure parameters," *Spectroscopy: An International Journal*, vol. 27, no. 5-6, pp. 349–353, 2012.
- [287] D. Zang, J. Li, Z. Chen, Z. Zhai, X. Geng, and B. P. Binks, "Switchable opening and closing of a liquid marble via ultrasonic levitation," *Langmuir*, vol. 31, no. 42, pp. 11502–11507, 2015.
- [288] X. Zhong, A. Crivoi, and F. Duan, "Sessile nanofluid droplet drying," *Advances in Colloid and Interface Science*, vol. 217, pp. 13–30, 2015.
- [289] C. Sadek, P. Schuck, Y. Fallourd, N. Pradeau, C. Le Floch-Fouéré, and R. Jeantet, "Drying of a single droplet to investigate process–structure–function relationships: a review," *Dairy Science & Technology*, vol. 95, no. 6, pp. 771–794, 2015.

## Research Article

# Formation of Hierarchical Porous Structure via Breath Figure Method

**Yongjian Zhang<sup>1</sup> and Zhiguang Li<sup>2</sup>**

<sup>1</sup>*Shaanxi Key Laboratory of Surface Engineering and Remanufacturing, Xian University, Xian 710065, China*

<sup>2</sup>*Key Laboratory of Eco-Textiles, Ministry of Education, College of Textiles and Clothing, Jiangnan University, Wuxi 214122, China*

Correspondence should be addressed to Zhiguang Li; lizg@jiangnan.edu.cn

Received 6 December 2017; Accepted 7 February 2018; Published 20 March 2018

Academic Editor: Liyuan Zhang

Copyright © 2018 Yongjian Zhang and Zhiguang Li. This is an open access article distributed under the Creative Commons Attribution License, which permits unrestricted use, distribution, and reproduction in any medium, provided the original work is properly cited.

The porous structure films of PS containing silica nanoparticles of different hydrophobicity were obtained from breath figure method. For the porous films, the pores at the peripheral region and the center region were compared. It was found that the pores at the peripheral region appeared more uniform in size and showed higher degree of ordering. In addition, the patterns of the porous film became more disordered with the enhancing concentration of nanoparticles, and the pore size of the pore was increased. With the increase of the content of SiOH, that is, decrease in particle hydrophobicity, the Si elements were aggregated at the surface of the film and the interior of the pores. A hierarchical porous structure had been obtained at appropriate humidity and particle concentration. Finally, a possible mechanism of the hierarchical structure was proposed.

## 1. Introduction

Breath figure (BF) has attracted great attention to prepare patterned ordered porous polymer films because of its facile, economical, time saving, and convenient implementation [1–3]. The prepared porous films have large surface area and ordered porosity, which have been proved to be promising in a variety of applications in the fields of superhydrophobic surfaces, micropatterned templates, catalysis, resolution separation, and responsive surfaces [4–12].

The BF method is an easy process to fabricate honeycomb patterned porous films because the water droplets are applied as templates and easily removed by simple evaporation. In this process, polymers dissolved in a volatile and water-immiscible solvent are cast under high humidity. The rapid evaporation of volatile solvent can decrease the solution surface temperature, initiating the nucleation of water droplets onto the surface of the solution [13]. At the same time, the polymer aggregates at the interface between solution and water to stabilize the water droplets. Through thermocapillary effect and Marangoni convection, water droplets self-organize into close packed hexagonal arrays

before their coagulation with each other [14, 15]. Eventually, after complete evaporation of the solvent and water droplets, hexagon-arranged honeycomb pores templating from water droplets are left on the polymer film surface. The surface morphologies of the porous films mainly depend on the polymer structure, humidity, concentration of solution, solvent, and the temperature of the solution surface [16–18]. A wide variety of polymers are devoted to obtain honeycomb structures. However, it is difficult to be applied if the polymer matrix requires complicated synthetic methods and high price. Polystyrene is a commercially available polymer, which is able to form porous structures by this process [19, 20].

Nanoparticles can be adsorbed at the fluid-fluid interfaces and significantly change the properties of these interfaces [21–23]. Introducing nanoparticles into the polymer matrix leads to the preparation of new honeycomb patterned composite and excellent property. Sun et al. [24, 25] utilized polymer and silica particles to assist in preparing honeycomb porous films through BF method. Particles are proven to be effective in serving as stabilizers for making fine patterned porous arrays. However, the silica particles with varied surface hydrophobicity have not been investigated systematically yet.

The wettability of ordered porous surfaces plays an important role in the practical applications. It is well known that the roughness of a surface can enhance the hydrophobic or hydrophilic properties. Ke et al. [26] prepared positively charged honeycomb films from PS-based block copolymer and silica particles by the breath figure method. The film surface is at a Cassie state where the negatively charged silica nanoparticles can selectively assemble on the external surface of films; however, silica nanoparticles assemble on both external and internal surfaces at a Wenzel state after prewetting. Consequently, by controlling the wetting states, nanoparticles selectively assemble inside or outside the pores influencing the wettability.

In addition to surface roughness, the investigations of surface chemistry of nanoparticles on the wettability are also important. In this paper, the porous structure films of the PS and silica nanoparticles of different surface hydrophobicity are fabricated from breath figure method. The surface morphology and the aggregation of Si elements of the porous structure films were investigated. The influences of important experimental factors, such as humidity and particle hydrophobicity, on the final morphology are discussed.

## 2. Experimental

**2.1. Materials.** Polystyrene (PS) ( $M_n = 1 \times 10^5$  g/mol) was purchased from Aldrich. The silica particles used were fumed silica nanoparticles (Wacker Chemie), with primary diameter of 20–30 nm. The hydrophobicity of the particles is characterized by the relative SiOH content on their surface. The hydrophobicity increases with a decrease of the content of SiOH. In this study, the relative silanol content was 25%, 75%, and 100%, respectively. The solvent of chloroform ( $\text{CHCl}_3$ ) was of analytical grade and used without further purification.

**2.2. Preparation of Honeycomb Films.** The honeycomb film was fabricated via BF technology [18, 27]. The concentrations of 30 mg/mL of the PS and  $\text{SiO}_2$  particles (1 mg/mL, 2 mg/mL, and 5 mg/mL) with different contents of -OH (25%, 75%, and 100%) were dissolved in chloroform solution and then cast onto a silicon wafer under a humid airflow. After the complete evaporation of solvent and water droplets, porous film was obtained.

**2.3. Characterization.** Surface morphologies of the films were characterized by optical microscopy (XJX-2, Nanjing, China) and a scanning electron microscope (SEM) carried on VEGA 3 LMH (Česko TESCAN) with 20 kV accelerating voltage. The quantitative analysis was using energy dispersive spectrometry (EDS) (Oxford INCA X-ACT). The water contact angle was tested using the sessile drop method (JC2000D4 Powereach Tensiometer).

## 3. Results and Discussion

**3.1. Spatial Variation of Porous Structures.** Before the BF process, the PS solution drop was deposited on the glass slide. The morphology of the drop is shown in Figure 1(a). The contact angle of the drop was measured to be  $\sim 15.5^\circ$ . The

peripheral area was marked as region B and the center area was region C. The SEM images of region B and region C are shown in Figures 1(b) and 1(c), respectively.

For the hole structure of the porous films, the morphology at the peripheral area is noticeably different from that at the center area. At the peripheral area, honeycomb like ordered pores with uniform sizes are observed. In contrast, the pores formed at the center of the films are evidently less ordered and the size distribution is much broader than that at the peripheral area. The hole is distributed in a monolayer at the periphery of the drop, whereas at the center part, multilayers of holes are examined. Moreover, the size of holes becomes multidispersed.

The differences in the pore morphology between the peripheral and center regions resulted from the difference in evaporation rate at different regions.

During the fast evaporation of the  $\text{CHCl}_3$ , Marangoni convection can actively transport most of the PS together with the water droplets from center to edge of the solution drop. Thus, the effective concentration of the PS is higher near the contact lines than that at the center of the solution drop [28]. During the volatilization of solvent, the contact line of the solution is pinned, possibly due to both surface roughness of the substrate and the deposition of the PS [29]. The pinning effect depends on the initial contact angle of the deposited solution on the silicon wafer substrate [30]. The evaporation rate is higher at the periphery than at the center. Correspondingly, the faster vitrification at the peripheral region also helps to limit the growth and coalescence of the trapped water droplets [31]. In comparison, the delayed gelation/vitrification at the center region results in longer growth and coalescence time for the water droplets, and thus the larger and polydisperse pores.

**3.2. Influence of Nanoparticles.** With the presence of particles, a particle layer could form at the water solution interface which possesses shear and dilational moduli [21]. The mechanical properties of the particle layer can influence the growth of droplets. It is reasonable to expect smaller droplet size corresponding to stronger particle layer, which is indeed in line with the previous rheological study of the particle layer [32]. Figure 2 shows different patterns using different concentrations of the silica nanoparticles with the same PS solution.

It is obvious that the patterns of the film surface become increasingly disordered with greater nanoparticle concentration. The ordered hexagonal arrangement of the pores has been compromised with increasing particle concentration, and the pore size is larger for higher application quantity of the particle. When the particle concentration exceeds a critical value above one concentration, the porous films are not formed. This is because the adsorption of too much nanoparticles at the water droplet surface may result in a jamming state to the interface, which hinders the droplet growth and leads to the formation of irregular shaped droplets instead of uniform droplet pattern [33].

At an appropriate particle concentration, ordered porous structure can be obtained. However, the average pore size depends on the hydrophobicity of the particles. The SEM

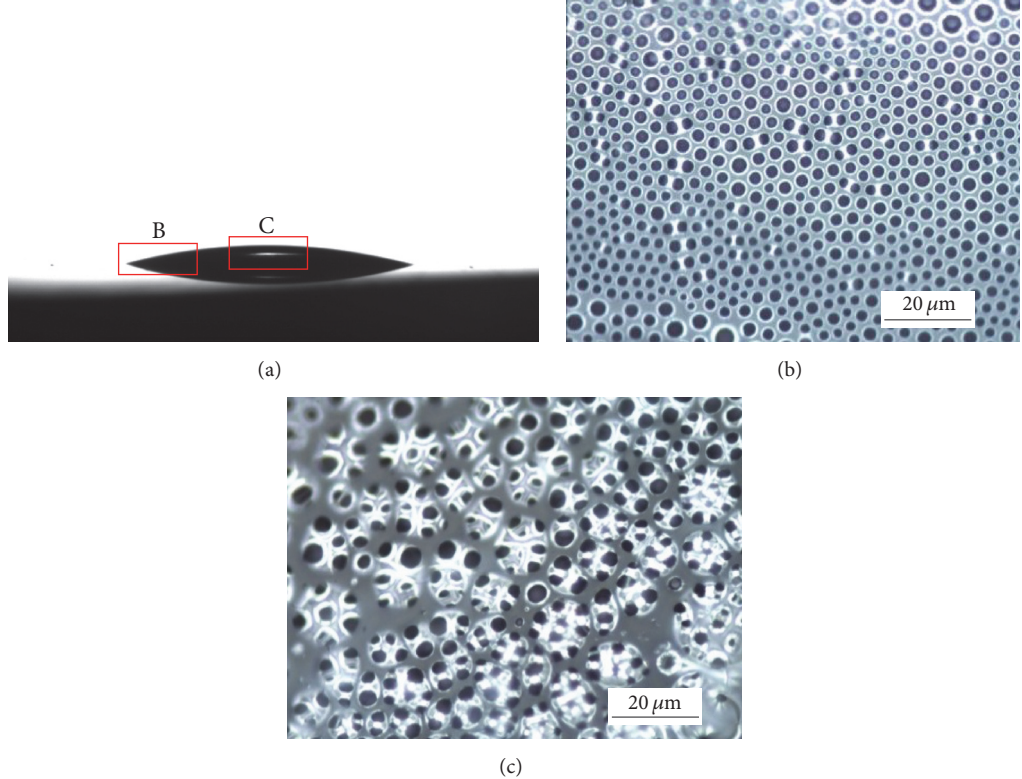


FIGURE 1: Spatial dependence of the porous structure obtained by BF method using PS solution (30 mg/mL). (a) Initial morphology of the PS solution drop; ((b) and (c)) the formed porous structures at the peripheral and center of the drop through breath figure method, respectively, as marked in (a).

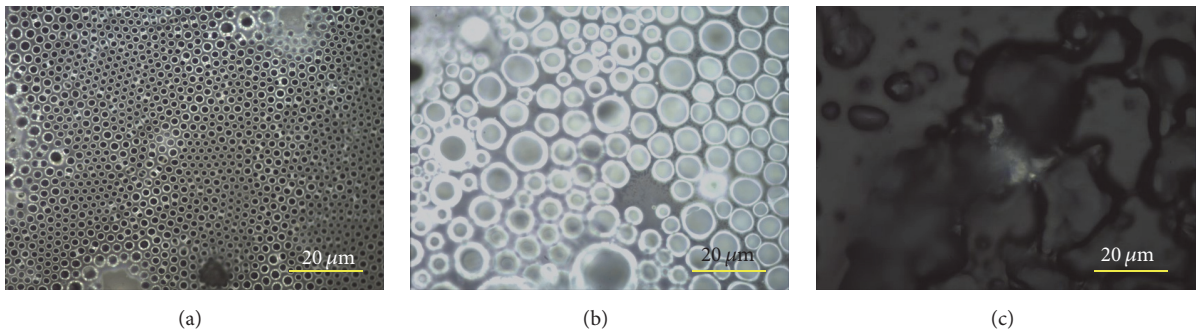


FIGURE 2: Influence of the nanoparticle (37% SiOH) concentration on the final porous structures obtained from the PS solution (30 mg/mL). (a) 1 mg/mL, (b) 2 mg/mL, and (c) 5 mg/mL.

images of the porous structure with particles of varied hydrophobicity are shown in Figure 3. The average pore size as a function of the hydrophobicity particles of the porous films are shown in Figure 4. It is noteworthy that the average pore sizes of the obtained films decrease from 0.83 μm, 1.09 μm to 1.29 μm when the SiOH contents increase from 25% to 100%. With the increase of -OH contents, the pore sizes are increased. It indicates that when the PS is fixed, the augment of units of -OH will enhance the capability of holding water during the water-organic interface, which enlarges the pore size. On the other hand, the existence of hydrophilic segment is beneficial to stabilize the water

droplets at the interface, resulting in forming more ordered porous film. Hydrophilic segment is known to form inverse structures in organic solvent [34]. When contacting with water, these inverse structures start interacting with water, leading to a rearrangement of PS around the water droplets. With the evaporation of the solvent and water, the pores enriched with hydrophilic functionality are formed.

In order to investigate where the particles were distributed, EDS was utilized and the Si elements were marked as red dots in Figure 3. For the most hydrophobic particle used in the present work (25% SiOH), most of the particle are distributed at the rim of the pores. With the increase of

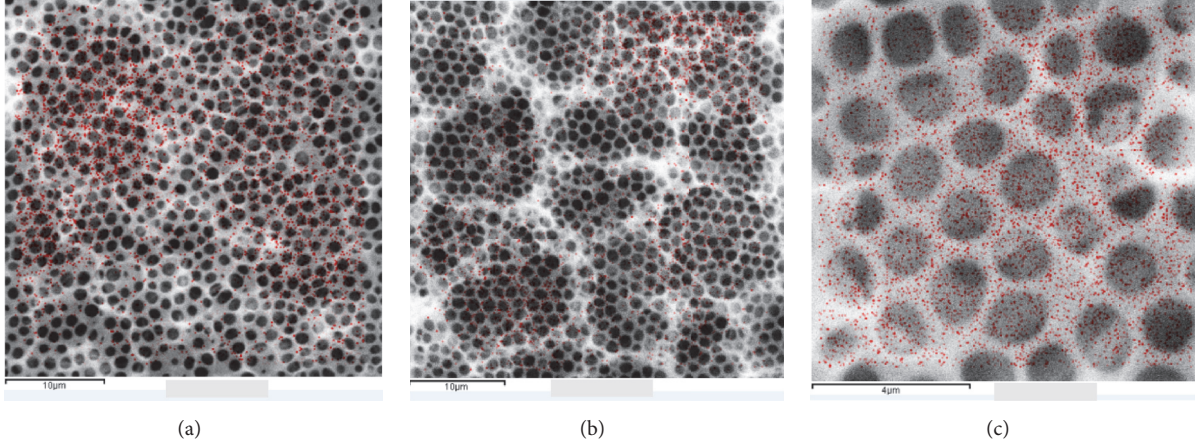


FIGURE 3: Influence of particle hydrophobicity concentration on the final porous structures. (a) 25% SiOH, (b) 75% SiOH, and (c) 100% SiOH. The red dots are the distribution of Si element.

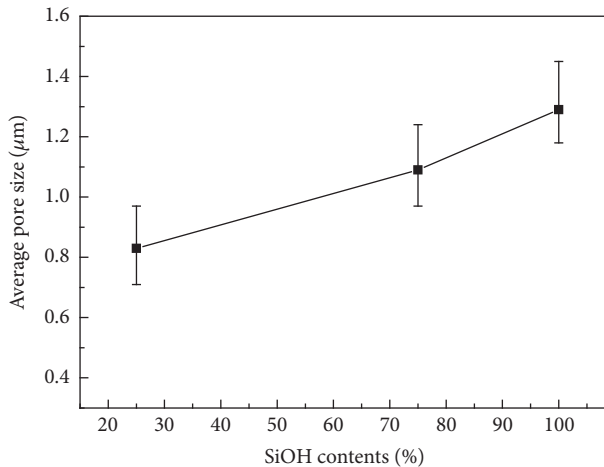


FIGURE 4: The average pore size as a function of the SiOH contents.

SiOH (100% SiOH), the particles also appear at the surface of the film and the interior of the pores. This is mainly attributed to the hydrophilic nature of these particles.

**3.3. Formation of Hierarchical Porous Structure.** When humidity is increased to 95%, the hierarchical porous structure has been obtained in Figure 5, which is characterized by large porous pores containing many small holes in their interiors with  $D_S/D_L \approx 1/10$  ( $D_S$  and  $D_L$  are the diameter for small and large holes, resp.).

This hierarchical porous structure can only be formed at high relative humidity (RH = 95%). In this case, coalescence among water droplets could be enhanced, consequently leading to polydispersity in droplet sizes [35]. The formation mechanism can be illustrated in Figure 6. The water droplets approach on the surface of the polymer solution (Figure 6(a)). The first unstable layer of water droplets was condensed at the solution surface as shown in Figure 6(b). Due to the high RH, the droplets close to the first layer condensation have coalesced to larger droplets. With the volatilization of

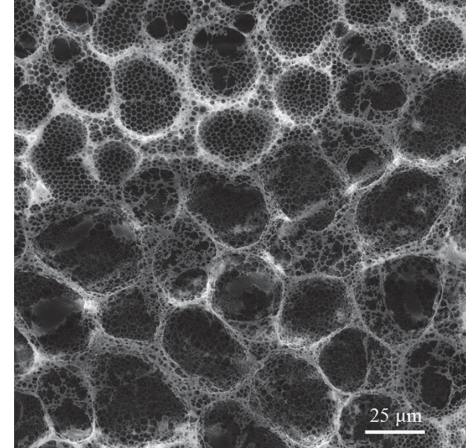


FIGURE 5: Hierarchical porous structure obtained at RH = 95%.

solvent and water droplets, the smaller pores with metastable state are formed in Figure 6(c). The coalesced larger water droplets are dragged into the polymer solution through a thermocapillary effect, and then the large pores are formed as shown in Figure 6(d). The first unstable layer is squeezed to form a spherical shape because of the gravity of the larger water droplet. This process can repeat to form multilayer structure until the solvent and water droplet are thoroughly evaporated (Figure 6(e)).

The size of the periodic microstructures in honeycomb porous falls within the range of hundreds of nanometers to tens of micrometers, matching the requirements of templates, separation, cell culture, biosensing, optical and optoelectronic devices, and so on [1, 36–38].

#### 4. Conclusions

In this paper, the porous films of PS and silica nanoparticles of different -OH are prepared through breath figure method. For all the porous films obtained, the pore morphology at

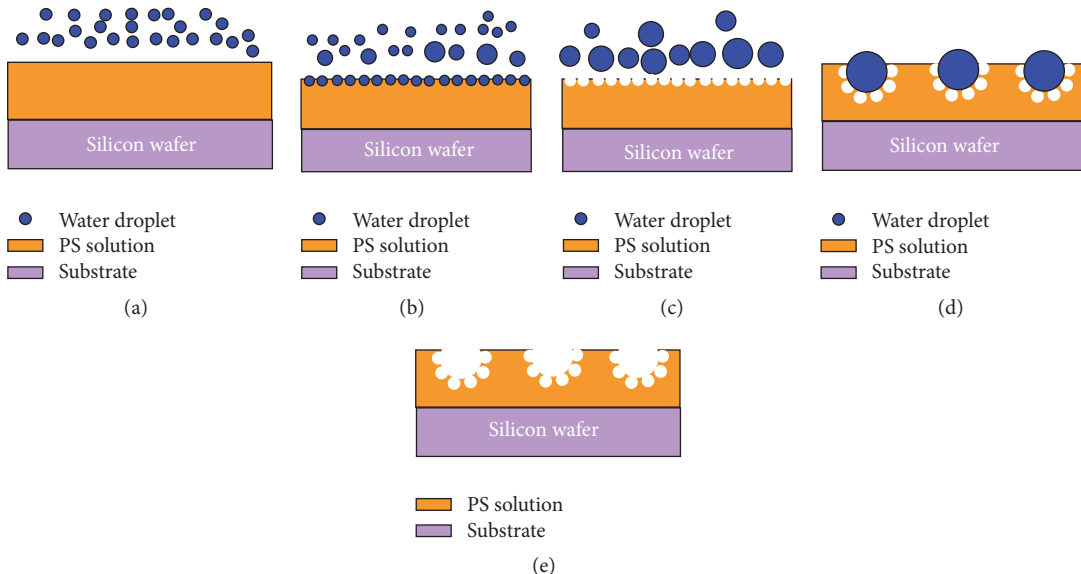


FIGURE 6: Schematic illustration for the formation of the hierarchical structure. (a) Water droplets approaching the PS solution. (b) Condensation of the first layer droplets. (c) Coalescence of the larger droplets. (d) Successive condensation and sedimentation of the coalesced droplets. (e) Formation of the final hierarchical structure.

the peripheral regions is found more uniform and ordered than that at the center region. Such a difference is attributed to the interplay between the contact line pinning and the evaporation rate. The patterns of the film become more disordered with the enhancing concentration of nanoparticles, and the pore size is increased. Moreover, the average pore size and the distribution of particles depend on the particle hydrophobicity. With the increase of SiOH content, the pore size tends to increase and the silica nanoparticle seems aggregate at the surface of the film and the interior of the pores. Interestingly, when the humidity is increasing to 95%, the hierarchical porous structure was observed, which is characterized by larger porous pores containing many small holes in the interior. This hierarchical porous structure is probably due to the humidity enhanced droplet coalescence and the thermocapillary effect caused by evaporation.

## Conflicts of Interest

The authors declare that there are no conflicts of interest regarding the publication of this paper.

## Acknowledgments

This work was supported by the Foundation of Shaanxi Provincial Education Department, China (Grant no. 17JK1123), the Xi'an Science and Technology Project (Grant no. 2017CGWLI5), and the Fundamental Research Funds for the Central Universities (Grant no. JUSRP11702). The authors thank Mr. H. B. Li and Mr. X. Lu for the help in experiments.

## References

- [1] A. J. Zhang, H. Bai, and L. Li, "Breath figure: a nature-inspired preparation method for ordered porous films," *Chemical Reviews*, vol. 115, no. 18, pp. 9801–9868, 2015.
- [2] L.-S. Wan, L.-W. Zhu, Y. Ou, and Z.-K. Xu, "Multiple interfaces in self-assembled breath figures," *Chemical Communications*, vol. 50, no. 31, pp. 4024–4039, 2014.
- [3] A. Muñoz-Bonilla, M. Fernández-García, and J. Rodríguez-Hernández, "Towards hierarchically ordered functional porous polymeric surfaces prepared by the breath figures approach," *Progress in Polymer Science*, vol. 39, no. 3, pp. 510–554, 2014.
- [4] Z. Li, X. Ma, Q. Kong, D. Zang, X. Guan, and X. Ren, "Static and Dynamic Hydrophobic Properties of Honeycomb Structured Films via Breath Figure Method," *The Journal of Physical Chemistry C*, vol. 120, no. 33, pp. 18659–18664, 2016.
- [5] Q. Hong, X. Ma, Z. Li, F. Chen, and Q. Zhang, "Tuning the surface hydrophobicity of honeycomb porous films fabricated by star-shaped POSS-fluorinated acrylates polymer via breath-figure-templated self-assembly," *Materials & Design*, vol. 96, pp. 1–9, 2016.
- [6] P. Zhang, H. Chen, L. Zhang, T. Ran, and D. Zhang, "Transparent self-cleaning lubricant-infused surfaces made with large-area breath figure patterns," *Applied Surface Science*, vol. 355, pp. 1083–1090, 2015.
- [7] L.-S. Wan, Q.-L. Li, P.-C. Chen, and Z.-K. Xu, "Patterned biocatalytic films via one-step self-assembly," *Chemical Communications*, vol. 48, no. 37, pp. 4417–4419, 2012.
- [8] H. Yuan, B. Yu, H. Cong et al., "Preparation of highly permeable BPPO microfiltration membrane with binary porous structures on a colloidal crystal substrate by the breath figure method," *Journal of Colloid and Interface Science*, vol. 461, pp. 232–238, 2016.

- [9] J. Mansouri, E. Yapit, and V. Chen, "Polysulfone filtration membranes with isoporous structures prepared by a combination of dip-coating and breath figure approach," *Journal of Membrane Science*, vol. 444, pp. 237–251, 2013.
- [10] C. Du, A. Zhang, H. Bai, and L. Li, "Robust microsieves with excellent solvent resistance: Cross-linkage of perforated polymer films with honeycomb structure," *ACS Macro Letters*, vol. 2, no. 1, pp. 27–30, 2013.
- [11] A. S. De León, M. Molina, S. Wedepohl, A. Muñoz-Bonilla, J. Rodríguez-Hernández, and M. Calderón, "Immobilization of Stimuli-Responsive Nanogels onto Honeycomb Porous Surfaces and Controlled Release of Proteins," *Langmuir*, vol. 32, no. 7, pp. 1854–1862, 2016.
- [12] P. Escalé, W. Van Camp, F. Du Prez, L. Rubatat, L. Billon, and M. Save, "Highly structured pH-responsive honeycomb films by a combination of a breath figure process and in situ thermolysis of a polystyrene-block-poly(ethoxy ethyl acrylate) precursor," *Polymer Chemistry*, vol. 4, no. 17, pp. 4710–4717, 2013.
- [13] Y.-C. Chiu, C.-C. Kuo, C.-J. Lin, and W.-C. Chen, "Highly ordered luminescent microporous films prepared from crystalline conjugated rod-coil diblock copolymers of PF-b-PSA and their superhydrophobic characteristics," *Soft Matter*, vol. 7, no. 19, pp. 9350–9358, 2011.
- [14] N. Maruyama, T. Koito, J. Nishida et al., "Mesoscopic patterns of molecular aggregates on solid substrates," *Thin Solid Films*, vol. 327–329, no. 1-2, pp. 854–856, 1998.
- [15] M. Srinivasarao, D. Collings, A. Philips, and S. Patel, "Three-dimensionally ordered array of air bubbles in a polymer film," *Science*, vol. 292, no. 5514, pp. 79–83, 2001.
- [16] H. Wu, T. Jiang, J. Zhu, K. Cui, Q. Zhao, and Z. Ma, "Synthesis of poly(ethylene-co-vinyl alcohol)-g-polystyrene graft copolymer and their applications for ordered porous film and compatibilizer," *Journal of Polymer Science Part A: Polymer Chemistry*, vol. 54, no. 4, pp. 516–524, 2016.
- [17] L.-W. Zhu, L.-S. Wan, J. Jin, and Z.-K. Xu, "Honeycomb porous films prepared from porphyrin-cored star polymers: Submicrometer pores induced by transition of monolayer into multilayer structures," *The Journal of Physical Chemistry C*, vol. 117, no. 12, pp. 6185–6194, 2013.
- [18] Z. Li, Z. Zhang, Q. Kong, and X. Ren, "Adhesive and repulsive properties of water droplet impact on honeycomb surfaces through breath figure method," *Journal of Applied Polymer Science*, vol. 134, no. 47, Article ID 45476, 2017.
- [19] L.-W. Zhu, W. Yang, Y. Ou, L.-S. Wan, and Z.-K. Xu, "Synthesis of polystyrene with cyclic, ionized and neutralized end groups and the self-assemblies templated by breath figures," *Polymer Chemistry*, vol. 5, no. 11, pp. 3666–3672, 2014.
- [20] E. Ferrari, P. Fabbri, and F. Pilati, "Solvent and substrate contributions to the formation of breath figure patterns in polystyrene films," *Langmuir*, vol. 27, no. 5, pp. 1874–1881, 2011.
- [21] D. Y. Zang, E. Rio, D. Langevin, B. Wei, and B. P. Binks, "Viscoelastic properties of silica nanoparticle monolayers at the air-water interface," *European Physical Journal E*, vol. 31, no. 2, pp. 125–134, 2010.
- [22] Z. Chen, D. Zang, L. Zhao et al., "Liquid Marble Coalescence and Triggered Microreaction Driven by Acoustic Levitation," *Langmuir*, vol. 33, no. 25, pp. 6232–6239, 2017.
- [23] D. Zang, Y. Yu, Z. Chen, X. Li, H. Wu, and X. Geng, "Acoustic levitation of liquid drops: Dynamics, manipulation and phase transitions," *Advances in Colloid and Interface Science*, vol. 243, pp. 77–85, 2017.
- [24] W. Sun, Y. Zhou, Y. Ju, L. Yang, T. Xu, and Z. Chen, "A study of morphology modulation of honeycomb hybrid films and the interfacial behavior of silica particles within a patterned polymeric matrix," *Macromolecular Chemistry and Physics*, vol. 215, no. 1, pp. 96–102, 2014.
- [25] W. Sun, Z. Shao, and J. Ji, "Particle-assisted fabrication of honeycomb-structured hybrid films via breath figures method," *Polymer*, vol. 51, no. 18, pp. 4169–4175, 2010.
- [26] B.-B. Ke, L.-S. Wan, P.-C. Chen, L.-Y. Zhang, and Z.-K. Xu, "Tunable assembly of nanoparticles on patterned porous film," *Langmuir*, vol. 26, no. 20, pp. 15982–15988, 2010.
- [27] Z. Li, Q. Kong, X. Ma, D. Zang, X. Guan, and X. Ren, "Dynamic effects and adhesion of water droplet impact on hydrophobic surfaces: Bouncing or sticking," *Nanoscale*, vol. 9, no. 24, pp. 8249–8255, 2017.
- [28] L. Wang, S. H. Maruf, D. Maniglio, and Y. Ding, "Fabrication and characterizations of crosslinked porous polymer films with varying chemical compositions," *Polymer*, vol. 53, no. 17, pp. 3749–3755, 2012.
- [29] R. D. Deegan, O. Bakajin, T. F. Dupont, G. Huber, S. R. Nagel, and T. A. Witten, "Contact line deposits in an evaporating drop," *Physical Review E*, vol. 62, no. 1 B, pp. 756–765, 2000.
- [30] T. Kajiyama, C. Monteux, T. Narita, F. Lequeux, and M. Doi, "Contact-line recession leaving a macroscopic polymer film in the drying droplets of water-poly(N, N-dimethylacrylamide) (PDMA) solution," *Langmuir*, vol. 25, no. 12, pp. 6934–6939, 2009.
- [31] T. Nishikawa, R. Ookura, J. Nishida et al., "Fabrication of honeycomb film of an amphiphilic copolymer at the air-water interface," *Langmuir*, vol. 18, no. 15, pp. 5734–5740, 2002.
- [32] D. Y. Zang, E. Rio, G. Delon, D. Langevin, B. Wei, and B. P. Binks, "Influence of the contact angle of silica nanoparticles at the air-water interface on the mechanical properties of the layers composed of these particles," *Molecular Physics*, vol. 109, no. 7–10, pp. 1057–1066, 2011.
- [33] W. Sun, Y. Zhou, and Z. Chen, "Fabrication of honeycomb-structured porous film from polystyrene via polymeric particle-assisted breath figures method," *Macromolecular Research*, vol. 21, no. 4, pp. 414–418, 2013.
- [34] X.-Y. Li, Q.-L. Zhao, T.-T. Xu, J. Huang, L.-H. Wei, and Z. Ma, "Highly ordered microporous polystyrene-b-poly(acrylic acid) films: Study on the influencing factors in their fabrication via a static breath-figure method," *European Polymer Journal*, vol. 50, no. 1, pp. 135–141, 2014.
- [35] C. Wang, Y. Mao, D. Wang, Q. Qu, G. Yang, and X. Hu, "Fabrication of highly ordered microporous thin films by PS-b-PAA self-assembly and investigation of their tunable surface properties," *Journal of Materials Chemistry*, vol. 18, no. 6, pp. 683–690, 2008.
- [36] B. Yao, Q. Zhu, L. Yao, and J. Hao, "Fabrication of honeycomb-structured poly(ethylene glycol)-block-poly(lactic acid) porous films and biomedical applications for cell growth," *Applied Surface Science*, vol. 332, pp. 287–294, 2015.
- [37] G. Leone, U. Giovanella, F. Bertini et al., "Hierarchically structured, blue-emitting polymer hybrids through surface-initiated nitroxide-mediated polymerization and water templated assembly," *Journal of Materials Chemistry C*, vol. 1, no. 40, pp. 6585–6593, 2013.
- [38] C. Zhang, X. Wang, K. Min et al., "Developing porous honeycomb films using miktoarm star copolymers and exploring their application in particle separation," *Macromolecular Rapid Communications*, vol. 35, no. 2, pp. 221–227, 2014.

## Research Article

# Effect of Direct Current on Solid-Liquid Interfacial Tension and Wetting Behavior of Ga-In-Sn Alloy Melt on Cu Substrate

Limin Zhang<sup>1</sup>, Ning Li,<sup>1</sup> Hui Xing,<sup>1</sup> Rong Zhang<sup>1</sup>,<sup>1</sup> and Kaikai Song<sup>2</sup>

<sup>1</sup>*Shaanxi Key Laboratory of Condensed Matter Structures and Properties and Key Laboratory of Space Applied Physics and Chemistry, Ministry of Education, School of Science, Northwestern Polytechnical University, 127 West Youyi Road, Xi'an, Shaanxi 710072, China*

<sup>2</sup>*School of Mechanical, Electrical & Information Engineering, Shandong University at Weihai, 180 Wenhua Xilu, Weihai, Shandong 264209, China*

Correspondence should be addressed to Rong Zhang; xbwl01@mail.nwpu.edu.cn

Received 22 November 2017; Accepted 11 January 2018; Published 1 March 2018

Academic Editor: Liyuan Zhang

Copyright © 2018 Limin Zhang et al. This is an open access article distributed under the Creative Commons Attribution License, which permits unrestricted use, distribution, and reproduction in any medium, provided the original work is properly cited.

The effect of direct current (DC) on the wetting behavior of Cu substrate by liquid Ga–25In–13Sn alloy at room temperature is investigated using a sessile drop method. It is found that there is a critical value for current intensity, below which the decrease of contact angle with increasing current intensity is approximately linear and above which contact angle tends to a stable value from drop shape. Current polarity is a negligible factor in the observed trend. Additionally, the observed change in contact angles is translated into the corresponding change in solid-liquid interfacial tension using the equation of state for liquid interfacial tensions. The solid-liquid interfacial tension decreases under DC. DC-induced promotion of solute diffusion coefficient is likely to play an important role in determining the wettability and solid-liquid interfacial tension under DC.

## 1. Introduction

During the solidification process of materials, the application of electric current including direct current, alternating current (AC), and electric current pulse (ECP) has developed into a promising technique to modify the solidifying structure in the past decades due to their high efficiency and cleanliness [1–3]. Consequently, much of the fundamental research has been performed towards understanding the mechanism behind the modification of the solidification structure by electric current [4–7]. However, the exact modification mechanism is not fully understood and it is still controversial.

To date, the main reasonable hypotheses proposed to explain the modification of the solidification structure are the increase in the solid-liquid interfacial tension [8], the reduction in the nucleation activation energy [9], the suppression of grain growth due to Joule heating [10], current crowding due to the differing electrical conductivities of solid and liquid [11], electromigration [12], and melt flow caused by Lorentz force [13], but all these taken together do not provide a consistent picture of the solidification structure evolution

under electric current. This is mainly due to the lack of conclusive evidence provided by theoretical and experimental studies in support of the proposed hypotheses, especially in the solid-liquid interfacial tension and its related wettability of solid phase by liquid phase which play an important role in determining the kinetics of crystal nucleation and growth [14]. To better understand the intrinsic mechanism of applied electric current to the solidification structure of alloys, a knowledge of the correlation between current parameter and the solid-liquid interfacial tension during solidification process of alloys is required. However, very little experimental investigations have been performed on this issue.

To our knowledge, although as yet no measuring method is applicable for the solid-liquid interfacial tension when DC passes through the solid-liquid interface, recent studies on effect of an applied DC on the solid-liquid interfacial reactions in metal-metal system have given an implication for the determination of the solid-liquid interfacial tension and the wettability. Xu et al. [15] found that the application of DC could improve the wettability of molten Bi on Cu substrate using a DC-coupled sessile drop method, and current polarity

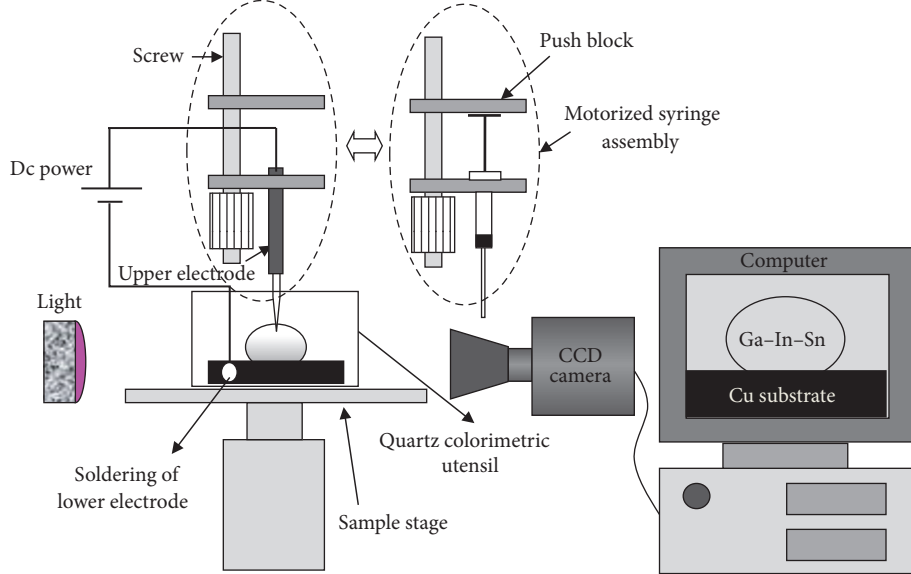


FIGURE 1: Schematic illustration of direct current-sessile drop apparatus.

did not give rise to significant difference on the wettability. Here, it should be pointed out that there are some drawbacks to their designed experiment. For example, the dissolution of the Cu electrode in liquid Sn at the setting temperature needs to be taken into account, and thus the wetting result is blemished. Gu et al. [16, 17] solved the above problem by selecting the graphite electrode to replace the Cu electrode. It was observed that similar results were obtained for the wettability of molten Sn on Cu substrate or Fe substrate. Moreover, the applied DC promoted the dissolution of the Cu substrate in molten Sn which was enhanced with increasing current intensity. It prevented the determination of solid-liquid interfacial tension from contact angles through Young's equation.

The aim of the present work is to obtain quantitative data on the wettability of Cu by molten alloy using a DC-coupled sessile drop method and to compare the solid-liquid interfacial tension under different current conditions. For the work, Ga–25In–13Sn ternary near-eutectic alloy is chosen as droplet at room temperature, because this alloy is liquid due to its low melting point. In this situation, the dissolution of the upper electrode in liquid alloy and the solid-liquid interfacial reaction can be neglected. This makes it possible to reveal the influence of DC on the solid-liquid interfacial tension and the wettability for the explanation of the solidification structure evolution under electric current. In addition, the potential mechanism of DC on the change of solid-liquid interfacial tension and wettability is also discussed in detail.

## 2. Experimental Procedure

The Ga–25In–13Sn (all percentages are wt-% unless otherwise stated) ternary near-eutectic alloy was prepared using high-purity metals of Ga (>99.999%), In (>99.99%), and Sn (>99.99%) in a resistance furnace. After allowing time for melt homogenization, the alloy was taken out and aspirated into a microinjector. Pure Cu plates (>99.9%) in a size of

$15 \times 15 \times 4 \text{ mm}^3$  were used as substrates. They were mechanically polished to a mirror surface with roughness of a few nanometers using diamond pastes and then ultrasonically cleaned in acetone. The measurements of contact angle and surface tension under DC were performed using a DC-coupled sessile drop apparatus, as schematically shown in Figure 1. As can be seen, it was comprised of two main devices: a high speed (frame rate = 200 Hz) contact angle instrument (Powereach, China) and the electric transmission mission device consisting of a DC power and a Cu wire of  $\Phi 1.8 \text{ mm}$  with a sharp-pointed head used as the upper electrode and Cu substrate, on the side of which the Cu wire was held, used as the bottom electrode. Cu substrate was put at the bottom of quartz colorimetric utensil and horizontally placed on the sample stage. Subsequently, liquid drop of Ga–In–Sn alloy with a volume of  $40 \mu\text{l}$  was injected on the Cu substrate surface with microinjector. After that the upper electrode, which replaced the position of microinjector, was fixed to the motorized syringe assembly. The sample stage can move in both horizontal and vertical direction to achieve a sufficient contact of the upper electrode with liquid drop.

In DC-coupled sessile drop experiments, the sharp-pointed upper electrode was initially moved down to be inserted into the liquid drop. This moment was defined as the starting time of the wettability (i.e.,  $t = 0 \text{ s}$ ), and then let the liquid drop stand for 5 minutes without DC. After that, DC of 1 A with a predetermined polarity was continuously applied for 5 minutes at room temperature, and then the 2D projection of 3D drop was recorded by a high speed framing camera. Repeating the above operations, each time current intensity added 1 A until current intensity increased to 11 A. Due to the existence of relaxation time for the steady-state contact angle, the wetting experiment without DC was performed at room temperature and image was taken by the camera every 5 minutes, one which lasted until 65 minutes. Contact angles were calculated from the

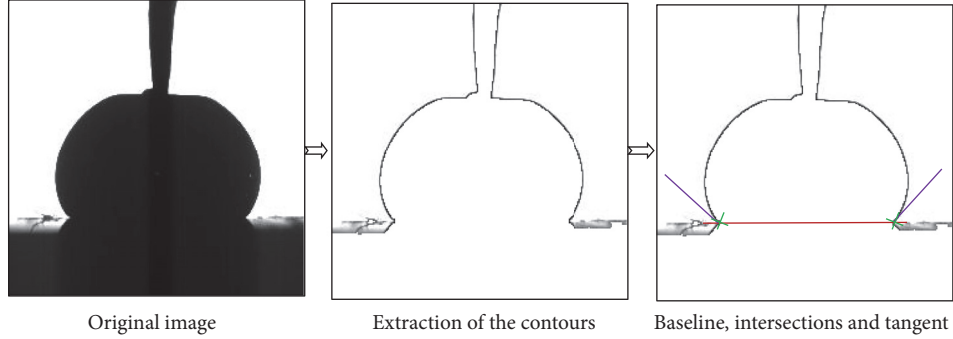


FIGURE 2: Measurement of contact angle using image-processing techniques.

captured images using drop shape analysis. First the drop profile and the surface of Cu substrate were extracted using image-processing techniques, and then the intersection of the baseline with the tangent was obtained. The different steps in the processing technique are presented in Figure 2.

### 3. Results and Discussion

In order to conveniently describe current polarity, the direction of DC is defined as a positive one with the Cu substrate connected to the cathode, while the corresponding negative DC is one with the Cu substrate connected to the anode. Typical liquid drop shapes of Ga-In-Sn alloy on Cu substrate under different conditions are illustrated in Figure 3. Figures 3(a)–3(c) represent the metal drop spreading on Cu substrate at different time without DC; the corresponding drop contours are overlapped in Figure 3(d). It can be seen that wetting degree of Cu substrate by Ga-In-Sn alloy drop is poor and does not vary with time in the absence of DC. It suggests that metal drop spreading on Cu substrate forms the quasi-equilibrium shape within 5 minutes. Since the spreading rate was accelerated by DC according to [15, 16], the time required to form the approximate equilibrium shape during application of DC should be less than 5 minutes. In the present experiment, the duration of DC is 5 minutes in order to ensure sufficient spreading of Ga-In-Sn alloy on Cu substrate. Effect of positive DC on the wetting behavior of liquid drop of Ga-In-Sn alloy on Cu substrate is depicted in Figures 3(e)–3(h), while the corresponding results under the condition of a negative DC are shown in Figures 3(i)–3(l). The wettability is still poor when DC is applied regardless of current polarity. However, the application of DC of +6 A deforms the drop shape compared with that without DC, and there is no increase in the deformation of drop when current intensity increases to +11 A, as shown in Figure 3(h). Similar deformation of drop is obtained upon DC reversal (Figure 3(l)).

Since wettability is usually characterized by contact angle of liquid on solid surface in three-phase equilibrium, contact angle measurements are necessary to profoundly understand effect of DC on the wettability of Cu substrate by Ga-In-Sn alloy melt. The plot of contact angle as a function of current intensity at room temperature is shown in Figure 4. As a result, DC reduces the contact angle regardless of current polarity. The decrease of contact angle with increasing current

intensity is approximately linear when the applied DC is not more than 6 A in current intensity, and there is a critical value for current intensity, above which contact angle remains almost constant. Moreover, current polarity seems to have no significant effect on contact angle.

According to Young's equation (1), the contact angle of liquid drop on solid surface is determined by the force balance between the interfacial tensions at the solid-liquid-gas interface:

$$\gamma_{lg} \cos \theta = \gamma_{sg} - \gamma_{sl}, \quad (1)$$

where  $\theta$  is the Young contact angle,  $\gamma_{lg}$  is the liquid-gas surface tension,  $\gamma_{sg}$  is the solid-gas surface tension, and  $\gamma_{sl}$  is the solid-liquid interfacial tension. It should be pointed out that (1) is only applicable to thermodynamically meaningful contact angles [18]. In that case, it suggests that the observed decrease in contact angles is a manifestation of the effect of DC on interfacial tensions. It is very probable that the solid-gas surface tension is unaffected by DC due to the lack of mobility of atom of the solid. Therefore, it is believed that the observed decrease in contact angles is a consequence of a change in liquid-gas and solid-liquid interfacial tensions.

Taking the solid-gas surface tension as a constant, effect of DC on contact angle can be translated into the corresponding effects in terms of the liquid-gas and solid-liquid interfacial tensions using the equation of state [19]:

$$\begin{aligned} \gamma_{lg} &= \frac{2\gamma_{sg}}{\left(\sqrt{1+\sin^2\theta} + \cos\theta\right)}, \\ \gamma_{sl} &= \frac{\gamma_{sg}\left(\sqrt{1+\sin^2\theta} - \cos\theta\right)}{\left(\sqrt{1+\sin^2\theta} + \cos\theta\right)}. \end{aligned} \quad (2)$$

Equation (2) describes the dependence of liquid-gas and solid-liquid interfacial tensions on contact angle, respectively. They can be employed to qualitatively estimate the change of liquid-gas and solid-liquid interfacial tensions under DC compared with those without DC. Figure 5 shows variation of the calculated solid-liquid and liquid-gas interfacial tensions ratio with current intensity and polarity. Obviously, with increasing current density, the ratio of calculated solid-liquid interfacial tension ( $\gamma_{sl}^e$ ) under DC to that ( $\gamma_{sl0}$ ) in the absence of DC decreases at first and tends to a constant when

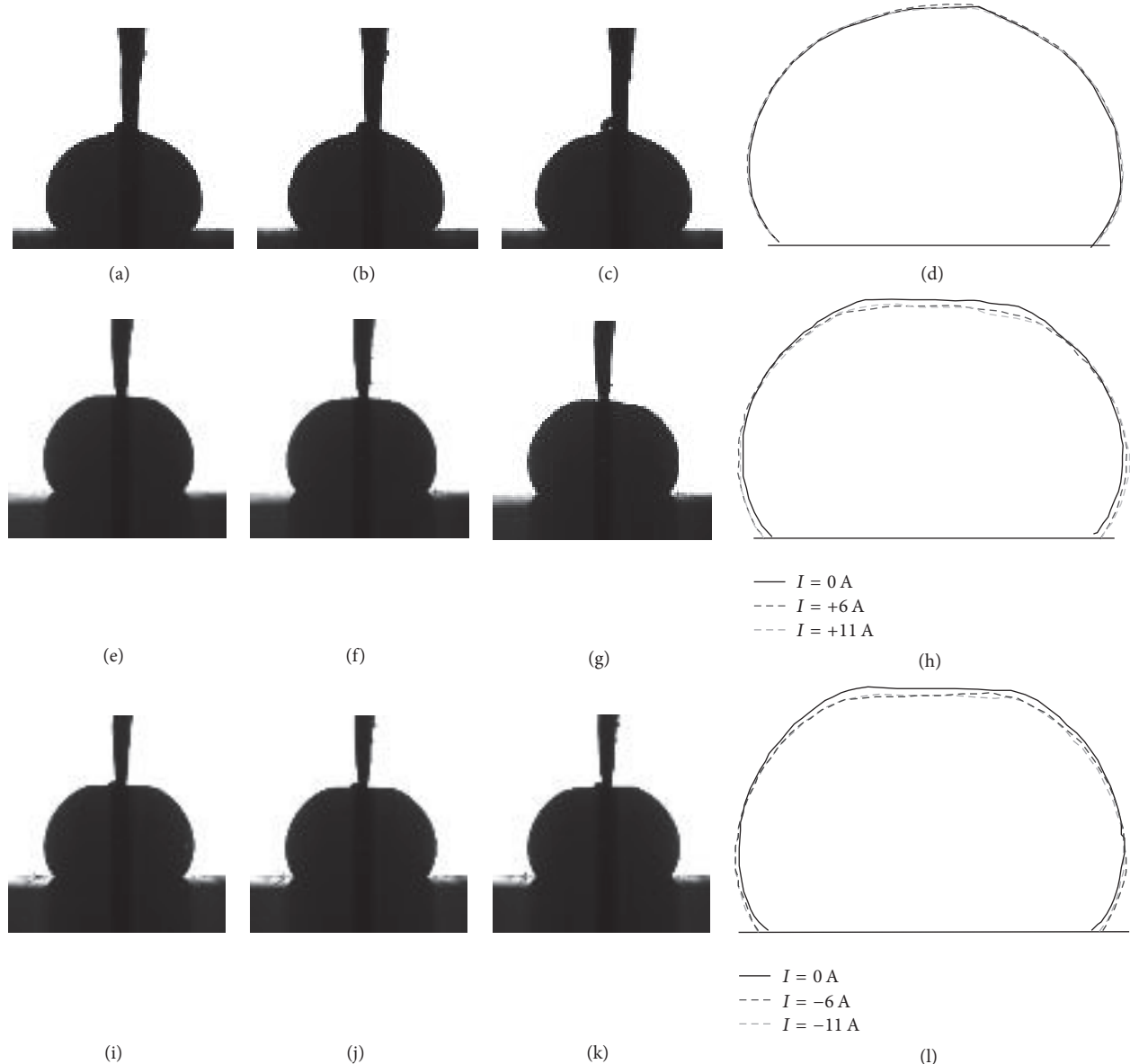


FIGURE 3: Typical liquid Ga-In-Sn drop shapes on Cu substrate under different conditions. Without DC after different standing time of (a) 5 min, (b) 35 min, and (c) 65 min, the three aforementioned drop shapes are amplified and overlapped in Figure (d). With positive DC (e) 0 A, (f) 6 A, and (g) 11 A, the three aforementioned drop shapes are amplified and overlapped in Figure (h). With negative DC (i) 0 A, (j) 6 A, and (k) 11 A, the three aforementioned drop shapes are amplified and overlapped in Figure (l).

current intensity exceeds 6 A regardless of current polarity (Figure 5(a)). Similar tendency is observed for the ratio of calculated liquid-gas interfacial tension ( $\gamma_{lg}^e$ ) under DC to that ( $\gamma_{lg0}$ ) in the absence of DC. It indicates that the observed change in contact angle is a consequence of the decrease in the liquid-gas and solid-liquid interfacial tensions.

Since the measurement of contact angle is performed using a DC-coupled sessile drop method at room temperature, the mass transfer and interfacial action at the triple-phase region are negligible. In this case, Young's equation and its extended formulas are applicable to determinate liquid-gas and solid-liquid interfacial tensions from contact angle in the present study. As indicated above, the observed decrease in

contact angle results from the decrease of liquid interfacial tensions. The potential mechanism causing the above change in liquid interfacial tensions refers to a series of current effects such as Joule heating, electromigration, electric potential energy, and convection caused by Lorentz force. Therefore, the contributions of these effects to liquid interfacial tensions should be seriously considered.

When electric current passes through a conductor, Gibbs free energy increases by adding an extra term ( $\delta G_e$ ) at the same temperature [20, 21]. It is speculated that solute atoms in alloys will be excited to a higher energy state under DC and affect the solute diffusion process. An explanation to the influence of DC on the diffusion activation energy ( $Q$ ) of

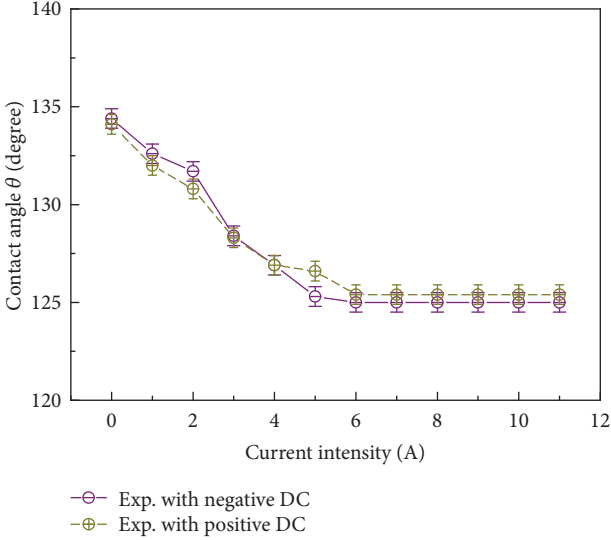


FIGURE 4: Contact angle versus current intensity and polarity.

solute is schematically illustrated in Figure 6(a). Generally, the diffusion activation energy, sometimes called the diffusion barrier, is defined as the minimum energy required to start atom migration. Position 1 and position 2 represent the initial location and target location of atom migration, respectively. In the absence of DC, the diffusion barrier ( $\Delta G$ ) is given by  $\Delta G = G_2 - G_1$ . The diffusion barrier ( $\Delta G_e$ ) decreases under DC due to the contribution of an extra term ( $\delta G_e$ ). It suggests that DC reduces the diffusion activation energy of solute and then increases its diffusion coefficient ( $D$ ) at the same temperature in terms of the relationship between  $D$ ,  $Q$ , and absolute temperature ( $T$ ) [22]. Similarly, Zhao and coworkers have found that the calculated diffusion coefficient for solid Ni in liquid Al increases with increasing current density under DC and approaches a relatively stable value at a certain critical current density, regardless of current polarity [23]. It is concluded that DC plays an important role in promoting the diffusion process of metal atoms.

Additionally, it should be noted that the physical parameters of liquid alloys, liquid-gas interfacial tension ( $\gamma_{lg0}$ ), viscosity ( $\eta$ ), and solute diffusion coefficient ( $D$ ) are intensively correlative. Therefore, the relationship between  $\gamma_{lg0}$ ,  $\eta$ , and  $D$  can be given with some empirical models [22]:

$$\eta = \frac{16}{15} \sqrt{\frac{M}{kT}} \cdot \gamma_{lg0}, \quad (3)$$

$$D = \frac{kT}{6\pi r\eta},$$

where  $M$  is the absolute atomic mass,  $k$  is the Boltzmann constant, and  $r$  is the characteristic radius of solute atom. According to (3), the liquid-gas interfacial tension is inversely proportional to the solute diffusion coefficient, implying that the DC-induced promotion of solute diffusion coefficient obviously decreases the liquid-gas interfacial tension of liquid Ga-In-Sn alloy regardless of current polarity, which is in agreement with the calculated results. As indicated above,

the changing trends for solid-liquid and liquid-gas interfacial tensions are similar regarding current intensity dependence. Thus, it is likely that the reduction of diffusion activation energy is the main factor for the reduction in contact angle and solid-liquid interfacial tension under DC.

Since previous studies have proved that Joule heating, electromigration, and convection caused by Lorentz force play significant roles in determining the dissolution wetting process of molten metal on solid substrate at higher temperature [15, 16], it is worth studying how to affect the wettability of Cu by liquid Ga-In-Sn alloy and its related solid-liquid interfacial tension at room temperature by the above-mentioned current effects. Here, current density as an important parameter in assessing current effects is essential to be determined and its average values are estimated as  $10\text{--}110 \text{ A cm}^{-2}$  in our experiment. In prior work it was observed that effect of Joule heating effect on temperature was negligible for Sn-Bi alloy under DC of  $50 \text{ A cm}^{-2}$ . The change of temperature ( $\Delta T$ ) under DC is proportional to current density squared ( $j^2$ ) and electrical resistivity of materials ( $\rho_e$ , approximately  $7.0 \times 10^{-7} \Omega \cdot \text{m}$  for Sn-Bi alloy at 500 K [24] and  $2.9 \times 10^{-7} \Omega \cdot \text{m}$  for Ga-In-Sn alloy at room temperature [25]) [26]. As a consequence, the obvious change of temperature occurs only when current density exceeds about  $120 \text{ A cm}^{-2}$  in this study. Thus, effect of Joule heating in liquid drop on the wettability should be negligible with the present DC range of  $1\text{--}11 \text{ A}$ . Generally, current densities of the order of  $10^2 \text{ A cm}^{-2}$  are required to produce a substantial electromigration, which enhances with increasing current density [12]. Composition fluctuation at the solid-liquid interface as the direct expression of electromigration [4] will affect the solid-liquid interfacial tension and depends on current polarity. Therefore, the difference of the solid-liquid interfacial tension occurs upon DC reversal and increases with increasing current density, which is inconsistent with our experimental results. It suggests that the contribution of electromigration is not expected to be significant to decrease the solid-liquid interfacial tension. As has been reported before, Lorentz force caused by the interaction between the applied DC and its own induced magnetic field gives rise to significant convection in liquid phase [23]. In our case, flow field in the drop, which is similar to that reported in [27], provides a driving force for composition homogenization and weakens composition fluctuation at the solid-liquid interface due to electromigration. According to drop shape, the liquid near the upper electrode has a higher current density, which is estimated as  $40\text{--}440 \text{ A cm}^{-2}$ . It implies that temperature gradient as a result of differences in Joule heating associated with differences in cross-sectional area of drop should be considered when current intensity of the applied DC exceeds  $3 \text{ A}$ , which can lead to Marangoni convection in drop, as schematically shown in Figure 6(b). Note that there is no significant difference between the direction of Marangoni convection and that of convection induced by Lorentz force. Marangoni convection also plays a role in restraining composition fluctuation at the solid-liquid interface. Suppression of electromigration by convection explains the fact that there is no distinction in the wettability upon DC reversal.

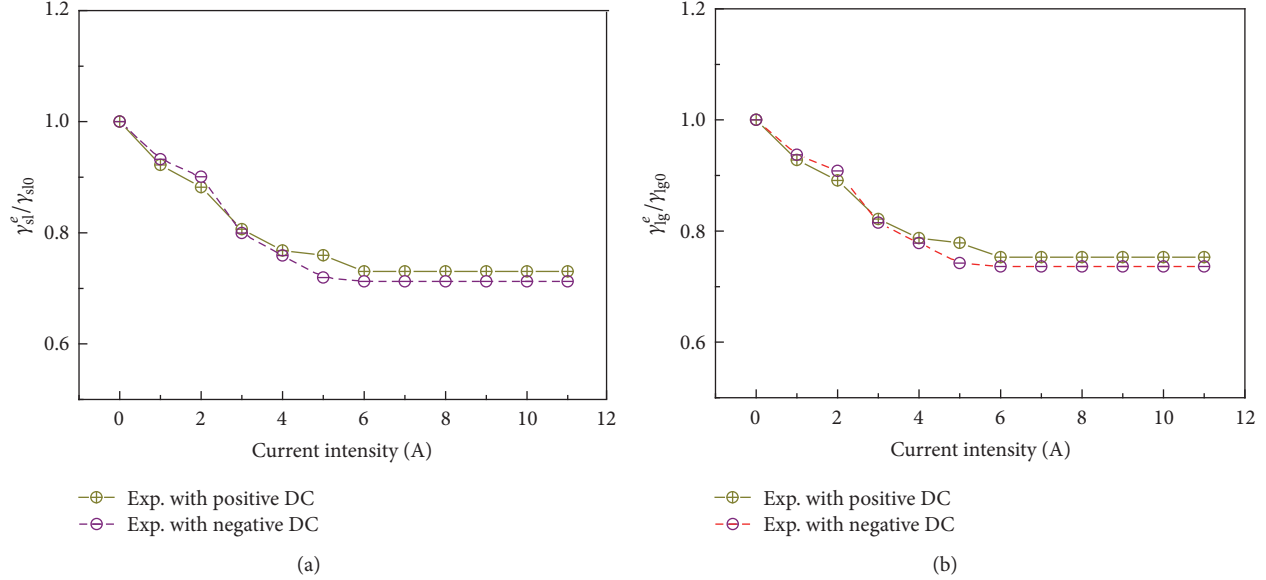


FIGURE 5: (a) Variation of solid-liquid interfacial tension ratio ( $\gamma_{sl}^e/\gamma_{sl0}$ ) with current intensity and polarity. (b) Variation of liquid-gas surface tension ( $\gamma_{lg}^e/\gamma_{lg0}$ ) with current intensity and polarity.

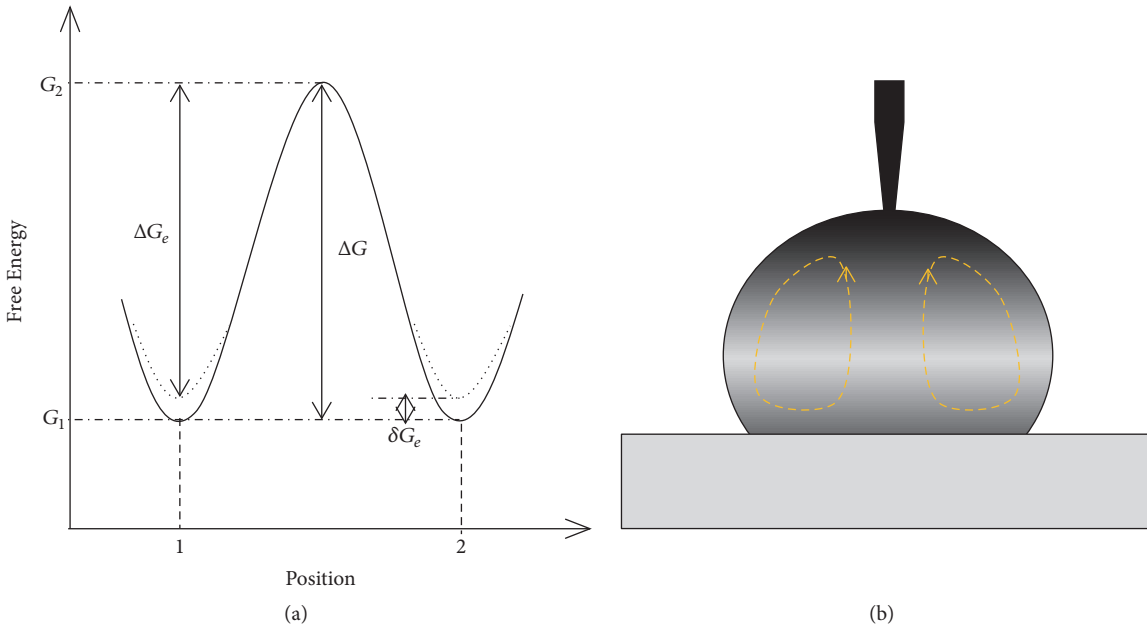


FIGURE 6: (a) Schematic explanation for the effect of DC on the diffusion activation energy. (b) Schematic of Marangoni convection in the Ga-In-Sn/Cu system under DC.

#### 4. Conclusions

We have investigated the wetting behavior of Ga-In-Sn alloy melt on Cu substrate and solid-liquid interfacial tension under DC at room temperature. The application of DC has a pronounced effect on the wettability. There is a critical value for current intensity, below which the steady-state contact angle decreases with increasing current intensity and above which contact angle remains almost constant. In addition, the direction of DC does not play a role in the

observed effects under the same current intensity. Using the equation of state that describes the dependence of solid-liquid interfacial tension on contact angle, the change of solid-liquid interfacial tension under DC can be qualitatively determined. The application of DC leads to significant reduction of solid-liquid interfacial tension. It is speculated that the reduction of contact angle and its corresponding solid-liquid interfacial tension is mainly attributed to the promotion of solute diffusion coefficient under DC. Moreover, Joule heating, Marangoni convection induced by nonuniform distribution

of temperature field, electromigration, and convection caused by Lorentz force do not have a noticeable effect.

## Conflicts of Interest

The authors declare that there are no conflicts of interest regarding the publication of this paper.

## Acknowledgments

This work is supported by the National Natural Science Foundation of China (Grant nos. 51704242 and 51701160), the Young Scholars Program of Shandong University (Weihai), and the NPU Foundation for Fundamental Research in China (JC201272).

## References

- [1] T. Wang, J. Xu, T. Xiao et al., "Evolution of dendrite morphology of a binary alloy under an applied electric current: An in situ observation," *Physical Review E: Statistical, Nonlinear, and Soft Matter Physics*, vol. 81, no. 4, Article ID 042601, 2010.
- [2] S. R. Coriell, G. B. McFadden, A. A. Wheeler, and D. T. J. Hurle, "The effect of an electric field on the morphological stability of the crystal-melt interface of a binary alloy. II. Joule heating and thermoelectric effects," *Journal of Crystal Growth*, vol. 94, no. 2, pp. 334–346, 1989.
- [3] M. Nakada, Y. Shiohara, and M. C. Flemings, "Modification of Solidification Structures by Pulse Electric Discharging," *ISIJ International*, vol. 30, no. 1, pp. 27–33, 1990.
- [4] L. Zhang, N. Li, R. Zhang et al., "Effect of Direct Current on Microstructure Evolution of Directionally Solidified Sn-70 wt pct Bi Alloy at Different Pulling Rates," *Metallurgical and Materials Transactions A: Physical Metallurgy and Materials Science*, vol. 46, no. 9, pp. 4174–4182, 2015.
- [5] X. Liao, Q. Zhai, J. Luo, W. Chen, and Y. Gong, "Refining mechanism of the electric current pulse on the solidification structure of pure aluminum," *Acta Materialia*, vol. 55, no. 9, pp. 3103–3109, 2007.
- [6] D. Räßiger, Y. Zhang, V. Galindo, S. Franke, B. Willers, and S. Eckert, "The relevance of melt convection to grain refinement in Al-Si alloys solidified under the impact of electric currents," *Acta Materialia*, vol. 79, pp. 327–338, 2014.
- [7] H. Conrad, "Influence of an electric or magnetic field on the liquid-solid transformation in materials and on the microstructure of the solid," *Materials Science and Engineering: A Structural Materials: Properties, Microstructure and Processing*, vol. 287, no. 2, pp. 205–212, 2000.
- [8] X. F. Zhang, W. J. Lu, and R. S. Qin, "Removal of MnS inclusions in molten steel using electropulsing," *Scripta Materialia*, vol. 69, no. 6, pp. 453–456, 2013.
- [9] L. Jianming, L. Shengli, L. Jin, and L. Hantong, "Modification of solidification structure by pulse electric discharging," *Scripta Materialia*, vol. 31, no. 12, pp. 1691–1694, 1994.
- [10] J. Zhu, T. Wang, F. Cao, W. Huang, H. Fu, and Z. Chen, "Real time observation of equiaxed growth of Sn-Pb alloy under an applied direct current by synchrotron microradiography," *Materials Letters*, vol. 89, pp. 137–139, 2012.
- [11] C. Song, Y. Guo, Y. Zhang et al., "Effect of currents on the microstructure of directionally solidified Al4.5 wt% Cu alloy," *Journal of Crystal Growth*, vol. 324, no. 1, pp. 235–242, 2011.
- [12] L. Zhang, N. Li, H. Xing et al., "Microstructure evolution of directionally solidified Sn-Bi alloy under different medium-density direct current," *Journal of Crystal Growth*, vol. 430, pp. 80–86, 2015.
- [13] L. Zhang, H. Liu, N. Li et al., "The relevance of forced melt flow to grain refinement in pure aluminum under a low-frequency alternating current pulse," *Journal of Materials Research*, vol. 31, no. 3, pp. 396–404, 2016.
- [14] K. Mondal and B. S. Murty, "On the prediction of solid-liquid interfacial energy of glass forming liquids from homogeneous nucleation theory," *Materials Science and Engineering: A Structural Materials: Properties, Microstructure and Processing*, vol. 454–455, pp. 654–661, 2007.
- [15] Q.-G. Xu, X.-B. Liu, and H.-F. Zhang, "Effect of direct electric current on wetting behavior of molten Bi on Cu substrate," *Transactions of Nonferrous Metals Society of China*, vol. 20, no. 8, pp. 1452–1457, 2010.
- [16] Y. Gu, P. Shen, N.-N. Yang, and K.-Z. Cao, "Effects of direct current on the wetting behavior and interfacial morphology between molten Sn and Cu substrate," *Journal of Alloys and Compounds*, vol. 586, pp. 80–86, 2014.
- [17] P. Shen, Y. Gu, N.-N. Yang, R.-P. Zheng, and L.-H. Ren, "Influences of electric current on the wettability and interfacial microstructure in Sn/Fe system," *Applied Surface Science*, vol. 328, pp. 380–386, 2015.
- [18] D. Y. Kwok and A. W. Neumann, "Contact angle measurement and contact angle interpretation," *Advances in Colloid and Interface Science*, vol. 81, no. 3, pp. 167–249, 1999.
- [19] D. Y. Zhu, P. Q. Pin, X. B. Luo et al., "Novel characterization of wetting properties and the calculation of liquid–solid interface tension (I)," *Science Technology and Engineering*, vol. 7, no. 13, pp. 3057–3062, 2007.
- [20] R. S. Qin, E. I. Samuel, and A. Bhowmik, "Electropulse-induced cementite nanoparticle formation in deformed pearlitic steels," *Journal of Materials Science*, vol. 46, no. 9, pp. 2838–2842, 2011.
- [21] X. L. Wang, J. D. Guo, Y. M. Wang, X. Y. Wu, and B. Q. Wang, "Segregation of lead in Cu-Zn alloy under electric current pulses," *Applied Physics Letters*, vol. 89, no. 6, Article ID 061910, 2006.
- [22] I. Egry, "On the relation between surface tension and viscosity for liquid metals," *Scripta Materialia*, vol. 28, no. 10, pp. 1273–1276, 1993.
- [23] J. F. Zhao, C. Unuvar, U. Anselmi-Tamburini, and Z. A. Munir, "Kinetics of current-enhanced dissolution of nickel in liquid aluminum," *Acta Materialia*, vol. 55, no. 16, pp. 5592–5600, 2007.
- [24] X.-F. Li, F.-Q. Zu, H.-F. Ding, J. Yu, L.-J. Liu, and Y. Xi, "High-temperature liquid-liquid structure transition in liquid Sn-Bi alloys: Experimental evidence by electrical resistivity method," *Physics Letters A*, vol. 354, no. 4, pp. 325–329, 2006.
- [25] Y. Plevachuk, V. Sklyarchuk, S. Eckert, G. Gerbeth, and R. Novakovic, "Thermophysical properties of the liquid Ga-In-Sn eutectic alloy," *Journal of Chemical & Engineering Data*, vol. 59, no. 3, pp. 757–763, 2014.
- [26] L. M. Zhang, N. Li, R. Zhang, H. Xing, K. Song, and J. Y. Wang, "Effect of medium-density direct current on dendrites of directionally solidified Pb–50Sn alloy," *Materials Science and Technology (United Kingdom)*, vol. 32, no. 18, pp. 1877–1885, 2016.
- [27] P. A. Nikrityuk, K. Eckert, R. Grundmann, and Y. S. Yang, "An impact of a low voltage steady electrical current on the solidification of a binary metal alloy: A numerical study," *Steel Research International*, vol. 78, no. 5, pp. 402–408, 2007.

## Research Article

# Anomalous Reflection of Acoustic Waves in Air with Metasurfaces at Low Frequency

Huaijun Chen 

College of Physics and Electronic Information Engineering, Engineering Research Center of Nanostructure and Functional Materials, Ningxia Normal University, Guyuan 756000, China

Correspondence should be addressed to Huaijun Chen; chenhuaijun79@163.com

Received 30 October 2017; Accepted 24 December 2017; Published 31 January 2018

Academic Editor: Yuri Tarasevich

Copyright © 2018 Huaijun Chen. This is an open access article distributed under the Creative Commons Attribution License, which permits unrestricted use, distribution, and reproduction in any medium, provided the original work is properly cited.

An acoustic metasurface made of a composite structure of cavity and membrane is proposed and numerically investigated. The target frequency is in the low frequency regime (570 Hz). The unit cells, which provide precise local phase modulation, are rather thin with thickness in the order around 1/5 of the working wavelength. The numerical simulations show that the designed metasurface can steer the reflected waves at will. By taking the advantage of this metasurface, an ultrathin planar acoustic axicon, acoustic lens, and acoustic nondiffracting Airy beam generator are realized. Our design method provides a new approach for the revolution of future acoustic devices.

## 1. Introduction

The rising acoustic metamaterials, whose structures are on a subwavelength scale, exhibit many novel properties that can not be realized by natural materials in controlling sound waves, such as negative mass density, negative modulus, and double-negative parameters [1–10]. Liu et al. embedded rubber-coated lead spheres into epoxy matrix and first realized a metamaterial with negative effective mass density [1]. Fang et al. designed an array of subwavelength Helmholtz resonators and first realized negative effective modulus [2]. However, these metamaterials are all bulk materials and much larger than the working wavelength, which is to the disadvantage of the miniaturization and integration of acoustic devices. Yang et al. designed a kind of metamaterial based on elastic membrane, which effectively reduced the size of metamaterials [11]. In recent years, a new type of metamaterial, namely, metasurface [12, 13], attracted the attention of researchers. Metasurface is an artificial lamellar structure composed of units with subwavelength thickness. By arranging the units in a particular way, the metasurface can modulate the direction of scattered waves at will. With this prominent advantage, the metasurface will lead to the revolution of many traditional devices. In the field of optics,

the metasurfaces have developed to realize many remarkable functions, such as light beam steering [14], ultrathin optical skin cloak [15], and holograms [16]. As the wavelengths of sound waves are much larger than that of light wave, the acoustic metasurfaces [17–24] are especially important for acoustic devices. Faure et al. realized an acoustic carpet cloaking by using a metasurface made of graded Helmholtz resonators [18]. Li et al. designed coiled space elements and realized a two-dimensional ultrathin acoustic metamaterial to support the extraordinary acoustic transmission [25]. Zhu et al. designed a subwavelength corrugated surface to control the acoustic wavefront arbitrarily without bandwidth limitation [26]. Esfahlani et al. designed a space-coiled cylindrical unit and generated acoustic vortices based on this passive acoustic metasurface [27]. Zhai et al. [24] and Esfahlani et al. [28], respectively, proposed an acoustic meta-surface carpet cloak based on membrane-capped cavities. However, the proposed metasurfaces still face the limits of complicated structures, large dimensions, and high working frequencies. Here, considering these factors, we presented a low frequency (570 Hz) ultrathin acoustic metasurface by using the composite structure of cavity and membrane. This kind of metasurface is capable of arbitrarily steering the reflected waves. Based on this metasurface, we designed some

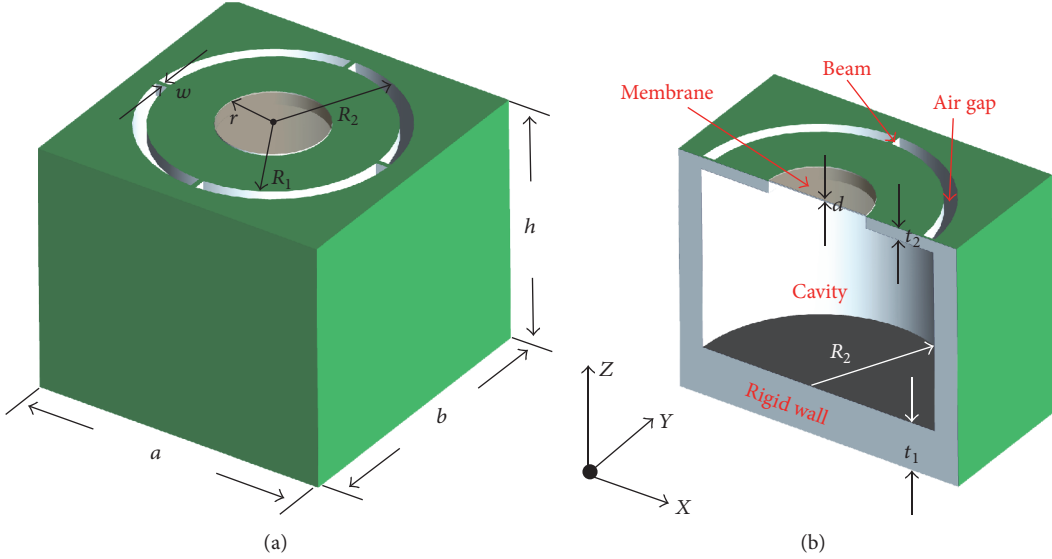


FIGURE 1: (a) Schematic map of acoustic metasurface unit cell and (b) longitudinal section of the unit cell. The unit cell is composed of a cavity with acoustically hard walls, which is capped with a rigid circular ring. The inside of the ring is a clamped membrane, and the outside is an air gap.

ultrathin acoustic planar devices, such as planar acoustic axicon, acoustic lens, and acoustic nondiffracting Airy beam generator. Our design method provides a new approach for the revolution of future acoustic devices.

## 2. Design of the Model

Figure 1(a) shows the schematic of unit for the planar acoustic metasurface. The unit is a cube (i.e.,  $a = b = h = 120$  mm) with a cylindrical cavity in it. The cavity is filled with air. Figure 1(b) displays the sectional view of the unit. The gray area indicates rigid wall that is opaque to sound waves. The thickness of the bottom wall is  $t_1 = 15$  mm. The radius  $R_2$  and height of the cavity are 50 mm and 100 mm, respectively. An annular lid whose inner circle is sealed by an elastic membrane is put on the top of the cavity. The thickness  $t_2$  and outer radius  $R_1$  of the lid are 5 mm and 45 mm, respectively. The edge of the tensioned membrane is fixed on the side wall. The radius of the membrane is  $r$ , while the thickness is  $d = 0.04$  mm. There are four beams connecting the lid and the cavity, which produces an annular air gap. The width of the beam is  $w = 2$  mm, which can be ignored comparing to the operating wavelength. The radial width of the gap is  $R_2 - R_1 = 5$  mm.

When there is no incident sound wave, the elastic membrane will be tensioned to be a straight line; however, when there are incident waves along the  $-z$  direction, the impinging of sound beams on the membrane will lead to forced vibration and deformation of the membrane. At the same time, the compression and expansion of the air in the cavity will result in the air in and out of the cavity through the gap, which greatly reduces the thermal loss of the sound energy. The vibration displacement of the membrane has delay compared

with the local velocity of air particles [29]. Compared with the propagation in complete air medium with the same length, there exists substantial phase delay as sound waves travel through the subunit, which shows promise for the altering of reflected phase in space. Thus, the reflected phase of the sound wave will be shifted compared with the incident phase. Previous works have demonstrated that physical parameters of the material (i.e., the mass density, Young's modulus, and Poisson's ratio), the geometric dimensions of the unit, and the working frequency all have influences on the sound behavior of the unit, including reflected ratio and phase [30–32]. In the present study, in order to guarantee the unitary subwavelength thickness of entire metasurface and for the simplicity of design, the thicknesses of the unit and the membrane are fixed. The only variable in this paper is the radius of the membrane  $r$ . Our following simulations will demonstrate that, by appropriately choosing  $r$ , eight units are enough to provide discrete reflected phases change ranging from 0 to  $2\pi$  with an interval of  $\pi/4$  between the adjacent units. The commercial software COMSOL 5.2a was employed to calculate the field distribution of reflected sound wave. The chosen medium in the simulation is air. The sound speed and mass density of air are 343 m/s and  $1.21 \text{ kg/m}^3$ , individually. The mass density, Young's modulus, and Poisson's ratio of the membrane are  $920 \text{ kg/m}^3$ ,  $9.6 \times 10^9 \text{ Pa}$ , and 0.36, individually, so that traditional polyethylene can be suitable for the practical fabrication of this membrane. Based on [30], the damping factor of the membrane material is set to be 0.01. The side walls were chosen to be aluminum and modeled as acoustically rigid. When we studied the reflected phase of unit with specific membrane radius, the simulation was individually performed for each unit. Under this circumstance, the periodic boundary condition is applied along  $x$ -axis direction to eliminate the boundary effects. In

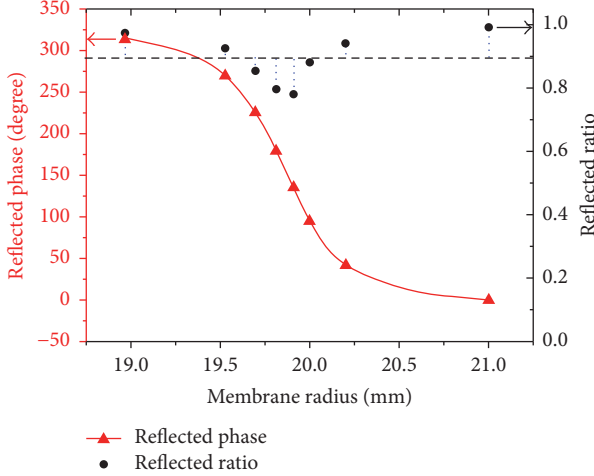


FIGURE 2: Reflected phases and ratios of the eight subunits as a function of  $r$ . The wavelength  $\lambda$  of the incident wave is 600 mm. The red triangles and black dots refer to discrete phases and ratios of eight subunits having specific membrane radius (i.e., 18.97, 19.53, 19.70, 19.81, 19.91, 20.00, 20.20, and 21.00 mm, respectively). The phase shift between two adjacent subunits is  $45^\circ$ . The mean reflected ratio is 0.89, as shown by the dashed line.

addition, the plane wave radiation boundary condition was applied for the incident plane wave propagating along the negative direction of  $z$ -axis.

The relation between the simulated reflected phase of the unit and the membrane radius is shown with the red curve in Figure 2. We can see that the designed units are able to realize  $2\pi$  phase change, when the membrane radius varies from 18.97 mm to 21.00 mm. In this paper, we choose eight units to provide discrete  $2\pi$  phase shifts with an interval of  $\pi/4$  between the adjacent subunits, denoted by the red triangles. In addition, we also obtained the reflected ratios of these eight units, as shown with the black dots in Figure 2. Based on [24], the reflected ratio of the metamaterial with membrane is also low at the resonant frequency, but the reflected ratio will be very high once the frequency is away from the resonant frequency. Therefore, the resonant frequencies of the structural units in this work are not at the designed working frequency (i.e., 570 Hz). Thus, it can be guaranteed not to have very low reflectivity, but also to provide sufficient phase delay. The dashed line represents the mean reflected ratio with the value of 0.89, which demonstrates that these units are suitable for assembling metasurfaces with high efficiency.

### 3. Abnormal Reflection of the Metasurface

The generalized Snell's law (GSL) was introduced to predict the anomalous propagation of incident wave across material interfaces characterized by a phase gradient [14, 20, 33, 34], which is suitable for both reflected wave and transmitted wave. The metasurfaces proposed in this study are also built based on GSL. According to the GSL, the direction of anomalous reflection is related to the direction of the incident

planar wave front and the phase gradient at the interface between the metasurface and air. The formula is as follows:

$$\sin \theta_r - \sin \theta_i = \frac{1}{k_0} \frac{d\phi}{dx}, \quad (1)$$

where  $\theta_i$  and  $\theta_r$  are the incident and reflected angles, respectively.  $k_0 = 2\pi/\lambda_0$  is the wave vector in air, while  $d\phi$  and  $dx$  are the phase and distance gradients along the  $x$ -direction separately. Equation (1) implies that the reflected beam can have an arbitrary direction, provided that a suitable phase gradient is produced along the interface of metasurface. In order to verify the validity of our model about the anomalous reflection, numerical simulations of the constructed metasurfaces were conducted for different distance gradients. Here, the incident angle was kept to be  $0^\circ$ . Figure 3 shows the simulated reflected fields of the designed metasurface with different unit spaces (i.e., 120 mm, 130 mm, 140 mm, 150 mm, 160 mm, 170 mm, and 180 mm, respectively). The corresponding  $d\phi/dx$  are 6.54 rad/m, 6.04 rad/m, 5.61 rad/m, 5.23 rad/m, 4.91 rad/m, 4.62 rad/m, and 4.36 rad/m, separately. The reflected angles are  $36^\circ$ ,  $34^\circ$ ,  $31^\circ$ ,  $29^\circ$ ,  $27^\circ$ ,  $25^\circ$ ,  $24^\circ$ , and  $22^\circ$ , respectively, while the theoretical reflected angles derived based on (1) should be  $35.93^\circ$ ,  $33.17^\circ$ ,  $30.80^\circ$ ,  $28.75^\circ$ ,  $26.95^\circ$ ,  $25.36^\circ$ ,  $23.96^\circ$ , and  $22.69^\circ$ , respectively. Good agreements can be found between the simulated results and the calculated results. Although these eight units possessing strict  $\pi/4$  phase shifts are designed for the working frequency of 570 Hz, based on [24] we can know that the shifts between adjacent units still maintain approximately  $\pi/4$  even when the frequency changes near the working frequency. Therefore, the phenomenon of abnormal reflection can still be found, but the effect of abnormal reflection may slightly decline in quality. It is worth pointing out that, except a strong reflection on the main direction, we can also find a weak reflection on the other direction. This phenomenon is caused by the phase shifts of the whole metasurface as a 1D phononic crystal [35].

### 4. Applications of the Metasurface

When acoustic waves impinge on a metasurface, the distribution of scattered pressure field follows generalized Snell's law. However, if we apply a slight modification to the metasurface, such as changing the phase gradients of different parts on it, the scattered field will be modulated to specific distribution. In the following, we show different wave manipulation effects by exploiting the proposed acoustic metasurfaces based on different combinations of fundamental units. In particular, we will show three mechanisms that could promote the development of future ultracompact acoustic devices, including an ultrathin planar acoustic axicon, an ultrathin planar lens, and a nondiffracting Airy beam [36, 37].

**4.1. Design of a Planar Acoustic Axicon.** In order to design the acoustic axicon, the reflected angle of sound wave is set to be  $10^\circ$ , which is symmetrical along  $z$ -axis. When the sound wave perpendicularly impinges on the surface, the phase gradient

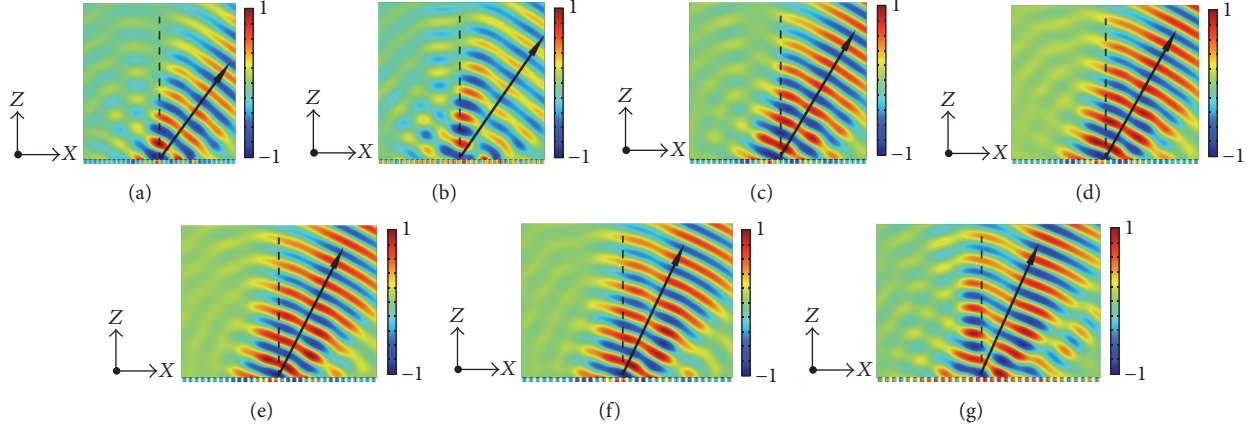


FIGURE 3: Simulated snapshots of pressure map for the reflected beams of the metasurfaces with seven different unit spaces ((a)~(g) correspond to 120, 130, 140, 150, 160, 170, and 180 mm, respectively). The metasurfaces are located on the  $x$ -axis. The incident waves with a Gaussian beam propagate along the negative direction of  $z$ -axis. The amplitudes of the acoustic pressures are normalized. The reflected angle changes with the unit space.

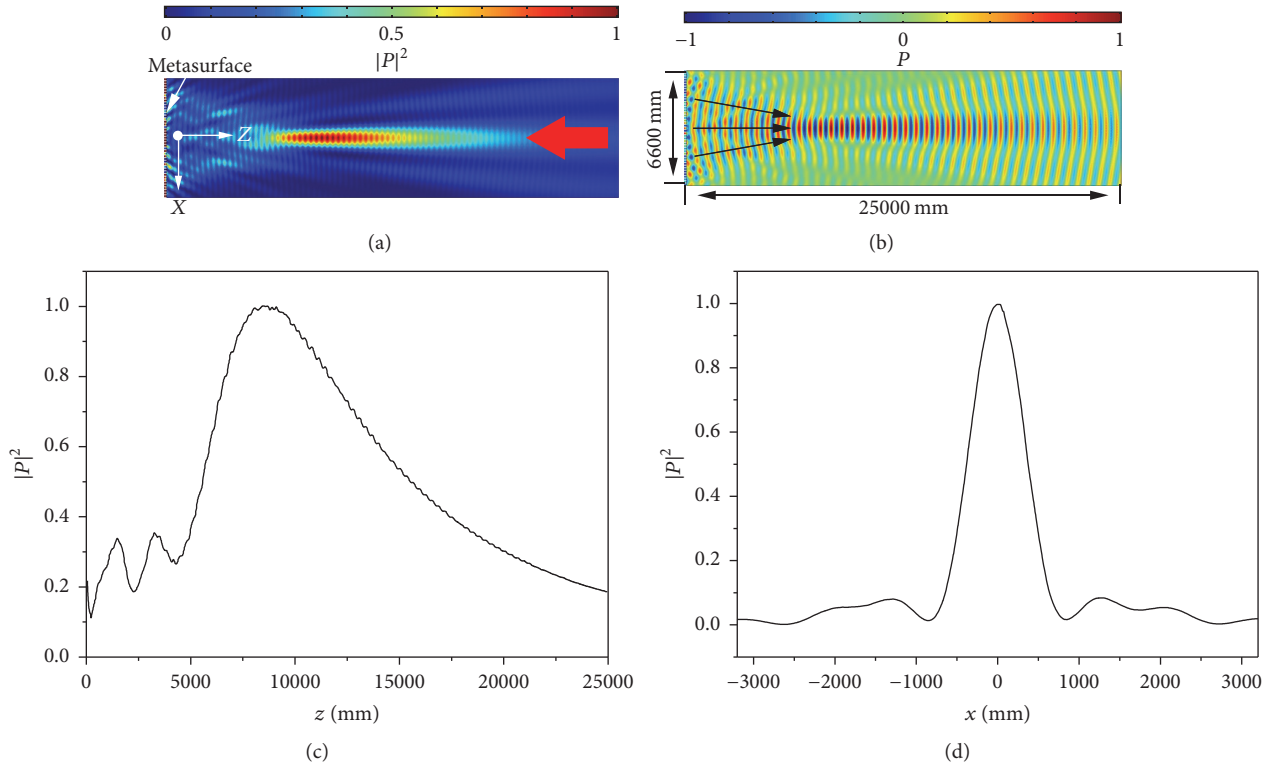


FIGURE 4: Acoustic axicon realized by the designed planar metasurface. (a) The normalized squared absolute pressure distribution of the reflected waves. The red arrow indicates the propagation direction of incident wave. (b) Transient sound pressure field distribution of reflected wave. The black arrows refer to the reflected directions. The angle between equiphase surface and  $x$ -axis is  $10^\circ$ . (c) The longitudinal distribution of acoustic intensity at  $x = 0$ . (d) The transverse distribution of acoustic intensity at  $z = 8500$  mm.

of the metasurface along  $x$ -axis should satisfy the following equation:

$$\left| \frac{d\phi}{dx} \right| = k_0 \sin 10^\circ. \quad (2)$$

Based on (2), the planar acoustic axicon is readily constructed by symmetrically arranging the units along the

positive and negative directions of  $x$ -axis, respectively. 43 units were employed to build this planar axicon, of which the whole size is  $x \times z = 6600 \times 120$  mm. The reflection behavior of this axicon was simulated using COMSOL. Figures 4(a) and 4(b) exhibit the patterns of normalized squared absolute pressure and transient pressure field of transmitted sound waves, respectively. The red arrow indicates the incident

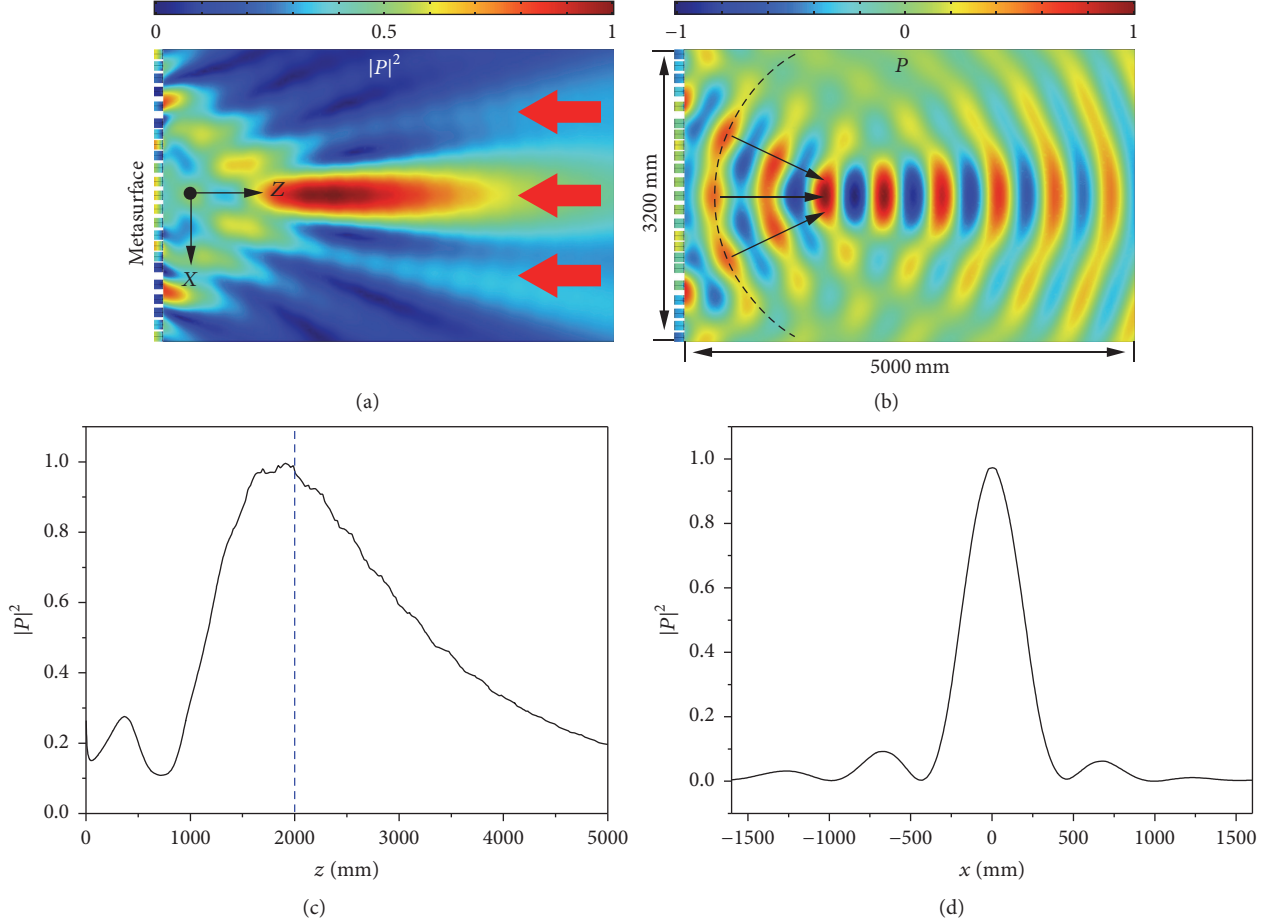


FIGURE 5: Planar acoustic lens. (a) The squared absolute pressure field of reflected waves. The red arrows represent the propagation direction of incident plane wave. (b) The transient pressure field distribution of reflected waves. The black dashed arc indicates the shape of reflected wavefront. (c) The longitudinal sound intensity distribution at  $x = 0$ . (d) The transverse distribution of intensity at  $z = 2000$  mm.

waves. In Figure 4(a), a high-intensity focal needle can be found to form a striking contrast with ambient quiet field. It is because the reflected waves propagate along the direction marked with black arrows, as shown in Figure 4(b). As a result, the acoustic energy concentrates toward the symmetric axis of the metasurface. Figure 4(c) displays the normalized field distribution of squared absolute pressure along  $z$ -axis. As the coordinate increases to 8500 mm, the acoustic intensity reaches the peak value. In addition, the focused spot is very long. For example, the acoustic intensity is over 60% of the peak within a wide coordinate region ( $6000 \text{ mm} < x < 13000 \text{ mm}$ ). The field distribution of square absolute pressure along  $x$ -axis at  $z = 8500 \text{ mm}$  is exhibited in Figure 4(d). The high-intensity area in transverse direction is much narrower, compared with the longitudinal field distribution.

**4.2. Design of a Planar Acoustic Lens.** To design a planar acoustic lens, a hyperboloidal phase profile is employed on the metasurfaces. For a given focal length  $F$ , the phase distribution along the surface must satisfy the following equation:

$$\phi(x) = \frac{2\pi}{\lambda} \left( \sqrt{x^2 + F^2} - F \right), \quad (3)$$

where  $F$  is set to be 2000 mm. In order to construct this planar lens, 23 units were employed. The dimension of this lens is  $x \times z = 3200 \times 120 \text{ mm}$ . The simulated squared absolute pressure of the reflected field is shown in Figure 5(a), in which a distinct focal spot appears. The red arrows indicate the incident waves. Figure 5(b) exhibits the transient pressure field distribution of reflected waves. An arc wavefront can be observed, as represented by the black dashed line. The black arrows indicate the propagation direction of reflected waves, from which we can clearly observe the phenomenon of energy convergence. The longitudinal intensity distribution at  $x = 0$  is shown in Figure 5(c). The peak location is exactly at the focal spot,  $z = 2000 \text{ mm}$ . Figure 5(d) shows the transverse intensity distribution at  $z = 2000 \text{ mm}$ .

**4.3. Acoustic Nondiffracting Airy Beam.** The acoustic nondiffracting Airy beam has unique features, such as self-bending and self-healing [38]. To realize the Airy beam using our metasurface, we need to rearrange the units according to a specific phase gradient. The bending trajectory is specified to be an arc  $x = f(z) = \sqrt{r^2 - (z - r)^2}$  with the center at  $(x, z) = (0, r)$ . A plane wave propagating along the negative direction of  $z$ -axis is chosen as the incident beam. The desired

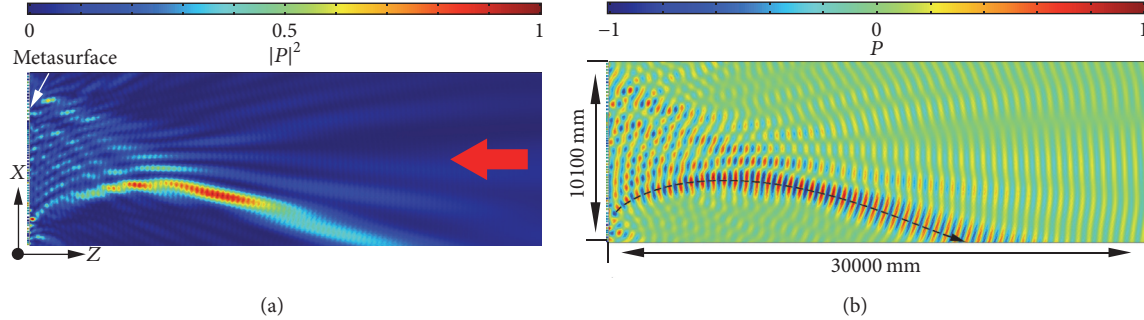


FIGURE 6: Acoustic nondiffracting Airy beam. (a) The squared absolute pressure field of reflected waves. The red arrows represent the propagation direction of incident plane wave. (b) The transient pressure field distribution of reflected waves. The black dashed arrow indicates the travel trajectory of the acoustic energy.

phase profile can be expressed as  $\phi(x) = k_0(x - 2r\sqrt{x/r})$ . In the simulations, the metasurface extends from 0 mm to 10100 mm along the  $x$ -axis. The arc radius is selected to be  $r = 5\lambda$ . Figures 6(a) and 6(b) exhibit the simulated squared absolute pressure and the transient pressure field distribution of the reflected waves, respectively. It is obvious that the reflected waves propagate along a bending trajectory, which makes the acoustic beam capable of bypassing obstacles on its path.

## 5. Conclusion

In summary, we designed a new kind of acoustic metasurface consisting of cubes with cylindrical cavities, whose endings are covered with elastic membrane and air gap. The simulated results demonstrate that this ultrathin acoustic metasurface (about  $\lambda/5$ ) can fully manipulate the propagation of sound waves. By employing linear phase gradient profiles, anomalous reflections were realized in a controllable manner. By utilizing nonlinear phase profiles, a planar lens and an axicon were constructed. Furthermore, an acoustic Airy beam was realized, which may find possible applications in the fields of biomedical ultrasound. As the structural dimensions of our units are the order of millimeter or even centimeter, the general 3D printing technology is ok for the future experimental preparation. The designed metasurface should open an avenue for the integration and miniaturization of acoustic equipment.

## Conflicts of Interest

The author declares that there are no conflicts of interest.

## Acknowledgments

This work was supported by the National Natural Science Foundation of China under Grant no. 11764033, Natural Science Foundation of Ningxia under Grant no. NZ17253, Higher School Science Research Project of Ningxia under Grant no. NGY2016173, Undergraduate Teaching Engineering Project in 2017 of Ningxia Normal University, and Ningxia Higher School First-Class Discipline Construction (Pedagogy) under Grant no. NXYLXK2017B11.

## References

- [1] Z. Liu, X. Zhang, Y. Mao et al., "Locally resonant sonic materials," *Science*, vol. 289, no. 5485, pp. 1734–1736, 2000.
- [2] N. Fang, D. Xi, J. Xu et al., "Ultrasonic metamaterials with negative modulus," *Nature Materials*, vol. 5, no. 6, pp. 452–456, 2006.
- [3] S. Yao, X. Zhou, and G. Hu, "Investigation of the negative-mass behaviors occurring below a cut-off frequency," *New Journal of Physics*, vol. 12, Article ID 103025, 2010.
- [4] S. H. Lee, C. M. Park, Y. M. Seo, Z. G. Wang, and C. K. Kim, "Composite acoustic medium with simultaneously negative density and modulus," *Physical Review Letters*, vol. 104, no. 5, Article ID 054301, 2010.
- [5] H. Chen, H. Zeng, C. Ding, C. Luo, and X. Zhao, "Double-negative acoustic metamaterial based on hollow steel tube meta-atom," *Journal of Applied Physics*, vol. 113, no. 10, Article ID 104902, 2013.
- [6] S. Zhai, H. Chen, C. Ding, and X. Zhao, "Double-negative acoustic metamaterial based on meta-molecule," *Journal of Physics D: Applied Physics*, vol. 46, no. 47, Article ID 475105, 2013.
- [7] S. L. Zhai, X. P. Zhao, S. Liu, F. L. Shen, L. L. Li, and C. R. Luo, "Inverse Doppler Effects in Broadband Acoustic Metamaterials," *Scientific Reports*, vol. 6, Article ID 32388, 2016.
- [8] C.-L. Ding and X.-P. Zhao, "Multi-band and broadband acoustic metamaterial with resonant structures," *Journal of Physics D: Applied Physics*, vol. 44, no. 21, Article ID 215402, 2011.
- [9] L. Fok and X. Zhang, "Negative acoustic index metamaterial," *Physical Review B: Condensed Matter and Materials Physics*, vol. 83, no. 21, Article ID 214304, 2011.
- [10] L. Zigoneanu, B.-I. Popa, A. F. Starr, and S. A. Cummer, "Design and measurements of a broadband two-dimensional acoustic metamaterial with anisotropic effective mass density," *Journal of Applied Physics*, vol. 109, no. 5, Article ID 054906, 2011.
- [11] Z. Yang, H. M. Dai, N. H. Chan, G. C. Ma, and P. Sheng, "Acoustic metamaterial panels for sound attenuation in the 50–1000 Hz regime," *Applied Physics Letters*, vol. 96, no. 4, Article ID 041906, 2010.
- [12] S. A. Kuznetsov, M. A. Astafev, M. Beruete, and M. Navarro-Ci  , "Planar holographic metasurfaces for terahertz focusing," *Scientific Reports*, vol. 5, article no. 7738, 2015.
- [13] A. Shalitout, J. Liu, V. M. Shalaev, and A. V. Kildishev, "Optically active metasurface with non-chiral plasmonic nanoantennas," *Nano Letters*, vol. 14, no. 8, pp. 4426–4431, 2014.

- [14] N. Yu, P. Genevet, M. A. Kats et al., "Light propagation with phase discontinuities: Generalized laws of reflection and refraction," *Science*, vol. 334, no. 6054, pp. 333–337, 2011.
- [15] X. Ni, Z. J. Wong, M. Mrejen, Y. Wang, and X. Zhang, "An ultrathin invisibility skin cloak for visible light," *Science*, vol. 349, no. 6254, pp. 1310–1314, 2015.
- [16] G. Zheng, H. Mühlenbernd, M. Kenney, G. Li, T. Zentgraf, and S. Zhang, "Metasurface holograms reaching 80% efficiency," *Nature Nanotechnology*, vol. 10, no. 4, pp. 308–312, 2015.
- [17] M. Dubois, C. Shi, Y. Wang, and X. Zhang, "A thin and conformal metasurface for illusion acoustics of rapidly changing profiles," *Applied Physics Letters*, vol. 110, no. 15, Article ID 151902, 2017.
- [18] C. Faure, O. Richoux, S. Félix, and V. Pagneux, "Experiments on metasurface carpet cloaking for audible acoustics," *Applied Physics Letters*, vol. 108, no. 6, Article ID 064103, 2016.
- [19] W. Tang and C. Ren, "Total transmission of airborne sound by impedance-matched ultra-thin metasurfaces," *Journal of Physics D: Applied Physics*, vol. 50, no. 10, Article ID 105102, 2017.
- [20] B. Liu, W. Zhao, and Y. Jiang, "Apparent Negative Reflection with the Gradient Acoustic Metasurface by Integrating Supercell Periodicity into the Generalized Law of Reflection," *Scientific Reports*, vol. 6, Article ID 38314, 2016.
- [21] X.-P. Wang, L.-L. Wan, T.-N. Chen, A.-L. Song, and F. Wang, "Broadband unidirectional acoustic cloak based on phase gradient metasurfaces with two flat acoustic lenses," *Journal of Applied Physics*, vol. 120, no. 1, Article ID 014902, 2016.
- [22] C. Shen, Y. Xie, J. Li, S. A. Cummer, and Y. Jing, "Asymmetric acoustic transmission through near-zero-index and gradient-index metasurfaces," *Applied Physics Letters*, vol. 108, no. 22, Article ID 223502, 2016.
- [23] C. Ding, X. Zhao, H. Chen, S. Zhai, and F. Shen, "Reflected wavefronts modulation with acoustic metasurface based on double-split hollow sphere," *Applied Physics A: Materials Science & Processing*, vol. 120, no. 2, pp. 487–493, 2015.
- [24] S. Zhai, H. Chen, C. Ding et al., "Ultrathin skin cloaks with metasurfaces for audible sound," *Journal of Physics D: Applied Physics*, vol. 49, no. 22, Article ID 225302, 2016.
- [25] Y. Li, B. Liang, X.-Y. Zou, and J.-C. Cheng, "Extraordinary acoustic transmission through ultrathin acoustic metamaterials by coiling up space," *Applied Physics Letters*, vol. 103, no. 6, Article ID 063509, 2013.
- [26] Y.-F. Zhu, X.-Y. Zou, R.-Q. Li et al., "Dispersionless manipulation of reflected acoustic wavefront by subwavelength corrugated surface," *Scientific Reports*, vol. 5, Article ID 10966, 2015.
- [27] H. Esfahlani, H. Lissek, and J. R. Mosig, "Generation of acoustic helical wavefronts using metasurfaces," *Physical Review B: Condensed Matter and Materials Physics*, vol. 95, no. 2, Article ID 024312, 2017.
- [28] H. Esfahlani, S. Karkar, H. Lissek, and J. R. Mosig, "Acoustic carpet cloak based on an ultrathin metasurface," *Physical Review B: Condensed Matter and Materials Physics*, vol. 94, no. 1, Article ID 014302, 2016.
- [29] G. Ma, M. Yang, Z. Yang, and P. Sheng, "Low-frequency narrow-band acoustic filter with large orifice," *Applied Physics Letters*, vol. 103, no. 1, Article ID 011903, 2013.
- [30] C. J. Naify, C.-M. Chang, G. McKnight, and S. R. Nutt, "Scaling of membrane-type locally resonant acoustic metamaterial arrays," *The Journal of the Acoustical Society of America*, vol. 132, no. 4, pp. 2784–2792, 2012.
- [31] C. J. Naify, C.-M. Chang, G. McKnight, and S. Nutt, "Transmission loss and dynamic response of membrane-type locally resonant acoustic metamaterials," *Journal of Applied Physics*, vol. 108, no. 11, Article ID 114905, 2010.
- [32] A. Leblanc and A. Lavie, "Three-dimensional-printed membrane-type acoustic metamaterial for low frequency sound attenuation," *The Journal of the Acoustical Society of America*, vol. 141, no. 6, pp. EL538–EL542, 2017.
- [33] H. Zhu and F. Semperlotti, "Anomalous Refraction of Acoustic Guided Waves in Solids with Geometrically Tapered Metasurfaces," *Physical Review Letters*, vol. 117, no. 3, Article ID 034302, 2016.
- [34] R. Yang, D. Li, D. Gao et al., "Negative Reflecting Meta-Mirrors," *Scientific Reports*, vol. 7, no. 1, article 5729, 2017.
- [35] K. Tang, C. Qiu, M. Ke, J. Lu, Y. Ye, and Z. Liu, "Anomalous refraction of airborne sound through ultrathin metasurfaces," *Scientific Reports*, vol. 4, article no. 6517, 2014.
- [36] Y. Li, B. Liang, Z.-M. Gu, X.-Y. Zou, and J.-C. Cheng, "Reflected wavefront manipulation based on ultrathin planar acoustic metasurfaces," *Scientific Reports*, vol. 3, article no. 2546, 2013.
- [37] Z. Lin, X. Guo, J. Tu, Q. Ma, J. Wu, and D. Zhang, "Acoustic non-diffracting Airy beam," *Journal of Applied Physics*, vol. 117, no. 10, Article ID 104503, 2015.
- [38] P. Zhang, T. Li, J. Zhu et al., "Generation of acoustic self-bending and bottle beams by phase engineering," *Nature Communications*, vol. 5, article no. 4316, 2014.

## Research Article

# Photocatalytic Surface Modification of PI Film for Electroless Copper Plating

Wenxia Zhao ,<sup>1</sup> Zenglin Wang,<sup>2</sup> Liang Qiao,<sup>3</sup> Shiwei Liu,<sup>1</sup> Hongjian Zhao,<sup>1</sup> and Yani Yan<sup>1</sup>

<sup>1</sup>School of Chemistry and Chemical Engineering, Ningxia Normal University, Guyuan 756000, China

<sup>2</sup>Key Laboratory of Applied Surface and Colloid Chemistry, Ministry of Education, School of Chemistry and Chemical Engineering, Shaanxi Normal University, Xi'an 710119, China

<sup>3</sup>Department of Chemical and Biological Engineering, University at Buffalo (SUNY), Buffalo, NY 14260, USA

Correspondence should be addressed to Wenxia Zhao; zwxchj2006@163.com

Received 21 October 2017; Accepted 12 December 2017; Published 14 January 2018

Academic Editor: Changlin Ding

Copyright © 2018 Wenxia Zhao et al. This is an open access article distributed under the Creative Commons Attribution License, which permits unrestricted use, distribution, and reproduction in any medium, provided the original work is properly cited.

This study investigated the surface modification of polyimide (PI) film through TiO<sub>2</sub> photocatalytic treatment. The effects of TiO<sub>2</sub> content, treatment duration, and UV power on the surface topography, surface contact angle, and adhesion strength of the surface-modified PI films were investigated. The results indicated that, after surface modification under the optimal photocatalytic conditions, the surface contact angle of the PI film decreased from 84.4° to 38.8°, and the adhesion strength between the PI film and the electroless copper film reached 0.78 kN/m. X-ray photoelectron spectroscopy analysis further demonstrated that carboxyl groups formed on the surface of the PI film after photocatalytic treatment. The surface hydrophilicity and adhesion strength of the surface-modified PI film were enhanced due to the numerous carboxyl groups formed on its surface. Therefore, the photocatalytic treatment is an environmentally friendly and effective method for the surface modification of PI films.

## 1. Introduction

Polyimides (PIs) possess many desirable traits, such as low dielectric constant, high breakdown voltage; good planarization, wear resistance, radiation resistance, inertness to solvents, and hydrolytic stability; low thermal expansion; long-term stability; and excellent mechanical properties. Given these attributes, PIs have been extensively used as substrates in the production of ultra-large-scale integrations, electronic packages, and circuit boards [1–3]. In several of these applications, the deposition of a metal layer on PI substrates is necessary to allow electrical conduction via interconnections [4]. However, poor adhesion strength between the copper film and the PI substrate is a serious problem in these applications.

Over the years, many studies have investigated surface modification methods for improving the adhesion of metals to PI film. The surfaces of PI films are commonly modified through plasma treatment [5–10], ion implantation [11, 12], chemical treatment [13–18], and UV/ozone treatment [19–21]. However, physical processes, such as plasma and ion implantation, require expensive equipment and are thus

associated with high investment costs. Chemical treatments, such as oxidation, polymer grafting, and etching, require expensive waste disposal. The surfaces of polymers can be modified with photoirradiation, which occurs through the formation of an electron-hole pair in the semiconducting material when the photon energy exceeds the band gap [22]. Photocatalysis has been received increasing attention as an advanced oxidation process due to its low cost and environmental friendliness. In addition, the high chemical stability of TiO<sub>2</sub> and the potential use of sunlight as the irradiation source make photocatalysis an attractive method for the surface modification of PI films.

Thomas reported that base hydrolysis and acidification resulted in the formation of poly(amic acid) on the surface of PI film [23]. In this study, we introduced a method that combines the surface formation of hydrophilic species and the cleavage of imide rings to enhance the adhesion of copper to PI film. The effects of TiO<sub>2</sub> content (0.5, 1.0, 2.5, and 5.0 g/L), UV light power (100 and 300 W), and treatment duration (10, 20, 30, and 40 min) on the surface topography, surface roughness, adhesion strength, and surface chemistry of the

TABLE 1: The compositions of the electroless copper plating bath.

Composition	Content
Copper sulfate ( $\text{CuSO}_4 \cdot 5\text{H}_2\text{O}$ )	10 g/L
Ethylenediaminetetraacetic acid disodium salt (EDTA·2Na)	30 g/L
Formaldehyde (HCHO, 37%)	3 ml/L
2,2'-Dipyridyl	15 mg/L
Poly(ethylene glycol) (PEG 1000)	0.5 g/L

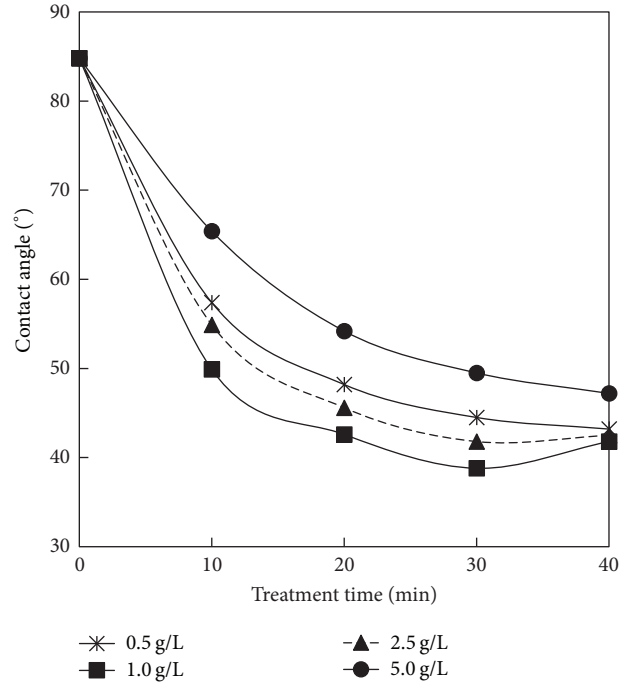
PI films were investigated. The surface topography and chemistry of the PI films were evaluated through scanning electron microscopy (SEM), atomic force microscopy (AFM), surface contact angle measurements, and X-ray photoelectron spectroscopy (XPS).

## 2. Experimental Section

PI films with a density of  $1.42 \text{ g/cm}^3$  were procured from DuPont Chemical Co., Ltd., as Kapton HN in rolls that were 40 mm wide and  $75 \mu\text{m}$  thick. The rolls were then cut into  $40 \text{ mm} \times 25 \text{ mm}$  samples for all experiments. Before photocatalytic treatment, the surfaces of the PI films were cleaned with acetone in an ultrasonic water bath for 30 min at room temperature and washed with deionized (DI) water. The photocatalysis experiments were conducted with a  $\text{TiO}_2$  suspension over the PI surface. Then, 0.5–5.0 g of  $\text{TiO}_2$  powder (JR05, Xuancheng Jingrui New Materials Co., Ltd., 5 nm), which was primarily in anatase phase, was dispersed in 1 L distilled water, respectively. Photocatalytic irradiation was conducted under a high-pressure mercury vapor lamp with a maximum wavelength of 365 nm. The distance between the PI film and the mercury lamp was fixed at 5 cm. After photocatalytic treatment, PI films were rinsed thrice with DI water.

The surface activation of the PI film was carried out in an activation solution (CATAPOSIT 44, purchased from Rohm and Haas Company) at  $45^\circ\text{C}$  for 5 min. Subsequently, the surface sensitization of the substrates was conducted by immersing the samples in 10% hydrochloric acid aqueous solution at  $30^\circ\text{C}$  for 1 min. The PI films were washed with distilled water after each step. The chemical composition of the electroless copper plating solution was the same as that in the literature [18], and the compositions are shown in Table 1. The pH of the solution was adjusted to 11.5 using NaOH, and the bath temperature was  $70^\circ\text{C}$ . After electroless plating for 40 min, the PIs were electroplated with copper at room temperature with a current density of  $0.03 \text{ A/cm}^2$  for 1 h. The copper layer was deposited at a thickness of  $20 \mu\text{m}$ . After annealing at  $100^\circ\text{C}$  for 120 min in an oven, the copper-coated PI films were cut into  $10 \text{ mm} \times 40 \text{ mm}$  strips. The adhesion strength of the PI films was measured through a  $90^\circ$  peel test at a peel rate of 25 mm/min [24]. The peel test was repeated four times, and the adhesion strength was reported as the average value of four measurements.

The surface topographies of the PI films were observed through SEM (Philips-FEI Quanta 200 electron microscope).

FIGURE 1: Dependence of the surface contact angle upon the  $\text{TiO}_2$  content and the treatment time under 300 W UV light.

Moreover, the surface roughness of the PI films was measured through AFM (WETSPM-9500-J3, Shimazu Co., Ltd.). Surface roughness was reported as average roughness ( $R_a$ ) and root-mean square roughness ( $R_{ms}$ ). The surface contact angles of the PI films were determined as quickly as possible after different time photocatalytic treatment with a video-based contact angle measurement instrument. The volume of the water drop used in the measurements was  $2 \mu\text{L}$ , and measurement values were taken at least five positions on the surface of the samples and averaged. The surface composition and chemistry groups of the PI films were determined by XPS measurements taken with a JPS90-MXV spectrometer from JEOL with a nonmonochromatized Mg Ka X-ray source. All binding energies were corrected on the basis of the C1s binding energy at 285 eV [25].

## 3. Results and Discussions

**3.1. Effects of UV Power and Treatment Time on the Surface Contact Angle of PI Films.** The wettability of the PI films was evaluated by measuring the surface contact angles of the film at room temperature. When the UV power was 300 W, effects of the  $\text{TiO}_2$  content and the treatment duration upon the surface contact angle were measured, and the results are shown in Figure 1. As seen in the figure, the surface without photocatalytic treatment PI film was hydrophobic. The contact angle between distilled water and the untreated PI film was  $84.8^\circ$ . The surface contact angle of the PI film continuously decreased with increasing treatment duration when the PI films were treated with  $0.5 \text{ g/L}$   $\text{TiO}_2$  suspension under 300 W of UV light, suggesting that  $0.5 \text{ g/L}$   $\text{TiO}_2$  content

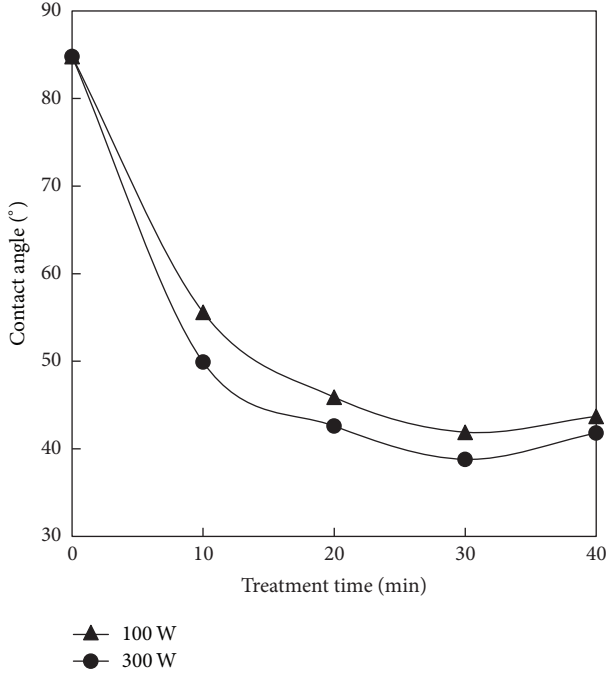


FIGURE 2: Dependence of the surface contact angle upon UV power and the treatment time at the  $\text{TiO}_2$  content of 1.0 g/L.

was insufficient for inducing hydrophilicity. The surface contact angle of the PI film treated with 1.0 g/L  $\text{TiO}_2$  suspension decreased with prolonged treatment duration and reached the minimum value with an irradiation time of 30 min; after that, the surface contact angle slowly increased with the further increase in the irradiation time. This result indicated that photocatalytic treatment induced the hydrophilicity of the PI film surface. Meanwhile, the surface contact angle of PI film treated with 1.0 g/L  $\text{TiO}_2$  suspension was considerably lower than that of the PI film treated with 5.0 g/L  $\text{TiO}_2$  suspension for the same treatment duration. This result was attributed to the agglomeration of  $\text{TiO}_2$  particles in the saturated  $\text{TiO}_2$  solution, because agglomeration decreases the oxidative capacity of generated  $\cdot\text{OH}$  radicals. Under 100 W of UV light, the change trend in the surface contact angle in response to  $\text{TiO}_2$  content and treatment duration was similar to that under 300 W of UV light. The results indicated that 1.0 g/L  $\text{TiO}_2$  suspension and 30 min of photocatalytic treatment are appropriate process parameters for the surface modification of PI film.

The effects of UV light power and treatment duration on the surface contact angle of PI films treated with 1.0 g/L  $\text{TiO}_2$  solution are shown in Figure 2. Under 100 and 300 W of UV light, the surface contact angle of the PI film first decreased with prolonged treatment time and reached the minimum value after 30 min of treatment, and then, the surface contact angle increased when treatment time was continuously prolonged. Furthermore, the surface contact angle decreased with increased UV power at the same treatment time and fixed  $\text{TiO}_2$  content. One potential reason for this result could be that the oxidation capacity of the photocatalytic system was strengthened by the increased intensity of UV light.

The roughness and hydrophilicity of the film surface affect the surface contact angle of the film. Specifically, the surface contact angle decreases with enhanced surface hydrophilicity and decreases with increasing surface roughness. Therefore, surface morphology and surface roughness observations were performed through SEM and AFM.

**3.2. Effects of Surface Modification on the Surface Morphology and the Surface Roughness of PI Substrates.** Figure 3 shows the changes in surface morphology before and after surface modification with 1.0 g/L  $\text{TiO}_2$  suspension under 100 or 300 W UV light. The wet-chemical pretreatment may induce changes in morphology and the removal of weakly cohesive surface material. Thus, the surface morphology of the film is very rough and uneven after wet-chemical pretreatment [26, 27]. However, as shown in Figure 3, the surface morphology of the PI film treated with 1.0 g/L  $\text{TiO}_2$  solution showed almost no change compared with that before photocatalytic treatment. Thus, the electroless copper film was more uniformly deposited through the photocatalytic reaction than through the wet-chemical pretreatment.

The AFM observations of the PI film morphology before and after pretreatment are shown in Figure 4. Before photocatalytic treatment, the PI film surface was flat and clean with  $R_a$  and  $R_{ms}$  of 13 and 17 nm, respectively.  $R_a$  and  $R_{ms}$  of the PI film modified under 100 W for 30 min were 14 and 19 nm, respectively. In addition,  $R_a$  and  $R_{ms}$  of the PI film modified under 300 W for 30 min were 15 and 21 nm, respectively. The results indicated that increasing UV power does not substantially change the surface topography of the PI films.

**3.3. Effects of Surface Modification on the Adhesion Strength.** The dependence of the adhesion strength on surface modification was investigated, and the results are shown in Figures 5 and 6. The adhesion strength between the electroless copper film and untreated PI film was zero. After photocatalytic treatment for 10 or 40 min, the adhesion strength between the electroless copper film and PI film increased with the increasing of  $\text{TiO}_2$  content when the treatment time was fixed. And the adhesion strength between the electroless copper film and PI film reached the highest value after the PI film was treated with 1.0 g/L  $\text{TiO}_2$  suspension. After that, the adhesion strength between the electroless copper film and PI film decreased when  $\text{TiO}_2$  content was further increased. It can be seen from Figure 6, when PI film was treated with 1.0 g/L  $\text{TiO}_2$  suspension, the adhesion strength between the electroless copper film and PI film increased with the increasing of UV power. Adhesion strength reached the maximum value when the PI film was treated for 30 min. This result was consistent with the changes in the surface contact angle of the PI film in response to  $\text{TiO}_2$  content, treatment duration, and UV power. Given that hydrophilicity can improve the wettability of the film surface, the overall increased wettability of the PI film improved the intimate contact between the PI substrate and the electroless deposited copper film.

Adhesion strength is dependent not only on the surface roughness but also on surface hydrophilicity or density of

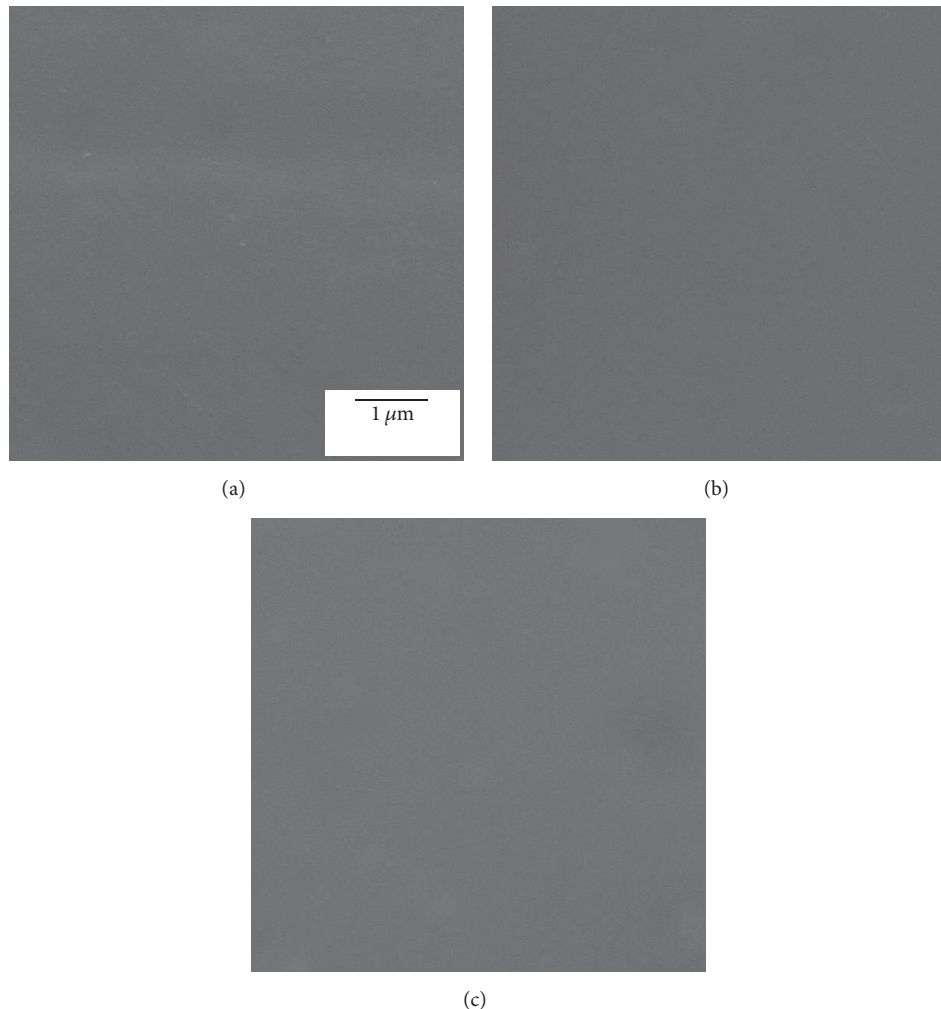


FIGURE 3: SEM images in surface morphology of PI films before and after surface modification with 1.0 g/L TiO<sub>2</sub> dispersed solution for 30 min, UV power: (a) 0 W, (b) 100 W, and (c) 300 W.

polar groups. Therefore, the effects of surface modification on the surface chemistry of PI films were investigated.

### 3.4. Surface Chemistry of the PI Film before and after $TiO_2$

**3.1. Surface Chemistry of the PI Film before and after  $\text{NO}_2$  Photocatalytic Treatment.** The surface chemical properties of the PI films before and after photocatalytic treatment were characterized by analyzing the XPS spectra of the PI films. The surface element contents of the PI films were determined through XPS, and the results are shown in Table 2. It can be seen that the carbon content decreased with the increasing UV power and the oxygen content increased with the increasing UV power. The surface carbon and oxygen contents of the untreated PI film were 78.2% and 15.8%, respectively. When the UV power was 300 W, after 30 min of photocatalytic treatment, the carbon content of the PI film decreased from 78.2% to 75.4%, and the oxygen content of the PI film increased from 15.8% to 19.3%. This result was attributed to the increased density of hydrophilic groups under increased UV power. The trend in the variation of the aforementioned elemental contents corresponded with that of the surface contact angle.

TABLE 2: The element contents of PI surface before and after surface modification with 1.0 g/L TiO<sub>2</sub> dispersed solution under different UV power.

Treatment condition	C (%)	O (%)	N (%)
Before treatment	78.2	15.8	6.0
100 W, 30 min	77.0	17.5	5.5
300 W, 30 min	75.4	19.3	5.3

The C1s XPS spectra of PI films before and after treated with 1.0 g/L TiO<sub>2</sub> and UV power of 300 W were obtained and the results are shown in Figure 7. Four peaks were observed in the spectrum of the PI film before photocatalytic treatment. The peaks at 285.0, 286.2, 288.6, and 291 eV were attributed to C-H/C-C/C=C, C-O/C-N, N(C=O)<sub>2</sub>, and  $\pi$ - $\pi^*$ , respectively. A peak at 289.0 eV appeared in the spectrum of the PI film treated with 1.0 g/L TiO<sub>2</sub> for 30 min under 300 W UV light. This peak could be attributed to the -COOH group. The same phenomenon was observed when the PI film was treated with 1.0 g/L TiO<sub>2</sub> for 30 min under 300 W UV light. The

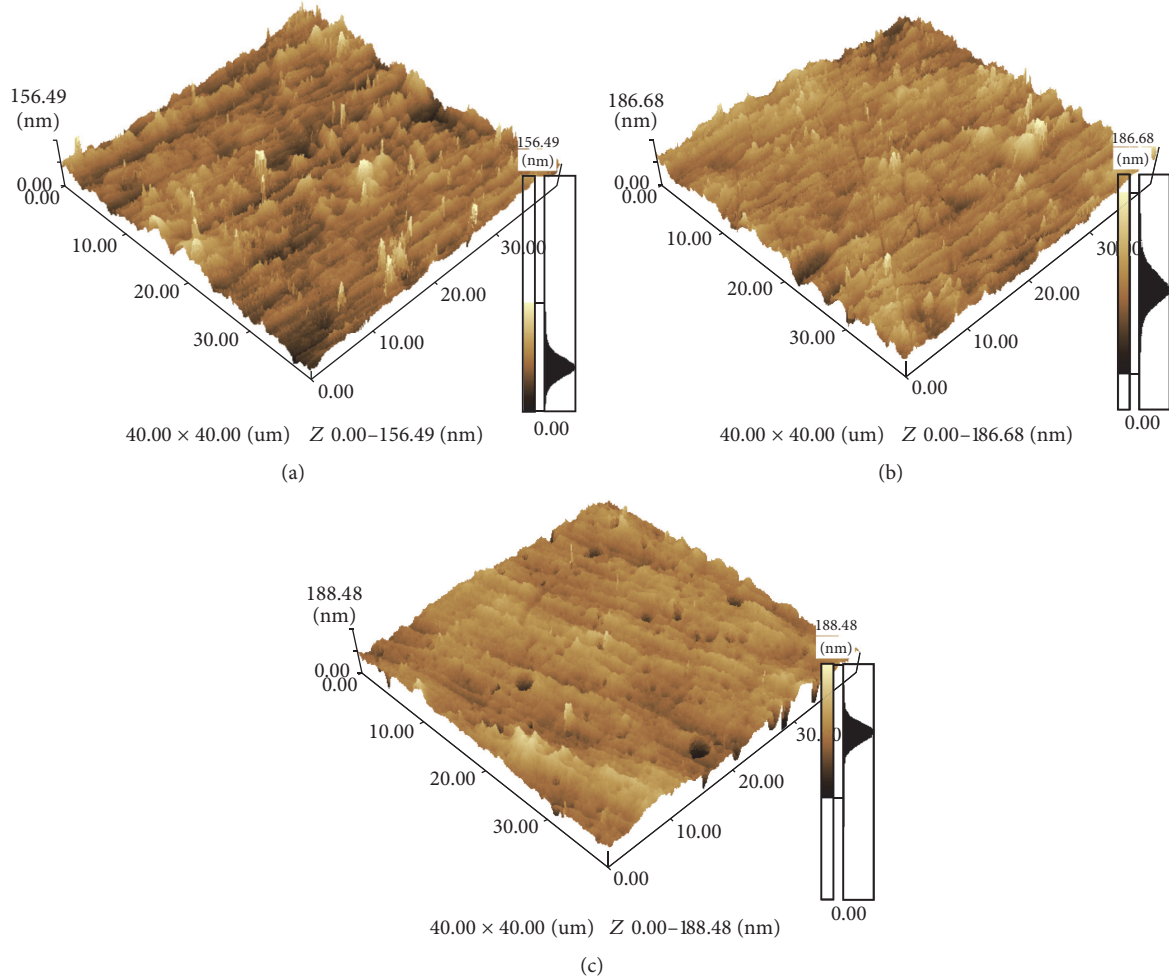


FIGURE 4: AFM images in surface morphology of PI films before and after surface modification with 1.0 g/L  $\text{TiO}_2$  dispersed solution for 30 min, UV power: (a) 0 W, (b) 100 W, and (c) 300 W.

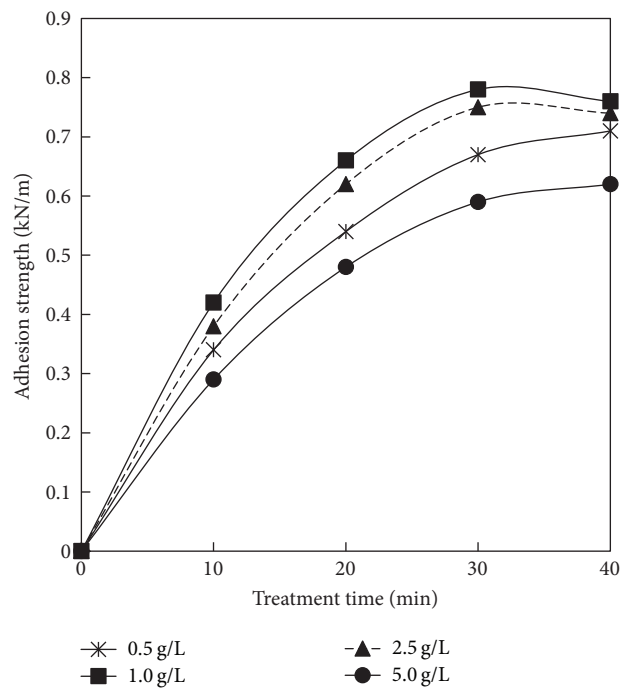


FIGURE 5: Dependence of the adhesion strength upon the  $\text{TiO}_2$  content and the treatment time under 300 W UV light.

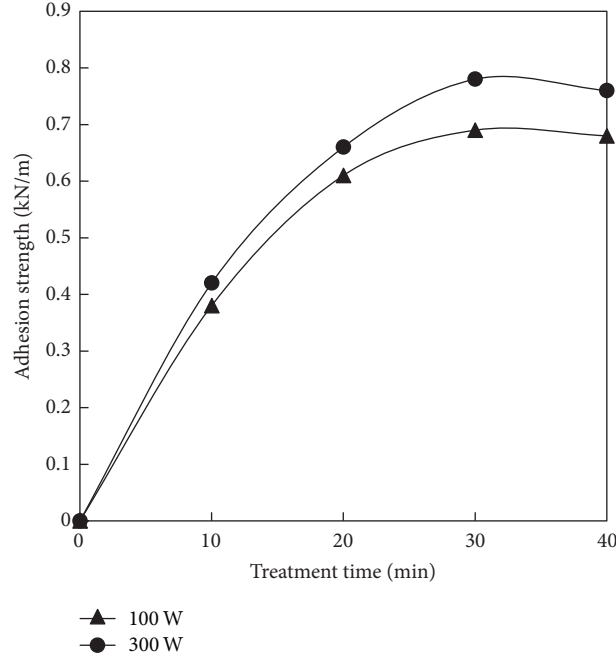


FIGURE 6: Dependence of the adhesion strength upon the UV power and the treatment time at the  $\text{TiO}_2$  content of 1.0 g/L.

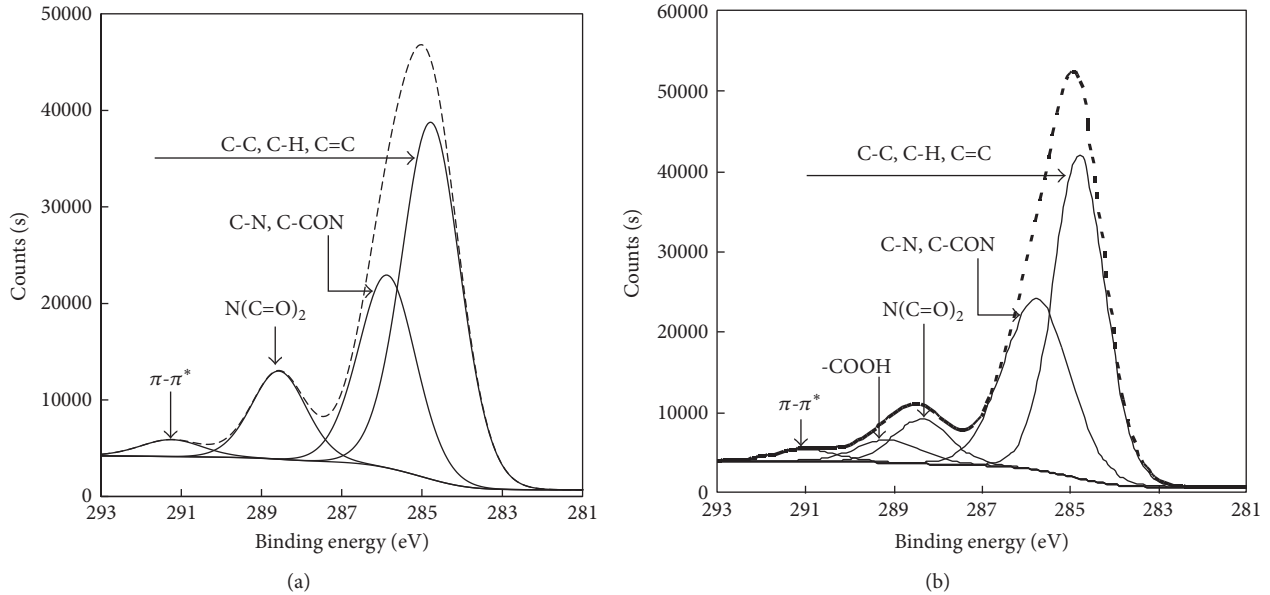


FIGURE 7: The C1s XPS spectra of the PI films before and after surface modification with 1.0 g/L  $\text{TiO}_2$  dispersed solution for 30 min under 300 W UV light. (a) The C1s XPS spectra of the PI films before surface modification. (b) The C1s XPS spectra of the PI films after surface modification.

carbon group contents of the PI films before and after being treated for 30 min under different UV powers and 1.0 g/L  $\text{TiO}_2$  content are shown in Table 3.

When the UV power increased from 0 W to 300 W, the content of hydrophobic groups ( $\text{C-H/C-C/C=C}$ ) decreased from 53.7% to 46.5%, that of the  $\text{N}(\text{C=O})_2$  group decreased from 14.8% to 6.8%, and that of  $\text{C-O/C-N}$  and  $\pi-\pi^*$  groups showed almost no change. However, the content of

hydrophilic groups ( $-\text{COOH}$ ) increased from 0% to 6.1%, indicating that partial bonds of the PI film were cleaved and that amide and carboxyl groups formed on the surface of PI films after treatment with  $\text{TiO}_2$ . Given that carboxyl and amide groups can coordinate with the copper atom, their quantities can affect the adhesion strength of copper film to the PI film [28]. As a result, the high contents of  $-\text{COOH}$  groups enhanced the surface hydrophilicity of the PI film and

TABLE 3: The contents of carbon groups on the PI film surface before and after photocatalytic treatment (treatment time: 30 min,  $C_{\text{TiO}_2}$ : 1.0 g/L).

UV power	C-C, C-H, C=C (%)	C-O, C-N (%)	$\text{N}(\text{C=O})_2$ (%)	$\pi-\pi^*$ (%)	-COOH (%)
0	53.7	38.7	14.8	2.8	0
100 W	48.0	37.6	7.3	2.2	4.9
300 W	46.5	38.3	6.8	2.3	6.1

thus improved the adhesion strength between the electroless copper film and the PI film.

## 4. Conclusion

An environmentally friendly and effective photocatalytic treatment method was used to modify PI films. The effects of  $\text{TiO}_2$  content, treatment duration, and UV power on the surface hydrophilicity and adhesion strength of the modified PI film were investigated through surface contact angle measurements, SEM observation, AFM, and XPS. The surface hydrophilicity and the adhesion strength of the photocatalytically treated PI film increased with increasing UV power and prolonged treatment duration. Surface modification with 1.0 g/L  $\text{TiO}_2$  suspension was more effective than with other  $\text{TiO}_2$  contents under 300 W of UV power. High  $\text{TiO}_2$  content facilitated the aggregation of  $\text{TiO}_2$  particles, thus decreasing the oxidative capacity of the hydroxyl radicals generated by the  $\text{TiO}_2$  suspension. Under the optimal conditions of photocatalytic treatment, the adhesion strength between the electroless copper film and the PI film reached 0.78 kN/m, and the surface topography and the surface roughness of the PI film slightly changed. XPS results indicated that surface oxygen content increased with prolonged treatment duration and increased UV power. Meanwhile, the surface carbon content decreased with prolonged treatment duration because the content of -COOH polar group increased. Photocatalytic treatment enhanced the surface hydrophilicity of PI film, thus resulting in high adhesion strength between the PI film and electroless copper film.

## Conflicts of Interest

The authors declare that there are no conflicts of interest regarding the publication of this article.

## Authors' Contributions

Wenxia Zhao and Zenglin Wang contributed equally to this paper.

## Acknowledgments

This work was partially supported by the Natural Science Foundation of China (Grants nos. 21561027 and 21273144), the Science and Technology Innovation Leading Talent Project of Ningxia Hui Autonomous Region (Grant no. Ning Ke Chuang Word [2016] 12), the Excellent Youth Teacher Training Fund Project for Institution of Higher Education of Ningxia (Grant no. NGY2016195), National Grade Academic

Technical Leader of Ningxia Youth Top-Notch Talent (Office of Human Resources and Social Security of Ningxia Grant no. [2017] 787), Liupanshan Resources Engineering Technology Center (Grant no. HGZDI7-03), and Key Disciplines of Inorganic Chemistry (Grant no. [2017] 83).

## References

- [1] K. S. Y. Lau, "High-Performance Polyimides and High Temperature Resistant Polymers," *Handbook of Thermoset Plastics*, pp. 297–424, 2013.
- [2] I. A. Ronova, M. Bruma, and H.-W. Schmidt, "Conformational rigidity and dielectric properties of polyimides," *Structural Chemistry*, vol. 23, no. 1, pp. 219–226, 2012.
- [3] D. Serbezeanu, I.-D. Carja, M. Bruma, and I. A. Ronova, "Correlation between physical properties and conformational rigidity of some aromatic polyimides having pendant phenolic groups," *Structural Chemistry*, vol. 27, no. 3, pp. 973–981, 2016.
- [4] S. Joshi, A. v. Loon, A. Savov, and R. Dekker, "Adhesion Improvement of Polyimide/PDMS Interface by Polyimide Surface Modification," *MRS Advances*, vol. 1, no. 01, pp. 33–38, 2016.
- [5] K. Fatyeyeva, A. Dahi, C. Chappay et al., "Effect of cold plasma treatment on surface properties and gas permeability of polyimide films," *RSC Advances*, vol. 4, no. 59, pp. 31036–31046, 2014.
- [6] Y. Zhang, E. T. Kang, K. G. Neoh et al., "Surface plasma characterization of polyimide films for flexible electronics," *Advanced Materials Research*, vol. 970, pp. 132–135, 2014.
- [7] A. B. Meddeb, Z. Ounaies, and M. Lanagan, "Enhancement of electrical properties of polyimide films by plasma treatment," *Chemical Physics Letters*, vol. 649, pp. 111–114, 2016.
- [8] W. Kaczorowski, W. Szymanski, D. Batory, and P. Niedzielski, "Effect of plasma treatment on the surface properties of polydimethylsiloxane," *Journal of Applied Polymer Science*, vol. 132, no. 11, Article ID 41635, 2015.
- [9] S.-H. Bang, "Improvement of NiMoNb to polyimide adhesion by inductively coupled nitrogen plasma treatment," *Applied Surface Science*, vol. 360, pp. 553–558, 2016.
- [10] M. Akram, K. M. B. Jansen, L. J. Ernst, and S. Bhowmik, "Atmospheric plasma modification of polyimide sheet for joining to titanium with high temperature adhesive," *International Journal of Adhesion and Adhesives*, vol. 65, pp. 63–69, 2016.
- [11] J. Won, M. H. Kim, Y. S. Kang et al., "Surface modification of polyimide and polysulfone membranes by ion beam for gas separation," *Journal of Applied Polymer Science*, vol. 75, no. 12, pp. 1554–1560, 2000.
- [12] R. Mikšová, A. Macková, H. Pupíkova, P. Malinský, P. Slepčka, and V. Švorčík, "Compositional, structural, and optical changes of polyimide implanted by 1.0 MeV Ni + ions," *Nuclear Instruments and Methods in Physics Research Section B: Beam Interactions with Materials and Atoms*, vol. 406, pp. 199–204, 2017.

- [13] F. J. Xu, J. P. Zhao, E. T. Kang, and K. G. Neoh, "Surface functionalization of polyimide films via chloromethylation and surface-initiated atom transfer radical polymerization," *Industrial & Engineering Chemistry Research*, vol. 46, no. 14, pp. 4866–4873, 2007.
- [14] Z. Wu, D. Wu, W. Yang, and R. Jin, "Preparation of highly reflective and conductive metallized polyimide films through surface modification: Processing, morphology and properties," *Journal of Materials Chemistry*, vol. 16, no. 3, pp. 310–316, 2006.
- [15] K. Akamatsu, S. Ikeda, H. Nawafune, and H. Yanagimoto, "Direct patterning of copper on polyimide using ion exchangeable surface templates generated by site-selective surface modification," *Journal of the American Chemical Society*, vol. 126, no. 35, pp. 10822–10823, 2004.
- [16] L. Li, Y. Ma, J. Xie et al., "Metallization Process of a Polyimide Surface with Palladium-Free Activation for Electronic Field Applications," *Journal of Electronic Materials (JEM)*, vol. 44, no. 10, pp. 4042–4051, 2015.
- [17] I. Ghosh, J. Konar, and A. K. Bhowmick, "Study of palladium catalyzation for electroless copper plating on polyimide film," *Journal of Nanoscience & Nanotechnology*, vol. 13, no. 1, pp. 517–522, 2013.
- [18] Z. Wang, A. Furuya, K. Yasuda et al., "Adhesion improvement of electroless copper to a polyimide film substrate by combining surface microroughening and imide ring cleavage," *Journal of Adhesion Science and Technology*, vol. 16, no. 8, pp. 1027–1040, 2002.
- [19] Y. I. Lee, Y. S. Goo, K. J. Lee, Y. G. Hwang, and Y. Byun, "Selective Cu patterning on polyimide using UV surface treatment and electroless plating," *Journal of Photopolymer Science & Technology*, vol. 28, no. 2, pp. 157–161, 2015.
- [20] Y.-I. Lee, Y.-S. Goo, K.-J. Lee et al., "Effect of UV/ozone treatment on interactions between ink-jet printed Cu patterns and polyimide substrates," *Thin Solid Films*, vol. 519, no. 20, pp. 6853–6857, 2011.
- [21] T. Kondo, R. Watanabe, Y. Shimoyama, K. Shinohe, S. A. Kulinich, and S. Iwamori, "Effect of reactive oxygen species generated with ultraviolet lamp and plasma on polyimide surface modification," *Surface and Interface Analysis*, vol. 49, no. 11, pp. 1069–1077, 2017.
- [22] H. Schmidt, M. Naumann, T. S. Müller, and M. Akarsu, "Application of spray techniques for new photocatalytic gradient coatings on plastics," *Thin Solid Films*, vol. 502, no. 1-2, pp. 132–137, 2006.
- [23] R. R. Thomas, "Wetting kinetics study of modified polyimide surfaces containing ionizable functional groups," *Langmuir*, vol. 19, no. 14, pp. 5763–5770, 2003.
- [24] Z. Wang, O. Yaegashi, H. Sakaue, T. Takahagi, and S. Shinogubara, "Suppression of native oxide growth in sputtered TaN films and its application to Cu electroless plating," *Journal of Applied Physics*, vol. 94, no. 7, pp. 4697–4701, 2003.
- [25] L. Chen, B. Liao, J. Yu et al., "Study of adhesion strength of electroplated copper to polyimide using different types of tie layers," *Nanoscience and Nanotechnology Letters (NNL)*, vol. 7, no. 3, pp. 240–247, 2015.
- [26] D. M. Brewis, "Electroless copper plating onto polyimide using polymer nanosheet as a nano-adhesive," *Polymer Journal*, vol. 39, no. 1, pp. 41–47, 2007.
- [27] K.-S. Chou, X.-Y. Chen, and I.-H. Lai, "Surface Roughness on Adhesion of Silver Colloids to a Polyimide Substrate," *International Journal of Adhesion and Adhesives*, vol. 92, no. 6, pp. 429–439, 2016.
- [28] T. Kondo, R. Watanabe, Y. Shimoyama, K. Shinohe, S. A. Kulinich, and S. Iwamori, "Effect of reactive oxygen species generated with ultraviolet lamp and plasma on polyimide surface modification," *Surface Interface Analysis*, vol. 49, no. 11, pp. 1069–1077, 2017.

## Research Article

# Tadpole-Shaped POSS-Based Copolymers and the Aggregation Behavior at Air/Water Interface

**Lin Zhu,<sup>1,2,3</sup> Fang Chen<sup>ID</sup>,<sup>1,2,3</sup> Xiaoyan Ma,<sup>1,2,3</sup> Xiu Qiang,<sup>2,3</sup> Zhiguang Li,<sup>2,3</sup> Chen Dong,<sup>2,3</sup> and Duyang Zang<sup>3</sup>**

<sup>1</sup>Research & Development Institute, Northwestern Polytechnical University, Shenzhen, China

<sup>2</sup>Key Laboratory of Polymer Science and Technology, Shaanxi Province, School of Science, Northwestern Polytechnical University, Xi'an 710129, China

<sup>3</sup>Key Laboratory of Space Applied Physics and Chemistry, Ministry of Education, School of Science, Northwestern Polytechnical University, Xi'an 710072, China

Correspondence should be addressed to Fang Chen; chenfang82081@nwpu.edu.cn

Received 21 August 2017; Accepted 18 October 2017; Published 1 January 2018

Academic Editor: Da-Ren Hang

Copyright © 2018 Lin Zhu et al. This is an open access article distributed under the Creative Commons Attribution License, which permits unrestricted use, distribution, and reproduction in any medium, provided the original work is properly cited.

The aggregation behavior of three tadpole-shaped Polyhedral oligomeric silsesquioxane (POSS) based block copolymers using different blocks poly(methyl methacrylate) (PMMA) and poly(trifluoroethyl methacrylate) (PTFEMA) with different block sequence and ratio (POSS-PTFEMA<sub>161</sub>-b-PMMA<sub>236</sub>, POSS-PMMA<sub>277</sub>-b-PTFEMA<sub>130</sub>, and POSS-PMMA<sub>466</sub>-b-PTFEMA<sub>172</sub>) was investigated on the air-water interface. The interfacial rheology of three block copolymers was studied by surface pressure isotherm, compression modulus measurements, and compression and expansion hysteresis analysis on the Langmuir trough. The block sequence and ratio play a great role in self-assembly behavior at the interface. Based on surface pressure isotherm analysis, a thin film with low elasticity was achieved for the POSS-PTFEMA<sub>161</sub>-b-PMMA<sub>236</sub>. Moreover, for the block copolymer with same segment sequence (POSS-PMMA<sub>2</sub>-b-PTFEMA), the thin film compression capability is increased with increasing the PMMA ratio. The morphology of the deposited LB thin film was illustrated by atomic force microscopy (AFM) and X-ray photoelectron spectroscopy (XPS). We observed that a thin film was composed by crater-shaped quasi-2D micelles for POSS-PTFEMA-b-PMMA, while it was proved that only flaky texture was observed for both POSS-PMMA<sub>277</sub>-b-PTFEMA<sub>130</sub> and POSS-PMMA<sub>466</sub>-b-PTFEMA<sub>172</sub>. The thickness and area of flaky aggregates were greatly related to PMMA ratio. The different interface self-assembly structure evolution was proposed based on the interfacial rheology and thin film morphology studies.

## 1. Introduction

Polyhedral oligomeric silsesquioxane (POSS), with the well-defined cage-like silica cubic nanoscale, has received considerable attention. POSS may be referred to as a silica nanoparticle consisting of a silica cage core, as well as other organic functional groups attached to the corners of the cage, which consist of hybrid organic-inorganic composition [1–3]. The cage-like core is a typical 3D hollow structure with a 1.5 nm scale, which provides excellent properties such as mechanical strength and dielectrical property. Moreover, the design ability and compatibility of POSS are improved by the higher reactivity of organic functional or reactive groups. Hence, POSS-based hybrid materials are widely applied in

packing, catalytic, thermal, and oxidative resistance, and a variety of hybrid nanocomposites [4–6].

Since reported by Seo and coworkers [7], interfacial self-assembly of POSS-based small molecules or polymers has attracted great interest during the past few decades. Subsequently, a variety of POSS-based small molecules or polymers were synthesized and the different self-assembly behavior was achieved as well [8–12]. Wamke et al. [13] successfully synthesized two open-cage TSiO-POSS and DSiB-POSS with short alkyl chains and compared the interfacial property of Langmuir monolayer. Jiang et al. [14] prepared a POSS-based amphiphilic supramolecule from the host-guest inclusion complexation between a mono adamantane-functionalized

TABLE 1: Characteristics of copolymers.

Sample	Total	Mean molecular weight (g/mol)		PDI
		PMMA	PTFEMA	
POSS-PTFEMA <sub>161</sub> - <i>b</i> -PMMA <sub>236</sub> ( <b>P1</b> )	52100	23600	27000	1.94
POSS-PMMA <sub>277</sub> - <i>b</i> -PTFEMA <sub>130</sub> ( <b>P2</b> )	50500	27700	21800	1.47
POSS-PMMA <sub>466</sub> - <i>b</i> -PTFEMA <sub>172</sub> ( <b>P3</b> )	76500	46600	28900	1.92

POSS (AD-POSS) and a  $\beta$ -cyclodextrin oligomer (P ( $\beta$ -CD)). Hollow nanospheres supramolecular hybrids with stable thick wall were obtained at the water/toluene interface. Gunawidjaja et al. [15] synthesized two series of organic-functionalized branched POSS with various hydrophobic-hydrophilic terminal groups probing different membrane assembly behavior among bulk state, monolayer, and multilayer films. Zhang et al. [16] designed and synthesized a new structure of amphiphilic copolymer brushes with POSS as side chains and their self-assembly behavior in aqueous media was also studied. The results showed that these alternating copolymer brushes could form spherical aggregates in water. Therefore, POSS is regarded as significant assembled materials at air/water interface since it can exhibit rich aggregated morphology and improve thermal and mechanical properties of thin films.

Diblock copolymers are a material of choice for achieving nanostructures based on phase separation between dissimilar blocks. And diblock copolymer monolayers with nanopattern and recognized assembling mechanism through interface self-assembly are increasingly studied [17–21]. Moreover, by changing structure and external condition such as temperature, irradiation, and pressure or by adding other substances, the tunable nanostructures with different size and shape could be achieved [22–28]. In particular, weakly amphiphilic diblock copolymers, containing both hydrophobic block and surface active but water insoluble block, are attractive for researchers due to excellent stability on the water surface, and the intermolecular interactions mainly drive the assembly of copolymers [29–32]. Therefore, the molecule structure such as chain segments, block ratio, and block sequence becomes a dominant influencing factor on aggregation behavior. Seo et al. [7, 22, 29, 33, 34] synthesized a series of Polystyrene-*b*-poly(methyl methacrylate) (PS-*b*-PMMA) diblock copolymers and found that these kind of copolymers could form ordered quasi-2D surface micelles at air/water interface. Moreover, the factors such as chemical constitutions, molecule weight, and block ratio could strongly affect the aggregation behavior and interfacial viscoelasticity. Li Destri et al. [30] further reported the viscoelastic behavior of three PS-*b*-PMMA copolymers with different block length ratio, proving that the viscoelastic behavior is changing from a predominantly elastic to a viscoelastic one before and after conformation transition. Chen et al. [35] found that the aggregation behavior of X-shaped block copolymers at air/water interface can be changed by the variation of the block sequence or temperature. Fluorinated copolymers, especially the fluorinated acrylate copolymers, are excellent choice for design weakly amphiphilic diblock copolymers due to hydrophobicity and high surface activity at air/water

interface [8, 36–41]. Zhu et al. [42] examined the formation of various PVDF Langmuir films. They found that the spreading solvents play a key role in the properties of PVDF Langmuir films at the air-water interface. Fluorinated materials are capable of self-migration to the surface, resulting in significant effect for surface properties [43–45].

In recent years, there are some very interesting works about combining the functional nanoparticles and copolymers in homogeneous system and constructed nanopatterned thin films. Although self-assembly of block copolymers and inorganic NPs complex have been studied in film form, few experiments of this sort have been conducted at the monolayer level on a Langmuir trough at air/water interface [40, 46, 47]. The copolymer's structure and nanoparticles' properties could both influence the interfacial aggregation behavior of thin films. Importantly, the resulting interaction between copolymers and nanoparticles, such as the location of nanoparticles within polymer matrices, the sequence they combined with each other, is considered to be of the predominant influencing factors in assemble process and received a lot attention [48–51].

Inspired by the above researches, we designed and synthesized three tadpole-shaped POSS-based PMMA-*b*-PTFEMA weakly diblock copolymers using step ATRP technique. Then the air/water interfacial aggregation behavior and surface morphology of all three copolymers were investigated using Langmuir-Blodgett technique. The result presented that all copolymers could form typical Langmuir thin films at air/water interface containing interesting patterns at air/water interface. The block sequence and ratio of PTFEMA-*b*-PMMA could affect the self-assembly behavior of copolymers in different way and reflected in the different properties. Meanwhile, these two factors both strongly affect the surface morphology of film.

## 2. Materials and Methods

**2.1. Materials.** The tadpole-shaped POSS-based copolymers used in this study were synthesized via atom transfer radical polymerization (ATRP) in our laboratory which is detailedly expressed in SI. The monofunctional POSS (POSS-Cl) was synthesized through vertex-cap measurement and used as initiator of ATRP. The structural characterizations of all three copolymers were verified by <sup>1</sup>H NMR spectra and GPC, as exhibited in Supporting Information. The structural characteristics of all three copolymers were shown Table 1 as a result.

**2.2. Langmuir Films and Langmuir-Blodgett Films.** The dilute solutions of all three copolymers were obtained via copolymers dissolved in chloroform. Concentration of 0.3 mg/mL

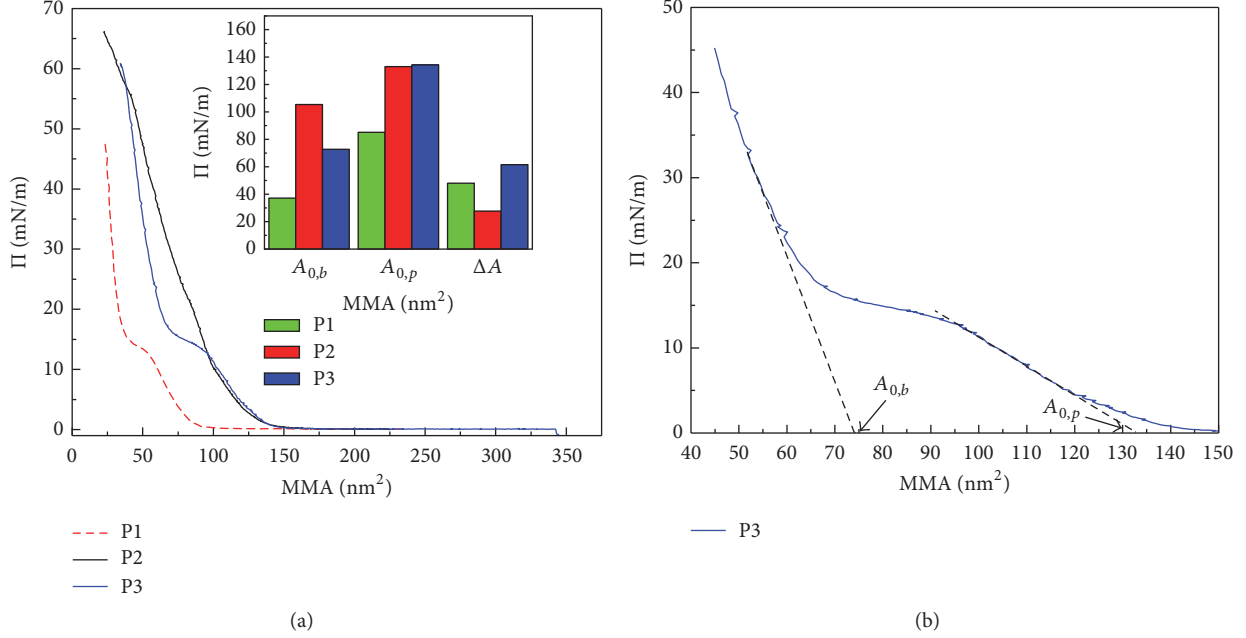


FIGURE 1: (a).  $\pi$ -MMA isotherm of all three copolymers at the air-water interface upon compression. The graph in top right corner is histogram of the characteristic limiting mean molecule area of all three copolymers for region 2 and region 3. (b). The calculation method of  $A_{0,p}$  and  $A_{0,b}$ .

and copolymer additive weight of 0.02 mg were employed for all dilute solutions. In order to make sure of the complete dissolution of copolymers, solutions were put in room temperature for at least 12 h before preparing Langmuir films. The Langmuir films and Langmuir-Blodgett Films were accomplished using the Langmuir trough with a surface of  $200 \times 310 \text{ mm}^2$  (JML04C3, power each Ltd., China) and equipped with surface pressure measurement, Langmuir-Blodgett film deposition. The subphase water was purified using an ultrapure water system. To prepare the Langmuir film, solutions were deposited drop by drop in a grid pattern on ultrapure water surface. Thirty minutes were allowed to wait for evaporating the solvent before compression. The surface was symmetrically compressed by barriers advancing at a speed of 9.71 mm/min. The glass substrate was immersed under the water before the polymer solution spread onto the water surface. It has been 30 min after chloroform volatilization that the submerged substrate was lifted vertically with a speed of 4.5 mm/min. All procedures are applied under 25°C.

**2.3. Atomic Force Microscopy.** All the LB films samples were scanned out with AFM (SPM-9700, Shimadzu, Japan) in tapping mode using silicon probes (FMR-10, Nanoworld, USA). Silicon cantilevers (MikroMasch) with a characteristic resonance frequency of 75 kHz and a force constant of 2.8 N/m were used. Tips had a radius of curvature of 10 nm.

**2.4. X-Ray Photoelectron Spectroscopy.** Structural properties of the LB films were characterized by XPS (K-Alpha, East Grinstead, England) with monochromatic Al Ka X-ray

excitation ( $h\nu = 1486.6 \text{ eV}$ ). The spectrum was analyzed by means of XPS-peak-differentiation-imitating.

### 3. Results and Discussion

**3.1. Surface Pressure-Mean Molecular Area ( $\pi$ -MMA) Isotherms.** After spreading polymer solution at the air/water interface in Langmuir trough, the surface pressure of copolymers is plotted as function of mean molecular area ( $\pi$ -MMA). By studying the  $\pi$  as a function of MMA, the aggregation behavior of copolymer at different surface pressure could be specifically revealed. Figure 1(a) showed the  $\pi$ -MMA isotherm obtained by all three copolymer solutions spreading on Langmuir trough and laterally compressed. The considerable large occupied molecular area is observed by all Langmuir films under low surface pressure in Region 1. Actually the surface pressure is close to 0 mN/m like pure water. There is no contact and interaction between each molecule at that region. Tiny difference of three copolymer films aggregation in region 1 is revealed, caused by large distance among molecules and similar molecular structures. Moreover, by Maestro et al's study [52, 53], the ester groups of PMMA and PTFEMA blocks tend to point downward the water phase. We supposed that the two blocks are partially immersed in the subphase (water). Meanwhile, the hydrophobic POSS float on the subphase to avoid unfavorable interaction with water. The initial compression causes only a decrease of distance among molecules.

In region 2 shown in Figure 1(a), all the isotherms present steeper slope than region 1, which indicate that the surface

pressure starts to increase with the decrease of MMA. P2 and P3 showed highly similarity of compression curve in region 2. But different behavior is detected between P1 and P2(P3) with respect to difference in slope of region 2. Besides, The limiting MMAs of the pancake and brush conformations ( $A_{0,p}$  and  $A_{0,b}$ , resp.) could be quantified by extrapolating tangents to the inflection points of the  $\pi$ -MMA curves to a surface pressure of zero in Figure 1(a). The difference of limiting MMA ( $\Delta A_{\text{pseudoplateau}}$ ) is an effective quantitative approach to determine the compressibility and a direct evidence of different self-assembly behavior during compression.

$A_{0,p}$  could provide information of the initial molecular spreading conformation of copolymer in region 2, which mainly depends on the block sequence and molecular weight. P1 shows a relative smaller  $A_{0,p}$  due to the more interaction between terminal PMMA groups compared to P2. And P3 presents the biggest  $A_{0,p}$  among the three copolymers mainly due to the highest molecular weight and longer PMMA block length. During compression, the phase-transition limiting area  $A_{0,b}$  will represent self-assembly behavior and rearrangement based on the difference in intermolecular interaction. It is shown that P1 still presents lowest value of  $A_{0,b}$ . When PMMA lies between POSS and PTFEMA blocks (P2 & P3), smaller  $A_{0,b}$  is observed for P3 due to the higher compressibility.

It is reasonable to propose P1 with the higher compressibility by comparing  $A_{0,b}$  in region 2 of P1 and P2, due to the direct bonding between PTFEMA blocks and POSS. Moreover, the block copolymer with longer PMMA length (P3) exhibits higher compressibility in a more compacted state (region 3) while the block sequence is the same.  $\Delta A_{\text{pseudoplateau}}$  further describes the compressibility of the three copolymer films from region 2 to region 3. P3 presents the highest  $\Delta A_{\text{pseudoplateau}}$  value attribute to the longest PMMA ratio. It is worth noting that although P1 could easily aggregate, some determined self-assembly structure might be formed and the compressibility is hard to change during the compression.

**3.2. Compression Modulus Isotherms.** The compression modulus represents the interfacial rheology of the formed Langmuir films at air/water interface; it can be obtained from the slope of  $\pi\text{-}\Gamma$  or  $\pi\text{-}A$ :

$$E = \Gamma \left( \frac{\partial \pi}{\partial \Gamma} \right). \quad (1)$$

The  $E\text{-}\Gamma$  plots will provide very important information such as the thin film rigidity and the ability of storing elastic energy. In general, high density of packed molecules will be determined by showing a high  $E$  value in Langmuir film.

As shown in Figure 2, one can clearly determine the difference in thin film elasticity. After comparing  $E$  of P1 and P2, P1 thin film presents lower elasticity and higher compressibility due to the sequence of PMMA block. While the PMMA is the terminal block, less repulsion is detected between the nearby molecules during compressing. The P3 shows the maximum  $E$  value; it is probable because interaction between PTFEMA adjacent molecular is stronger than

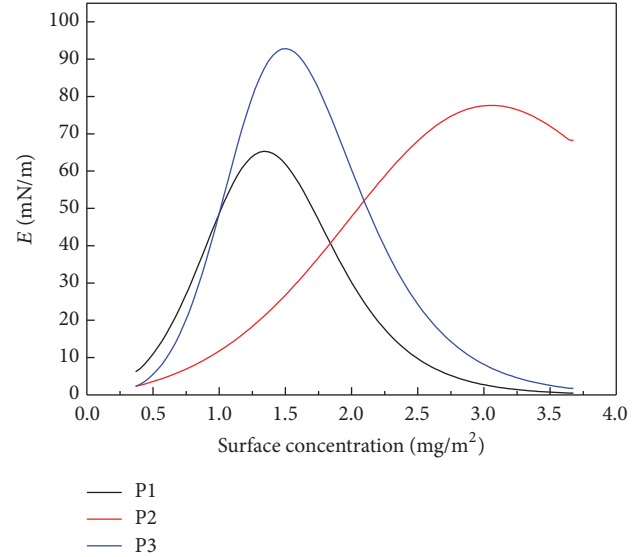


FIGURE 2:  $E$ -surface concentration plots of three block copolymers.

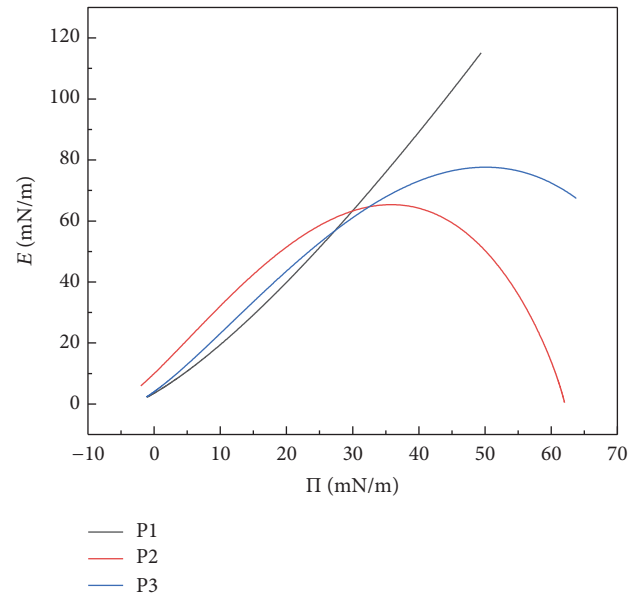


FIGURE 3: Compression modulus as a function of surface pressure of three copolymers.

that of P1. Meanwhile, the thin film is storing higher elastic energy attributed rearrangement during the compression for the P3 with longer PMMA block.

The surface pressure is assumed to be proportional to the surface density following a scaling law  $\pi\text{-}\Gamma^y$  with a scaling exponent  $y = 2v/(2v - 1)$  [54]. With the combination of the equilibrium compression modulus is as follows:  $E = y\Gamma$ . Three different regions are shown in the fitted curves, including dilute, semidilute, and concentrated. In the semidilute region, the compression modulus increased linearly with the increasing of surface pressure with a linear relationship. The  $E\text{-}\Gamma$  plots are shown in Figure 3, and  $y$  values are obtained by

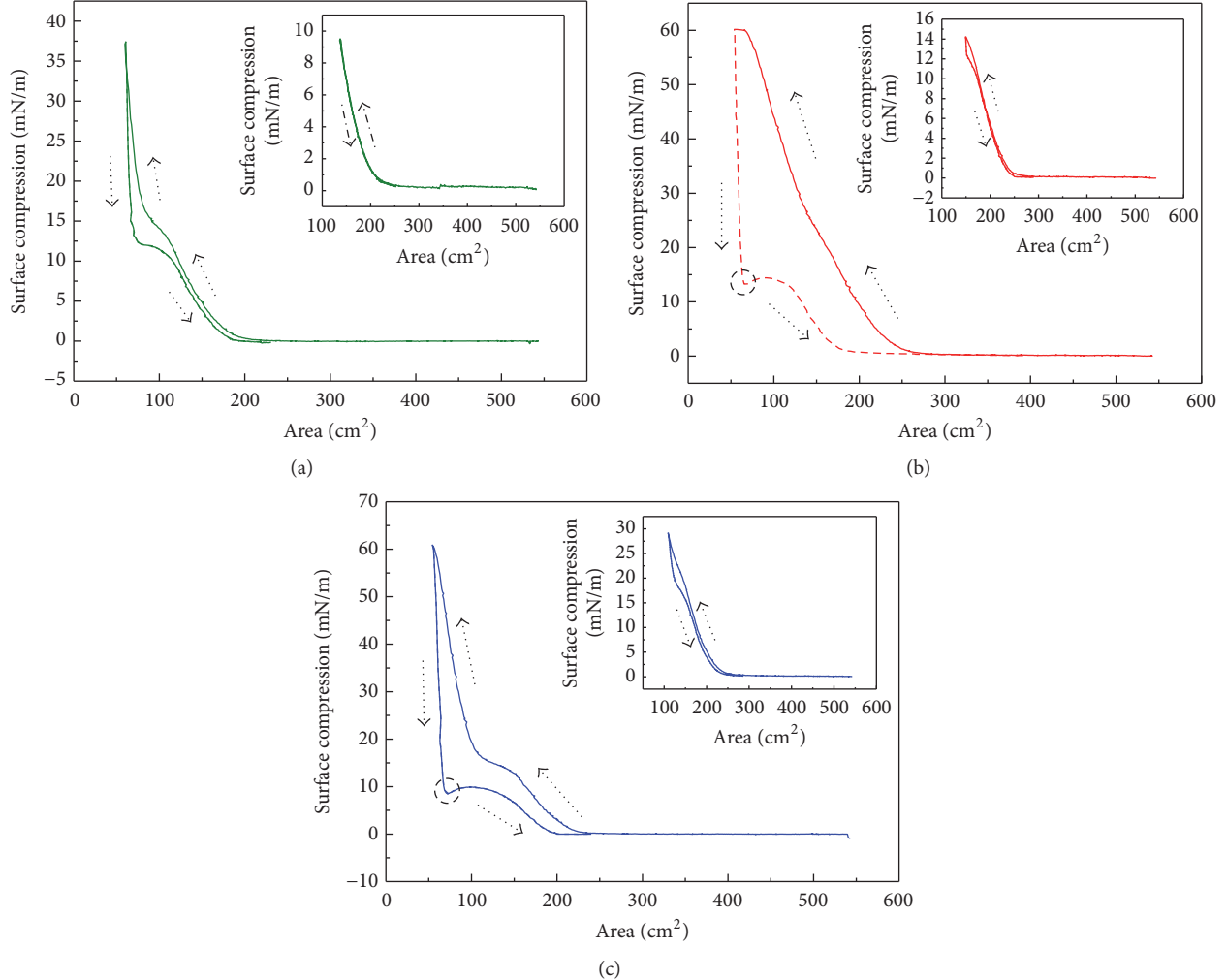


FIGURE 4: The hysteresis cycles of (a) P1, (b) P2, and (c) P3. The main graphs are hysteresis cycles observed at region 3. Each embedded graph at the top right corner of main graph is hysteresis cycles at region 2.

fitting the slope of semidilute region of  $E$ - $\Gamma$ , while the  $v_1$ ,  $v_2$ , and  $v_3$  are calculated as 0.5, 0.55, and 0.55, respectively. It is clear that the interface exhibits as a poor solvent for the three copolymers.

**Hysteresis.** To reveal the viscoelastic property of Langmuir films, the hysteresis cycles of P1, P2, and P3 formed thin films under pancake (inset images) and brush regions are, respectively, shown in Figures 4(a), 4(b), and 4(c). From the hysteresis cycles from three copolymers under pancake region (before liquid-solid transition), we could figure out the weak interaction between the molecules since no apparent hysteresis behavior is determined. However, different hysteresis behavior is obtained for all three copolymers in brush region during compression and expansion processes. It is worth noting that all the three copolymer present hysteresis loop in the brush region. In particular, surface pressures of both P2 and P3 drop to a certain area during the expansion process; there is an apparently minimum surface pressure observed and highlighted by dashed circles. During

expansion, the surface pressure is always lower than that of the compression at the same MMA. Based on Seo et al's arguments, the minimum surface pressure represents structural rearrangement under a slow compression and expansion rate due to higher compressibility of PMMA segment. In our cases, P2 and P3 showed a higher elasticity because of larger repulsion of terminal PTFEMA blocks. At the same time, the highest  $E$  of P3 are mainly attributed to higher entanglement among longer PMMA block. Among the hysteresis cycles of three copolymers, only the P1 does not show the minimum surface pressure during expansion, probably because a relative stable self-assembly structure is formed due to sequence and PMMA block and we will discuss that in the following morphology analysis.

**3.3. Surface Morphologies of Langmuir-Blodgett Films.** To characterize the interfacial aggregating behavior and thin film morphology formed in region 3, series of LB solid films are obtained using deposition on the glass substrate. AFM images of all three thin LB films are shown in Figure 5.

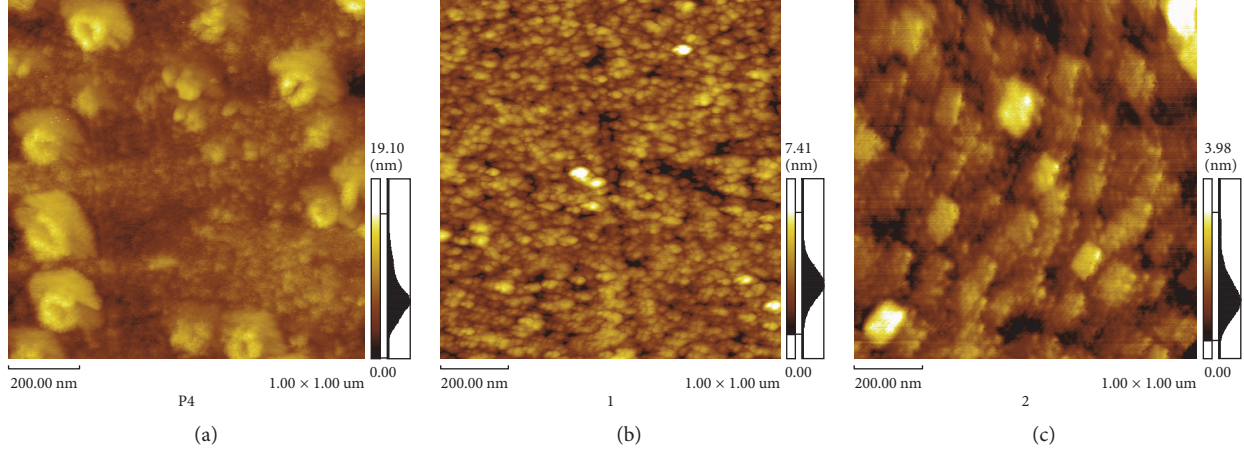


FIGURE 5: AFM images of thin film observed by P1 (a), P2 (b), and P3 (c) in region 3.

Figure 5(a) shows the morphology of LB film P1 formed. The micelles with volcano like structure are observed. The average thickness of the film is about 17.2 nm. Correspondingly, the films prepared by P2 and P3 are, respectively, shown in Figures 4(b) and 4(c). The morphology of two LB films was completely different with P1. The light areas consisted of PTFEMA blocks which cannot form micelle or other regular arrangement but constitute flaky texture. The average thicknesses of those two films are 7.4 nm and 3.9 nm, respectively. The great difference of thin film morphology and thickness is contributed to the different self-assembly behavior due to difference of block copolymer sequence. Based on the discussion of interfacial rheology, the lowest elasticity of P1 could easily be explained by the combination of AFM images. A core-corona shape 2D micelles is clearly detected from the AFM of P1 thin film; it probably formed due to the self-assembly during compression. Since both POSS and PTFEMA exhibit lower compressibility, the corona is formed by thick loop and tail structure to desorption of ester groups of PMMA as well as the higher compressibility of POSS and PTFEMA during compression. The light area in the images represents loop and tail structures of PTFEMA blocks, while compact PMMA blocks adsorbed on the surface form majority of dark area. Besides, when PMMA lies between POSS and PTFEMA blocks (P2 & P3), the possibility of loop and tail structures formation is decreased, which is attributed to the lower aggregation behavior between POSS and PTFEMA blocks. While the PMMA block lies as the terminal group, the compressibility of Langmuir films is mainly contributed to the formation of compact PMMA aggregation in region 3.

In order to further confirm the morphology of the three LB thin films, the surface elemental compositions of bulk material and the thin film are, respectively, analyzed by XPS as shown in Table 2. It is reasonable paying attention to Fluorine-to-Carbon (F/C) ratio which reflects the PTFEMA morphology at surface. Compared with the bulk material, a decrease of the F/C ratio is detected on LB film formed by P1, while increase of F/C ratio is observed by P2 and P3. It can be

TABLE 2: Surface elemental composition of three copolymers characterized by XPS.

Copolymer	Sample	C%	O%	F%	F/C
P1	Bulk	50.40	24.80	17.60	0.35
	LB film	38.77	41.20	8.43	0.22
P2	Bulk	52.40	14.70	14.70	0.28
	LB film	36.14	33.93	11.31	0.31
P3	Bulk	53.40	26.90	12.80	0.24
	LB film	34.74	32.86	11.70	0.34

explained by the different migration behavior of fluorine alkyl group during compressing process. On the other hand, the detection thickness of surface XPS is around 1 to 3 nm, which will only represent the top layer composition of the thin film. For the thin film formed by P1, the average film thickness is 17.2 nm, higher than XPS detection depth, so the surface composition is much influenced by coating effect, causing the obviously decrease of F/C ratio. It is quite possible that more PTFEMA chains are enshrouded and cannot be checked out due to the loop structure. In detail, the F/C ratio of the films is supposed to higher than the bulk materials. In the case of thin films formed by P2 and P3, PTFEMA block are easier to be compressed upward to the air/water interface due to the hydrophobicity of fluorine alkyl group. Therefore the upright of PTFEMA chain on the surface and the migration of fluoride to surface play a major role, increasing F/C ratio.

Based on the arguments from interfacial rheology and surface morphology, a qualitative surface morphology model of thin films formed by different copolymers is shown in Figure 6(a).

The PMMA domain (blue part) with minimum thickness is still adsorbed on the surface. The PTFEMA domain (red part) with higher thickness is almost absorbed from the surface and upward to air and exposed to air, forming loop and tail structures. The POSS particles (black part) are partly coated in the PTFEMA chain. Meanwhile, the micelles

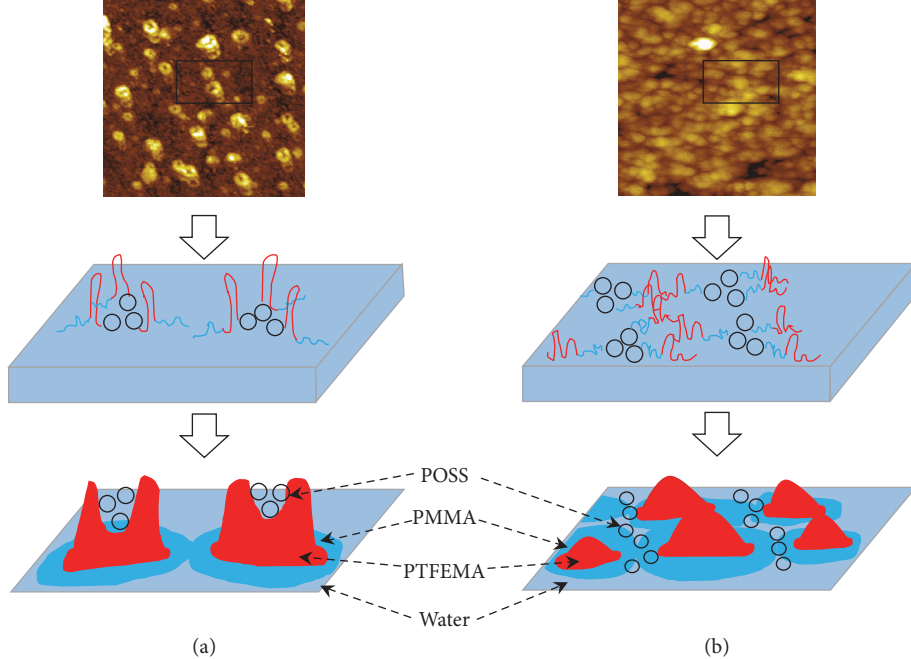


FIGURE 6: Qualitative surface morphology model of thin films formed by (a) P1, (b) P2, and P3 in high concentration at air/water interface.

showed a cave with certain depth in center of these cores, forming what we call crater-shaped structure.

Figure 6(b) showed the qualitative model of P2 formed LB film, the red PTFEMA chain only compressing to a relatively low level, and the blue PMMA chain is still absorbed on the subphase; the POSS particles are distributed around, coated in, or covered on the PTFEMA chain. P3 formed monolayer was similar as P2 and we just use the same model. The conclusion is that P2 is more likely to form thicker and sharper morphology of film like needle felting at region 3 while P3 tends to form lower and gentle terrains like mastoid.

**3.4. The Interfacial Self-Assembly Structure Evolution.** From the  $\pi$ -MMA isotherms, hysteresis cycles, AFM images, and XPS analysis, we could propose the mechanism of the two dimensional aggregation of all three tadpole-shaped POSS-based copolymers at air/water interface, shown in Figure 7.

At the initial stage of compression (region 1), all three copolymers freely stretch at the air/water interface and P1 is taken as representative. Both PMMA and PTFEMA blocks are adsorbed on the interface and the thickness of Langmuir film is limited. All three copolymers present free conformations change in two dimension in region 1. As compressing in region 2, the molecules begin to touch with each other. PTFEMA and PMMA blocks are, respectively, aggregated to adapt to the decrease of surface area. The aggregation behavior of P1 formed film in this region is shown in Figure 6. The quasi-2D micelles were initially formed, which showed the core-corona micelles with the POSS core and looped PTFEMA and PMMA as corona. For P2 and P3, although the PTFEMA blocks aggregated upward to the air, but with restriction to the location of PTFEMA and PTFEMA blocks,

the POSS core was only distributed around the PMMA aggregation and quasi-2D micelle cannot be formed.

With the deeper compression process, copolymer concentration at air/water interface was increased. The morphology of P1 formed film was shown in Figure 6(a). In this region, the desorption of ester groups from PTFEMA occurred; most of PTFEMA blocks were exposed to air to form loop and tail structures with further compressing. Much thicker film with specific quasi-2D micelles is further obtained. Besides, the morphology of P2 and P3 formed films is, respectively, shown in Figures 6(b) and 6(c). Obviously there's no any micelle formed, but only the flaky texture without regular pattern is shown. The thickness of loop and tail structures caused by further compressing is much lower than P1. As the thickness of film mainly depended on PMMA ratio; P2 formed film is thicker than P3. In brief, the intermolecular force on the interface plays a great role in thin film structure. A weak intramolecular repulsion is determined for P1 and the thin film could form 2D micelle structure due to the low elasticity. And thin film of P3 showed flaky aggregates mainly due to the higher intermolecular repulsive force.

#### 4. Conclusion

In this work, the air/water interfacial self-assembly of tadpole-shaped fluorine containing POSS-based copolymers with different sequence and block ratio was carried out by Langmuir technique. Based on study of the interfacial rheology, the relationship between compressibility of the thin film and molecular structure of the block copolymer is illustrated. While two blocks are shown in comparable length, the compressibility was higher while POSS and

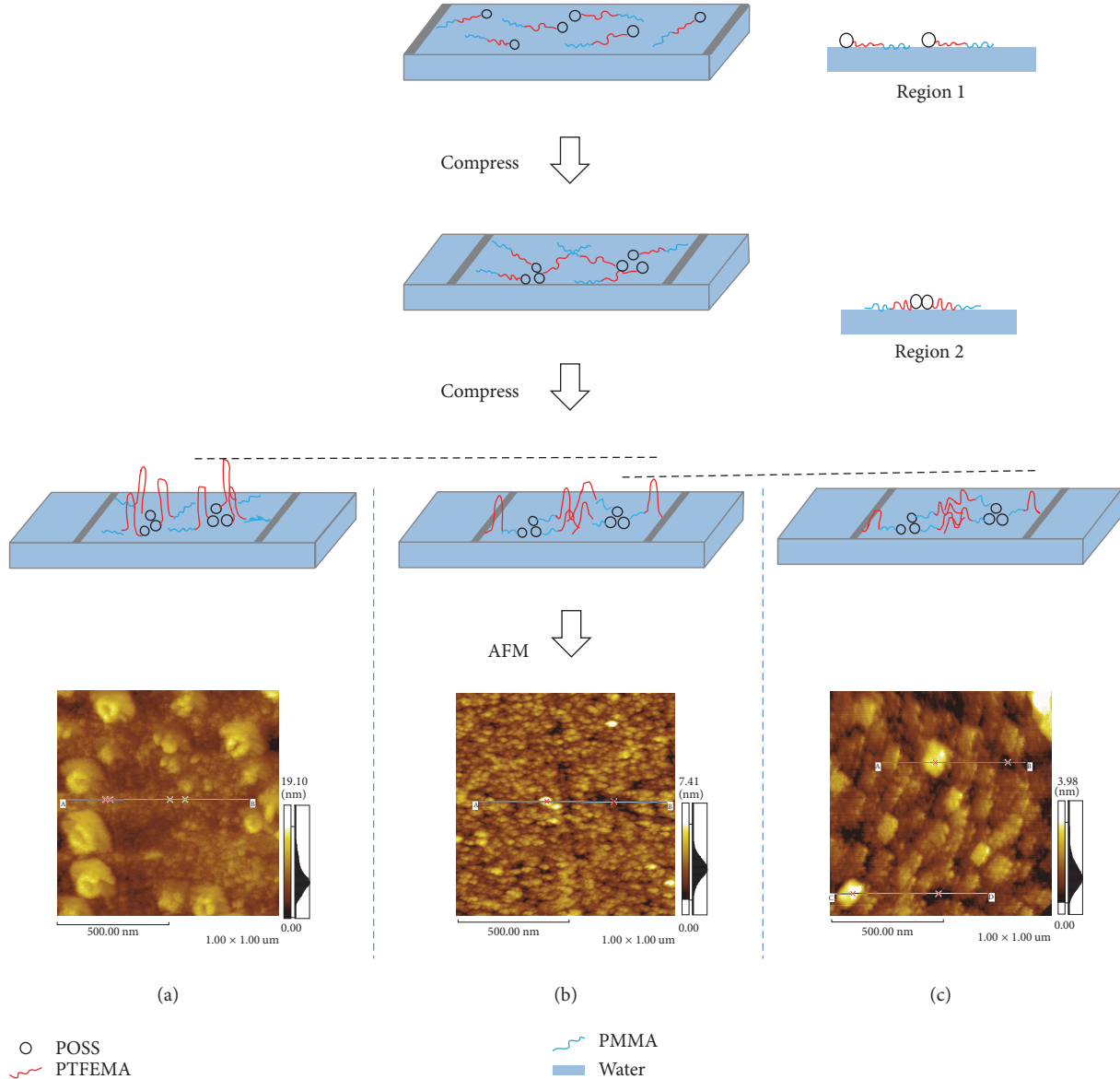


FIGURE 7: Mechanism for the formation of copolymer POSS-PTFEMA-*b*-PMMA at air/water interface during compressing process.

PTFEMA were connected to each other. However, P2 and P3 both showed higher elasticity because of larger repulsion of terminal PTFEMA blocks and P3 presented higher compressibility attribute to entanglement between nearby PMMA blocks. The formation of quasi-2D micelle with core-corona during compression of P1 was proved by analyzing the AFM images and XPS. Accordingly, copolymers POSS-PMMA<sub>277</sub>-*b*-PTFEMA<sub>130</sub> and POSS-PMMA<sub>466</sub>-*b*-PTFEMA<sub>172</sub> could form gentle terrains like mastoid. The thickness and diameter of mastoid were greatly related to PMMA block ratio as well.

## Conflicts of Interest

The authors declare no potential conflicts of interest.

## Acknowledgments

This research is supported by Natural Science Foundation of Shaanxi Province (no. 2016JM2023) and Natural Science Foundation of Shenzhen (JCYJ20170306161101003).

## Supplementary Materials

Figure S1. Synthesis route of POSS-PTFEMA-*b*-PMMA. Figure S2. <sup>1</sup>H NMR spectra of POSS-Cl and all three tadpole-shaped copolymers: (a) POSS-Cl, (b) POSS-PTFEMA-*b*-PMMA, (c) POSS-PMMA<sub>1</sub>-*b*-PTFEMA, and (d) POSS-PMMA<sub>2</sub>-*b*-PTFEMA. Table S1. Characteristics of all three copolymers. (*Supplementary Materials*)

## References

- [1] K. Pielichowski, J. Njuguna, B. Janowski, and J. Pielichowski, "Polyhedral oligomeric silsesquioxanes (POSS)-containing nanohybrid polymers," in *Supramolecular Polymers Polymeric Betains Oligomers*, vol. 201 of *Advances in Polymer Science*, pp. 225–296, Springer, Berlin, Germany, 2006.
- [2] D. Gnanasekaran, K. Madhavpan, and R. S. R. Reddy, "Developments of polyhedral oligomeric silsesquioxanes (POSS), POSS nanocomposites and their applications: a review," *Journal of Scientific and Industrial Research*, vol. 68, no. 6, pp. 437–464, 2009.
- [3] E. Ayandele, B. Sarkar, and P. Alexandridis, "Polyhedral Oligomeric Silsesquioxane (POSS)-containing polymer nanocomposites," *Nanomaterials*, vol. 2, no. 4, pp. 445–475, 2012.
- [4] X. T. Cao, A. M. Showkat, L. G. Bach et al., "Synthesis and characterization of photoluminescent hybrids of poly( $\epsilon$ -caprolactone)-grafted-polyhedral oligosilsesquioxane by using a combination of ring-opening polymerization and click chemistry," *Journal of the Korean Physical Society*, vol. 66, no. 1, pp. 108–112, 2015.
- [5] S. Li, Y. Liu, S. Ji, Z. Zhou, and Q. Li, "Synthesis and self-assembly behavior of thermoresponsive poly(oligo(ethylene glycol) methyl ether methacrylate)-POSS with tunable lower critical solution temperature," *Colloid and Polymer Science*, vol. 292, no. 11, pp. 2993–3001, 2014.
- [6] H. Hou, Y. Gan, J. Yin, and X. Jiang, "Multifunctional POSS-based nano-photo-initiator for overcoming the oxygen inhibition of photo-polymerization and for creating self-wrinkled patterns," *Advanced Materials Interfaces*, vol. 1, no. 9, Article ID 1400385, 2014.
- [7] Y. S. Seo, H. Yu, J. Kim, and S. Park, *Abstr Pap Am Chem S*, Thin-film behavior of polystyrene-block-poly(methyl methacrylate) diblock copolymer at the air-water interface. *Abstr Pap Am Chem S* 21, U419-U419, 1999.
- [8] X. Qiang, X. Ma, Z. Li, and X. Hou, "Synthesis of star-shaped polyhedral oligomeric silsesquioxane (POSS) fluorinated acrylates for hydrophobic honeycomb porous film application," *Colloid and Polymer Science*, vol. 292, no. 7, pp. 1531–1544, 2014.
- [9] J. Miao, L. Cui, H. P. Lau, P. T. Mather, and L. Zhu, "Self-assembly and chain-folding in hybrid coil-coil-cube tri-block oligomers of polyethylene-b-poly(ethylene oxide)-b-polyhedral oligomeric silsesquioxane," *Macromolecules*, vol. 40, no. 15, pp. 5460–5470, 2007.
- [10] K. Koh, S. Sugiyama, T. Morinaga et al., "Precision synthesis of a fluorinated polyhedral oligomeric silsesquioxane-terminated polymer and surface characterization of its blend film with poly(methyl methacrylate)," *Macromolecules*, vol. 38, no. 4, pp. 1264–1270, 2005.
- [11] A. C. Kucuk, J. Matsui, and T. Miyashita, "Erratum: Effects of hydrogen bonding on the monolayer properties of amphiphilic double-decker-shaped polyhedral silsesquioxanes (Langmuir (2011) 27 (6381) DOI:10.1021/la200604w)," *Langmuir*, vol. 27, no. 14, p. 9068, 2011.
- [12] Y. Seo, S. G. Youm, J. H. Kim et al., "Aggregation behavior of a polystyrene-b-poly(phenylsilsesquioxane) H-type copolymer at the air/water interface," *Polymer Journal*, vol. 53, no. 11, pp. 2223–2232, 2012.
- [13] A. Wamke, K. Dopierała, K. Prochaska, H. Maciejewski, A. Biadasz, and A. Dudkowiak, "Characterization of Langmuir monolayer, Langmuir-Blodgett and Langmuir-Schafer films formed by POSS compounds," *Colloids and Surfaces A: Physicochemical and Engineering Aspects*, vol. 464, pp. 110–120, 2015.
- [14] B. Jiang, W. Tao, X. Lu et al., "A POSS-based supramolecular amphiphile and its hierarchical self-assembly behaviors," *Macromolecular Rapid Communications*, vol. 33, no. 9, pp. 767–772, 2012.
- [15] R. Gunawidjaja, F. Huang, M. Gumenna et al., "Bulk and surface assembly of branched amphiphilic polyhedral oligomer silsesquioxane compounds," *Langmuir*, vol. 25, no. 2, pp. 1196–1209, 2009.
- [16] Z. Zhang, L. Hong, J. Li et al., "One-pot synthesis of well-defined amphiphilic alternating copolymer brushes based on POSS and their self-assembly in aqueous solution," *RSC Advances*, vol. 5, no. 28, pp. 21580–21587, 2015.
- [17] W. T. E. Bosker, M. A. Cohen Stuart, and W. Norde, "(Quasi-) 2D aggregation of polystyrene-b-Dextran at the air-water interface," *Langmuir*, vol. 29, no. 8, pp. 2667–2675, 2013.
- [18] Y.-S. Seo, F. Ahmad, K. Shin et al., "Interfacial behavior of randomly charged sulfonated polystyrene (PSS) at the air/water interface," *Colloids and Surfaces A: Physicochemical and Engineering Aspects*, vol. 313–314, pp. 660–665, 2008.
- [19] I. I. Perepichka, A. Badia, and C. G. Bazuin, "Nanostrand formation of block copolymers at the air/water interface," *ACS Nano*, vol. 4, no. 11, pp. 6825–6835, 2010.
- [20] T. J. Joncheray, K. M. Denoncourt, M. A. R. Meier, U. S. Schubert, and R. S. Duran, "Two-dimensional self-assembly of linear polyethylene oxide-b-poly( $\epsilon$ -caprolactone) copolymers at the air-water interface," *Langmuir*, vol. 23, no. 5, pp. 2423–2429, 2007.
- [21] Y.-S. Seo, K.-S. Kim, K. Shin et al., "Morphology of amphiphilic gold/dendrimer nanocomposite monolayers," *Langmuir*, vol. 18, no. 15, pp. 5927–5932, 2002.
- [22] Y. Seo, C. Y. Cho, M. Hwangbo, H. J. Choi, and S. M. Hong, "Effect of temperature on the interfacial behavior of a polystyrene-b-poly(methyl methacrylate) diblock copolymer at the air/water interface," *Langmuir*, vol. 24, no. 6, pp. 2381–2386, 2008.
- [23] H. Tanaka, Y. Kunai, N. Sato, and T. Matsuyama, "Effect of the graft chain length and density on the morphology of radiation-modified polysilane monolayers at the air/water interface," *Journal of Colloid and Interface Science*, vol. 363, no. 2, pp. 440–445, 2011.
- [24] I. I. Perepichka, Q. Lu, A. Badia, and C. G. Bazuin, "Understanding and controlling morphology formation in Langmuir-Blodgett block copolymer films using PS-P4VP and PS-P4VP/PDP," *Langmuir*, vol. 29, no. 14, pp. 4502–4519, 2013.
- [25] Q. Lu and C. G. Bazuin, "Solvent-assisted formation of nanostand networks from supramolecular diblock copolymer/surfactant complexes at the air/water interface," *Nano Letters*, vol. 5, no. 7, pp. 1309–1314, 2005.
- [26] I. I. Perepichka, K. Borozenko, A. Badia, and C. G. Bazuin, "Pressure-induced order transition in nanodot-forming diblock copolymers at the air/water interface," *Journal of the American Chemical Society*, vol. 133, no. 49, pp. 19702–19705, 2011.
- [27] V. Ferri, M. Elbing, G. Pace et al., "Light-powered electrical switch based on cargo-lifting azobenzene monolayers," *Angewandte Chemie International Edition*, vol. 47, no. 18, pp. 3407–3409, 2008.
- [28] J. M. Mativetsky, G. Pace, M. Elbing, M. A. Rampi, M. Mayor, and P. Samori, "Azobenzenes as light-controlled molecular electronic switches in nanoscale metal-molecule-metal junctions," *Journal of the American Chemical Society*, vol. 130, no. 29, pp. 9192–9193, 2008.

- [29] Y. Seo, A. R. Esker, D. Sohn, H.-J. Kim, S. Park, and H. Yu, "Study on the behaviors of different polystyrene-block-poly(methyl methacrylate) diblock copolymers adsorbed at the air/water interface," *Langmuir*, vol. 19, no. 8, pp. 3313–3322, 2003.
- [30] G. Li Destri, F. Miano, and G. Marletta, "Structure-rheology relationship in weakly amphiphilic block copolymer langmuir monolayers," *Langmuir*, vol. 30, no. 12, pp. 3345–3353, 2014.
- [31] G. Liu, S. Yang, and G. Zhang, "Conformational changes of poly(N-isopropylacrylamide) chains at air/water interface: Effects of temperature, compression rate, and packing density," *The Journal of Physical Chemistry B*, vol. 111, no. 14, pp. 3633–3639, 2007.
- [32] A. Brzozowska, J. Paczesny, P. Parzuchowski et al., "Hyperbranched polyesters terminated with alkyl chains of different length at the air/water interface and on solid substrates," *Macromolecules*, vol. 47, no. 15, pp. 5256–5268, 2014.
- [33] Y. Seo, J.-H. Im, J.-S. Lee, and J.-H. Kim, "Aggregation behaviors of a polystyrene-b-poly(methyl methacrylate) diblock copolymer at the air/water interface," *Macromolecules*, vol. 34, no. 14, pp. 4842–4851, 2001.
- [34] Y. Seo, K. Paeng, and S. Park, "Molecular weight effect on the behaviors of polystyrene-block-poly(methyl methacrylate) diblock copolymers at air/water interface," *Macromolecules*, vol. 34, no. 25, pp. 8735–8744, 2001.
- [35] Y. Chen, T. Liu, G. Xu et al., "Aggregation behavior of X-shaped branched block copolymers at the air/water interface: effect of block sequence and temperature," *Colloid and Polymer Science*, vol. 293, no. 1, pp. 97–107, 2014.
- [36] R. R. Thomas, D. R. Anton, W. F. Graham et al., "Preparation and surface properties of acrylic polymers containing fluorinated monomers," *Macromolecules*, vol. 30, no. 10, pp. 2883–2890, 1997.
- [37] B. B. Akhremitchev, B. K. Mohney, K. G. Marra, T. M. Chapman, and G. C. Walker, "Atomic force microscopy studies of hydration of fluorinated amide/urethane copolymer film surfaces," *Langmuir*, vol. 14, no. 15, pp. 3976–3982, 1998.
- [38] D. Han, L. Zhu, Y. Chen, W. Li, X. Wang, and L. Ning, "Synthesis of fluorosilicone monomer and application in hydrophobic surface of acrylic copolymer," *Journal of Applied Polymer Science*, vol. 132, no. 18, Article ID 41926, 2015.
- [39] H. Zou, S. Lin, Y. Tu et al., "Simple approach towards fabrication of highly durable and robust superhydrophobic cotton fabric from functional diblock copolymer," *Journal of Materials Chemistry A*, vol. 1, no. 37, pp. 11246–11260, 2013.
- [40] G. Li, A. Xu, B. Geng, S. Yang, G. Wu, and S. Zhang, "Synthesis and characterization of fluorinated diblock copolymer of 2,2,2-trifluoroethyl methacrylate and methyl methacrylate based on RAFT polymerization," *Journal of Fluorine Chemistry*, vol. 165, pp. 132–137, 2014.
- [41] Y. Zhang, Y. Wang, H. Zhang et al., "Synthesis and surface-active behavior of new fluorinated hyperbranched polymer," *Journal of Surfactants and Detergents*, vol. 17, no. 5, pp. 967–975, 2014.
- [42] H. Zhu, J. Matsui, S. Yamamoto, T. Miyashita, and M. Mitsuishi, "Solvent-dependent properties of poly(vinylidene fluoride) monolayers at the air-water interface," *Soft Matter*, vol. 11, no. 10, pp. 1962–1972, 2015.
- [43] A. Qu, X. Wen, P. Pi, J. Cheng, and Z. Yang, "Gradient distribution of fluorine on the film surface of the organic-inorganic hybrid fluoropolymer," *Colloids and Surfaces A: Physicochemical and Engineering Aspects*, vol. 345, no. 1-3, pp. 18–25, 2009.
- [44] B. J. Privett, J. Youn, S. A. Hong et al., "Antibacterial fluorinated silica colloid superhydrophobic surfaces," *Langmuir*, vol. 27, no. 15, pp. 9597–9601, 2011.
- [45] A. Stoffers, C. Oberdorfer, and G. Schmitz, "Controlled field evaporation of fluorinated self-assembled monolayers," *Langmuir*, vol. 28, no. 1, pp. 56–59, 2012.
- [46] R. B. Cheyne and M. G. Moffitt, "Controllable organization of quantum dots into mesoscale wires and cables via interfacial block copolymer self-assembly," *Macromolecules*, vol. 40, no. 6, pp. 2046–2057, 2007.
- [47] H. Li, R. Sachsenhofer, W. H. Binder et al., "Hierarchical organization of poly(ethylene oxide)-block-poly(isobutylene) and hydrophobically modified fe<sub>2</sub>o<sub>3</sub> nanoparticles at the air/water interface and on solid supports," *Langmuir*, vol. 25, no. 14, pp. 8320–8329, 2009.
- [48] S. S. Lamarre, C. Lemay, C. Labrecque, and A. M. Ritcey, "Controlled 2D organization of gold nanoparticles in block copolymer monolayers," *Langmuir*, vol. 29, no. 34, pp. 10891–10898, 2013.
- [49] S. S. Lamarre, H. Yockell-Lelièvre, and A. M. Ritcey, "Assembly of polystyrene-coated gold nanoparticles at the air-water interface," *Journal of Colloid and Interface Science*, vol. 443, pp. 131–s136, 2015.
- [50] R. B. Cheyne and M. G. Moffitt, "Hierarchical nanoparticle/block copolymer surface features via synergistic self-assembly at the air - Water interface," *Langmuir*, vol. 21, no. 23, pp. 10297–10300, 2005.
- [51] B. P. Gagnon and M.-V. Meli, "Effects on the self-assembly of n-Alkane/gold nanoparticle mixtures spread at the air-water interface," *Langmuir*, vol. 30, no. 1, pp. 179–185, 2014.
- [52] A. Maestro, H. M. Hilles, F. Ortega, R. G. Rubio, D. Langevin, and F. Monroy, "Reptation in langmuir polymer monolayers," *Soft Matter*, vol. 6, no. 18, pp. 4407–4412, 2010.
- [53] A. Maestro, F. Ortega, R. G. Rubio, M. A. Rubio, J. Kärgel, and R. Miller, "Rheology of poly(methyl methacrylate) Langmuir monolayers: Percolation transition to a soft glasslike system," *The Journal of Chemical Physics*, vol. 134, no. 10, Article ID 104704, 2011.
- [54] L. Dominique and M. Francisco, "Interfacial rheology of polyelectrolytes and polymer monolayers at the airwater interface," *Current Opinion in Colloid & Interface Science*, vol. 15, pp. 283–293, 2010.